UNIVERSITÀ DI PARMA

UNIVERSITA' DEGLI STUDI DI PARMA

DOTTORATO DI RICERCA IN
Scienza e Tecnologia dei Materiali

CICLO XXXVII

Control of electrical and structural properties in Ga_2O_3 epitaxy

Coordinatore:
Chiar.mo Prof. Enrico Dalcanale

Tutore:
Dr. Piero Mazzolini

Dottorando: Anna Sacchi

Anni Accademici 2021/2022 – 2023/2024

Abstract

The ultrawide bandgap semiconductor material gallium oxide (Ga_2O_3) features promising properties for next generation electronic devices. In particular, the bandgap of ≈ 5 eV, the high predicted breakdown field, the possibility to engineer its *n*-type conductivity through extrinsic doping, and the high chemical stability, are key factors to foresee its extensive application in the field of (power) electronics and optoelectronics devices, especially in the case of the thermodynamically stable β phase. In fact, this material system presents polymorphism: different metastable structures of Ga_2O_3 (α, β, γ, δ and κ) can be stabilized though various epitaxial growth techniques. Among the metastable polymorphs, κ-Ga_2O_3 has been theoretically predicted to be characterized by a large spontaneous polarization, driving significant interest into this material system. Nonetheless, for κ-Ga_2O_3 a throughout understanding over the structural and point defects towards the determination of its functional properties is still at the early stage. Therefore, the present work focuses primarily on these aspects related to the κ-Ga_2O_3 material system. The heteroepitaxy of κ-Ga_2O_3 results on various substrates in the formation of an intrinsically structurally defective structure (*e.g.*, vertically oriented rotational domains). This work investigates the defective nature of κ-Ga_2O_3 to gain a comprehensive understanding of its impact on the functional properties of this material, presenting the first evidence of defect-mediated in-plane transport. The study then explores potential strategies to mitigate the presence of structural defects in two different epitaxial growth techniques, MOVPE and MBE. Following the analysis of structural defects, the focus shifts to the role of point defects in κ-Ga_2O_3, offering a practical approach to engineer them through mild annealing treatments well-below its temperature stability threshold. In the final section, the diffusion of Li into different Ga_2O_3 structures is discussed, along with insights into the diffusion mechanism driven by the defective nature of the studied layer.

Abbreviations

2DEG	Two-dimensional electron-gas
3D	Three dimensional
AFM	Atomic force microscopy
ALD	Atomic layer deposition
APB	Anti-phase boundary
APT	Atom probe tomography
ARPES	Angular resolved photoelectron spectroscopy
BEP	Beam equivalent pressure
CB	Conduction band
CL	Cathodoluminescence
c-TLM	Circular TLM
CVD	Chemical vapour deposition
DFT	Density functional theory
DRCL	Depth resolved cathodoluminescence
EBSD	Electron back-scattered diffraction
EDX	Energy dispersive X-ray spectroscopy
EFG	Edge-defined film-fed growth
ELOG	Epitaxial lateral overgrowth
EtOH	Ethanol
FFT	Fast Fourier transform
FIB	Focused ion beam
FWHM	Full width half maximum
FZ	Float-zone
GC	Growth chamber
GGA	Generalized gradient approximation
GR	Growth rate
HAADF	High angle annular dark field
HEMT	High electron mobility transistors
HRTEM	High resolution TEM
HVPE	Halide vapour phase epitaxy
ICP- RIE	Inductively couple plasma - reactive ion etching
I-V	Current-voltage
LL	Load lock
LR	Laser reflectometry
l-TLM	Linear TLM
MEXCAT	Metal exchange catalysis
MFC	Mass flow controller
MH	Middle heater
MOVPE	Metalorganic vapour phase epitaxy
MSM	Metal-semiconductor-metal
nl	Nucleation layer
PAMBE	Plasma assisted molecular beam epitaxy
PBE	Perdew-Burke-Ernzerhof
PCS	Photocurrent spectroscopy
PD	Photodetector
PID	Proportional-integrative-derivative
PL	Photoluminescence
PLD	Pulsed laser deposited
PLE	Photoluminescence excitation
PVD	Physical vapour deposition
QTH	Quartz Tungsten Halogen
RF	Radio frequency
RHEED	Reflection high energy diffraction
RM	Raman modes
RMS	Root-mean-square roughness
RSF	Relative sensitivity factor
RSM	Reciprocal space maps
RT	Room-temperature

SBD	Schottky-barrier diode
SC	Semiconductor
SEM	Scanning electron microscopy
STH	Self-trapped holes
TB	Twin boundary
TEG	Triethylgallium
TEM	Transmission electron microscopy
TLM	Transmission line model/transfer length method
TMG	Trimethylgallium
ToF-SIMS	Time of flight second ion mass spectrometry
UHV	Ultra high vacuum
UID	Unintentionally doped
UV	Ultraviolet
UWBG	Ultra-wide bandgap
VB	Valence band
VBM	Valence band maximum
VdP	Van-der-Pauw

Contents

List of Figures

List of Tables

1 Introduction

The semiconductor technology, even though relatively young, has already had an undeniable impact on modern society. Beginning in the 1940s, during War World II, when silicon (Si) and germanium (Ge) gained interest for implementation of high frequencies radar receivers.[1] Their extensive study allows for increased knowledge in the fields of semiconductors and achievement of increasingly performant materials. In 1947, the first Ge-based transistor was created at Bell's Laboratory by J. Bardeen, W. Shockley, and W. Brattain, awarded with the Nobel Prize in Physics in 1956 for their groundbreaking discovery, which is often described as the "nerve cell" of the Information Age. While the crucible of war furnished the ignition for technological breakthroughs, driving humanity to push the boundaries of innovation, it is the relentless curiosity of researchers that has continually fuelled the discovery of new materials, propelling science forward in times of both urgency and peace. The history of semiconductors (SCs) can be divided into four generations, *i.e.,* (1st) Si and Ge, the forerunners; (2nd) the "conventional" III-V compounds, *i.e.,* constituted with elements from the III and V column of the periodic table, *e.g.,* GaAs and GaP; (3rd) the wide-bandgap and (4th) the ultrawide bandgap (UWBG) SCs. If the 1st generation posed the foundations of the SCs landscape, the "conventional" III-V, still characterized by relatively narrow band gap, *i.e.,* E_g < 2.3 eV, foresees the possibility of band-gap engineering when playing with compound composition/doping and leads to implementation of the first electronic and optoelectronic devices, *e.g.,* high-electron mobility transistor[2] and laser diodes.[3] The 3rd generation, comprising materials with higher bandgap, *i.e.,* 2.3 eV < E_g < 3.4 eV, such as SiC, GaN, unlocks the light emission in the visible and presents higher breakdown voltages, fundamentals features for optoelectronics[4–6] and electronics devices, respectively. As the research is still facing the opportunities and challenges offered by the 3rd generations SCs, also the UWBG material comes in the pictures. This category includes compounds with E_g > 3.4 eV, *e.g.,* AlGaN, diamond, cubic BN[7] and Ga_2O_3.[8] The direct consequences of UWBG values is an elevated predicted breakdown-field, E_{BR} ≈ 6 - 8 MV/cm, and deep-UV sensitivity coupled with visible blindness, ideal for UV-photodetectors implementation without the employment of filters.[9] Furthermore, as in the case of the $Al_xGa_{1-x}N$ alloy system, the possibility of bandgap tuning through variation of the alloy composition leads to a wide range of accessible E_g, *i.e.,* from 3.4 eV (x = 0, GaN) up to 6 eV (x = 1, AlN).[8–10] Although this field is still considered immature, extensive research has focused on three main areas: (i) the quality of bulk substrates, (ii) the maximum diameter of these substrates, and (iii) the achievement of both n-type and p-type doping. So far, none of the investigated UWBG compounds fully satisfy all three criteria, but this does not necessarily mean that high-performance devices cannot be achieved.[11–13]

Among the UWBG, Ga_2O_3 is of particular interest. It can be stabilized in the shape of five different polymorphs,[14] *i.e.*, the trigonal α,[15] the monoclinic β,[16,17] the cubic defective-spinel γ,[18] the cubic bixbyte δ[19] and the orthorhombic κ,[20] all featuring unique properties. The β-polymorph, being the thermodynamically stable phase, can be produced through several bulk growth techniques, *i.e.*, Czochralski,[21,22] edge-defined film-fed growth (EFG),[23–25] float-zone (FZ),[26,27] and vertical Bridgman,[28] with reported commercially available bulk substrates up to 4-inch diameter.[29] The reported E_g for β-Ga_2O_3 is approximately 4.8 eV, leading to the predicted breakdown electric field ≈ 8 MV/cm.[13] It offers good tunability of n-type conductivity, with carrier concentrations n spanning over the 10^{15} – 10^{19} cm^{-3} range, when doped with Si or Sn.[26,30,31] β-Ga_2O_3 is already widely involved in electronic[32–34] and optoelectronic[35–37] devices, and its high stability against oxidation, as an oxide semiconductor, makes it suitable also for harsh-environments electronics, high-temperature signal processing applications and wireless communication devices/circuits.[8,38] However, the intrinsic asymmetry of its crystal structure, has driven researchers to explore also its metastable polymorphs. In particular, the α- and κ-phases that exhibit a higher degree of crystal symmetry and can be stabilized through different epitaxial techniques[39] on top of different substrates, *e.g.,* sapphire,[40] MgO,[41] GaN.[42] While the corundum α phase possess the highest bandgap among the Ga_2O_3 polymorphs (E_g ≈ 5.2 eV), the peculiarity of the orthorhombic κ-Ga_2O_3 is the predicted high spontaneous polarization along its c-direction (which is also the growth orientation resulting in heteroepitaxy)[43–45] together with suggested ferroelectricity.[46] An other degree of freedom of the Ga_2O_3 material system lays on the fact that all its β, α, and κ- polymorphs can be alloyed with In and Al over a wide range offering the ability to engineer their bandgap.[47–54] Considering all these aspects, especially in the particular case of the polar κ-phase, there is the potential to opens up to a plethora of possible different devices with appropriately designed heterostructures, *e.g.,* high electron mobility transistors (HEMTs), non-volatile memory devices, quantum-well infrared photodetectors.[55–57] However the biggest challenge for the orthorhombic polymorph is coming from its intrinsic defective structure, characterized by vertically oriented extended defects, that are mediating its functional properties and hindering its full potential disclosure.[20,58,59] In this framework, the work discussed in this dissertation set place, primarily focusing on κ-Ga_2O_3, with particular emphasis on the full understanding and control of its structural and electrical properties, which are closely interrelated. However, an overview of the Ga_2O_3 material system as a whole is provided, and throughout the work, the investigation of the κ-polymorph is consistently compared with β-Ga_2O_3, given the parallels between the two polymorphs. The thesis work is structured as follows:

- Chapter 2 – *Ga_2O_3 material system* – provides an overview over the Ga_2O_3 material system properties, highlighting strengths and weaknesses of the different polymorphs to end up focusing on the orthorhombic κ-phase that represents the main character of the work here discussed;
- Chapter 3 – *Experimental methods* – outlines both growth and characterization techniques the candidate was exposed to during the full PhD programme;
- Chapter 4 – *Role of structural defects in κ-Ga_2O_3* – discusses one of the key challenges associated with this material system: its intrinsic defective nature in heteroepitaxy and the impact on its functional properties;
- Chapter 5 – *Towards suppression of κ-Ga_2O_3 rotational domains* – presents the extensive study conducted by the candidate aimed at mitigating the structural defects;
- Chapter 6 – *Point defects in κ-Ga_2O_3* – discusses the different shallow and deep level defects associated to different growth techniques and suggests the role of annealing treatments to possibly engineer them;
- Chapter 7 – *Lithium diffusion in Ga_2O_3 thin films* – reports the possibility to diffuse Li and its effect on the functional properties of different Ga_2O_3 structures, highlighting the role of structural defects in mediating the diffusion processes itself.

1.1 Personal contributions

The research presented in this thesis is the result of an extensive collaboration among universities and research institutes worldwide. At the opening of each chapter detailing the experimental data (Chapters 4 – 7), the contributions of all participants will be highlighted to acknowledge the work of all the people involved. The personal contribution of the candidate is also summed-up hereafter, having the candidate actively performed: the TLM investigations of the κ-Ga_2O_3 layers and relative photodetectors characterizations reported in Chapter 4 – 6 – 7; the Raman data elaboration reported in Chapter 4; all the substrates pre-treatments and MBE growths reported in Chapter 5 and associated experimental investigation (AFM – XRD); the overall coordination of the work discussed in Chapter 6 together with AFM and XRD investigation.

1.2 Scientific contributions

(in reverse chronological order)

Part of the work discussed in the thesis have been published in peer-reviewed journals:

- A. Ardenghi, O. Bierwagen, J, J. Lähnemann, E. Luna, J. Kler, A. Falkenstein, M. Martin, **A. Sacchi**, P. Mazzolini
  "Phase-selective growth of κ- vs β -Ga_2O_3 and $(In_xGa_{1-x})_2O_3$ by In-mediated metal exchange catalysis in plasma-assisted molecular beam epitaxy"

APL Materials, 12, 1011101 (2024)

- P. Mazzolini, J.B. Varley, A. Parisini, **A. Sacchi**, M. Pavesi, A. Bosio, M. Bosi, L. Seravalli, B.M. Janzen, M.N. Marggraf, N. Bernhardt, M.R. Wagner, A. Ardenghi, O. Bierwagen, A. Falkenstein, J. Kler, R.A. De Souza, M. Martin, F. Mezzadri, C. Borelli, R. Fornari
  "Engineering shallow and deep level defects in κ-Ga_2O_3 thin films: comparing metal-organic vapour phase epitaxy to molecular beam epitaxy and the effect of annealing treatments"
  Material Today Physics, 45, 101463 (2024)

- P. Mazzolini, Z. Fogarassy, A. Parisini, F. Mezzadri, D. Diercks, M. Bosi, L. Seravalli, **A. Sacchi**, G. Spaggiari, D. Bersani, O. Bierwagen, B. M. Janzen, M. N. Marggraf, M. R. Wagner, I. Cora, B. Pécz, A. Tahraoui, A. Bosio, C. Borelli, S. Leone, R. Fornari
  "Silane-mediated expansion of domains in Si-doped κ-Ga_2O_3 epitaxy and its impact on the in-plane electronic conduction"
  Advanced Functional Materials, 33, 2207821, (2023)

- A. Parisini, P. Mazzolini, O. Bierwagen, C. Borelli, K. Egbo, **A. Sacchi**, M. Bosi, L. Seravalli, A. Tahraoui, and R. Fornari
  "Study of SnO/ε-Ga_2O_3 p–n diodes in planar geometry"
  Journal of Vacuum Science & Technology A 40, 042701 (2022)

The candidate was also involved in other publications:

- Th. Dittrich, A. Parisini, M. Pavesi, A. Baraldi, **A. Sacchi**, F. Mezzadri, P. Mazzolini, M. Bosi, L. Seravalli, A. Bosio, R. Fornari
  "Electronic states near surfaces and interfaces of β-Ga_2O_3 and κ-Ga_2O_3 epilayers investigated by surface photovoltage spectroscopy, photoconductivity and optical absorption"
  Surfaces and Interfaces, 51, 104642 (2024)

- G. Spaggiari, R. Fornari, P. Mazzolini, F. Mezzadri, A. Parisini, M. Bosi, L. Seravalli, F. Pattini, M. Pavesi, A. Baraldi, S. Rampino, **A. Sacchi**, D. Bersani
  "Raman Spectroscopy as an Effective Tool for Assessment of Structural Quality and Polymorphism of Gallium Oxide (Ga_2O_3) Thin Films"
  Applied Spectroscopy (2024)

Parts of the work are planned to be published in peer-reviewed journals:

- **A. Sacchi,** M. Sidoli, A. Ardenghi, O. Bierwagen, J. Kler, A. Falkenstein, R. De Souza, M. Martin, D. Spallek, J. Lähnemann, H. Tornatzky, M. R. Wagner, A. Parisini, M. Pavesi, M. Bosi, L. Seravalli, G.Spaggiari, D. Bersani, K. Mizohata, F. Tuomisto, G. Magnani, D. Pontiroli, M. Riccò, F. Mezzadri, S. Pasini, A. Bosio, R. Fornari, P. Mazzolini
  "Effect of lithium diffusion in Ga_2O_3 thin films"
  In preparation

- **A. Sacchi**, F. Mezzadri, A. Ardenghi, O. Bierwagen, J. Lähanemann, H. Tornatzky, M. R. Wagner, H.Nishinaka, R. Fornari, P. Mazzolini
  "Molecular beam epitaxy of (001) κ-Ga_2O_3 thin films on ε-$GaFeO_3$ and offcut c-plane sapphire substrates"
  In preparation

Parts of the work have been presented at conferences and workshops:

- **A. Sacchi**, M. Sidoli, A. Ardenghi, O. Bierwagen, J. Kler, A. Falkenstein, R. De Souza, M. Martin, D. Spallek, J. Lähnemann, H. Tornatzky, M. R. Wagner, A. Parisini, M. Pavesi, M. Bosi, L. Seravalli, G.Spaggiari, D. Bersani, K. Mizohata, F. Tuomisto, G. Magnani, D. Pontiroli, M. Riccò, F. Mezzadri, S. Pasini, A. Bosio, R. Fornari, P. Mazzolini
  "Effect of lithium diffusion in Ga_2O_3 epitaxial thin films"
  4th International Workshop on Gallium Oxide and Related Materials, Berlin 2024
  Poster

- **A. Sacchi**, F. Mezzadri, A. Ardenghi, O. Bierwagen, J. Lähnemann, H. Tornatzky, M. R. Wagner, H. Nishinaka, R. Fornari, P. Mazzolini
  "Molecular beam epitaxy of (001) κ-Ga_2O_3 thin films on ε-$GaFeO_3$ substrates"
  4th International Workshop on Gallium Oxide and Related Materials, Berlin 2024
  Contributed talk

- A. Sacchi, F. Mezzadri, A. Ardenghi, O. Bierwagen, J. Lähnemann, H. Tornatzky, M. R. Wagner, H. Nishinaka, R. Fornari, P. Mazzolini
  "Towards epitaxial growth of a κ-Ga_2O_3 single domain"
  European Cost Action Network for Innovative and Advance Epitaxy, online
  Contributed talk

- **A. Sacchi**, P. Mazzolini, G. Magnani, M. Sidoli, D. Pontiroli, M. Riccò, A. Bosio, F. Mezzadri, M. Pavesi, G. Spaggiari, D. Bersani, A. Ardenghi, O. Bierwagen, M. Bosi, L. Seravalli, A. Parisini, B. M. Janzen, M. R. Wagner, A. Falkenstein, M. Martin, R. Fornari
  " Li-diffusion effect in Ga_2O_3 thin films"
  3rd International Workshop on Gallium Oxide and Related Materials, Nagano 2022
  Poster

- **A. Sacchi**, G. Magnani, M. Sidoli, D. Pontiroli, M. Riccò, A. Bosio, F. Mezzadri, M. Pavesi, G. Spaggiari, D. Bersani, A. Ardenghi, O. Bierwagen, M. Bosi, L. Seravalli, A. Parisini, B. Janzen, M. Wagner, A. Falkenstein, M. Martin, R. Fornari, P. Mazzolini
  "Control of the electrical and optical properties of doped Ga_2O_3 epitaxial thin films"
  Training School - Characterization Techniques for Epitaxial Material, Aveiro 2023
  Poster

- **A. Sacchi**, P. Mazzolini, G. Magnani, M. Sidoli, D. Pontiroli, M. Riccò, A. Bosio, F. Mezzadri, M. Pavesi, G.Spaggiari, D. Bersani, A. Ardenghi, O. Bierwagen, M. Bosi, L. Seravalli, A. Parisini, B. Janzen, M. Wagner, A. Falkenstein, M. Martin, R. Fornari
  "Tailoring semiconducting properties of orthorhombic κ-Ga_2O_3 layers: towards domain suppression and Li-doping"
  GrafOx fall meeting, Berlin 2022
  Poster

2 Ga_2O_3 material system

2.1 Ga_2O_3 polymorphism

Ga_2O_3, as an UWBG metal-oxide semiconductor, brings together the advantages of a ultra-wide bandgap, high breakdown field, transparency to visible light and high chemical stability. Furthermore, the possibility to obtain five different polymorphic structures, all showing peculiar features, spans further the potential of this material system. The polymorphism of Ga_2O_3 was unveiled in 1952 by Roy *et al.*,[14] with the identification of five different crystal structures, all showing a unit cell accommodating Ga and O atoms in the 2:3 stoichiometry. The five different phases are labelled with greek letters, *i.e.,* α, β, γ, δ, ε/κ, with the monoclinic β being the thermodynamically stable one and all the others reported to be metastable, *i.e.*, they can be stabilized through different deposition techniques but would eventually convert to the stable β-polymorph at sufficiently high temperature. The unit cells of the five different polymorphs are reported in Figure 2.1.

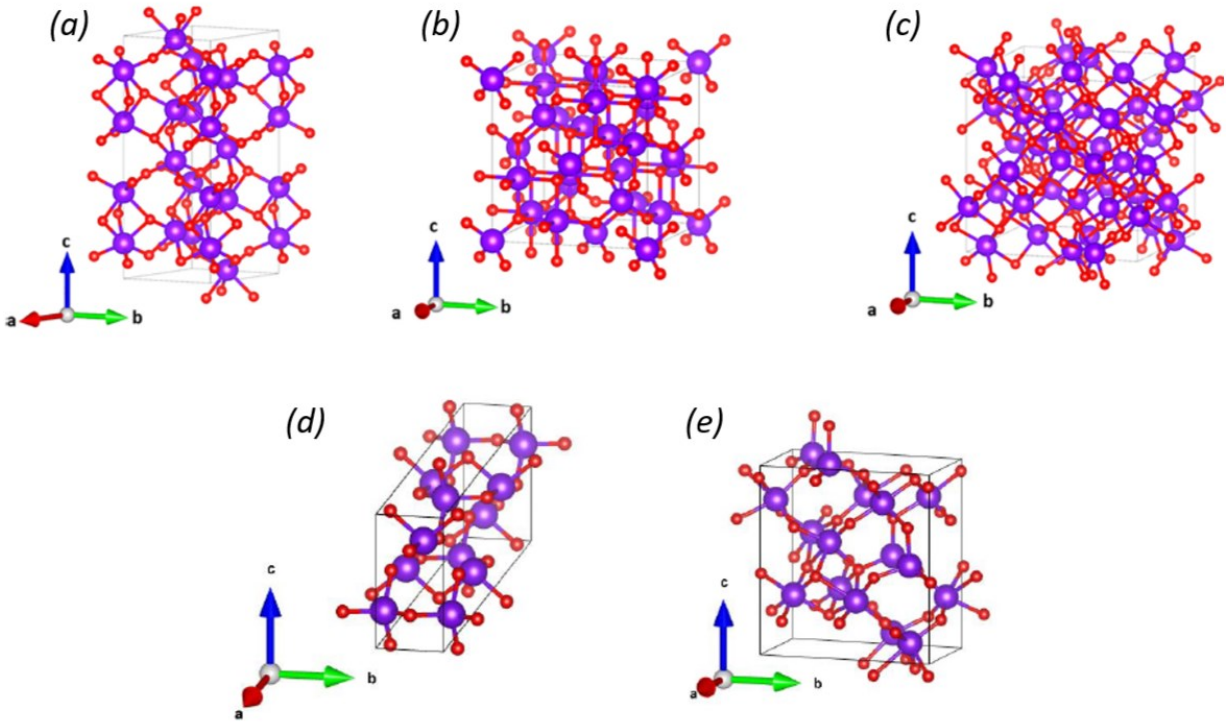

Figure 2.1 Schematics of the unit cells of (a) trigonal α-Ga_2O_3, (b) defective-spinel γ-Ga_2O_3, (c) cubic bixbyite δ-Ga_2O_3, (d) monoclinic β-Ga_2O_3, and (e) orthorhombic κ-Ga_2O_3. Ga (purple) or O (red) atoms are indicated. Image reproduced from B. M. Janzen PhD thesis elaborate.[60]

The α-polymorph possesses a trigonal corundum structure, space group symmetry $R\bar{3}c$, lattice constants of $a = b = 4.997$ Å; $c = 13.447$ Å [see Figure 2.1 (a)]. Due to the shared symmetry with materials like α-Al_2O_3 and In_2O_3, this polymorph is considered a promising candidate for

heterostructures and alloys with these well-studied materials.[51,61] The α-Ga_2O_3 also reports the highest bandgap among the Ga_2O_3 polymorphs, *i.e.,* $E_g \approx 5.3$ - 5.6 eV[62,63] and n-type conductivity through Si and Sn doping has been already experimentally reported.[64–66] This polymorph can be obtained through several epitaxial techniques, either CVD[40,64,66,67] as well as PVD.[52,62,68] The major challenges posed by the α-Ga_2O_3 is related to: (i) the high dislocation density reported when grown on α-Al_2O_3 due to the high lattice mismatch ≈ 4.8%;[69] (ii) the lack of *p*-type conductivity (common issue for all the Ga_2O_3 polymorphs) and (iii) its metastable nature.[70] These factors have significantly hindered the development of α-Ga_2O_3-based devices, as they lead to (i) relatively low electron mobilities, (ii) the impossibility to design bipolar homo-junctions and (iii) the inability to perform high-temperature post-growth annealing, which is typically desired for semiconductors (*e.g.*, implantation processes).[71] The latter drawback is naturally valid for all the metastable polymorphs of Ga_2O_3.

The γ-phase possesses a cubic unit cell, space group symmetry $Fd\bar{3}m$, lattice constant of $a = b = c = 8.23760$ Å [see Figure 2.1 (b)]. The identification of the crystal structure through X-ray diffraction was tricked by its inherent disorder.[72,73] It was only in recent years, thanks to the successful growth of c-plane oriented films, that the cubic-defective spinel structure was unveiled.[18,74] Noteworthy, inclusions of γ-Ga_2O_3 are often detected at the substrate interface for β- and κ-Ga_2O_3 heteroepitaxy.[20,58,75,76] Its formation can be induced by the strain of the epi-layer nucleation accommodated in the defective spinel structure.[77]

The existence of the δ-phase of Ga_2O_3 remains controversial. While some reports suggest it has a cubic bixbyite structure (space group symmetry $Ia\bar{3}$, lattice constant of $a = b = c = 9.292$ Å)[19,78] [see Figure 2.1 (c)], neutron diffraction data[73] indicate that this phase is merely a mixture of the β- and κ-phases.

The description of the stable β- and of the metastable κ-Ga_2O_3, being both involved in the work of the candidate, are reported with a higher level of details in the next sections, separately.

2.2 Monoclinic β-Ga_2O_3

2.2.1 Crystal structure

The β-Ga_2O_3 is showing a monoclinic unit cell belonging to the space group symmetry $C2/m$.[16] The arrangement of Ga and O atoms in the unit cell foresees two and three inequivalent sites for Ga and O, labelled as Ga_I and Ga_{II} and O_I, O_{II} and O_{III} [see Figure 2.2 (a)]. The O atoms are tetrahedrally coordinated to the Ga_I and octahedrally coordinated to the Ga_{II} sites, as reported with different colours in Figure 2.2 (b). The monoclinic unit cell is characterized by an intrinsic anisotropy due to the

presence of the monoclinic angle $\beta \neq 90°$[see Figure 2.2 (a)] between the [100] and [001] directions. The experimental values for the lattice constants are: $a = 12.21$ Å, $b = 3.04$ Å, $c = 5.80$ Å, $\beta \approx 103.8°$.[79]

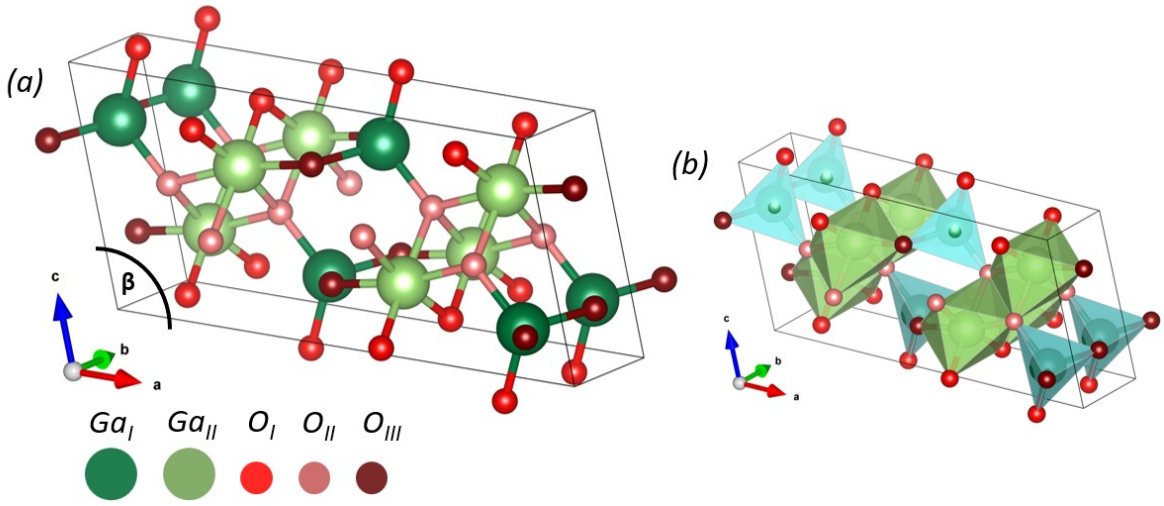

Figure 2.2 (a) Unit cell of the monoclinic β-Ga_2O_3. The two inequivalent sites of Ga_I and Ga_{II} as well as the three inequivalent $O_{I\text{-}III}$ are reported with slight change of colours. The legend in provided under the picture. The monoclinic angle $\beta \approx 103.8°$ is labelled as well. (b) The monoclinic unit cell is reported again with the tetrahedral and octahedral coordination of Ga atoms reported in blue and green, respectively. The unit cell plots were created with VESTA.

2.2.2 Electronic structure

The electronic band structure of β-Ga_2O_3 is a non-trivial topic. Indeed, a discrepancy has been reported for the energy band gap values among different experimental investigations, *e.g.,* absorption,[80–82] transmittance and reflectance,[83] depending on the polarization of the incident electric field w.r.t. the crystallographic direction, strictly related to the structural asymmetry. Several theoretical works addressed the band diagram structure with different density functional theory (DFT) approaches.[81,84,85] Figure 2.3 reports the band diagram structure provided by Mock *et al.,*[85] according to the Perdew, Burke and Ernzerhof (PBE) DFT calculations on the level of the generalized gradient approximation (GGA); here the bottom edge of the conduction band (CB) is shaped by Ga *4s*, *4p* and *4d* states (bottom-top order), while the top of the valence band (VB) comes from the O *2p*, Ga *3d* and O *2s* states (top-bottom order). Although a wide range of E_g values have been reported from different DFT approaches, there is a shared insight that the CB edge is located at the Γ-point [see Figure 2.3], while VB is largely flat.[86] β-Ga_2O_3 has been confirmed as an indirect band-gap semiconductor: its VB maximum (VBM) is found near the L-point, ≈ 50 meV higher than the top valence band at the Γ-point;[85] nonetheless, due to this relatively small difference in energy, β-Ga_2O_3 is often treated as a direct band-gap semiconductor.

From the parabolic shape of the CB edge (Γ-point), the electron effective mass for β-Ga_2O_3 is reported from several different DFT approaches with values in the range (0.12 – 0.34)m_e.[87–90] The hole effective mass, due to the flatness of the VB, was found to be significantly higher and highly directional-dependent. These factors contributes to the material's inherent n-type conductivity[90,91] and the impossibility to achieve p-type conductivity. Indeed, both theoretical[92,93] and experimental[94] investigations, report the self-trapping of holes (STHs), characterized by high effective mass, hence resulting in practically immobile holes.

Theoretical studies[90,91,95–100] have explored the role of Ga- and O-related point defects to better understand the origins of the experimentally determined n-type conductivity in unintentionally doped β-Ga_2O_3 material. However, both intrinsic donor and acceptor defects in β-Ga_2O_3 have been found to be deep levels, suggesting they are not directly responsible for the intrinsic material's n-type conductivity.[101] However, other impurities that can be incorporated from the growth environment either in the bulk as well as in thin films, *e.g.*, H, Si, F, can act as shallow donors.[90,97] Moreover, the n-type conductivity of β-Ga_2O_3 can be tuned by intentional extrinsic doping, when Si,[30,102] Sn,[103–105] Ge[106] or Nb[107] are introduced in the material in substitutional positions of Ga; this allows to obtain free carrier concentrations in the range of $n \approx 10^{17} – 10^{20}$ cm^{-3}. However, the efficiency of the extrinsic dopant can be influenced by compensation from deep intrinsic acceptor levels, *e.g.,* Ga vacancies (V_{Ga}) and related complexes, as well as extrinsic acceptors, *e.g.,* Mg_{Ga}, Fe_{Ga}, Li_{Ga}, Zn_{Ga}.[99] Within this context, Chapter 7 discusses the effect of a Li diffusion in improving the efficiency of Si extrinsic doping in (010) β-Ga_2O_3 homoepitaxial layers.

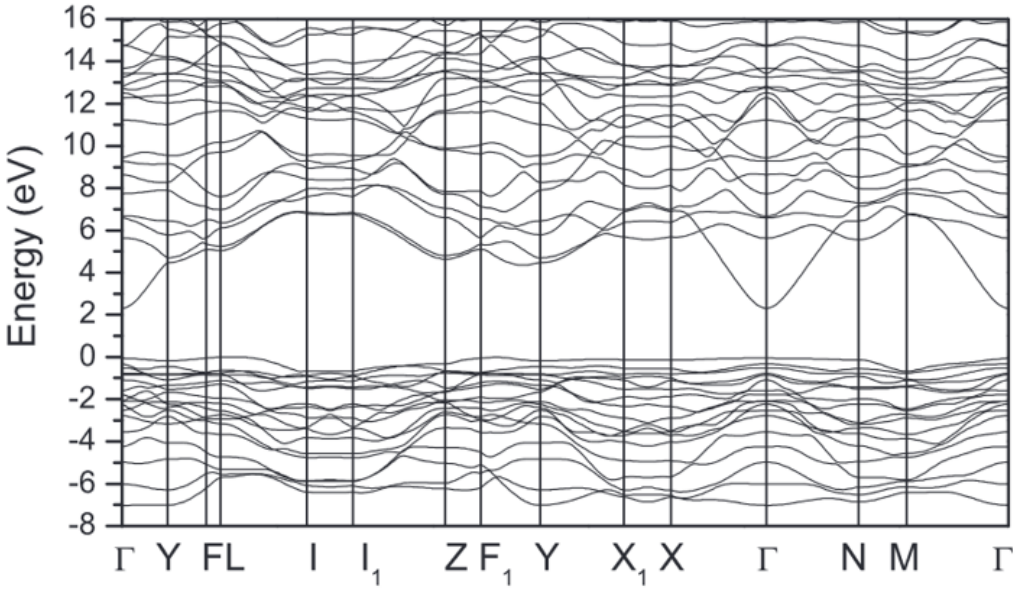

Figure 2.3 Computed band structure for β-Ga_2O_3 with the GGA-DFT (PBE) approach. Reproduced with permission from Mock *et al.*, Phys. Rev B 96, 245205 (2017).[85] Copyright (2017) American Physical Society.

2.2.3 Epitaxy of β-Ga_2O_3

The availability of single crystal β-Ga_2O_3 bulk material grown from the melt, gave the opportunity to develop the homoepitaxy of this material through different CVD (*e.g.*, metal organic vapour phase epitaxy MOVPE) and PVD (*e.g.*, molecular beam epitaxy MBE) growth techniques.[108] In the context of low pressure PVD growth methods like the MBE, the two-step growth kinetics involving the preliminary formation of the volatile Ga_2O[109] can strongly limit the growth rate of β-Ga_2O_3. This is also found to be dependent on the surface orientation in the MBE β-Ga_2O_3 homoepitaxy,[110] mostly due to the different surface energies of the commercially available (100), (-201), (001), and (010) oriented substrates.[111,112] Different strategies can be employed to mitigate the relatively low growth rates encountered in the PVD growth of β-Ga_2O_3, like the use of a metal catalyst (*e.g.*, In [113]or Sn[114], as will be further discussed in Chapter 5) or the use in MBE of suboxide Ga_2O[115] source material in place of Ga metal. On the other hand, CVD growth is generally not showing the orientation dependent limitations of the growth rate and can reach the range of the μm/hour in high quality homoepitaxial layers.[116]

The biggest challenge in β-Ga_2O_3 epitaxy lays though in the intrinsic low symmetry of the monoclinic cell. In fact, even in the case of homoepitaxy, just some growth orientations [*i.e.*, (010), (001)][110] or the employment of well-defined substrate offcuts [*i.e.*, (100) with 2°- 6°offcut towards the c- in-plane direction][112] would result in high-quality β-Ga_2O_3 thin films. Other crystalline orientations, like the nominally oriented (100) and the (-201) always result in the formation of incoherent layer twinning.[110,117] Such incoherent twin boundaries represent an actual barrier for the electronic transport.[118] This poses serious limitations also in the heteroepitaxy of β-Ga_2O_3 layers; in fact, on various substrates (*e.g.*, c-plane sapphire) the (-201) is its preferential epitaxial growth direction that therefore results in a high concentration of incoherent rotational domains with different orientations due to the presence of the monoclinic angle. The presence of such structural defects in the heteroepitaxy of β-Ga_2O_3 (-201) heteroepitaxial layers and how to experimentally address their presence (*i.e.*, through X-ray diffraction) will be recalled in Chapter 5 and 7.

2.3 Orthorhombic κ-Ga_2O_3

The κ-Ga_2O_3, being a metastable phase, cannot be stabilized via bulk growth methods and would eventually convert to the stable β-Ga_2O_3 at temperatures $T_{\kappa\rightarrow\beta} \geq 700°C$.[119] However several different CVD and PVD epitaxial techniques, *e.g.*, metalorganic vapour phase epitaxy (MOVPE),[20,120] mist-CVD,[41,42] halide vapour phase epitaxy (HVPE),[121,122] pulsed laser deposition (PLD),[123,124] molecular beam epitaxy (MBE),[114,125–127] atomic layer deposition (ALD),[128] allow for the κ-Ga_2O_3

layer stabilization on top of different substrates, *e.g.*, (0001) α-Al_2O_3, (0001) GaN, 6H-SiC, (111) MgO, (111) $SrTiO_3$, (-201) β-Ga_2O_3.

2.3.1 Crystal structure

κ-Ga_2O_3 is showing a orthorhombic unit cell (space group symmetry $Pna2_1$) and lattice constants of a = 5.0463 Å, b = 8.7020 Å and c = 9.2833 Å [see Figure 2.4 (a)]. The Ga atoms are accommodated in four inequivalent sites in the unit cell, Ga_I in tetrahedral coordination and Ga_{II-IV} in octahedral coordination. O atoms display six inequivalent sites (O_{I-VI}) arranged in a 4H (ABAC) close-packed stacking [see Figure 2.4 (b)]; their tetra- and octahedral coordination around Ga atoms results in two types of polyhedral ribbons, *i.e.,* pure octa or mixed tetra-octahedral [see Figure 2.4 (c-e)], laying in the (001) plane and aligned to [100] direction.[20]

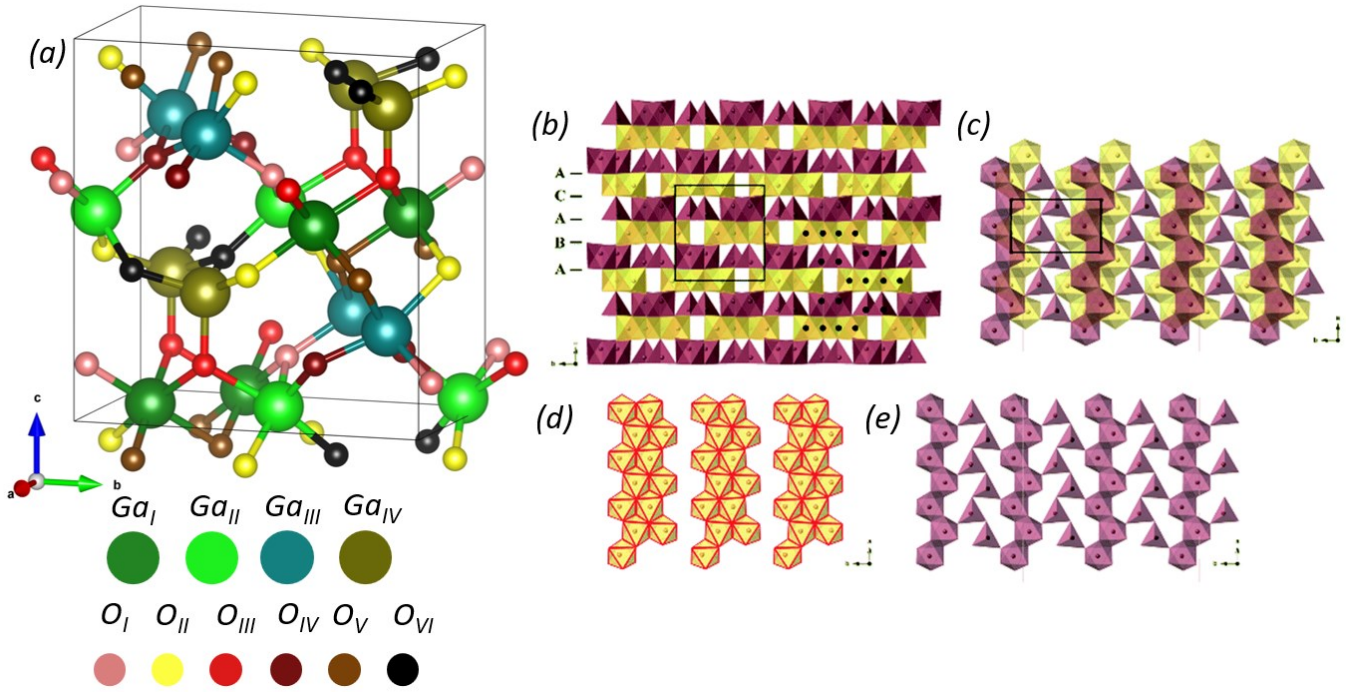

Figure 2.4 (a) Unit cell of the orthorhombic κ-Ga_2O_3. The crystallographic representation was created using VESTA, based on the lattice parameters reported by ref. [20]. The four inequivalent Ga sites and the six inequivalent O sites are reported with different colours and the legend in provided under the picture. (b) and (c) The tetrahedral and octahedral coordination of O and Ga in [100] and [001] projections, respectively. (d) The octahedral and (e) the mixed tetra-octahedral ribbon laying in the (001) plane and aligned to [100] direction. Images (b-e) reproduced with permission from Cora *et al.*, CrystEngComm 19, 1509 – 1516 (2017).[20] Copyright (2017) Royal Society of Chemistry.

The real structure of κ-Ga_2O_3 as just described, was unveiled only in 2017 by the first combined XRD-TEM investigation performed on this material by Cora *et al.*[20] Indeed, for long time the polymorph was believed to possess an hexagonal symmetry, *i.e.*, assigned to $P6_3mc$ space group, and commonly referred to ε. The TEM study of (001) κ-Ga_2O_3 layers grown by MOVPE on top of

sapphire substrates, revealed that the Ga_2O_3 polymorph was actually characterized by an orthorhombic unit cell with three different in-plane orientations rotated by 120° [see fast Fourier transform (FFTs) of 5×5 nm^2 large areas in Figure 2.5 (B-E)]. When the structural information is mediated on a wider region of the area with respect to the average rotational domain size, the result suggests the presence of an hexagonal symmetry [see FFT in Figure 2.5 (F)]. A schematic representation of the in-plane arrangement of the κ-Ga_2O_3 unit cell is reported by Nishinaka *et al.*[42] [Figure 2.5 (g)]. Usually, the κ-Ga_2O_3 MOVPE deposited layers result in 120° rotated nanosized domains with a typical lateral size distribution in the range of 2-20 nm (equivalent diameter). The improper assignment to hexagonal phase due to previous XRD investigation, was related to the impossibility to discriminate the nanoscale arrangement with the instrument inherent probed volume.

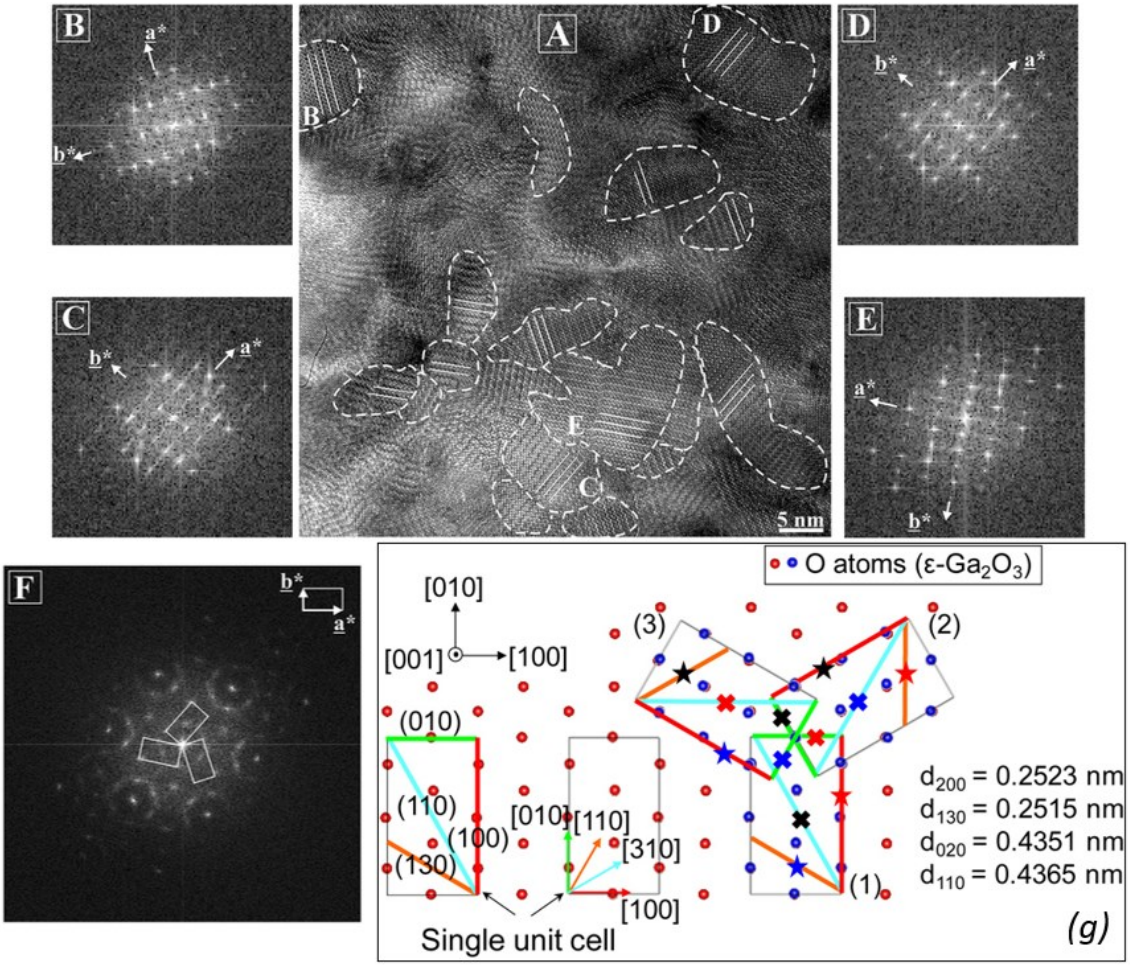

Figure 2.5 (A) HRTEM image of the plane-view section of a κ-Ga_2O_3/sapphire sample in [001] projection. In (B-E) corresponding FFTs from the labelled areas in (A). The FFTs are from 5×5 nm^2 large area. (F) FFT of the whole image in (A). (g) The schematic representation of the orthorhombic κ-Ga_2O_3 atomic arrangement in the (001) plane. The single unit cell, on the left, is then rotated on the right of (1) 0°, (2) 120° and (3) 240°, respectively. Images (A-F) Reproduced with permission from Cora *et al.*, CrystEngComm 19, 1509 – 1516 (2017).[20] Copyright (2017) Royal Society of Chemistry. Image (g) reproduced with permission from H. Nishinaka *et al.*, Jpn. J. Appl. Phys. 57, 115601.[42]

Nonetheless, in 2018 Nishinaka *et al.*[42] provided a useful method to exploit XRD to either discriminate between an hexagonal and orthorhombic unit cell as well as to detect the rotational domains presence without a destructive characterization technique, *e.g.*, TEM. These two aspects are discussed in detail in Chapter 3 after an overview over the XRD technique. Nishinaka *et al.*,[42] ascribed the formation of the in-plane rotational domains to a twofold reason related to (i) the orthorhombic unit cell inherent symmetry when rotated of 120° and (ii) the underlying substrate symmetry. Indeed as per (i), when the orthorhombic unit cell undergoes a 120° rotation, the oxygen sublattice almost overlaps with the un-rotated one [blue and red colour, respectively in Figure 2.5 (g)] and the lattice planes (100) and (110) are equivalent with the (130) and (010), respectively. Hence, the structure itself of the orthorhombic κ-Ga_2O_3 inherently permits the formation of the three rotational domains. As per (ii), also the crystal symmetry of the substrates, could itself promote the in-plane rotation [as schematically depicted in Figure 2.6 for (0001) GaN and (111) $SrTiO_3$, but a similar argument is also valid in the case of c-plane sapphire]. In 2020, Nishinaka *et al.*,[129] proved that the symmetry of the underlying substrates was the prevailing reason for the rotational domains formation; indeed, when κ-Ga_2O_3 is epitaxially grown on top of another orthorhombic substrate, *i.e.,* ε-$GaFeO_3$[1] the first single-domain κ-Ga_2O_3 was obtained. Further details are found in Chapter 5, where the dedicated study performed by the candidate towards suppression of κ-Ga_2O_3 rotational domains is reported.

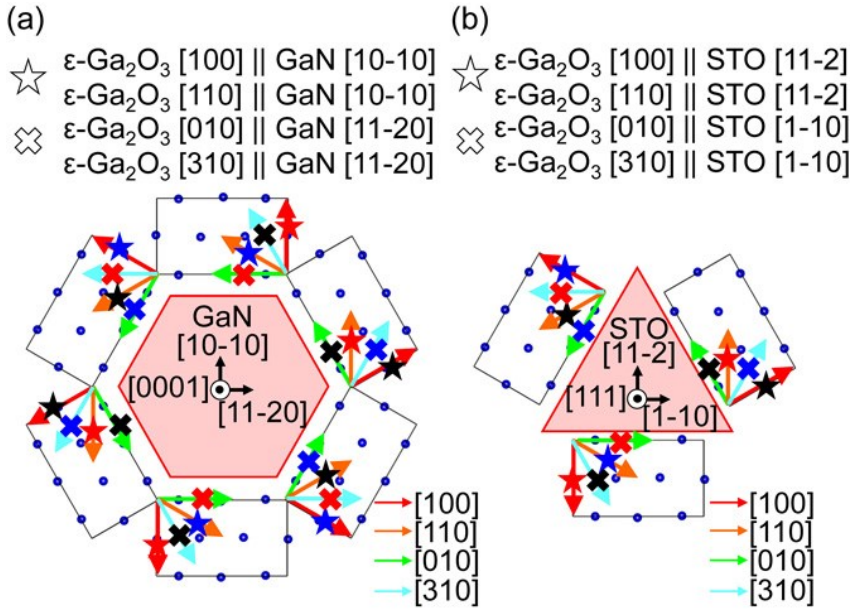

Figure 2.6 Schematics of the occurrence of three rotational domains for κ-Ga_2O_3 due to the crystal structure of the (a) GaN template and (b) STO substrate. The orientation of the κ-Ga_2O_3 with the GaN and STO directions are reported on

[1] The ε-$GaFeO_3$ substrates are showing an orthorhombic unit cell as the κ-Ga_2O_3 polymorph (belonging to the same *Pna2₁* space group), however they are commonly labelled as ε. Also in this work they will be referred to as ε even though the κ-indexing would be more rigorous.

top of each image. Images reproduced with permission from H. Nishinaka *et al.*, Jpn. J. Appl. Phys. 57, 115601.[42] © The Japan Society of Applied Physics. Reproduced by permission of IOP Publishing Ltd. All rights reserved.

2.3.2 Electronic and optical properties

Similarly to β-Ga_2O_3, also in the case of κ-Ga_2O_3, theoretical studies reported different values of band-gap according to the different DFT approaches employed.[44,78] In 2016, Furthmüller *et al.*[78] reported a band-gap of about 2.47 eV using the GGA-DFT method. Later, in 2018, Kim *et al.*[44] calculated two values: 2.32 eV with the PBEsol functional and 4.62 eV with the B3LYP functional. The lower values significantly underestimate the experimentally observed band-gap (≈ 4.9 – 5 eV),[130] while the 4.62 eV value aligns more closely with experimental results. In Figure 2.7 the band diagram structure for such calculation is hence reported. The CB edge and the VB maximum are both located at the Γ-point, resulting in a direct band gap for κ-Ga_2O_3. As already discussed for β, also the orthorhombic polymorph, according to the CB and VB shape, is characterized by an inherent n-type conductivity. Furthermore, extrinsic n-type doping can be achieved with Si and Sn,[131,132] with reported carrier concentrations though that are limited to the $n = 10^{17} – 10^{18}$ cm^{-3} range. Nonetheless, Si_{Ga} has been experimentally demonstrated (electron paramagnetic resonance,[132] photoelectron spectroscopy and photoelectron holography)[133] to be a shallow donor in κ-Ga_2O_3 layers. The conduction though has been found to be governed by a variable-range hopping mechanism.[132] Chapter 4, reports a detailed discussion of the transport properties of Si-doped κ-Ga_2O_3 layers and the first experimental proof of the effect of rotational domains over the in-plane conduction in such epilayers, previously suggested by Kneiß *et al*.[59]

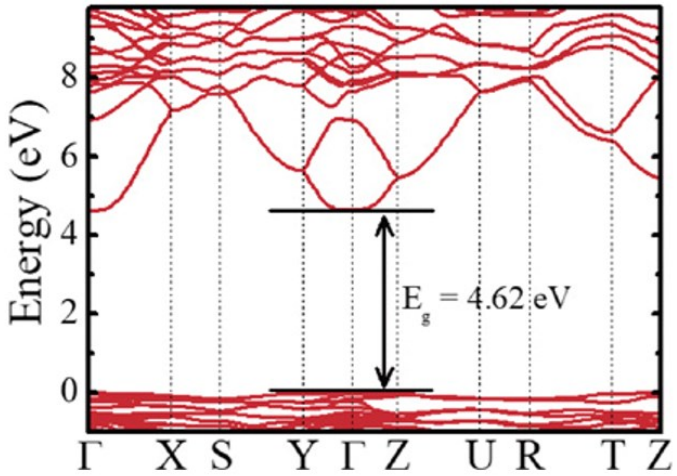

Figure 2.7 Band structure of κ-Ga_2O_3 with the *Pna2₁* orthorhombic phase, calculated using the hybrid functional B3LYP potential (E_g = 4.62 eV). The VBM is set to 0 eV. Reproduced with permission from J. Kim et al., Appl. Phys. Express 11 061101 (2018).[44] Copyright (2018) The Japan Society of Applied Physics.

In 2018, Pavesi *et al.*,[130] reported the first κ-Ga_2O_3-based UVC-photodetectors, recording already promising performances despites the intrinsic defective structure of such epilayers deposited on c-plane sapphire substrates. Furthermore, the same study combined absorbance and cathodoluminescence investigation providing the first schematic representation of the in-gap defects for κ-Ga_2O_3. The detailed study of the optical properties combined with investigation of defects levels in κ-Ga_2O_3 is provided in Chapter 6.

2.3.3 Unique properties of κ-Ga_2O_3

The extensive research and interest over κ-Ga_2O_3, despite its intrinsic defective structure, was driven also by additional unique properties not displayed by the other polymorphs. Indeed, in 2016 Maccioni *et al.*,[43] reported that due to the unit cell symmetry, non-centrosymmetric and without inversion, the structure shows polar properties along the c-axis, $\boldsymbol{P}$ = (0, 0, P), with a calculated value of P = 0.23 C/m^2; such intrinsic polarization is about 3 and 10 times higher than AlN and GaN, respectively. Consistent values were also calculated in 2017 by Shimada *et al.*[45] Subsequently, Mezzadri *et al.*[46] suggested the presence of a ferroelectric behaviour in κ-Ga_2O_3 MOVPE layers grown on (0001) α-Al_2O_3 substrates, further enhancing the appeal towards this polymorph for potential development of heterostructures for 2DEG confinement,[57,134] non-volatile memory devices[55] and quantum well infrared photodetectors.[135] However, the primary obstacle preventing wider exploitation of κ-Ga_2O_3 is again its intrinsic defective structure. This issue is addressed in the present work, with Chapter 4 demonstrating the impact of the rotational domains over the in-plane transport properties, followed by the efforts to suppress them, detailed in Chapter 5.

3 Experimental methods

This chapter gives an overview on the epitaxial growth techniques, *i.e.,* metalorganic vapour phase epitaxy (MOVPE) and plasma oxygen assisted (PA) molecular beam epitaxy (MBE), used for the growth of the samples discussed throughout the dissertation. Also the *in-situ* and *ex-situ* characterization techniques are introduced.

3.1 Growth techniques

Epitaxy describes the ordered growth of a material over a substrate, largely applied for the growth of high crystal quality thin films. A distinction can be made between (i) homoepitaxy, when the epitaxial layer and the substrate share chemical composition and structural symmetry or (ii) heteroepitaxy, when the epilayer and substrate have different chemical composition and/or crystallographic structure. In heteroepitaxy, a fundamental step is the choice of the correct epi-layer/substrate match. Indeed, when the epi-layer is grown over a substrate, it will arrange its own structure keeping at least a certain degree of symmetry with the underlaying structure. Therefore, several aspects must be carefully considered, *e.g.*, lattice strain, thermal expansion mismatch, rotational domains formation, interdiffusion mechanisms. Several different epitaxial techniques are present, which can be mostly grouped in the two macro-families of the chemical vapour- and the physical vapour-deposition means (CVD and PVD, respectively). The Ga_2O_3 layers reported in this work are all heteroepitaxial (no availability of bulk substrate for the metastable polymorph), grown by two different epitaxial techniques: MOVPE (a CVD process) and PA-MBE (a PVD process).

3.1.1 Metalorganic vapour phase epitaxy (MOVPE)

The metalorganic vapour phase epitaxy (MOVPE) is listed among the CVD methods, *i.e.,* the epitaxial growth happens from the vapour phase of the precursors involving chemical reactions. For Ga_2O_3 growth, a controlled flux of the metalorganic precursor (trimethyl gallium TMGa or triethyl gallium TEGa), is transported in the growth chamber (GC) through a carrier gas (H_2, He or Ar). The oxidizing element (O_2 or H_2O) is provided through a separate line [see Figure 3.1 (a)]. The chemical reactions are happening at the substrate surface [see Figure 3.1 (b)] thanks to the cracking of the metalorganic precursor followed by the Ga-metal oxidation leading to the deposition of the Ga_2O_3 layers. The by-products (*e.g.*, CH_4, H_2), are expelled through the exhaust gas line. The substrate is heated to furnish the activation energy for the reaction to occurs and it could be rotated in order to obtain higher homogeneity of the deposited layer. The common deposition pressure range in a MOVPE reactor is around $10 – 10^2$ mbar.

Two different reactor configurations were employed to grow the κ-Ga_2O_3 layers the candidate studied during the PhD program: an horizontal and a vertical one, both set-up in Parma at the Institute of Materials for Electronics and Magnetism (IMEM) and operated by M. Bosi, L. Seravalli, and P. Mazzolini (IMEM – Unipr). In both geometrical configurations the employed metalorganic precursors was TMGa and ultrapure water as oxidizing element, both stored in stainless steel bubblers and kept at temperatures of 1 - 5 °C and 30 °C, respectively. Different carrier gases were involved: H_2, He and Ar.

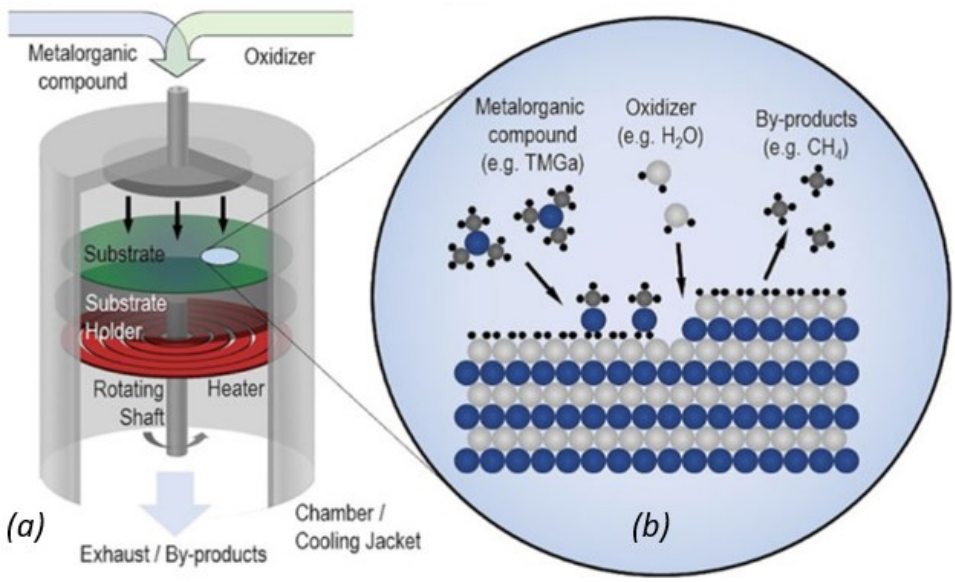

Figure 3.1 Schematic representation of (a) a vertical MOVPE reactor and (b) the reaction happening at the substrate surface for Ga_2O_3 deposition. Image reproduced from Y. Tao *et al.*, Springer International Publishing, 171–184 (2020).[136] Copyright 2020, Springer Nature Switzerland AG.

3.1.1.1 Horizontal MOVPE reactor

In the horizontal MOVPE reactor all the UID and Si-doped κ-layers studied in Chapter 4 – 7 were grown. The standard conditions for κ-Ga_2O_3 growths are reported in Table 3.1. The growth temperature (T_g), TMG and H_2O fluxes were kept fixed while the carrier gas was either H_2 or He, resulting respectively in lower or higher resistivities in the deposited κ-Ga_2O_3 layers (topic discussed in details in Chapter 6). The pressure (p) in the GC is controlled by a rotary pump and the partial pressures of the precursors through mass flow controllers (MFCs). Two separate gas lines are present, for delivering the precursors into the growth chamber, along with a vent line that ensures a controlled gas flow prior to injection into the chamber. Reaction by-products and residual process gases are directed to a cracking furnace heated to approximately 800 °C, where unreacted species are decomposed. To obtain Si:doped κ-Ga_2O_3 samples, the system is equipped with a separate line with

an H_2-diluted mixture of 0.05% silane SiH_4 [Φ_{SiH4}] that can be fluxed in the GC with the vapour precursors with a controlled flux through its own MFC.

Carrier	T_g [°C]	p chamber [mbar]	P_{H2O}/P_{TMGa}
H_2	650	60	350
He	650	100	200

Table 3.1 Standard MOVPE growth parameters for κ-Ga_2O_3 layer growth with H_2 and He carrier gas.

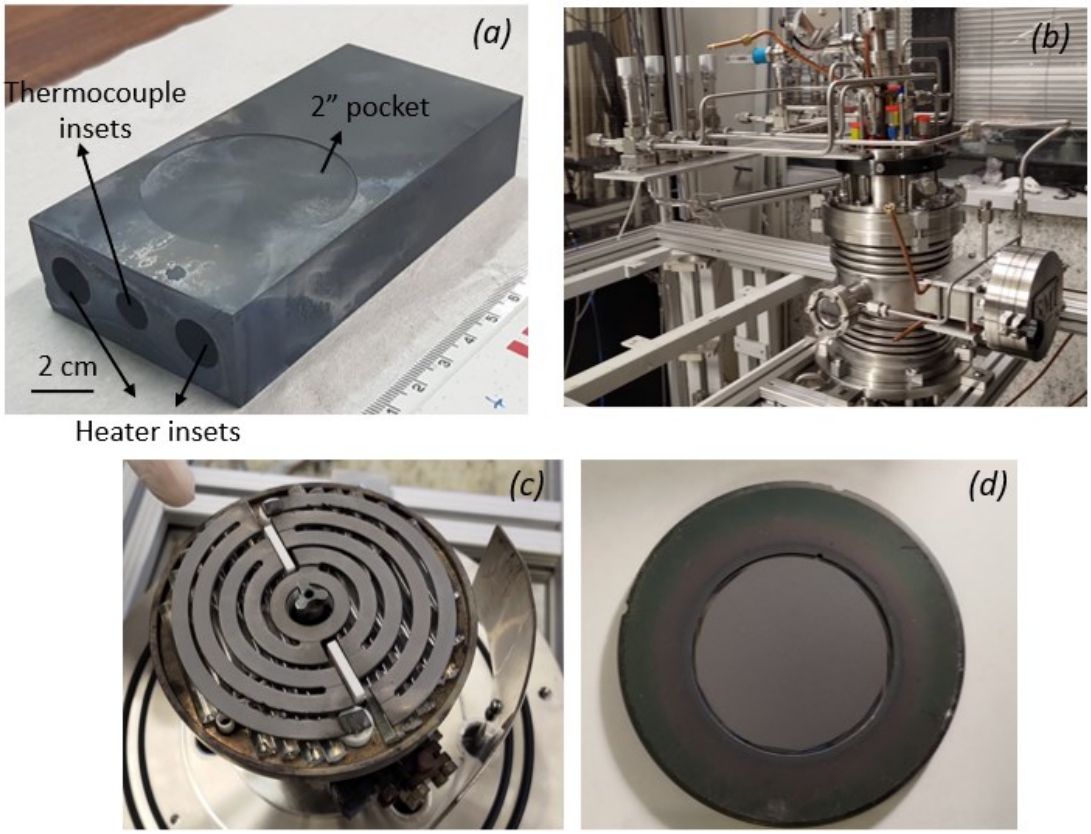

Figure 3.2 (a) Graphite substrate holder of the horizontal MOVPE reactor at IMEM (Parma) with the 2" substrate pocket and the thermocouple and heating insets. (b-d) Images of the vertical MOVPE reactor at IMEM (Parma), substrate heater and 2" substrate holder.

The susceptor used in this configuration was made of graphite [see Figure 3.2 (a)]. The growth temperature is regulated by a proportional-integral-derivative (PID) controller, connected to a thermocouple positioned at the center of the susceptor. The horizontal configuration adopted do not allow for the substrate rotation during the growth and therefore resulted in a gradient of thickness from the region closer to the inlet of the precursors (higher thickness – higher grow rate). Also, as reported by Bosi *et al.,*[120] for growth performed in this very same reactor, a relationship was found between the κ- or β-Ga_2O_3 phase stabilization and the grow rate. In particular, lower growth rates (*G.R.* < 5 nm/min) were found to stabilize the β-phase. In light of this, together with T_g < 700°C and H_2O as oxidizing precursor, one additional fundamental parameter in the MOVPE growth for the

stabilization of the κ-polymorph is the grow rate that for single phase layers must usually be equal or exceed the threshold of 10 nm/min.[120]

3.1.1.2 Vertical MOVPE reactor

The vertical MOVPE reactor [see Figure 3.2 (b)] was installed and calibrated during the candidate second year of PhD. For this reason, even though the candidate was directly involved in the new epilayers optimization procedures, providing a continuous feedback on the quality of the grown Ga_2O_3 samples (X-ray diffraction and photodetectors characterization), in this dissertation are not included samples grown with this new reactor. The vertical configuration, foresees a columnar structure with the susceptor [see Figure 3.2 (c)], substrate holder [see Figure 3.2 (d)] and a "shower head". This set-up allows for rotation up to 1000 rpm of the substrate holder resulting in higher thickness homogeneity of the deposited layer over 2" substrates. The system is also designed in order to realize mist-CVD deposition, even though so far the set-up was not optimized in this direction.

3.1.2 Molecular beam epitaxy (MBE)

This section is based on the materials and methods section presented in the PhD thesis of M. Budde.[137] The MBE system described hereafter is the one the candidate worked on, for a total of seven months spent ad the Paul Drude Institute as a PhD visiting student in the oxides epitaxy group of Oliver Bierwagen. The results of this work are extensively reported in Chapter 5. Figure 3.3 (a) reports a schematic representation of the used MBE system. In the growth chamber (GC), an ultra-high vacuum (UHV) environment, *i.e.*, base pressure $p_{GC} \approx 10^{-9}$ mbar, is achieved through different pumps, *i.e.,* turbomolecular, cryogenic and ion. Additionally, the GC is enclosed by a double-walled structure filled with liquid nitrogen, forming a cryo-shield that reduces the density of condensable contaminants (*e.g.*, H_2O and CO_2) and lowers the overall pressure inside the chamber. The system is also equipped with two additional pre-chambers that allow not to affect the base vacuum of the GC: the load lock (LL) to introduce/extract the samples in/from the MBE system and the middle chamber (MC) to transfer samples between LL and GC. Both LL and MC are equipped with vacuum pumps as well as heaters to degas the substrates and sample holders prior the introduction in the GC.

In contrast to MOVPE, MBE foresees the employment of high purity sources that do not have to be cracked like in the case of the metalorganic precursors used in CVD methods; this is ideal to potentially reduce the possible contaminations and impurities incorporation in the epitaxial layers (*e.g.*, C and H). Indeed, at the bottom of the GC, several different effusion cells contain either high purity metals or metal-oxides, that can be individually heated at different temperatures; their opening in individually controlled by shutters [see Figure 3.3 (b)]. A larger main shutter covers the substrate and can be used to precisely control the start of the growth process (*e.g.*, possible fluctuations of the

individual T of the cells when their shutter is opened), even when using multiple metal sources. In this work Ga, In and SnO effusion cells where used (see Chapter 5 for additional details). To calibrate the metal fluxes, the beam equivalent pressure (BEP) is recorded. BEP is the local pressure induced by the metal flux coming from the cells. It is measured at the substrate position through a retractable ion gauge that is placed at the substrate position before the growth; the BEP is proportional to the generated particle flux according to the heating temperature of the metal effusion cells (T_{cell}). The active oxygen flux is supplied by a radio frequency (RF) O-plasma source equipped with a mass flow controller. The plasma source enhances oxidation efficiency by generating activated oxygen atoms; the actual oxidation power provided by the RF plasma source can be controlled by either the plasma power (P_{RF}) and/or by the provided O_2-flow. The RF plasma source is required to obtain a full oxidation of the provided metal fluxes given the low p_{GC} associated to the MBE growth process. Nonetheless, it is important to highlight that the cavity of the RF plasma source mounted on the PAMBE system at PDI is made of quartz. This has been found to cause the incorporation of Si impurities in the deposited Ga_2O_3 layers that were subject of the following studies. According to the different growth conditions (*e.g.*, provided O_2-flux as well as P_{RF}) as well as usage of the system (*i.e.*, usage time of the RF-plasma source), the background Si concentration had been found to vary in the range of 10^{17} to 10^{18} cm^{-3} (see Chapters 6 – 7). The possible contamination of Si from the quartz cavity in a PAMBE system had already been previously reported in literature.[31,138,139]

In PAMBE, two main advantages come from the UHV environment: (i) the atomic/molecular fluxes propagates from the source to the substrate with minimized scattering events, (ii) the use of *in-situ* measurement techniques, *e.g.*, reflection high-energy electron diffraction (RHEED) and laser reflectometry (LR) is allowed (*in-situ* techniques described in the section below).

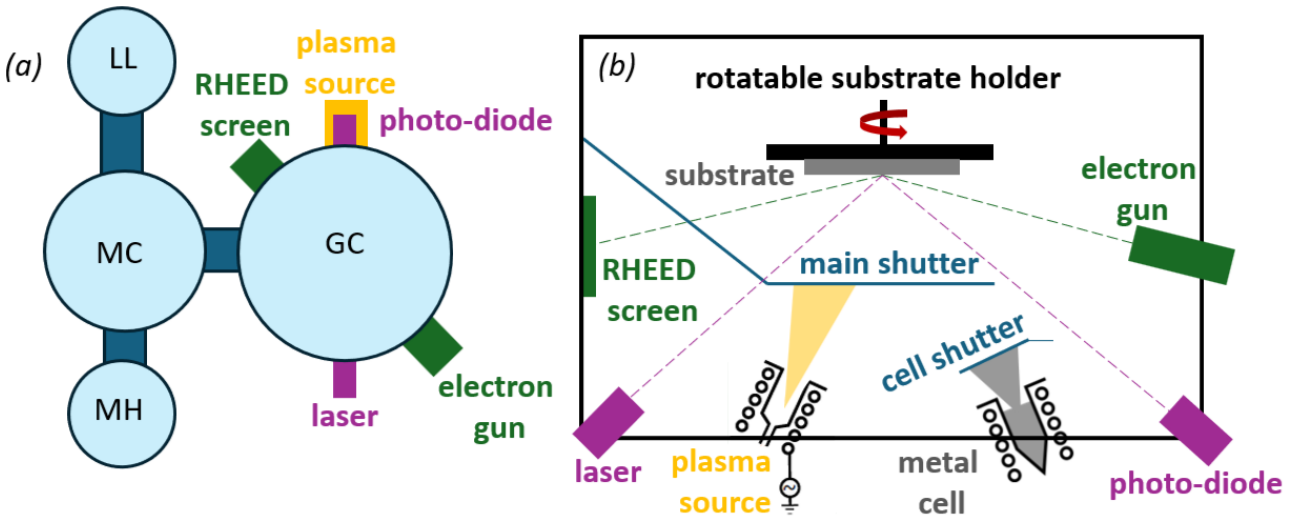

Figure 3.3 (a) Schematic image of the MBE system used in this work showing the load lock (LL), middle heater (MH), middle chamber (MC) and growth chamber (GC). The growth chamber has seven metal cells including Ga, In and SnO.

In addition, for *in-situ* analysis, LR and RHEED apparatus are present. (b) Schematic view inside the growth chamber including shutters, fluxes (shaded areas) and *in-situ* measurement setups. The images are not in scale.

The substrate can be independently heated in the 100 - 1100 °C range; the temperature of the substrate heater is measured by either a thermocouple positioned between the substrate and the heating filament as well as a pyrometer, allocated at the bottom of the GC and aligned with the center of the substrate holder. The heat adsorption from the substrate can be granted either by a back-coating of strontium ruthenate (starting with a $SrRuO_3$ powder in suspension in isopropanol applied with a brush on the back side of the substrate),[140] or by indium bonding on a silicon wafer; for the latter case, further details will be provided in Chapter 5. A motor mounted on top of the chamber allows for the substrate rotation during growth (2 rotations per minute), ensuring uniform thickness and heating.

3.2 In-situ characterization techniques

3.2.1 Laser reflectometry (LR)

Laser reflectometry (LR) is used to real-time monitoring of the grow rate *GR* and thickness (*t*) of a sample during MBE growth. Figure 3.4 (a) schematically reports the working principle of the method, based on the interference between two reflected waves with defined λ at the vacuum/epi-layer and epi-layer/substrate interfaces. The interference of the reflected waves is given by the additional path of the transmitted wave through the epi-layer, hence it depends on the layer thickness (*t*). The reflected light is then collected by a photodiode and the variation of the laser intensity would result in a sinusoidal curve during a steady growth, assuming a constant incidence angle (for the used system: α = 60°) [see Figure 3.4 (b)]. Noteworthy, the interference phenomenon of the reflected waves is observed only if a difference in the refractive index is present for the substrate and the epi-layer, *i.e.,* LR is applicable exclusively for heteroepitaxy.

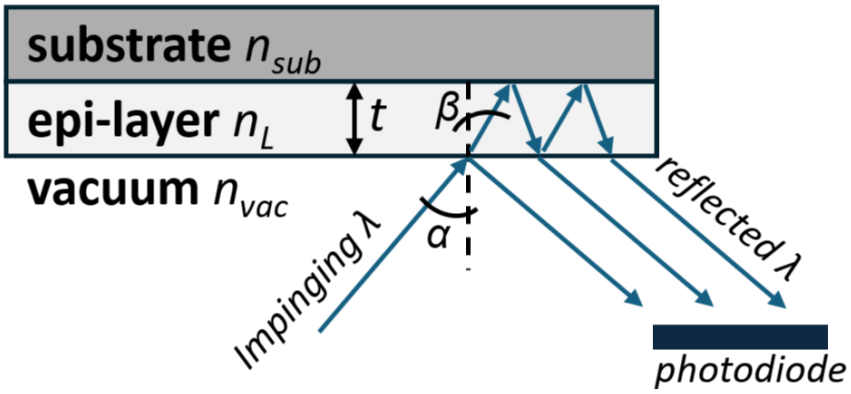

Figure 3.4 Schematic image of the LR mechanism resulting in interference between reflected waves. Laser light reflects at the sample surface and heterointerface, resulting in a phase difference for the two waves function of the thickness *t* and the incidence angle *α*.

From the oscillation length (τ) of the recorded sinusoidal curve, the *GR* of the epitaxial film can be extracted, according to Equation 3.1, with the refractive index n_L for κ-Ga_2O_3 $n_L = 2$ and λ_{laser} used by the candidate was either blue (λ_{laser} = 402 nm) or red (λ_{laser} = 650 nm).

$$\tau = \frac{\lambda_{laser}}{2n_L GR}$$

Equation 3.1 Extraction of the *GR* of the epilayer from the oscillation τ of the sinusoidal variation of the LR signal over time. λ_{laser} used was either blue or red and $n_L = 2$ for κ-Ga_2O_3.

Each full oscillation of the LR would have a fixed length $\tau = t_{min}$, *i.e.*, a minimum thickness of the epilayer to extract the *GR*, calculated as per in Equation 3.2. For κ-Ga_2O_3, the t_{min} with the blue and red laser were ≈ 175 and 112 nm, respectively.

$$t_{min} = \frac{\lambda_{laser}}{2n_L}(\cos(\arcsin(\sin(\alpha)\, n_L^{-1})))^{-1}$$

Equation 3.2 Minimum layer thickness resulting from a full oscillation of the LR given the laser wavelength λ_{laser}, the layer refractive index n_L and the laser incident angle α.

3.2.2 Reflection high energy electron diffraction (RHEED)

Reflection High-Energy Electron Diffraction (RHEED) is a powerful *in-situ* tool to study: (i) the quality of the substrate surface, (ii) the epi-layer growth mode and (iii) surface kinetics.[141] In this work, an electron gun provided by Createc GmbH, generates high energy (E_{kin} = 20 keV) electrons (wavelength ~ 0.062 nm) directed on the sample surface at a grazing incidence angle (< 2°). Due to the low incident angle and the strong Coulomb interaction between the electron beam and the electron cloud of the atoms of the layer, RHEED technique has a low penetration depth, making it highly surface-sensitive investigation tool. The scattered electrons are then collected on a phosphorous screen, placed on the diffracted beam path. The diffraction spots recorded on the screen, represent the sample's reciprocal lattice; their formation is given when constructive interference of the incident and diffracted waves are obtained. Laue equation furnishes the condition for constructive interference in the reciprocal space [considering the impinging ($\overrightarrow{k}$) and diffracted ($\overrightarrow{k'}$) wave vector] given the reciprocal lattice vector of the probed crystal lattice (see Equation 3.3).

$$\overrightarrow{k'} - \overrightarrow{k} = \vec{G} = n\left(\frac{2\pi}{\|a\|}\right)$$

Equation 3.3 Laue equation setting the condition for the constructive interference of the impinging ($\overrightarrow{k}$) and diffracted ($\overrightarrow{k'}$) waves in the reciprocal space, given by the reciprocal lattice vector $\left(\frac{2\pi}{\|a\|}\right)$

The graphical representation of the Laue equation is the Ewald sphere, (see Figure 3.5), which has a radius of $k = \frac{2\pi}{\lambda}$ and all points on the sphere satisfy the Laue equation. Since RHEED primarily probes the first few monolayers due to its high surface sensitivity, there is no periodicity in the z-direction, leading to a transformation from discrete reciprocal lattice points into continuous rods, called reciprocal lattice rods (grey points in Figure 3.5), which intersect the Ewald sphere (in red) at various heights, forming diffraction spots arranged in a circle, known as the Laue circle. Figure 3.5 also reports two exemplarily RHEED patterns generated by diffraction from a flat and a rough surface. When surface quality degrades due to extended defects, steps, or roughness, the reciprocal rods become broader, and the diffraction spots elongate, creating a streaky pattern (Figure 3.5). For further details about the RHEED technique, see ref. [141,142].

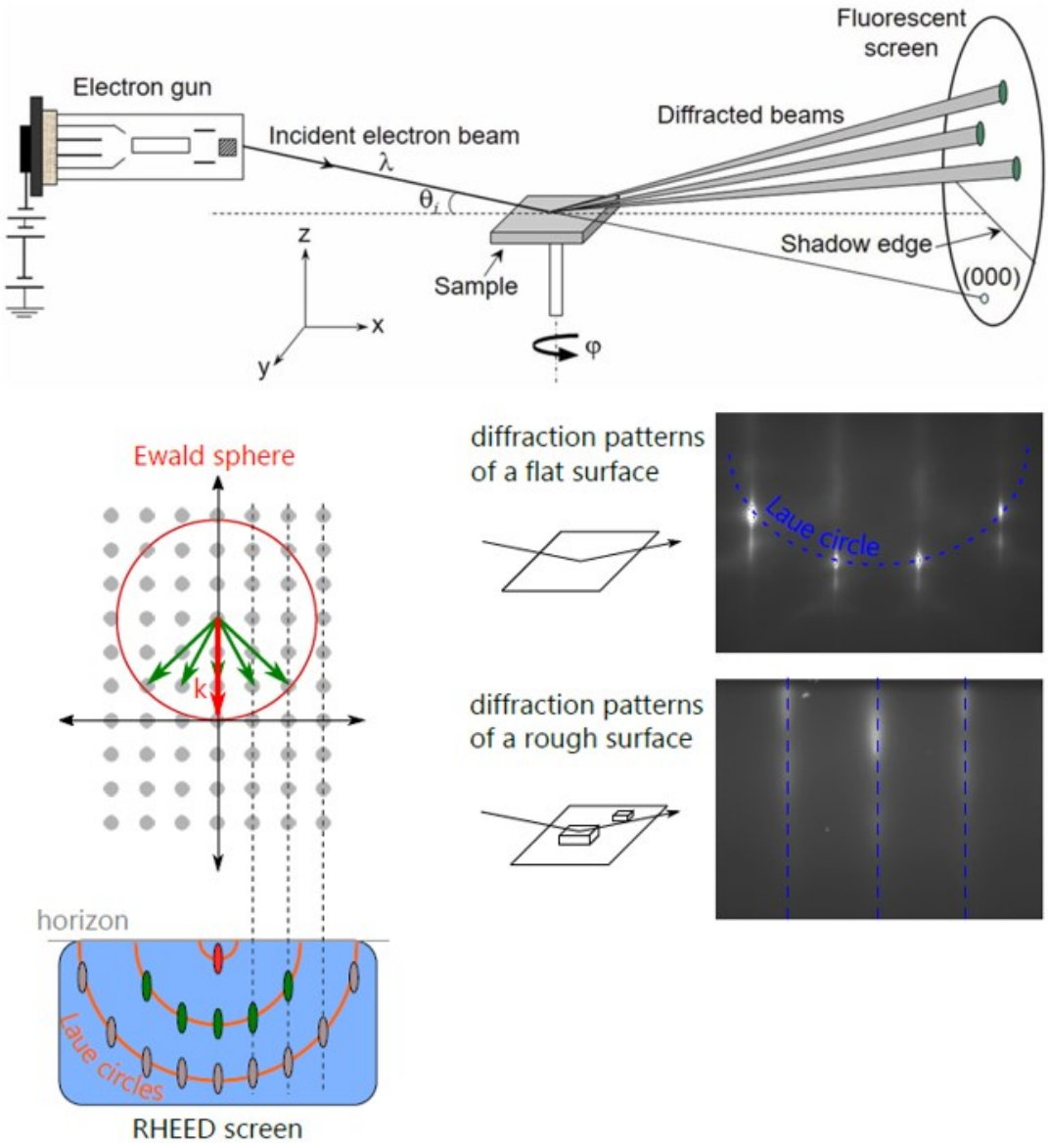

Figure 3.5 On the top, schematic diagram of the RHEED set-up geometry. The parameters λ, θ_i, and φ are the incident electron wavelength, incident angle, and surface azimuthal angle of the sample. The transmitted (000) corresponds to the primary electron beam. Reproduced with permission from ref.[142]. At the bottom, schematic representation of the top-view of the Ewalds sphere and the resulting diffraction spots, Laue circles, on the phosphorus screen. On the right, exemplary RHEED pattern from a flat and rough surface. Reproduced from ref.[137].

3.3 Ex-situ characterization techniques

3.3.1 Atomic force microscopy (AFM)

Atomic force microscopy (AFM) is a scanning probe technique used to collect information over the surface morphology of thin films at the nanometer scale. It employs a sharp tip (few nanometers radius) mounted on a flexible cantilever that scans the surface of the sample. A piezoelectric crystal (piezo scanner) is used to move the sample precisely. As the AFM tip interacts

with the sample surface - either repelled or attracted due to electrostatic forces - the cantilever bends. A laser light, aligned on and reflected by the cantilever, is recorded on an array of diodes (see Figure 3.6). The distribution of the reflected laser spot on the detector generates a specific voltage, which, combined with an electronic feedback system, enables the derivation of the sample's surface morphology. AFM can commonly operates in three different modes: (i) contact mode (constant-force or constant-height), (ii) non-contact mode, and (iii) tapping mode. Even though contact mode offers the highest resolution, it can lead to tip or surface damage. In contrast, non-contact mode minimizes this risks but it is however is more susceptible to interference from surface contaminants. Therefore, tapping mode was employed in this work, representing a good trade-off between resolution and damage control.

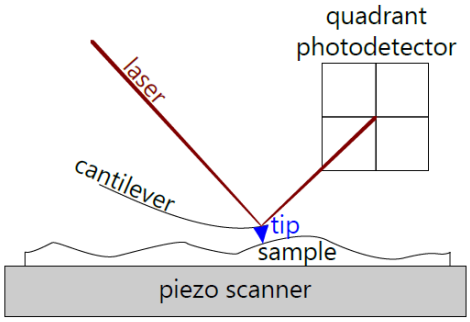

Figure 3.6 AFM schematic set-up. The bending of the cantilever, monitored with the laser reflection, is recording the topography variation. The optical input is then converted in an electrically signal ending up with generation of height scans profiles. Reproduced from ref.[137].

The lateral resolution of the AFM is determined by the diameter of the tip, with commercially available tips usually ranging from 2 nm to 20 nm. From the height profiles obtained from AFM measurements, the digital images of the surface morphology are generated and the surface root-mean-square roughness (*RMS*) can be extracted (see Equation 3.4). The *RMS* is provided as an indication of the layer roughness. In this work two different AFM instruments were used by the candidate: (i) Bruker Dimension Edge and (ii) XE-100 microscope. The AFM data and images reported in this work have been elaborated by the candidate with the open source Gwydion software.

$$RMS = \sqrt{\frac{\sum_{n=1}^{N}(z_n - \bar{z})^2)}{N}}$$

Equation 3.4 RMS value extraction considering the number of point *N*, the single point height z_n and their average $\bar{z}$

3.3.2 X-ray diffraction (XRD)

X-ray diffraction (XRD) is probably the most applied non-destructive technique for the structural characterization of thin films, providing insights into *e.g.*, crystal quality, phase and relative lattice constants. The working principle of XRD is schematically reported in Figure 3.7 (a): the X-rays impinge the sample at an incident angle θ and interact with the atoms of the deposited layer. If the atoms are arranged in the form of a crystal with well-defined spaced lattice planes, the X-rays are scattered at well-defined incident θ angles. The scattered waves can interfere constructively or destructively. The condition to obtain constructive interference, *i.e.,* diffraction signals, is governed by the Bragg's Law (see Equation 3.5), where λ_{XRD} = 0.15406 nm for Cu K_α, d is the lattice spacing for a defined crystal plane labelled with the Miller indexes hkl and n defines the order of the diffraction maxima.

$$n\lambda_{XRD} = 2d_{hkl}sin(\theta)$$

Equation 3.5 Bragg's law

In this study, two different diffractometers are employed: (i) a Rigaku Smartlab XE with HyPix 3000 detector (located at UniPR) and (ii) a X'Pert Pro MRD system from PANalytical (located at PDI), both using copper Kα radiation and equipped with a monochromator and an Eulerian cradle. The cradle allows to access, besides 2θ and ω angle (defined by the detector and X-ray source position) also φ and χ for rotation around z and x axes, respectively [see Figure 3.7 (b)].

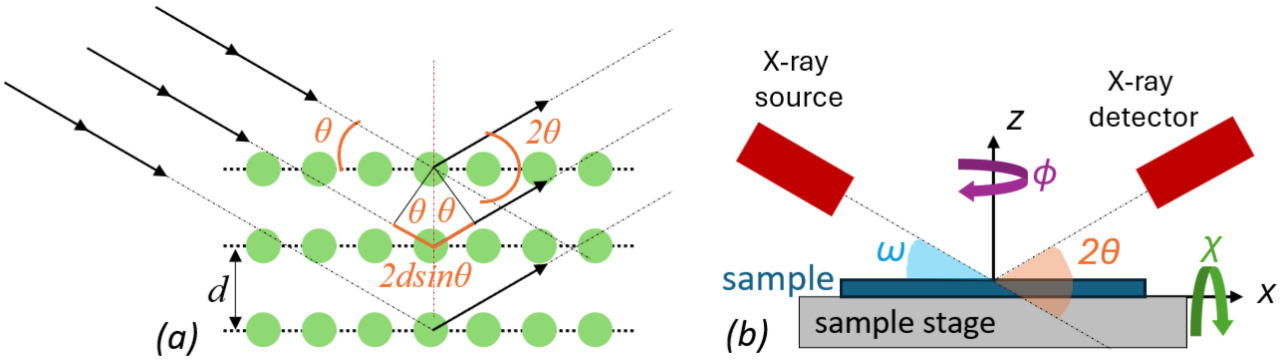

Figure 3.7 (a) Bragg's law represented through a schematic draw. Waves scatter at atoms of parallel lattice planes with the distance d. Constructive interference occurs for certain angles, as described by Equation 3.5. (b) Schematic of the XR setup used for this study. The Eulerian cradle setup allows the variation of four angles: θ, ω, φ and χ.

Different measurement configurations can be adopted in XR diffractometry. The ones, mostly applied by the candidate, and recurring throughout the data discussion (Chapter 4 – 7) are:

(i) *2θ-ω scan*: this mode involves scanning the Bragg peaks by adjusting $\omega/2\theta$ in a 1:2 ratio to effectively probe the lattice spacing d (as per Bragg's Law). When χ = 0,

symmetric reflections (out-of-plane) are measured, while for $\chi \neq 0$, asymmetric reflections (in-plane) are accessible. Nonetheless, the independent adjustment of the ω angle can also account for the offcut of a substrate when its in-plane direction is laying on the detector-source plane [see Figure 3.8.(a)]. For the candidate's work, *2θ-ω* scans are acquired to assess phase of the layers, epitaxial relation with the substrate and incorporation of catalyst (see Chapter 5 for more details).

(ii) *ω scan (Rocking Curve)*: in this mode, the detector is held at a fixed *2θ* while the X-ray source is moved. The fixed *2θ* is set at the value corresponding to the most indicative reflection for the specific material under investigation [*e.g.,* for κ-Ga_2O_3 the (004) reflection with *2θ* = 38.88°]. The full width at half maximum (FWHM) of the rocking curve is a key indicator of the crystalline quality of a probed layer;

(iii) *φ scan*: this mode is applied for fixed *2θ-ω* relation for either out-of-plane ($\chi = 0$) or in-plane ($\chi \neq 0$) reflections, while the sample is rotated around the vertical *z* axes [see Figure 3.7 (b)]. In this dissertation, φ scans are involved for a twofold reason: investigation of the absolute value and direction of an unintentional offcut of the substrates (see Section 5.2) for out-of-plane reflection ($\chi = 0$) and to address the presence of additional phases or rotational domains in Ga_2O_3 layers.

(iv) *Pole figures*: configuration adopted to study epi-layers grown on substrates with intentional offcut (≥ 1°), *i.e.,* the scattering vector of the substrate normal reflection is not normal to the diffractometer *xy* plane [see Figure 3.8 (a)]. In this case, a single φ-scan, *i.e*., a single 360° *φ* rotation around a selected diffraction vector either out-of-plane ($\chi = 0$) or in-plane ($\chi \neq 0$), would not account for the processional motion of the scattering vector [see Figure 3.8 (b)] due to the presence of the substrate offcut. In order to account for the offcut, a pole figure acquires multiple 360° *φ* scans for different steps of χ in the range $\Delta\chi = \chi_{hkl} \pm offcut$

(v) *Reciprocal space maps (RSM)*: acquired to evaluate the strain/relaxation of the in-plane epi-layer. Indicative reflections should be identified, [*e.g.*, (*h0l*) and (*0kl*) in the case of a (*00l*) oriented epilayer] that provides information to its in-plane parameters with respect to the ones of the substrate; RSM are built via subsequent *2θ* scans for each *ω* step, allowing for a mapping in the reciprocal space around the chosen reflection.

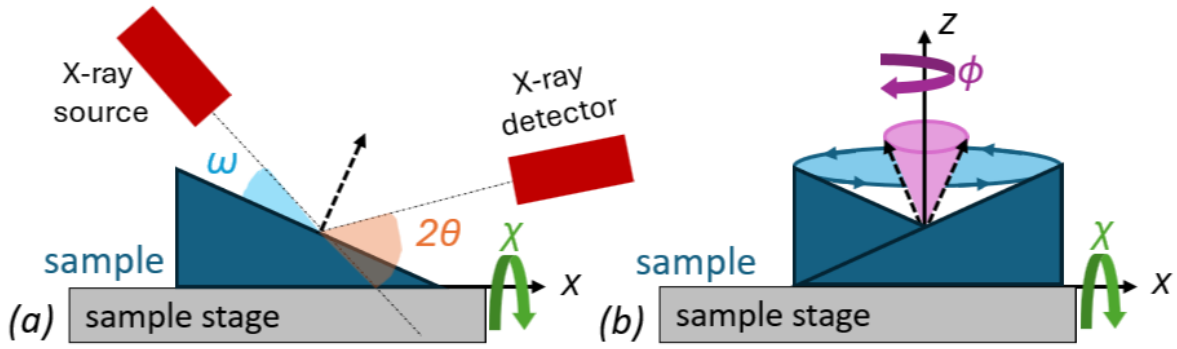

Figure 3.8 (a) Schematic representation of an offcut-substrate with the diffraction vector normal to the surface reported in black-dashed line. A standard 2θ-ω scan is performed by compensating the offcut with ω, *i.e.*, the relationship $\omega = 2\theta/2$ employed for nominally oriented substrates, is now considering the offcut value and becomes $\omega = (2\theta/2 - offcut)$. (b) Reports schematically the processional motion (purple shaded area) of a general scattering vector, when a standard φ scan is performed. To compensate the offcut effect, *i.e.,* to keep the scattering vector in the *zx* plane of the X-ray source-detector, the χ angle is involved (tilting the sample around *x* axes). Hence, the pole figure is the result of multiple 360° φ scans in a range $\Delta\chi = \chi_{hkl} \pm offcut$.

3.3.2.1 XRD applied to κ-Ga_2O_3

As anticipated in Chapter 2, in 2018 Nishinaka *et al.*[42] provided a useful method to (i) discriminate between the hexagonal (ε) and the orthorhombic (κ) phase in Ga_2O_3 and (ii) address the rotational domains presence with XRD, *i.e.,* non-destructive characterization technique. As per (i), Figure 3.9 (a) reports the XRD relations of angles 2θ-χ for the reflections of the orthorhombic κ and hexagonal ε structure of Ga_2O_3. It can be noted that for $\chi = 0°$, *i.e.*, out-of-plane, the {00l}-κ and {000l}-ε reflections are perfectly overlapping; in this set-up it is thus impossible to discriminate between the two structures. However, if $\chi \neq 0°$, it is possible to access reflections, *e.g.,* (122) [highlighted with the red arrow in Figure 3.9 (a)], where only the orthorhombic structure has reflexes, allowing to the unambiguous discrimination between ε and κ-Ga_2O_3 from XRD analysis. As per (ii), the in-plane rotation of the orthorhombic unit cell in (001)-oriented epitaxial layers is not detectable when observing the normal reflections, *e.g.*, {00l}, since the plane spacing in the [001] direction is not affected by the in-plane rotated domains. However, if the investigated reflection has in-plane contributions [*e.g.,* (122)], the use of in-plane rotations (φ) at given diffraction conditions (fixed 2θ-ω and χ) can allow to highlight the presence of rotational domains considering the unit cell symmetry [see φ-scan reported in Figure 3.9 (b) highlighting the presence of three rotational domains in a κ-Ga_2O_3 layer deposited on c-plane sapphire]. In Chapter 4, this investigation tool will be largely exploited to investigate the κ-Ga_2O_3 rotational domains presence. Similar considerations will be also used to identify the presence of traces of β in the MBE grown κ-Ga_2O_3 layers as well as rotational domains in the monoclinic polymorph.

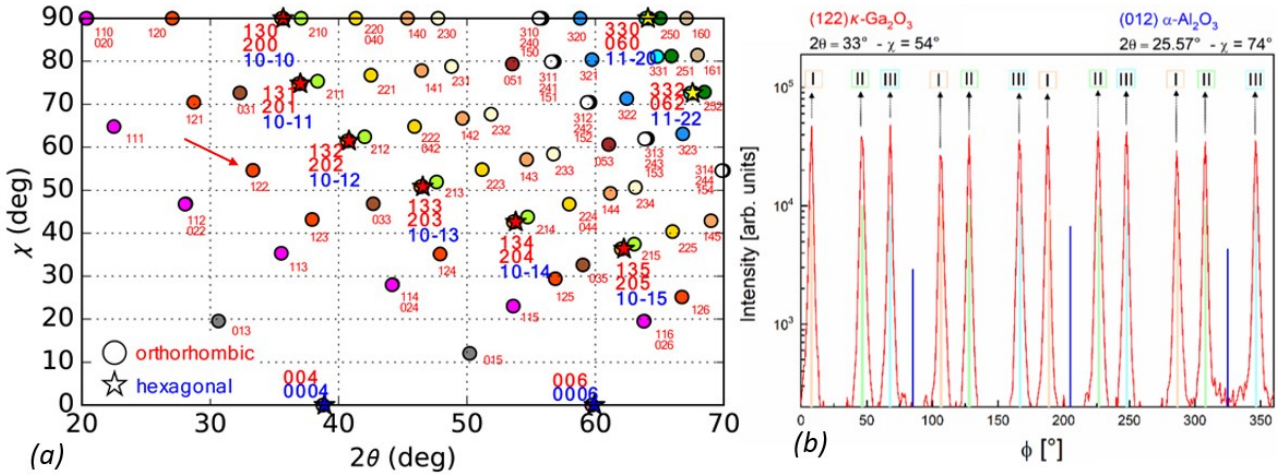

Figure 3.9 (a) XRD angle relationships (2θ-χ) of the orthorhombic (κ) and hexagonal (ε) structures of Ga_2O_3; image reproduced with permission from H. Nishinaka *et al.*, Jpn. J. Appl. Phys. 57, 115601 (2018). Copyright (2018).The Japan Society of Applied Physics. Reproduced by permission of IOP Publishing Ltd. All rights reserved. (b) φ-scan of the (122) reflection of a (001) κ-Ga_2O_3 layer deposited on c-plane sapphire highlighting the presence of three rotational domains (peaks belonging to each domain labelled with roman numbers I, II, III). Image reproduced from ref.[58].

3.3.3 Electro-optical measurements

3.3.3.1 Transfer length method (TLM)

Transfer length method or transmission line model (TLM) is a powerful tool to evaluate the resistivity (ρ_{sem}) of the probed layer as well as the contact resistance of the deposited contacts. A series of metal-semiconductor contacts are deposited (in this case via magnetron sputtering)[143] at increasing distances $L_{1\text{-}4}$ for the linear TLM (l-TLM) geometry, or with increasing spacing between concentric contacts, for the circular geometry (c-TLM) [see Figure 3.10 (a - b)]. In the case of l-TLM two probes are placed on adjacent contacts and the characteristic current-voltage (*I-V*) is acquired. From the *I-V* curve, the measured resistance R_m is extracted according to the Ohm's law ($R_m = m^{-1}$ with m, slope of the linear fit of I vs. V plot).

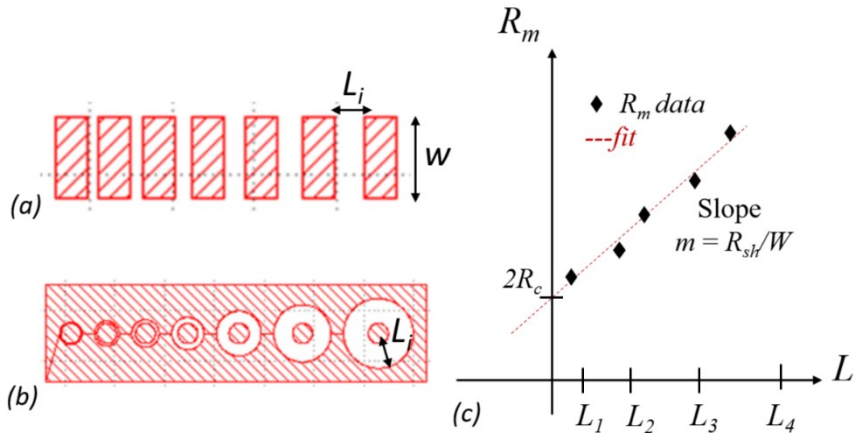

Figure 3.10 (a) and (b) schematic representation of the linear and circular TLM contacts configuration. (c) R_m vs. L for the linear TLM geometry obtained from *I-V* measurements for each couple of contacts with spacing L_i.

The measured resistance (R_m) is a linear combination of the contact resistance ($2 \cdot R_c$), as well as the resistance of the semiconductor material between the contacts R_{sem}. Equation 3.6 reports the expression of R_m with the resistance of the material expressed as $R_{sem} = \frac{R_{sh}L}{W}$ considering the sheet resistance (2D) of the layer (R_{sh}) and the geometrical parameter of the conduction channel (L and W).

$$R_m = R_{sem} + 2R_C = \frac{R_{sh}L}{W} + 2R_C$$

Equation 3.6 Linear dependence of the measured R_m from the semiconductor 2D sheet resistance R_{sh} and contacts resistance R_c. L and W are the geometrical parameters of the contacts spacing and width [see Figure 3.10 (a)]

From the linear dependence R_m vs. L [see Figure 3.10 (c)], the R_{sh} of the semiconductor as well as R_c for the metal contacts can be extracted from the slope and the intercept with the y axes, respectively. From R_{sh}, the resistivity of the investigated semiconductor (ρ_{sem}) is extracted according to Equation 3.7 with t being the thickness of the investigated layer.

$$\rho_{sem} = R_{sh}Wt$$

Equation 3.7 ρ_{sem} for l-TLM.

For the c-TLM, the approach is very similar, but a correction factor must be introduced to account for the geometry of the contacts.[144] Indeed, from the R_m obtained from the *I-V* characteristics for increasing L_i, the $R_{corrected}$ is calculated according to Equation 3.8, with r_i is the radius of the inner contact (fixed). The ρ_{sem} is then obtained, similarly to l-TLM, considering the contact geometry and layer thickness, as reported in Equation 3.9.

$$R_{corrected} = \frac{R_m}{(\frac{r_i}{L_i}) \cdot \ln(1 + \frac{L_i}{r_i})}$$

Equation 3.8 $R_{corrected}$ for c-TLM.

$$\rho_{sem} = R_{sh} 2\pi r_i t$$

Equation 3.9 ρ_{sem} for c-TLM.

3.3.3.2 Photocurrent spectroscopy (PCS)

Photocurrent spectroscopy (PCS) is used to investigate the electrical conduction properties of a material when exposed to a defined light stimuli, *i.e.*, by measuring the current generated in a semiconductor material at a fixed applied bias when illuminated at different wavelengths. The working principle of the method is based on the photoelectric effect, *i.e.*, photon-generation of electron-hole pairs in the investigated material. The effect is described by Equation 3.10, where the change in conductivity Δσ of an ideal material is described as the excess of photocarriers generated (electrons Δn and holes Δp) and their mobilities (μ_n and μ_p) and is directly related to the photocurrent density J_{ph}.

$$\Delta\sigma = e\left(\mu_n \Delta n + \mu_p \Delta p\right) = \frac{J_{ph}}{E}$$

Equation 3.10 Conductivity variation induced by illumination

In an ideal semiconductor (nominally free of structural and point defect), only when $E_{light} > E_g$, the photoelectric effect should be expected with generation of electrons in the CB and holes in VB that would eventually recombine with emission of photons. However, in the PCS analysis, the specimen has metal contacts on its surface (see 3.3.3.1 for a schematic representation of metal contacts) and an external bias is applied to collect the photogenerated charges. The applied external electric field E, prevents the recombination of the electron-hole pairs and allows for PC extraction. Moreover, if the light source is equipped with a monochromator, a spectral response of the sample can be obtained by recording the PC generated as function of the different impinging wavelengths.

In the case of κ-Ga_2O_3, having $E_g \approx 4.9 – 5$ eV, the PCS is expected to have its maximum for $\lambda \approx 250$ nm. To collect information about a wider photoresponse of the material, the PC is acquired in the 250 – 650 nm range. The PCS measurements reported in Chapter 6 and 7, were performed by the candidate to characterize the optical performances of the materials, *i.e.*, photodetectors (PDs) performances. The configuration set-up foresees an Oriel optical system equipped with a 250 W Quartz Tungsten Halogen Lamp (QTH) and a monochromator 130/74000 CornerStone covering the range (200 - 700 nm) with 1 nm resolution. The fabrication of PDs foresees a simple resistor device

configuration (metal-semiconductor-metal) that requires the deposition of Ohmic Ti/Au or SnO_{2-x}/ITO/Au contacts through magnetron sputtering, according to ref.[143].

The external bias (in our case kept at 200 V) is applied through a Keithley source-meter 2400 between the metal contacts (geometrical details of the contacts reported in Chapter 6). The sample is illuminated with the monochromatic light and the generated PC is measured with the Keithley source-meter, for each selected wavelength in the 250 – 650 nm range. From the recorded PC, the responsivity curve *R(λ)* is defined according to Equation 3.11 considering the incident optical power $P_{inc}(\lambda)$ over the effective collection area, *i.e.,* area between the metal contacts. The $P_{inc}(\lambda)$ is obtained with a calibrated photodiode sensor (Newport 818 UV).

$$R(\lambda) = \frac{PC}{P_{inc}(\lambda)}$$

Equation 3.11 Responsivity *R(λ)*

3.4 Additional characterization methods

Here after, some of the additional characterization methods used by collaborators are briefly listed, pointing out the relative information extracted in the framework of the candidate work. References are provided if the reader would be interested in additional details.

Van der Pauw – Hall measurements The Van-der-Pauw method, developed in 1958,[145] allows for the measurements of the resistivity and Hall coefficients of arbitrarily shaped sample. Two major requirements should be met: (i) continuity of the layer (*e.g.*, no holes) and (ii) presence of four ohmic contacts with dimensions negligible w.r.t to their spacing. In the case of a thin film characterization, it is also necessary that the substrate/template over which this is deposited is electrically insulating, so to allow for the decoupling of its influence in the collected data. By applying a current between two adjacent contacts and measuring the voltage drop between the other two, the resistivity can be determined. Repeating this process with different contact pairs provides more data for accuracy. If a magnetic field is applied, the Hall coefficient can also be measured by detecting the Hall voltage. For a detailed description of the method, please refer to ref.[145].

Mercury (Hg) probed Capacitance-Voltage measurements A mercury probe system was used to determine the 3D carrier density of Ga_2O_3 thin films through Capacitance-Voltage (*C-V*) measurements. This method utilizes temporary metallic contacts formed by liquid Hg, which are applied to adhere to the film surface. The Hg contacts usually allow to form a Schottky barrier with a geometry that is defined by the experimental setup; a *C-V* measurement can allow for a carrier

profiling from the probed surface of the sample. For additional details over the technique, please refer to ref.[146,147].

Raman spectroscopy is a non-destructive technique used to study lattice vibrations by measuring the inelastic scattering of light. When the light interacts with the lattice atoms, most photons are elastically scattered, while a small fraction undergoes energy shifts due to interactions with lattice vibration. The energy shifts provide a "fingerprint" of the structure, allowing for material identification, characterization, and analysis of chemical bonds. An exhaustive Raman investigation of β- and κ-Ga_2O_3 is reported in ref. [60,102,148].

X-ray photoelectron spectroscopy (XPS) is a surface-sensitive non-destructive analytical technique based on soft X-ray-matter interactions. It is mainly used to determine the chemical surrounding of the surface atoms and chemical composition of the sample superficial layers (first 0.5-10 nm). For additional details please refer to ref.[149].

Time of flight second ion mass spectroscopy (ToF – SIMS) exploits energetic primary ions to sputter a sample and collect information over the sputtered species in terms of mass-to-charge ratio. It can be used to collect depth profiles of different elements in thin films. Quantification of the species require a calibration sample, *e.g.,* implantation standard (see Appendix A). For additional details see ref.[150].

Electron back-scattered diffraction (EBSD) is a surface sensitive non-destructive technique. The backscattered electrons from the specimen surface provide information about the local crystallographic structure and orientation at the microscopic level of the material.[151]

Photoluminescence spectroscopy (PL) and **Photoluminescence excitation** (PLE) are both non-destructive techniques based on light-matter interaction. They use a light source to investigate the optical and electronic properties of the material. In PL, the sample is excited by a light source, with a fixed energy and its spectral emission is recorded. PLE is performed by recording the PL emission as a function of the excitation energy. An exhaustive description of the PL – PLE combined techniques applied on the Ga_2O_3 material system is reported in ref. [60].

Depth resolved cathodoluminescence (DRCL) is used to investigate the optical properties of the materials, with depth sensitivity controlled by increasing the electron acceleration voltage (non-destructive). The collected emission of the sample provides information about intrinsic optical properties as well as defects presence.[152]

Transmission electron microscopy (TEM) allows to investigate the atomic arrangement of the specimen for crystal structure identification, structural defects detection and interface quality at the atomic level. Further details can be found in ref.[[149]].

4 Role of structural defects in κ-Ga_2O_3

The core of this chapter is the investigation of the structural defective nature of κ-Ga_2O_3 and its effect on the functional properties of the material. Section 4.1, shows (i) the proof of the rotational-domains mediated anisotropy of κ-Ga_2O_3 and (ii) the effect of the structural defects over the in-plane transport properties of Si-doped κ-Ga_2O_3. In this latter section, focus is given on the role of the silane flux (Φ_{SiH4}), *i.e.,* the Si-doping source, over the expansion of the rotational domains, with particular attention to the non-destructive characterization techniques, *e.g.,* Raman and XRD, for rotational-domains characterization. Section 4.2 reports the characterization of the SnO/κ-Ga_2O_3 p-n diode in planar geometry, emphasizing the role of the κ-Ga_2O_3 structural defects on the performances of the relative devices. The results reported in section 4.1 and 4.2 are collected in publications [58] and [153], respectively.

4.1 The role of structural defects on the functional properties of UID and Si-doped κ-Ga_2O_3

As discussed in Chapter 2, the κ-Ga_2O_3 epitaxy on most single crystalline substrates is characterized by the presence of 120° rotated nanosized domains, arranged in a columnar structure along its growth direction, *i.e.*, (001). Their presence was firstly detected in 2017 by I. Cora *et al.,*[20] with a TEM-XRD combined investigation on UID (001) κ-Ga_2O_3 (MOVPE grown on (0001) α-Al_2O_3 substrates). The study allowed for the correct identification of the orthorhombic κ-Ga_2O_3 unit cell (space group $Pna2_1$) instead of the previously assigned one, *i.e.,* hexagonal (ε – space group $P6_3mc$) (additional details reported in Section 2.3). The TEM study also highlighted the presence of numerous planar-defects/boundaries and distinguished them in: (i) twin-boundaries (TBs), coinciding with the (110) twinning planes and (ii) antiphase-boundaries (APBs), detected inside the twin domains and parallel to (100) planes. The nature of the TBs, *i.e.,* coherent (nominally free of dangling bonds) or incoherent (otherwise), was not addressed. Only in November 2023, a new TEM investigation by Vyvenko *et al.,*[154] on microcrystals of κ-Ga_2O_3 (HVPE grown on GaN/(0001) α-Al_2O_3 template), suggested the incoherent nature of the TBs and the presence in every twin-domain of a parallel array of APBs. The APBs are also showing steps and interruptions when crossing the TBs; the combination of incoherent TBs and APBs could play a role in the in-plane transport mechanism. A similar situation has been already discussed for β-Ga_2O_3,[102] where the presence of incoherent twin boundaries [especially in (100)[112] and (-201)[110,117,155] epitaxy] is accounted responsible for the carrier mobility collapse and inefficient extrinsic doping. However, differently from the case of β-Ga_2O_3, in (001) κ-epitaxy both the extended defects previously discussed are mostly vertically oriented.[20,58]

The possible active role of TBs over the κ-Ga_2O_3 transport properties was firstly investigated by Kneiß *et al.*:[59] through the development of vertical κ-Ga_2O_3-based SBDs, the benefits in terms of device performances when the in-plane transport in κ-Ga_2O_3, *i.e.,* crossing TBs and APBs, is avoided, are qualitatively reported. In January 2023, P. Mazzolini *et al.*,[58] furnished the direct proof of the extended defects mediated anisotropy through a direct comparison of in-plane vs out-of-plane resistance measurements in (001) κ-Ga_2O_3 layers; on top of that, the same work also demonstrates the role of an additional silane flow during growth on the overall domain width expansion and its effect on the resulting crystalline quality and in-plane transport properties. Both these aspects are thoroughly described in the following subsections.

4.1.1 In-plane vs. out-of-plane transport measurements

The current-voltage (I-V) measurements reported in this section were directly performed by the candidate at the University of Parma (UniPr) with the help of S. Vantaggio (UniPr). The MOVPE growth of all the κ-Ga_2O_3 samples were performed by M. Bosi, L. Seravalli and P. Mazzolini at the Institute of Materials for Electronics and Magnetism (IMEM - Parma). The GaN templates were MOVPE deposited by S. Leone from Fraunhofer Institute for Applied Solid State Physics (IAF)(Freiburg). The metal contacts deposition and etching/lithography processes were performed by A. Tarahoui from the Paul Drude Institute for Solid State Electronics (PDI - Berlin). Data interpretation was performed by the candidate with the support of P. Mazzolini (UniPr) and O. Bierwagen (PDI).

4.1.1.1 Samples design

To probe (i) in-plane/lateral and (ii) out-of-plane/vertical transport properties, κ-Ga_2O_3 layers were deposited on electrically insulating C-doped and conducting Si-doped (0001) GaN epitaxial templates on top of (0001) α-Al_2O_3 for (i) and (ii), respectively. The GaN templates were grown by MOVPE as reported in ref. [102] (nominal thickness t = 4.5 μm, ρ = 0.2 Ωcm for Si-doped, not measurable for C-doped – from Van der Pauw - Hall measurements performed by S. Leone). All the κ-Ga_2O_3 layers were grown by MOVPE, under the very same synthesis conditions, with H_2 as carrier gas (growth details reported in Section 3.1.1). Two different thicknesses of the κ-Ga_2O_3 layers, ≈ 110 and 1100 nm, are deposited on each of the insulating and conducting GaN templates, C- and Si-doped respectively. In order to exclude a possible role of the insulating template on the in-plane conduction, an additional 590 nm thick κ-Ga_2O_3 layer, directly deposited with the very same synthesis conditions on a bare (0001) α-Al_2O_3 substrate, was also investigated.

The κ-Ga_2O_3 layers grown on the two different GaN templates exhibited a very similar crystal quality from an X-ray diffraction investigation. Moreover, no major differences can be highlighted

from XRD for the orthorhombic layers grown on GaN templates and directly deposited on sapphire, pointing towards an overall similar crystal quality despite the different investigated templates [see *2θ-θ* scans reported in Figure 4.1 (a)]. The FWHM of the rocking curve values are in the range expected for UID κ-layers (*i.e.,* 0.3708° on sapphire – 0.3339° on Si:GaN – 0.4836° on C:GaN). Furthermore, as expected all the κ-Ga_2O_3 layers here investigated are characterized by the presence of the same 120° rotated domains. Finally, considering the average domain size determined from top-view TEM[58] for the κ-layer grown directly on sapphire [see Figure 4.1 (b)], and the rocking value-domain size correlation, it can be stated that the different substrate/template should not have affected the overall κ-Ga_2O_3 domain size distribution which is expected to be in the ≈ 5 - 20 nm range for all these samples. Last structural aspect to be considered for the (001) κ-Ga_2O_3/GaN samples, is the reasonable presence of a γ-Ga_2O_3 interlayer at the epi-layer/GaN interface. Even though a dedicated TEM study was not performed on these specific samples, its presence is detected in the TEM investigation for the MOVPE κ-sample grown directly on (0001) α-Al_2O_3 substrates [see Figure 4.1 (c)] and its widely reported in literature for κ heteroepitaxy[20,75,156] (see also Section 2.1 for additional details).

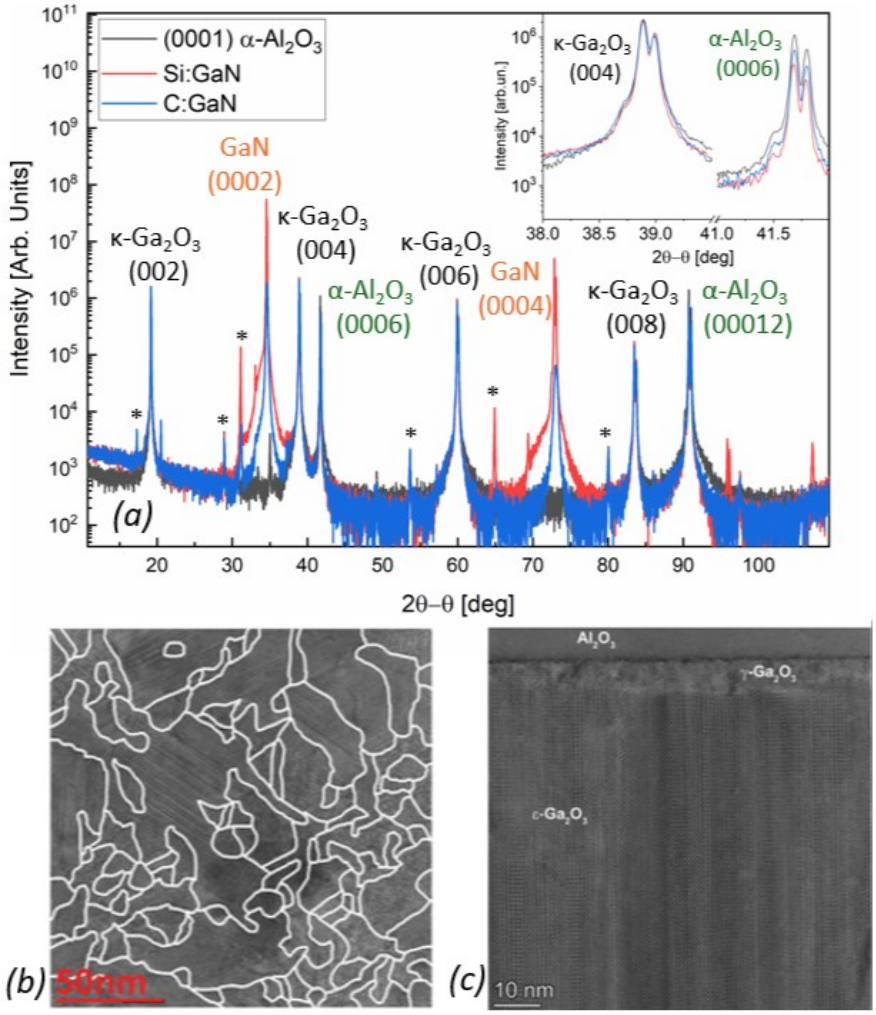

Figure 4.1 (a) XRD symmetric *2θ-θ* of the κ-Ga_2O_3 samples grown by MOVPE in identical conditions on top of the Si- and C-doped GaN template/(0001) α-Al_2O_3 substrate (in red and blue) and directly on top of (0001) α-Al_2O_3 (in black). In the inset close-up on the (004) κ-Ga_2O_3 reflection and (0006) α-Al_2O_3 are reported. (b) and (c) HRTEM images of plane- and cross-view of the κ-Ga_2O_3 sample grown directly on top of (0001) α-Al_2O_3. Images readapted from ref.[58]

To probe the in-plane transport, ohmic Ti/Au contacts (t = 20 nm/100 nm) were deposited via electron-beam evaporation and a lift-off process on top of the κ-Ga_2O_3/insulating-GaN layers. Two different geometries of contacts are deposited, *i.e.,* linear [l-TLM] and circular [c-TLM], with well-defined spacing [see geometrical details in Table 4.1 and representation in Figure 4.2 (c)] that allow in-plane transport investigation via the transfer length method [TLM] (TLM details in section 3.3.3.1).

TLM geometry	Fixed size	Gap spacing [μm]
linear (l-TLM)	width 200 μm	70, 60, 50, 40, 30, 20
circular (c-TLM)	inner diameter 80 μm	100, 75, 50, 25, 15, 10, 5

Table 4.1 Geometrical details for the linear and circular TLM structures investigated for the in-plane/lateral transport probing. The structure are highlighted in Figure 4.2 (c) in green frames.

Figure 4.2 (a) reports the schematic representation of the sample design for vertical transport probing, highlighting the multilayered structure and the suggested current path.

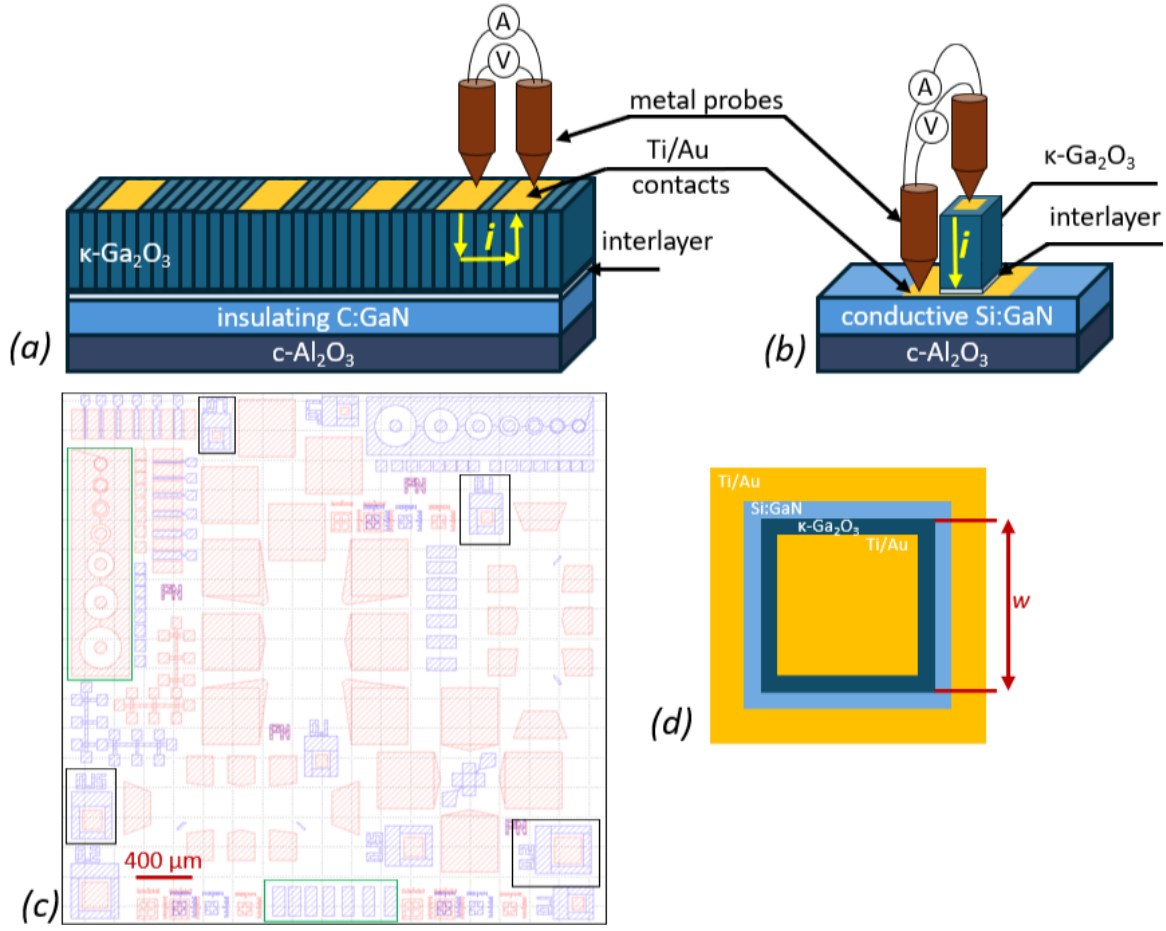

Figure 4.2 Schematic representations of the two different measurements configuration used for (a) lateral/in-plane and (b) vertical/out-of-plane transport measurements. (c) Contact mask geometry used for (i) metal contacts deposition for lateral configuration (blue and red contacts both deposited on κ-Ga_2O_3 and linear and circular TLM in green frame are the investigated structures) and (ii) the etching/lithography steps applied to obtain the structure depicted in (b). In red the top contacts (on κ-Ga_2O_3) and in blue the bottom contacts (on GaN). The four different squared mesa size are highlighted in black squares. (d) Schematic top-view of the isolated vertical mesa structures for the out-of-plane transport.

To probe the out-of-plane transport, well-defined vertical structures of κ-Ga_2O_3 were isolated on top of the conductive-GaN via dry etching (inductively couple plasma - reactive ion etching ICP-RIE, gas combination of 5 sccm Cl_2 and 20 sccm BCl_3, 1.1 nm s^{-1} etch rate for κ-Ga_2O_3 – additional process details reported in reference [157]). The isolated mesa structures have a squared geometry with different area size ($A = 200 \times 200, 150 \times 150, 100 \times 100$ *and* $70 \times 70\ \mu m^2$). After the dry etching process, ohmic Ti/Au contacts have been deposited, following the same electron beam evaporation described hereabove, around (on the conductive-GaN layer) and on top of the κ-Ga_2O_3 squared mesas [see the metal contacts mask in Figure 4.2 (c)]. The effective area of the metal contacts on top of the

κ-Ga_2O_3 squared mesas results to be: $A = 180 \times 180, 130 \times 130, 80 \times 80\ and\ 55 \times 55\ \mu m^2$. The sketch of the sample design and the top view of the mesa structure for vertical transport are reported in Figure 4.2 (b) and (d), respectively. In Table 4.2, the different mesa sizes and relative areas of the top metal contacts are summed-up. As schematically reported in Figure 4.2 (b), the isolation of the vertical κ-Ga_2O_3 squared mesas forces the current to flow only along the vertical direction, *i.e.,* avoiding the crossing of the vertically oriented extended defects.

Mesa label	Mesa lateral size (*w*) [μm]	Squared lateral top contact size [μm]
1	200	180
2	150	130
3	100	80
4	70	55

Table 4.2 Geometrical details of the different squared mesa structures.

The details of the samples just described and the list of the relative transport measurements performed on them are summed-up in Table 4.3, while the results obtained from in-plane and out-of-plane measurements are reported in details in the next sections.

Sample nr.	Substrate	Thickness *t* [*nm*]	Contacts geometry	Transport measurements
S1	C:GaN/(0001) α-Al_2O_3	110	TLM	in-plane
S2	C:GaN/(0001) α-Al_2O_3	1100	TLM	in-plane
S3	(0001) α-Al_2O_3	590	TLM	in-plane
S4	Si:GaN/(0001) α-Al_2O_3	110	Mesa	out-of-plane
S5	Si:GaN/(0001) α-Al_2O_3	1100	Mesa	out-of-plane

Table 4.3 Details of the five samples of the MOVPE κ-Ga_2O_3 grown on (S1 – S2) C:GaN, (S3) on (0001) α-Al_2O_3 and (S4 – S5) Si:GaN templates to access in-plane/lateral and out-of-plane/vertical conduction.

4.1.1.2 In-plane transport measurements

Two point probes *I-V* were performed on several l-TLM and c-TLM structures deposited on samples S1 - S3. Figure 4.3 (a) reports an optical image of the two different TLM geometries on the surface of sample S2. The *I-V* characteristics were acquired using a micromanipulator station. Applying the TLM approach, the $\rho_{in\text{-}plane}$ value is extracted for each investigated structure. Figure 4.3 (b) and (c) report the $R_{in\text{-}plane}$ [Ω] vs. gap spacing [μm] of three different TLM, *i.e.,* l-TLM and c-TLM, investigated on sample S2, together with their linear fit and the extracted $\rho_{in\text{-}plane}$ values. Table 4.4 reports the $\rho_{in\text{-}plane}$ values extracted for the three different samples, *i.e.*, S1 - S3, and different TLM geometry investigated. The consistently higher $\rho_{in\text{-}plane}$ values obtained with c-TLM w.r.t. to l-TLM, was reported by Grover *et al.*,[144] for a different material system and ascribed to the l-TLM inherent geometry.

From this set of data, the mean $\rho_{in-plane} \approx 8\,x\,10^4 \pm 4 \cdot 10^4\ \Omega cm$ was obtained. The total absolute error δ was calculated according to Equation 4.1, from the mean $\rho_{in\text{-}plane}$ standard deviation (σ) and the mean experimental error (ε).

$$\delta = \pm (\sigma^2 + \varepsilon^2)^{\frac{1}{2}}$$

Equation 4.1 Total absolute error δ calculate from the mean standard deviation on $\rho_{in\text{-}plane}$ (σ) and the mean experimental error (ε).

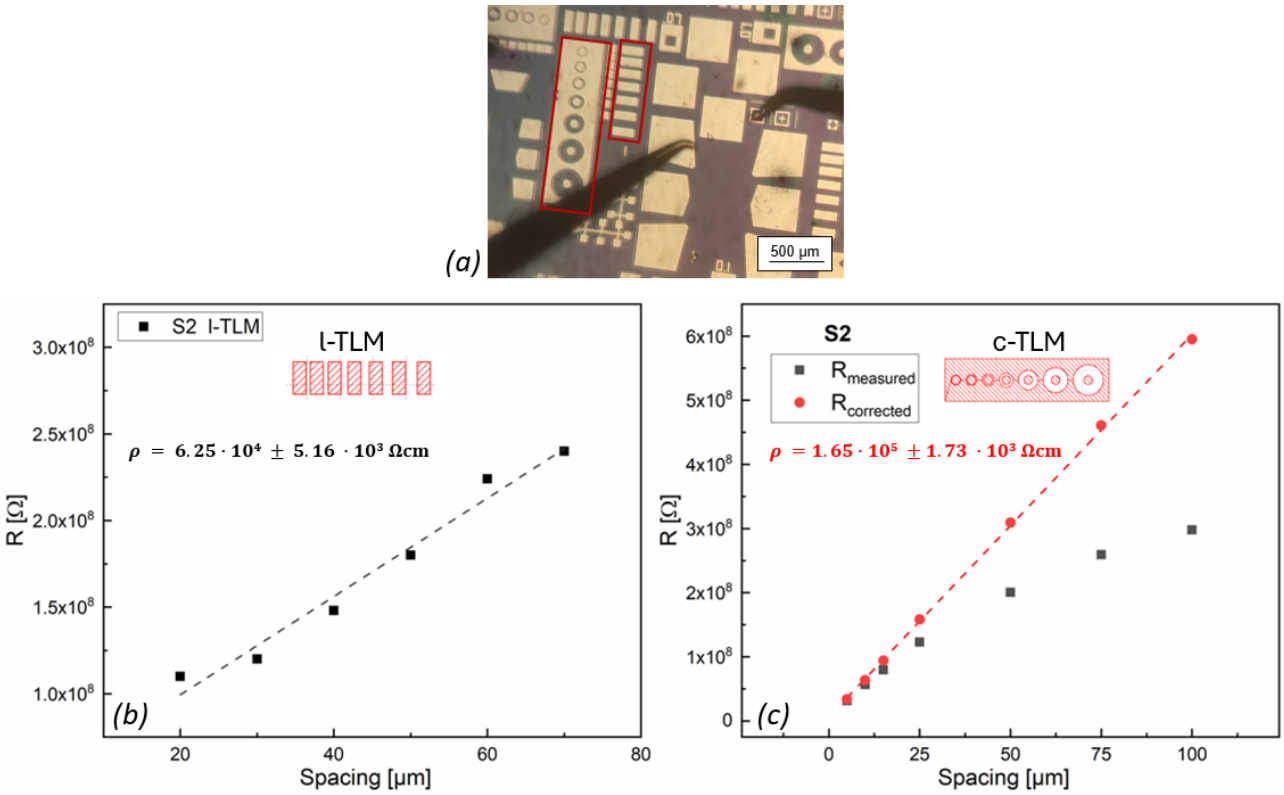

Figure 4.3 (a) optical image of sample S2 surface acquired with the optical microscope of the micromanipulator station. The micromanipulators metal tips are visible slightly out of focus. The red frames highlight the l-TLM and c-TLM structures. (b) and (c) the $\rho_{in\text{-}plane}$ values extracted for l-TLM and c-TLM, respectively. These measurements are referred to sample S2.

Sample	*t* [nm]	ρ (l-TLM) [Ω cm]	ρ (c-TLM) [Ω cm]
S1	110	$4.40 \cdot 10^4\ (\pm\ 1.2\ \cdot 10^4)$	--
S2	1100	$7.86 \cdot 10^4\ (\pm\ 2.83 \cdot 10^3)$ $6.25 \cdot 10^4\ (\pm\ 5.16 \cdot 10^3)$	$1.65 \cdot 10^5\ (\pm\ 1.73 \cdot 10^3)$ $1.21 \cdot 10^5\ (\pm\ 2.50 \cdot 10^3)$
S3	590	$4.56 \cdot 10^4\ (\pm\ 5.50 \cdot 10^3)$	$1.10 \cdot 10^5\ (\pm\ 8.00 \cdot 10^3)$ $1.17 \cdot 10^5\ (\pm\ 9.20 \cdot 10^3)$

Table 4.4 Sum-up of the $\rho_{in\text{-}plane}$ values extracted from samples S1 - S3 from l-TLM and c-TLM.

It is noteworthy the fact that all samples have been investigated avoiding exposure to light. Indeed, in the first steps of the in-plane transport analysis, a current build-up was detected for subsequent measurements, if the sample was kept under ambient/microscope light during and after *I-V* data acquisition. As reported in Figure 4.4, for the *I-V* curves acquired on the 70 µm spaced l-TLM contacts of sample S3, the $R_{in\text{-}plane}$, extracted according to Ohm's law, is increasing of about 24% if the measurement is performed after resting the sample in dark (avoiding both ambient and microscope light) for ≈ 5 min, and of about 38% if the sample is kept in dark for at least 24h (both percentages with respect to the measurement performed while keeping the microscope light on). The reasons behind the current build up will be discussed in Chapter 6.

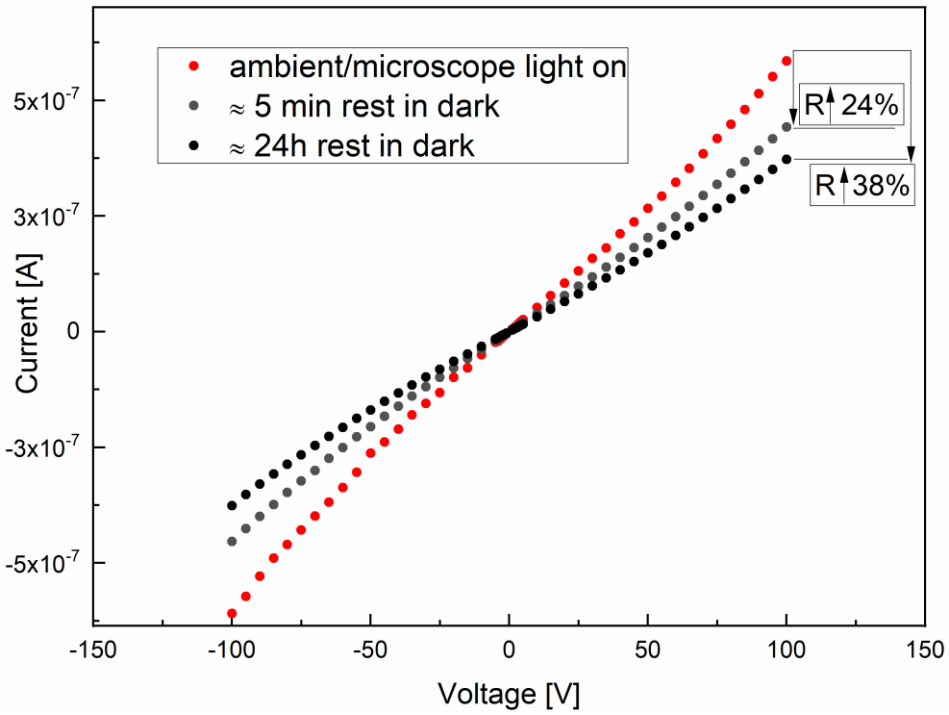

Figure 4.4 *I-V* curves acquired on the 70 µm spaced contacts of a l-TLM on sample S3. The three curves were acquired exposing the sample to light (in red), turning off light (in grey) and keeping the sample for 24h in dark before acquiring the curve (in black).

4.1.1.3 Out-of-plane transport measurements

The out-of-plane transport measurements were conducted on samples S4 and S5, *i.e.*, κ-Ga_2O_3 layers grown on conductive Si:GaN templates (refer to Table 4.4 for samples details). The experimental set-up was the same described in the previous section for the in-plane measurements (two point probes – micromanipulator station). For both S4 and S5 samples (110 nm and 1100 nm thick respectively), several *I-V* curves were acquired for all the different available squared mesa sizes (lateral dimensions 70, 100, 150, and 200 µm) and their respective $R_{measured}$ [Ω] values were extracted according to the Ohm's law. A thorough analysis considering also the spatial distribution of the

analysed mesas was conducted to address possible inhomogeneities of the samples (*e.g.,* thickness gradients or lithography/lift-off process-related issues, especially at the samples border) and to collect enough data for statistics purposes.

The mapping of the $R_{measured}$ was performed adopting a *xy* reference system to track the mesa coordinates on the sample surface, as depicted in Figure 4.5 (a) for sample S4. For each mesa size, the $R_{measured}$ 3D contour plot was outlined [see Figure 4.5 (b-e)]. The data point of the $R_{measured}$ are reported as black dots in each plot and the colour scale adopted is going from green to red for increasing $R_{measured}$ values. The investigated areas for the different mesa size were mostly located around the central part of the samples, where the presence of macroscopic defects related to the processing of the sample was limited/absent.

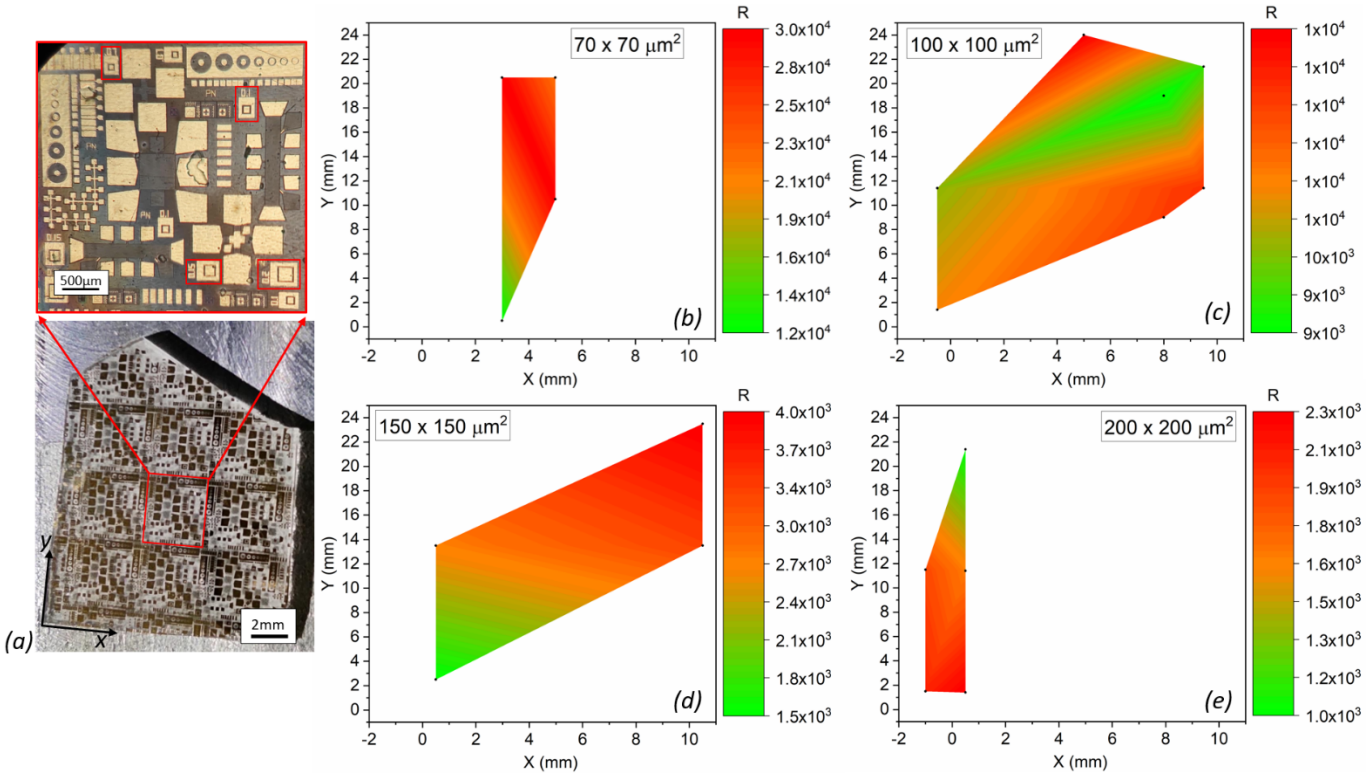

Figure 4.5 (a) Picture of the surface of sample S4 with the indication of *xy* axes directions used to map the mesas positions. The microscope optical image of the area in the red square region is reported on the top of the sample picture. In the zoom is depicted the repeating unit masks of the metal contacts and the four different mesa size are highlighted in red squares. (b - e) The 3D contour plots of the $R_{measured}$ distribution on the surface of the sample for the four different mesa size, *i.e.*, $70 \times 70, 100 \times 100, 150 \times 150, 200 \times 200\ \mu m^2$. The colour scale is reported near each map and it is going from green to red for increasing $R_{measured}$ values.

A significant set of data was acquired, allowing to obtain a reliable trend of the mean $R_{measured}$ vs. size of the vertical conduction channel [see Figure 4.6 (a)]. In this regard, the collected $R_{measured}$ are plotted vs. the lateral size of the Ohmic contacts (deposited on top of the columnar κ-Ga_2O_3 mesa

structures), *i.e.,* 55, 80, 130 and 180 µm for the 70, 100, 150, 200 µm mesas, respectively. It is noteworthy that, despite the thickness difference [sample S4 - 110 nm and sample S5 - 1100 nm], the $R_{measured}$ values of the two samples almost overlap, *i.e.,* $R_{measured}$ is not scaling with the sample thickness. As a direct comparison under the assumption of the isotropy of the transport properties, the $R_{isotropy}$ values were calculated according to Equation 4.2 and are reported in Figure 4.6 (a) for both the samples thicknesses.

$$R_{isotropy} = \rho_{in-plane} \frac{layer\ thickness}{area\ metal\ contacts}$$

Equation 4.2 $R_{isotropy}$

The $R_{measured}$ is indeed in line with the $R_{isotropy}$ for the thin sample S4 while the thick sample, S5, is showing values around one order of magnitude lower than $R_{isotropy}$. It is here fundamental to make a consideration about the physical meaning of the $R_{measured}$.

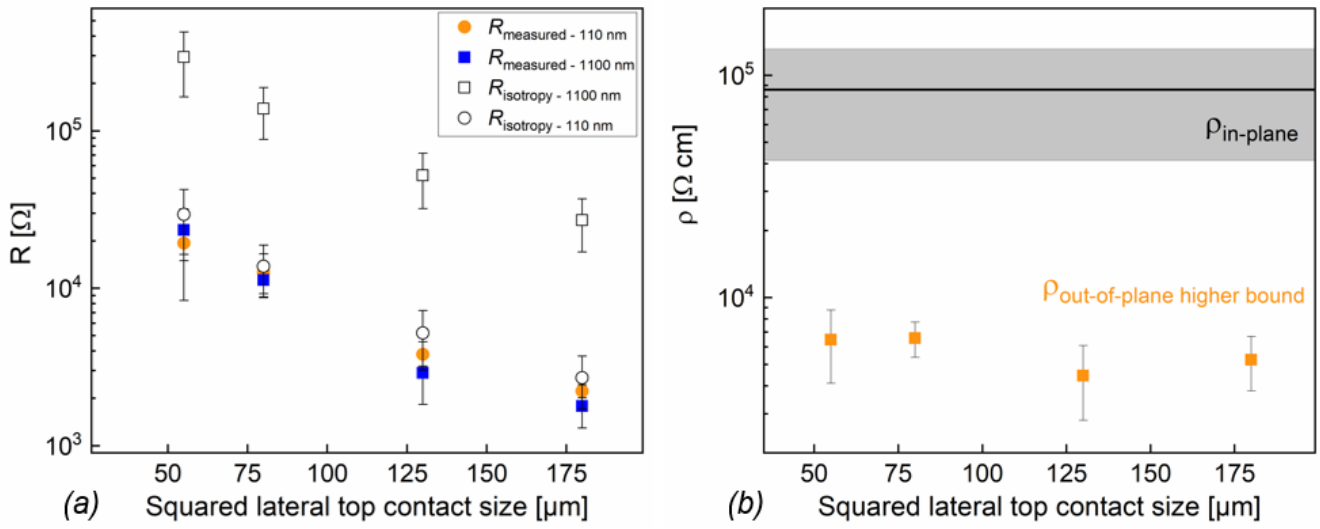

Figure 4.6 (a) the trend of the $R_{measured}$ vs. squared lateral top contact size for the two samples analysed, *i.e.,* S4 - 110 nm thick (orange circle) and S5 - 1100 nm thick (blue square). The trend of the $R_{isotropy}$ vs. squared lateral top contact size is reported in this graph as well, calculated for both 110 and 1100 nm, considering for the calculation the $\rho_{in\text{-}plane}$ (see Equation 4.2). (b) The value of the mean $\rho_{in\text{-}plane}$, the black horizontal line with the standard deviation represented by the grey area, compared to the $\rho_{out\text{-}of\text{-}plane\ higher\ bound}$ calculated for sample S5, for each mesa size.

Considering the structure of the samples investigated for the out-of-plane-transport [Figure 4.2 (b)], the overall $R_{measured}$ values are given by the contributions from the different materials (Ti/Au metal contacts, κ-Ga_2O_3, interlayer, GaN) and relative interfaces. $R_{measured}$ can then be expressed as the R series reported in Equation 4.3, out of which the $R_{\kappa Ga_2O_3}$, *i.e.,* intrinsic out-of-plane resistance of the κ-Ga_2O_3 mesa, is the one here investigated.

$$R_{measured} = R_{Ti/Au-\kappa Ga_2O_3} + \boldsymbol{R_{\kappa Ga_2O_3}} + R_{\kappa Ga_2O_3-interlayer} + R_{interlayer-GaN} + R_{GaN} + R_{GaN-Ti/Au}$$

Equation 4.3 $R_{measured}$ expressed as the contributions from all the different materials/interfaces.

Noteworthy, the fact that by increasing the thickness of the κ-Ga_2O_3 mesa of one order of magnitude [*i.e.,* sample S4 vs. sample S5] is not affecting the $R_{measured}$, indicates that the $R_{measured}$ itself is not dominated by the $R_{\kappa Ga_2O_3}$ contributions. Furthermore, it is unquestionable that $R_{\kappa Ga_2O_3} < R_{measured}$. Therefore, given (i) the $R_{measured}$ values for each mesa size, (ii) the well-defined geometry of the κ-Ga_2O_3 mesa and (iii) the layer thickness, *i.e.,* sample S5 - t = 1100 nm, it was possible to define the upper bound estimate for the $\rho_{out\text{-}of\text{-}plane}$, as per in Equation 4.4.

$$\rho_{out-of-plane-higher-bound} = \frac{R_{measured} A_{top\ contacts}}{\kappa Ga_2O_3\ thickness} > \rho_{out-of-plane}$$

Equation 4.4 $\rho_{out\text{-}of\text{-}plane\text{-}higher\text{-}bound}$

Figure 4.6 (b) reports the calculated values of $\rho_{out\text{-}of\text{-}plane\text{-}higher\text{-}bound}$ vs. lateral top metal contact size (orange square). In the same graph, the $\rho_{in\text{-}plane}$ value (obtained from the in-plane transport $\rho_{in-plane} \approx 8\,x\,10^4 \pm 4 \cdot 10^4\ \Omega cm$) is reported (horizontal black line) with its absolute error bars (grey area). This furnishes the direct comparison of the $\rho_{in\text{-}plane}$ vs. $\rho_{out\text{-}of\text{-}plane}$, being the latter at least one order of magnitude lower and it demonstrates the anisotropy of transport properties due to the presence of vertically oriented structural defects.

4.1.2 Silane-mediated expansion of rotational domains and their effect on the in-plane transport of Si-doped κ-Ga_2O_3 layers

In the following section, the results related to the effect of the silane flux (Φ_{SiH4}), *i.e.,* extrinsic Si doping source, on the expansion of the rotational-domains of the Si-doped κ-Ga_2O_3 layers grown via MOVPE are reported. SiH_4 has already proven to be successful into obtaining extrinsic Si-doping of κ-Ga_2O_3 layers.[131] However, the Si-doped κ-Ga_2O_3 layers were characterized by a limited RT mobility, *i.e,* $\mu \approx 1$ - 4 $cm^2V^{-1}s^{-1}$ and the transport mechanism in such layers had been identified as variable range hopping (VRH), most likely related to their defectivity.[102,131] As thoroughly discussed in the section 4.1.1, the ability to engineer the functional properties of κ-Ga_2O_3 epilayers must account for the role of structural defects like the rotational domains; therefore, the possibility to obtain a single crystal epitaxial layer or to at least control the rotational-domains size are fundamental steps to address the intrinsic properties of this material system, eventually allowing for its application in electronic devices. In this framework, the current section focuses on the relation between the structural quality of Si-doped κ-Ga_2O_3 layers deposited on c-plane sapphire (XRD, Raman, TEM, APT) in relation to the provided Φ_{SiH4} flux during MOVPE growth. Moreover, the in-plane transport

properties (Van der Pauw and Hall measurements) are shown with particular attention on their relation with the structural defects of each Si-doped κ-Ga_2O_3 epilayer.

The MOVPE growths of the κ-Ga_2O_3 epilayers were performed by M. Bosi, L. Serravalli and P. Mazzolini (IMEM - Parma). The XRD measurements and data elaboration were performed by F. Mezzadri and P. Mazzolini (UniPr). The Raman measurements were performed by M.N. Marggraf and B. M. Janzen under the supervision of M. R. Wagner from TU (Berlin) and from G. Spaggiari under the supervision of D. Bersani (UniPr). The Raman data elaboration was directly performed by the candidate with the support of P. Mazzolini (UniPr) and M. R. Wagner (TU). The Ti/Au contact deposition for the Van-der-Pauw/Hall measurements was performed by A. Bosio (UniPr). The Van-der-Pauw/Hall, the temperature-dependent I-V measurements and their data elaboration were performed by S. Vantaggio and A. Parisini (UniPr). The TEM investigation was performed by I. Cora, Z. Fogarassy and B. Pécz from the Hungarian Academy of Science (Budapest). The APT measurements and interpretation were provided by D. Diercks from Shared Instrumentation Facility (Golden, Colorado).

4.1.2.1 Samples preparation

The results presented hereafter relates to a set of MOVPE grown Si-doped κ-Ga_2O_3 layers, deposited on top of (0001) α-Al_2O_3. The set of Si:κ-Ga_2O_3 layers were grown with H_2 as carrier gas using different fluxes of an H_2-diluted mixture of 0.05% SiH_4 (Φ_{SiH4} from 0 sccm up to 17.5 sccm), under otherwise identical synthesis conditions (growth details reported in Section 3.1.1). The layer thickness was kept in the 800 - 900 nm range for all the samples.

4.1.2.2 X-ray diffraction

The samples were firstly analysed through X-ray diffraction. Figure 4.7 (a) reports an exemplary *2θ-θ* symmetric scans acquired for a Si:κ-Ga_2O_3 layer (deposited with Φ_{SiH4} =10 sccm). No additional diffraction peaks were identified besides the {00l} family of planes of κ-Ga_2O_3 and the {000l} ones of c-sapphire. All the investigated Si:κ-Ga_2O_3 layers are found to have similar diffraction spectra regardless of the Φ_{SiH4} involved in the deposition. The crystal structure is purely orthorhombic and all the samples are characterized by the 120° in-plane rotated domains. Their presence was assessed through φ-scans of the (122) reflection; Figure 4.7(b) shows the (122) φ-scan for the Φ_{SiH4} =10 sccm κ-Ga_2O_3 sample, the positions of the four peaks associated to each rotational domains were calculated and labelled with roman numbers I, II and III and are perfectly matching the experimental data. It is though remarkable that, for increasing Φ_{SiH4}, a significant reduction in the FWHM values of the rocking curve, *i.e.,* ω-scans of the most intense (004) κ-Ga_2O_3 peak, is recorded [see Figure 4.7(c)]. In particular, the values go from a maximum of 0.371° (for Φ_{SiH4} = 0) down to

0.153° (for Φ_{SiH4} = 15 sccm). This is suggesting a decrease of the crystal mosaicity with respect to the substrate normal. The FWHM values here shown for the layers deposited with silane, *i.e.,* mostly < 0.2° for Φ_{SiH4} > 7.5 sccm, are among the best reported so far for κ-Ga_2O_3 layers characterized by rotational domains.[47,121,124,158]

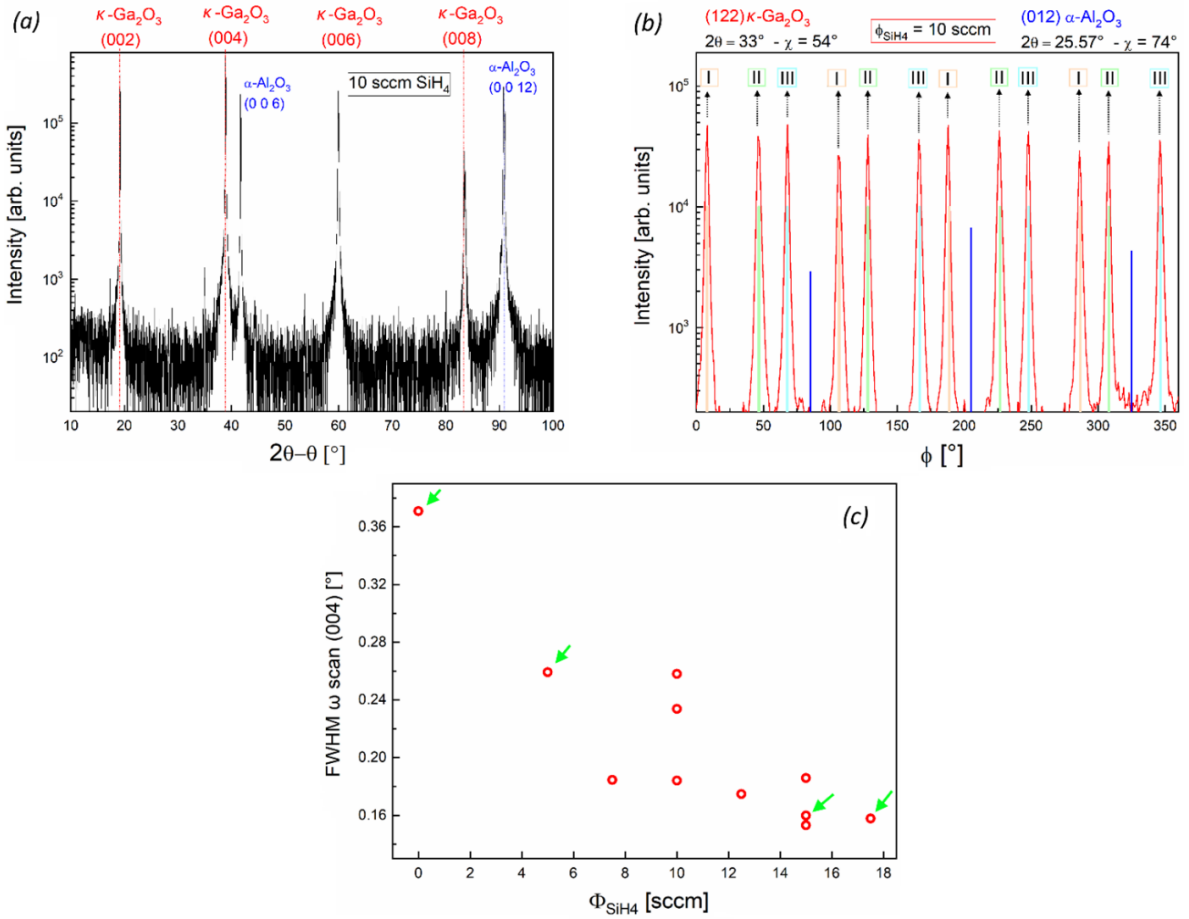

Figure 4.7 XRD (a) *2θ-θ* scan and (b) *φ*-scan of a (001) κ-Ga_2O_3 layer deposited on c-plane sapphire with 10 sccm silane flux; the roman numbers I, II, III and respective orange, green and cyan lines refer to the calculated and expected positions for the three 120° rotated domains. (c) Full width at half maximum (FWHM) of the *ω*-scans (rocking curve) of the (004) peak as a function of the Φ_{SiH4} The green arrows in (c) highlight the samples that have been further investigated by TEM. Image readapted from ref. [58].

4.1.2.3 Transmission electron microscopy and atom probe tomography

Four selected samples deposited with different silane fluxes, *i.e.,* Φ_{SiH4} = 0 – 5 – 15 – 17.5 sccm, were further investigated with transmission electron microscopy (TEM) combined with energy dispersive X-ray spectroscopy (EDX). The cross-sectional and plan view samples were prepared with focused ion beam (FIB) and Ar-ion beam milling technique, respectively. Figure 4.8 (a-d) reports the plan view images that reveals a remarkable enlargement of the overall size of the rotational domains for increasing Φ_{SiH4}. A quantitative estimation of their average size was performed considering the area of each domain and translating it into regular circles. The largest domains size vs. Φ_{SiH4} is

reported in Figure 4.8 (e). In line with previous reports,[20] the typical domain size for the nominally undoped sample is not exceeding the 20 nm while for the highest investigated Φ_{SiH4}, *i.e.,* 17.5 sccm, the size of the domains is reaching up to 320 nm. In addition to the TBs, from plan view images it is also possible to identify extended defects within the domains [see Figure 4.8 (f) for Φ_{SiH4} = 15 sccm]

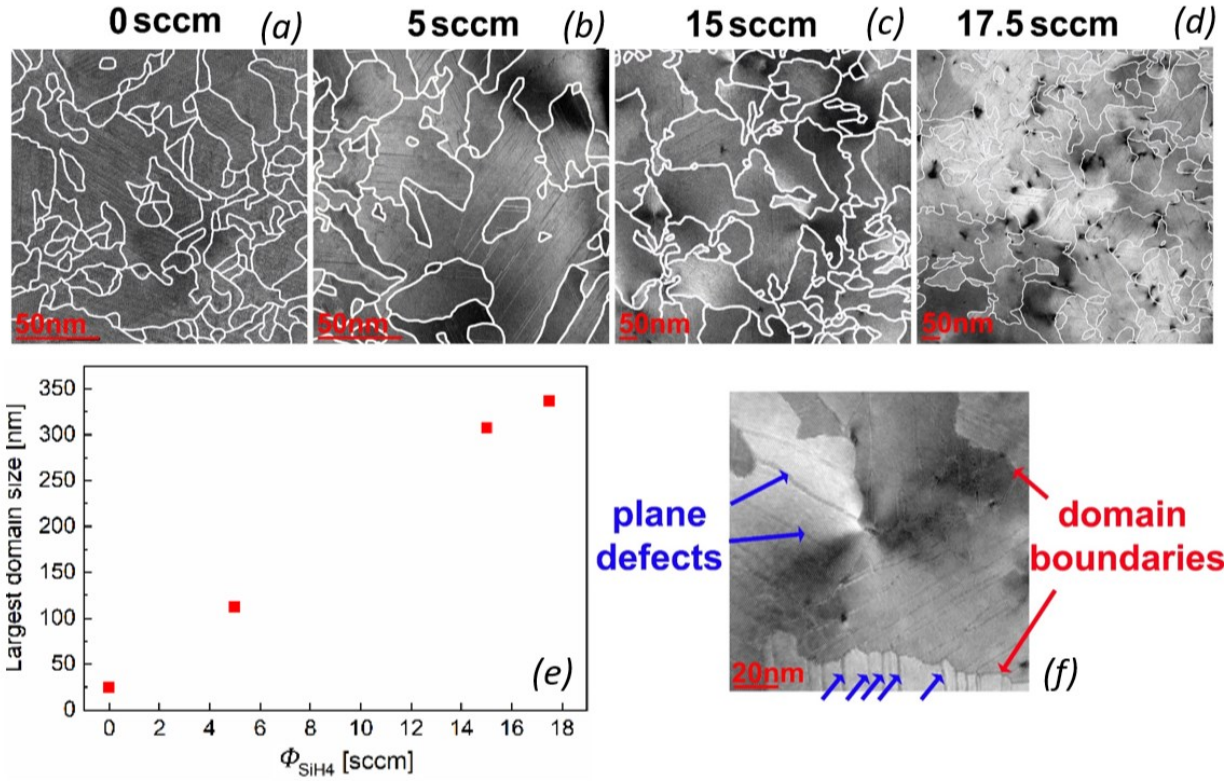

Figure 4.8 (a-d) Plan view TEM images of samples deposited at $\Phi_{SiH_4} = 0 - 5 - 15 - 17.5\ sccm$. (d) Largest domain size vs.Φ_{SiH4}. (f) Plan view image for the $\Phi_{SiH_4} = 15\ sccm$ sample. Plane defects and domain boundaries highlighted by blue and red arrows, respectively. Images readapted from ref. [58].

The cross-sectional TEM images [see Figure 4.9 ($a_{1\text{-}5}$) and ($b_{1\text{-}3}$)] highlights the presence of the γ-Ga_2O_3 interlayer at the κ-Ga_2O_3/sapphire interface, independent on the used Φ_{SiH4}. Nonetheless, the adoption of a silane flow results in the precipitation of amorphous triangular-shaped SiO_x clusters (identified in combination with EDX spectroscopy). It is important to highlight that their presence is detected in the vicinity of the layer/substrate interface and only up to 200-300 nm in the layers. Their density is increasing while their average size is diminishing for increasing Φ_{SiH4}, *i.e.,* the base length going from ≈ 50 nm to ≈ 5 nm for 5 and 17.5 sccm, respectively. The SiO_x precipitates are also found to possibly interact with the vertically oriented extended defects inside the rotational domain bulk matrix [blue and white arrows in Figure 4.9 (a_5)].

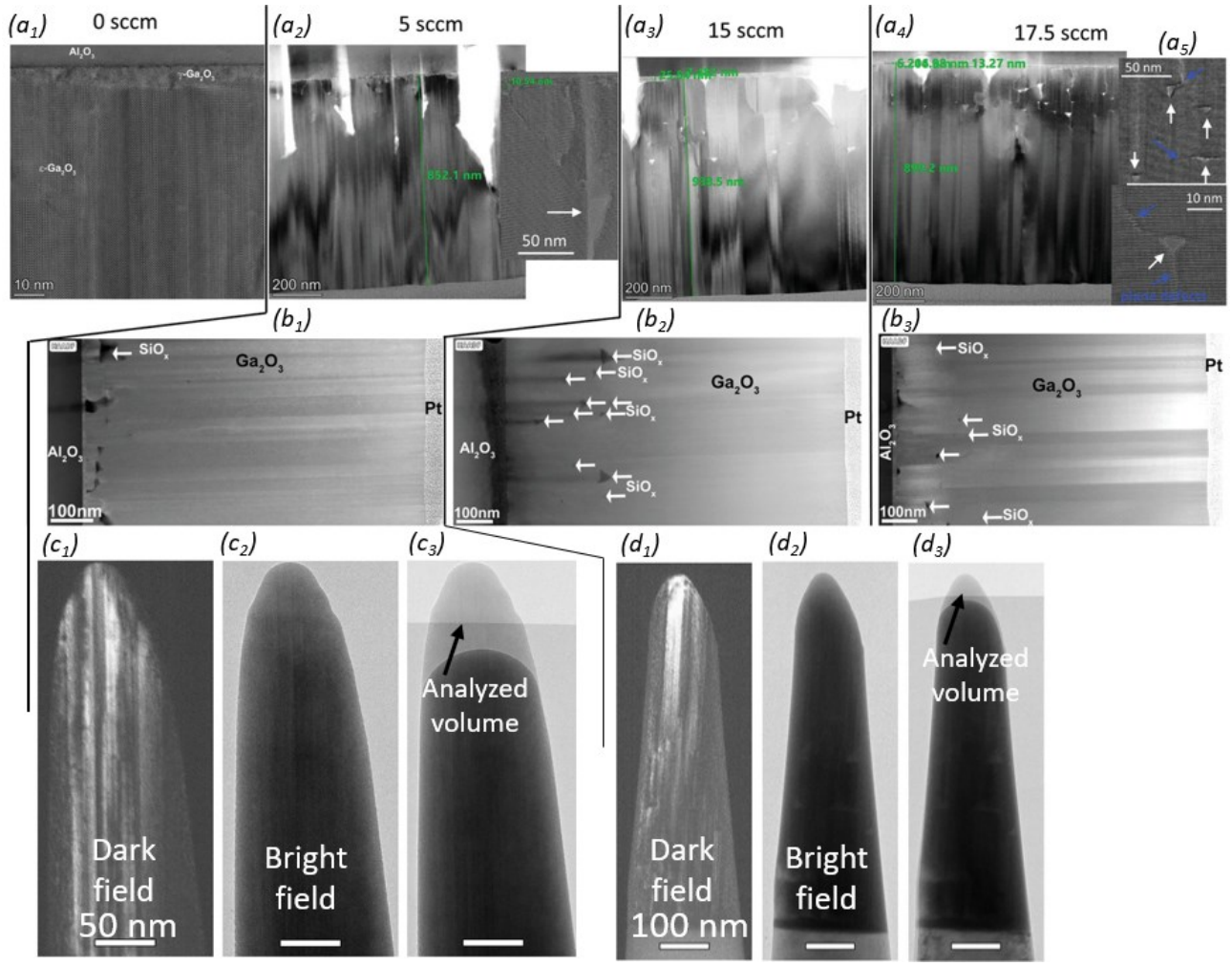

Figure 4.9 ($a_{1\text{-}5}$) and ($b_{1\text{-}3}$), cross sectional TEM and HRTEM images for samples deposited at different Φ_{SiH_4}. In (a_5) the white arrows highlight some of the SiO_x precipitates and the blue arrows the plane defects starting from the apexes of the SiO_x precipitates. ($c_{1\text{-}2}$) and ($d_{1\text{-}2}$) dark and bright field TEM image of FIB prepared APT lamellae of the 5 and 15 sccm Φ_{SiH_4} samples, respectively; c_3 and d_3 overlay of the bright field image prior and after APT analysis volume removal (investigated volume corresponds to the shady region). Image readapted from ref. [58].

Based on the presented results, SiH_4 is found to play an important role either (i) in increasing the mobility of the adsorbed species on the growth front during the κ-Ga_2O_3 growth, or (ii) the accumulation of Si or SiH_x in the initial stages of the growth could prevent the formation of critical size nuclei resulting in a general lower density of nucleation centers, in turn resulting in larger size of rotational domains. Additionally, TEM-combined-atom probe tomography (APT) investigation was conducted on two samples already studied with TEM, *i.e.,* Φ_{SiH4} = 5 and 15 sccm. APT, more spatially resolved and sensible to the Si concentration w.r.t. the already discussed TEM/EDX one, can provide a precise spatial information of the detected chemical species, giving the chance, for example, to investigate possible elemental accumulations at extended defects sites. The specimens, prepared with FIB technique, were obtained from the surface region, *i.e.,* far from the SiO_x precipitates identified in the vicinity of epi-layer/substrate interface. Dark and bright field TEM images of the lamellae [see

Figure 4.9 (c_{1-2}) and (d_{1-2})] were acquired before and after APT [the volume investigated highlighted by the shady area in Figure 4.9 (c_3-d_3)] From TEM dark field, higher density of planar defects [APBs] is detected for the 5 sccm sample, *i.e.,* smaller rotational domains, reasonably related to the domains border walls. However, the precise quantification of Si in the volumes investigated resulted in an homogeneous distribution in the investigated volumes, *i.e.,* Si-accumulations or SiO_x precipitates are not detected no matter the high density of defects; for the Φ_{SiH4} = 15 sccm sample, only a slight difference in the Si concentration, *i.e.,* 0.95% and 1.25%, is detected for two different investigated regions, attributed to two different rotational domains.

4.1.2.4 In-plane transport properties

To assess the effect of Si over the in-plane transport properties of the κ-Ga_2O_3 layers, all samples were characterized at RT via 4-point probe Van der Pauw configuration for resistivity and Hall measurements. To do so, four metal contacts (Ti/Au or SnO_{2-x}/ITO/Au) were deposited via RT magnetron sputtering at the corners of the square shaped samples; the four contacts were then soldered with Ag paste to Cu wires for the instrument set-up purposes. The resistivity of some selected samples was also investigated in the 10-300 K temperature range. The RT values of ρ [Ωcm], μ [$cm^2V^{-1}s^{-1}$] and n [cm^{-3}] are reported in Figure 4.10 (a), (c) and (d), respectively, for increasing Φ_{SiH4}.

The ρ is following a trend similar to the FWHM values [see Figure 4.7 (c)], showing a steep decrease, *i.e.,* ρ going from ≈ 10^3 – 10^4 Ωcm down to ≈ 10^{-1} Ωcm when the Φ_{SiH4} is increased up to 7.5 sccm. A further increase of Φ_{SiH4} did not seem to induce significant variation of the ρ values, *i.e.,* steady plateaux value of ≈ 0.5 Ωcm. The scattering of the ρ values for the three different UID (Φ_{SiH4} = 0) samples could be related to different unintentional Si-background levels from growth chamber memory (prior Si-doped layers growths). Moreover, the relatively low ρ values w.r.t. the ones reported for UID κ-layers[131] is related to the H_2 used as carrier gas (aspect discussed in detail in Chapter 6). The behaviour in temperature of ρ was also investigated for three different samples, *i.e.,* Φ_{SiH4} = 0, 5 and 15 sccm, and it suggested the electronic conduction to be dominated by VRH mechanism. Indeed, the $ln(\rho)$ for the three investigated samples reported as Mott's plots, *i.e.,* $ln(\rho)$ vs. $T^{-1/4}$, in Figure 4.10 (b), are showing a double linear slope behaviour, as already recorded for Si-doped κ-Ga_2O_3 layers and attributed to two distinct VRH mechanisms of transport prevailing at low and high T, respectively.[102,131]

The RT μ on the other side increases from ≈ 1 up to ≈ 10 $cm^2V^{-1}s^{-1}$ [see Figure 4.10 (c)] when increasing the Φ_{SiH4}. Mobility values in this range are typically associated to a transport between localized states. Vice versa, the RT n is showing the opposite trend, decreasing from ≈ 3-5 ·10^{18} down to ≈ 1·10^{18} cm^{-3} [see Figure 4.10 (d)] when increasing Φ_{SiH4}.

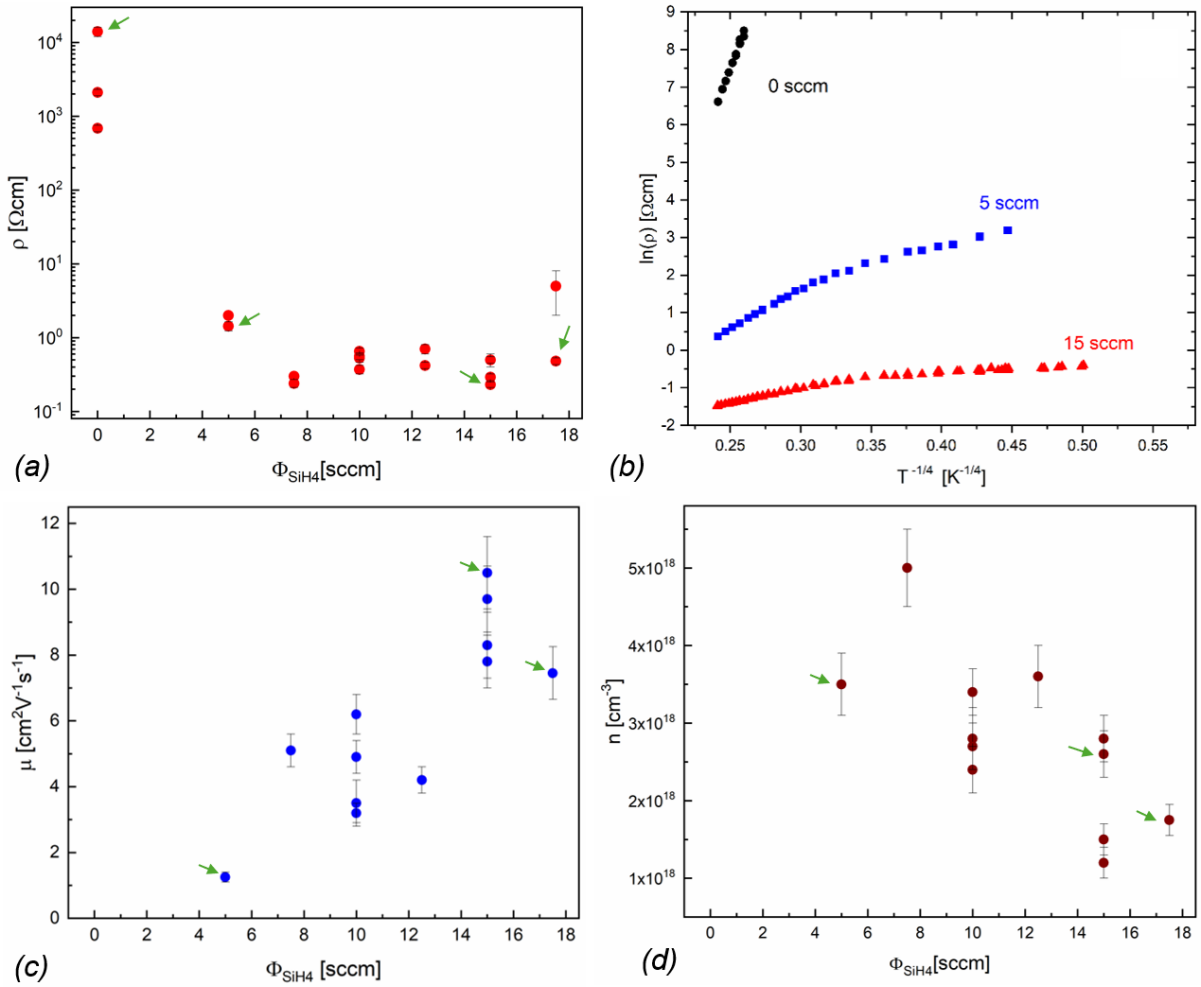

Figure 4.10 (a) RT electrical resistivity ρ and (b) $ln(\rho)$ vs. $T^{-1/4}$ for three samples deposited with Φ_{SiH4} = 0, 5, and 15 sccm (c) RT mobility μ and (d) RT charge carrier density n extracted from van der Pauw–Hall electrical measurements of Si-doped κ-Ga_2O_3 layers as a function of the Φ_{SiH4} provided during the deposition. Samples highlighted with green arrows in (a), (c) and (d) were further investigated with TEM. Figure readapted from ref. [58].

Noteworthy, the Hall effect measurement in combination with the APT results unveil an extreme high level of compensation. Particularly, for Φ_{SiH4} = 15 sccm sample, APT detected a 1% Si concentration, while Hall data highlights a net electron concentration n in the 10^{18} cm^{-3} range, *i.e.*, about two orders of magnitude lower with respect to a 100% extrinsic dopant efficiency . Moreover, it is also found that increasing the dopant concentration generally leads to a decreasing trend of n. This could point towards a higher compensation accompanying the increase of silane; nonetheless, a dedicated study (*e.g.*, Hall measurements in temperature) would be important to further clarify this aspect. On the other side, the μ increase with Φ_{SiH4} can be justified by the rising of hopping probability which could be tentatively connected to the general enlargement of the domains.

4.1.2.5 Raman spectroscopy

An independent further characterization of the undoped and Si-doped κ-Ga_2O_3 layers was conducted with Raman spectroscopy in back-scattering geometry from sample surface and edge. The surface measurements were performed on all the samples investigated with TEM and APT, *i.e.,* Φ_{SiH4} = 0 – 5 – 15 – 17.5 sccm, with a 633 nm laser wavelength. The edge measurements were performed on the same Φ_{SiH4} = 0 – 5 – 15 sccm and on an additional 10 sccm layer, with a 532 laser wavelength in parallel polarization to the c-plane. All the spectra are the result of 60 accumulations of 10 s each in order to increase the signal/noise ratio. Moreover, each spectrum underwent a baseline, air spectrum subtraction and normalization on the most intense substrate peak, *i.e.,* 417 cm^{-1}. Indeed, as reported in Figure 4.11, the air signal is showing high density of Raman modes in the region 50 – 150 cm^{-1}, *i.e.,* the region most interested by the orthorhombic Ga_2O_3 Raman active modes.[148]

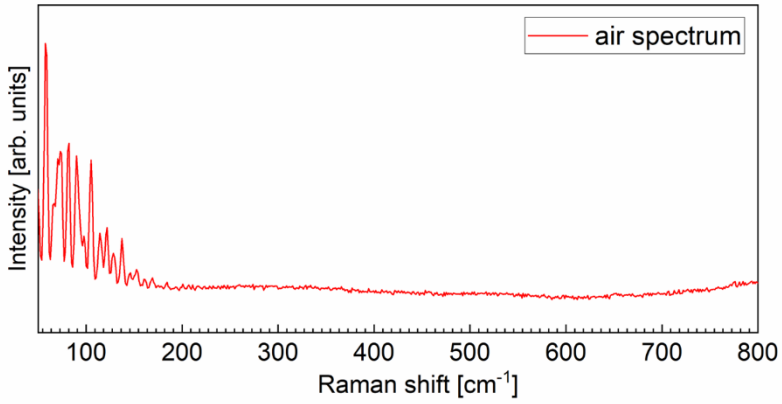

Figure 4.11 Raman spectrum of air acquired with λ_{laser} = 633 nm.

Figure 4.12 (a) and Figure 4.13 (a) reports the Raman spectra acquired in surface and edge back-scattering configuration, respectively. The spectra are vertically shifted for sake of clarity. Only the Raman modes (RM) of the orthorhombic κ-Ga_2O_3 are detected apart from the sapphire ones, in both set-up. In the edge configuration, the contribution of the substrates is less prominent, hence the κ-Ga_2O_3 RM are more defined. Nevertheless, both analysis highlighted two main aspects: (i) a change of the relative intensity of some of the Raman modes, *i.e.,* 82 cm^{-1} and 113 cm^{-1}, between the nominally undoped and Si-doped samples, [see insets of Figure 4.12 (a) and Figure 4.13 (a)]; (ii) after the identification of the more defined κ-Ga_2O_3 RMs detected in both the acquisition configurations [see colour/shape labelling in Figure 4.12 (a) and Figure 4.13 (a)], a gaussian fit of the peaks was performed and the trend of each peak width [FWHM] vs. Φ_{SiH4} was evaluated. As reported in Figure 4.12 (b) and (c) and even more clear in Figure 4.13 (b) and (c), the peak width of all Raman modes is decreasing for increasing Φ_{SiH4}, *i.e.,* increasing mean domain size.

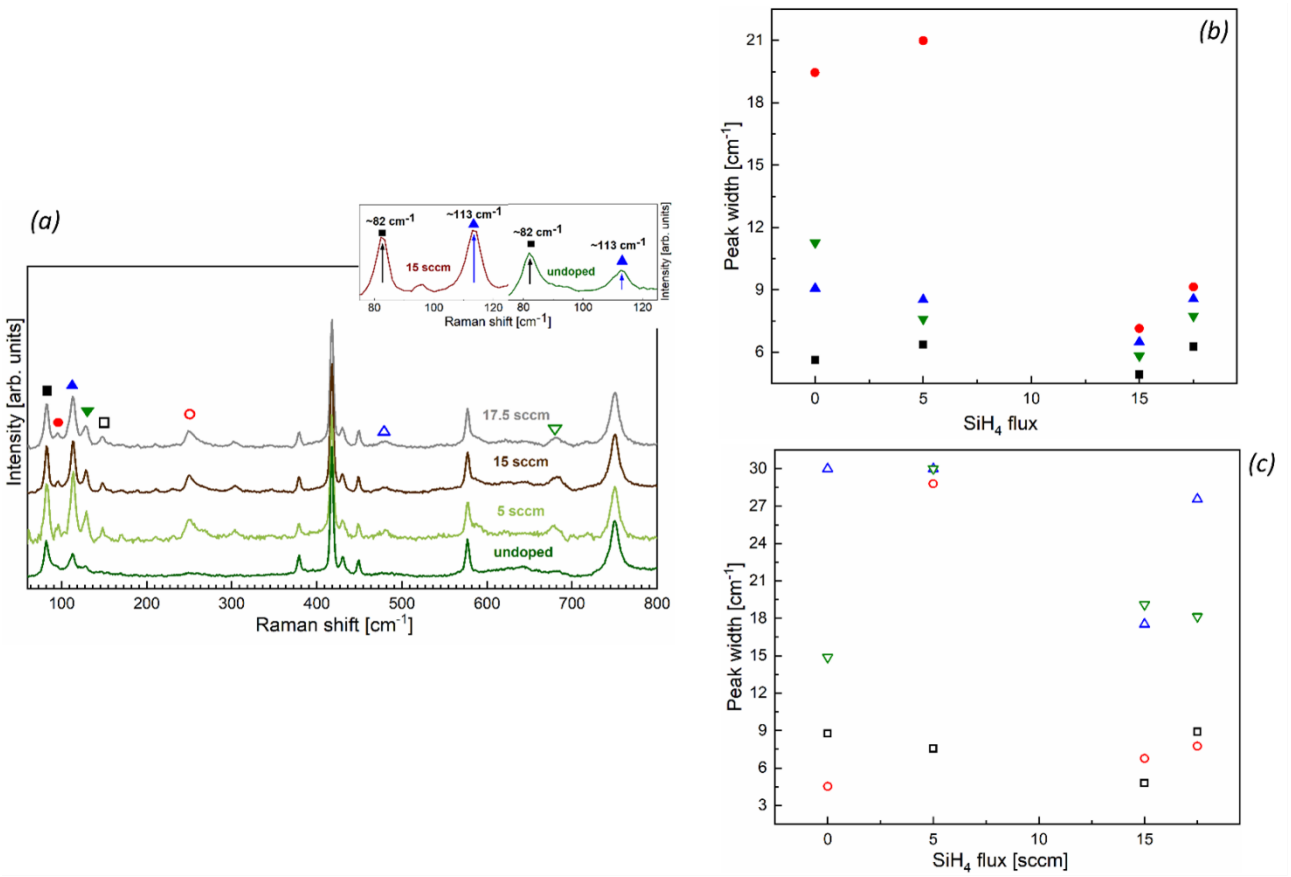

Figure 4.12 (a) Raman surface spectra (λ_{laser} = 633 nm) for the κ-Ga_2O_3 samples deposited at $\Phi_{SiH_4} = 0 - 5 - 15 - 17.5\ sccm$. In the inset close-up on the two peaks at ≈ 82 and 113 cm^{-1} for the undoped and 15 sccm samples. (b) and (c) the fitted peak widths vs. Φ_{SiH_4} (colour/shape match with the symbols reported on the Raman spectra); this analysis is performed on selected peaks, *i.e.,* the ones clearly visible in both acquisition configurations (see Figure 4.13) and split in two different graphs for sake of clarity. Image reproduced from ref. [58].

The peak width narrowing for increasing mean size of the rotational domains can be related to the phonon mean lifetime being affected by the different rotational domain size. Indeed, for the undoped layer, *i.e.,* 5 - 20 nm mean size, the phonon diffusion length and lifetime is diminished by scattering phenomena happening at the domains borders, resulting in the broadening of the peak width. On the contrary, in the layers characterized by wider domains, *i.e.,* Φ_{SiH4} = 5 sccm, the phonon propagation is less affected by the borders scattering, hence a steep decrease in the peak width was observed. For even larger domains, *i.e.,* > 100 nm, the effect is less evident since other scattering mechanisms can affect the phonons lifetime.

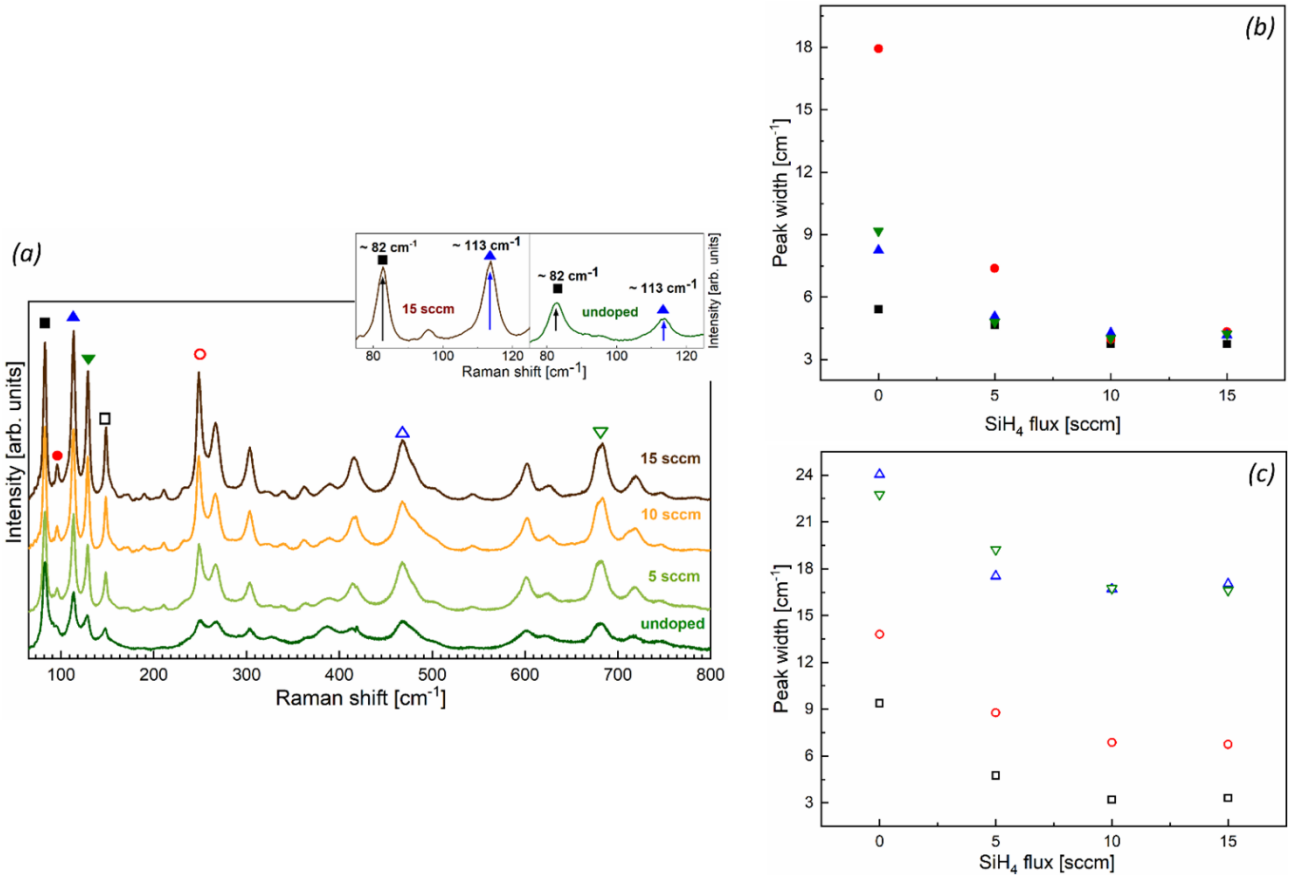

Figure 4.13 (a) Raman edge spectra (λ_{laser} = 532 nm) for the κ-Ga_2O_3 samples deposited at $\Phi_{SiH_4} = 0 - 5 - 10 - 15\ sccm$. In the inset close-up on the two peaks at ≈ 82 and 113 cm^{-1} for the undoped and 15 sccm samples. (b) and (c) the fitted peak widths vs. Φ_{SiH_4} (colour/shape match with the symbols reported on the Raman spectra); this analysis is performed on selected peaks, *i.e.,* the ones clearly visible in both acquisition configurations (see Figure 4.12) and split in two different graphs for sake of clarity. Image reproduced from ref. [58].

To conclude, in the work described it has been provided (i) a direct proof of the rotational-domains mediated anisotropy of the in-plane vs. out-of-plane conductivity: (ii) a possible strategy to mitigate the effect of rotational domains, *i.e.,* enlargement of their mean size with Φ_{SiH4}; (iii) an interpretation of the role of the structural defects over the in-plane transport properties of Si-doped κ-Ga_2O_3 and (iv) a comprehensive analysis through non-destructive techniques, *i.e.,* XRD and Raman, to address the crystal quality of the layers characterized by rotational domains.

4.2 Study of SnO/ε-Ga_2O_3 p–n diodes in planar geometry

In the second work mentioned in the introduction of this chapter, a device structure has been analysed: the SnO/κ-Ga_2O_3 p-n diodes in planar geometry.

The MOVPE growth of the Si-doped κ-Ga_2O_3 layer was performed by M. Bosi, L. Serravalli and P. Mazzolini (IMEM - Parma). The MBE growth of the SnO layer was performed by K. Egbo (PDI). The metal contacts deposition and etching/lithography processes were performed by A.

Tarahoui (PDI). The RT I-V characteristics and their data elaboration were performed directly by the candidate with the support of S. Vantaggio, A. Parisini and P. Mazzolini (UniPr). The temperature dependence I-V measurements as well as data interpretation were performed by P. R. Kalvani and A. Parisini (UniPr).

The structure of the device, reported in Figure 4.14 (a), foresees a 500 nm thick layer of MOVPE grown Si-doped κ-Ga_2O_3 grown on top of c-oriented α-Al_2O_3. As seen in the previous section, the Si-doping of κ-Ga_2O_3 has been obtained via injection of a diluted mixture of SiH_4 and H_2 in the growth chamber. The n-type conductivity of the Si:κ-Ga_2O_3 has been confirmed by RT Van der Pauw method. The layer was characterized by a Hall density $n = 3.7 \cdot 10^{18}$ cm^{-3}, Hall mobility $\mu = 4$ $cm^2V^{-1}s^{-1}$ and a resistivity $\rho = 0.4$ Ωcm. After the n-type layer characterization, a 150 nm thick p-type (001) SnO layer was grown on top of the κ-Ga_2O_3 via PAMBE (growth technique described in section 3.1.2). The details of the growth are reported in the reference.[157] As depicted in Figure 4.14, vertical squared mesa structures of the SnO layer (in red) are then isolated and Ti/Au ohmic metal contacts[143,157] are deposited on top of the Si:κ-Ga_2O_3 and SnO layers (mesa structure isolation and metal contacts deposition techniques already described in the section 4.1.1). The mesa geometries are the same reported in Table 4.2. The characterization of the diodes has then been conducted via RT and temperature dependent *I-V* characteristics in the two-point probes configuration.

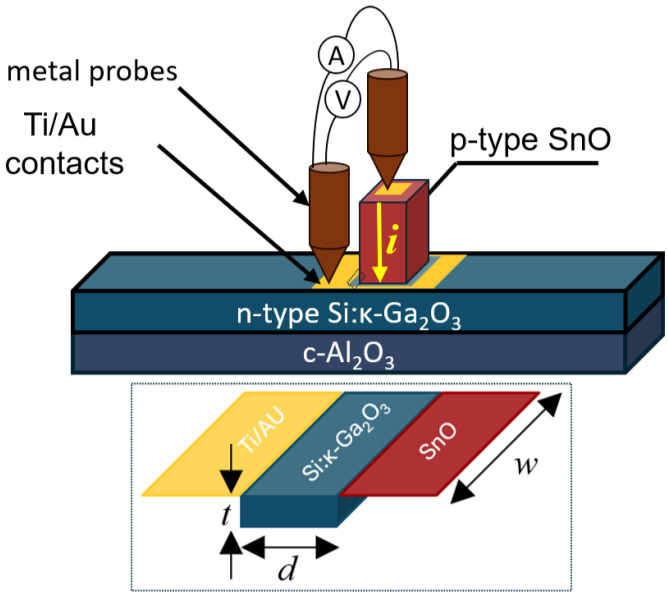

Figure 4.14 Schematic representation of the SnO/κ-Ga_2O_3 pn diode. In the dashed frame, sketch of one of the four Si:κ-Ga_2O_3 conduction channels at the bottom of each diode, between the p-type SnO mesa structure and the Ti/Au ohmic contact. The geometrical parameters of the channels, *i.e., w* and *d*, are known for each mesa as reported in Table 4.2 while *t* is the thickness of the n-type Si:κ-Ga_2O_3.

4.2.1 RT *I-V* characteristics

The RT *I-V* characteristics were acquired to confirm the rectifying behaviour of the SnO/κ-Ga_2O_3 *p-n* diodes. The measurements were performed using a micromanipulator station (details reported in section 4.1.1). The *I-V* characteristic of two/three geometrically identical diodes are acquired for statistical purposes. Figure 4.15 (a) and (b) reports the *I-V* characteristics of the four different mesa/diode sizes in linear and semilogarithmic scale, respectively

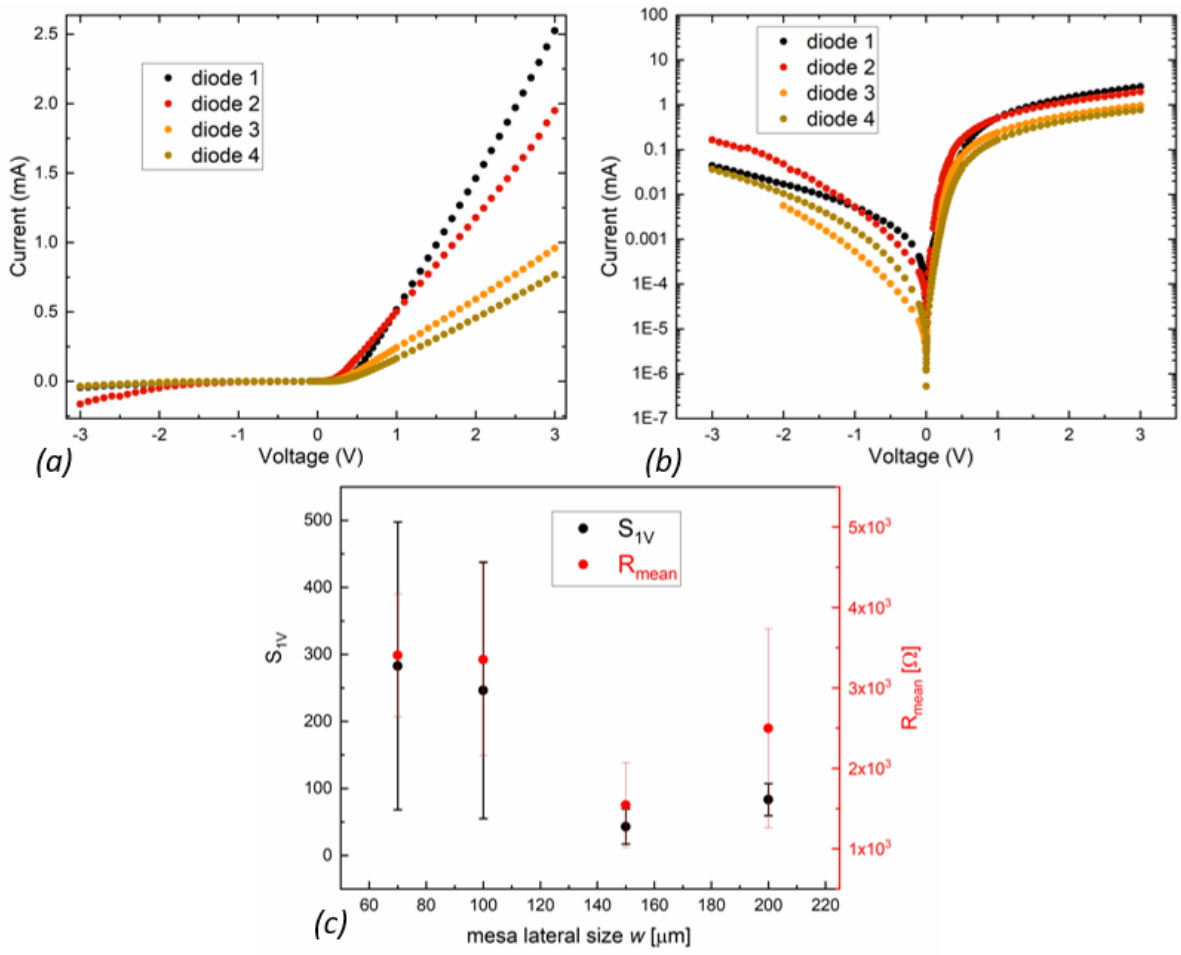

Figure 4.15 (a) and (b) the *I-V* characteristics of the four mesa/diode size are reported in linear and semilogarithmic scale, respectively. (c) the S_{1V} and R_{mean} vs. mesa lateral size are reported on the left and right *y* axes, respectively. Both S_{1V} and R_{mean} showed a certain scattering within the set of diodes analysed and that is reported through their standard deviation. This can be due to in-homogeneity of the sample, *i.e.*, thickness gradient, and/or imperfect Ti/Au metallization (some diodes were slightly damaged when observed at the optical microscope).

In the linear graph in Figure 4.15 (a), the rectifying behaviour of the diodes is confirmed. The rectification ratio at +/- 1V was calculated according to Equation 4.5. The S_{1V} values, averaged on the different diodes of same geometry analysed, are reported in Figure 4.15 (c) on the left *y* axes, with their standard deviation, as function of the mesa lateral size *w*. The values reported, even though are

confirming the rectifying behaviour for all diodes size, are however much lower compared to that reported for SnO/(-201) β-Ga_2O_3 diodes (*i.e.,* $S_{1V} = 2x10^8$).[157]

$$S_{1V} = \left|\frac{I(+1V)}{I(-1V)}\right|$$

Equation 4.5 Rectification ratio S_{1V}

The relatively low S_{1V} values here obtained can be explained by: (i) the high reverse leakage current, clearly visible in Figure 4.15 (b) for negative applied bias and (ii) the high R_{mean} extracted from the linear *I-V* in forward bias [see red circle on the right *y* axe reported in Figure 4.15 (c)]. Regarding point (i), the high reverse leakage current was here tentatively attribute to the high donor concentration of the Si:κ-Ga_2O_3 layer, *i.e.,* n = 3.7 x 10^{18} cm^{-3} compared to n = 2 x 10^{17} cm^{-3} of ref.[157]. This will result in a thin depletion region that will allow easier reverse leakage current, *i.e., I*(-1V), by tunnelling. Regarding point (ii), the R_{mean} extracted seems to point toward the presence of an external series resistance R_e that is dominating over the expected Shockley-like diode behaviour, resulting in a limitation in the forward current [*I*(+1V)] and contributing to the low S_{1V} obtained.

Furthermore, as depicted in Figure 4.15 (c), the R_{mean} scales approximately inversely with the mesa lateral size *w*, *i.e,* lateral dimension of the *p-n* junction. Here, it must be recalled the fact that, as depicted in the sketch of Figure 4.14 (b), there is a region of length *d* and section *wt* of Si:κ-Ga_2O_3 that is interested by in-plane current flow. The inverse proportionality between the linear dimension *w* of the p-n junction and the R_{mean} seems to suggests that the measured resistance is strictly related to the in-plane resistance of the Si:κ-Ga_2O_3 conduction channels.

4.2.2 Temperature-dependent *I-V* characteristics

To further understand the results obtained from RT *I-V* measurements and consolidate the given interpretation, the behaviour in temperature of the diode with larger area, *i.e.,* diode 1, 200 × 200 μm^2, has been studied. To do so the metal contacts are contacted with Cu wires bonds, soldered with Ag paste. The *I-V* characteristics have been acquired in the temperature range RT - 11K. As reported in Figure 4.16 (a), the linear trend of the curves in forward bias is maintained even at lower *T*. The behaviour in temperature of the R_e, extracted from the linear trend of the *I-V* characteristics in forward bias, is then evaluated and reported vs. $T^{-1/4}$ (Mott plot) [see Figure 4.16(b)]. The two-slopes linear trend showed in the Mott plot is resembling the one reported for the in-plane resistivity of Si:κ-Ga_2O_3, reported for direct comparison from ref. [131] in the inset of Figure 4.16(b). This behaviour has been already investigated and attributed to two distinct variable range hopping (VRH) mechanisms of transport prevailing at low and high *T,* respectively.[58,102,131] The similarities between the two curves seems to suggest that the Si:κ-Ga_2O_3 channels are responsible for the R_e

behaviour and that they are significantly affecting the properties of the diodes. The VRH transport mechanism has been associated to the presence of structural defects in κ-Ga_2O_3.

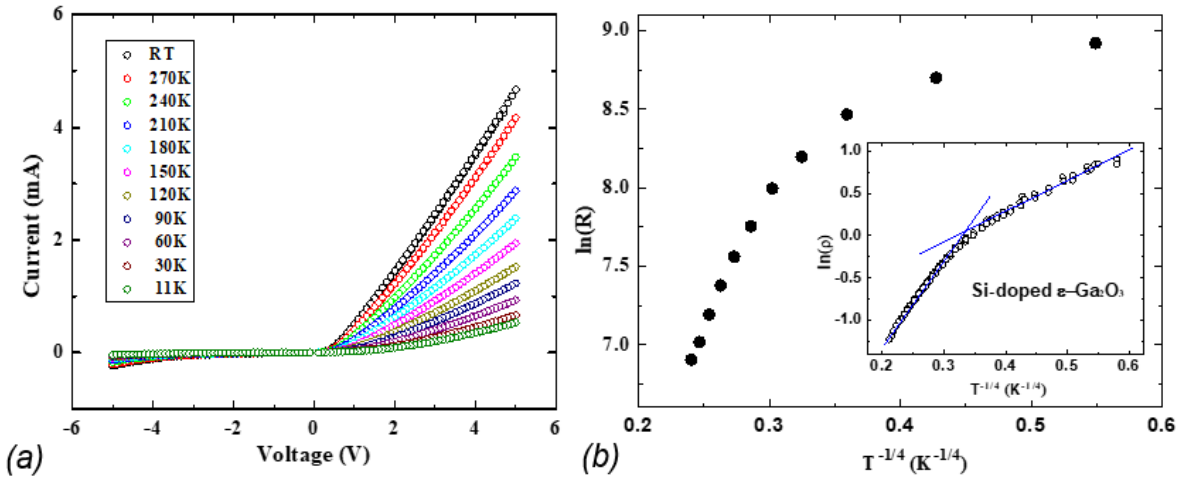

Figure 4.16 In (a) temperature-dependant *I-V* characteristics for diode 1 (200 x 200 μm^2). (b) the $ln(R_e)$ vs. $T^{-1/4}$ (Mott plot). R_e values are extracted from the linear trend in forward bias on the *I-V* reported in (a). In the inset of (b) is reported the Mott plot of the in-plane ρ of Si doped κ-Ga_2O_3 layers.[131] The pictures are taken and readapted with permission from ref. [153].

Therefore, also this study on the planar SnO/κ-Ga_2O_3 *p-n* junction, proves once again that the structural defects of this polymorph are significantly affecting the in-plane functional properties of the material/performance of the κ-Ga_2O_3 based devices. This evidence is naturally leading to investigation of alternative solutions, *e.g.,* different device architectures (vertical diode structures[59]), growth engineering[58,129,159], to overcome the κ-Ga_2O_3 rotational domains-related disadvantages. In the next chapter, different strategies to overcome the rotational domains of the κ-Ga_2O_3 layers will be described.

5 Towards suppression of κ-Ga_2O_3 rotational domains

This chapter focuses on the growth of κ-Ga_2O_3 layers performed by plasma assisted molecular beam epitaxy (PAMBE) aiming at the suppression of the κ-Ga_2O_3 rotational domains. The chapter is divided in three major sections: section 5.1 shortly describes the MEXCAT mechanism needed to stabilize the κ-polymorph in the MBE growth system; sections 5.2 and 5.3 report the results obtained from the MEXCAT-MBE growths on (001) ε-$GaFeO_3$ and (0001) α-Al_2O_3 substrates with intentional offcuts, respectively.

As described in Chapter 4, the structural defective nature of κ-Ga_2O_3 epitaxial layers is affecting and mediating its functional properties.[58,59,153] Hence, different approaches have been explored in order to overcome the κ-Ga_2O_3 defective nature. So far, four different studies proved to be successful into affecting/modifying the rotational-domains structure of the orthorhombic Ga_2O_3 polymorph: (i) a silane flux (Φ_{SiH4}) during growth can mediate the enlargement of the domains average size,[58] (ii) the epitaxial lateral overgrowth technique (ELOG) for the selection of the in-plane growth direction,[159,160] (iii) the growth on an unintentional 0.2° miscut angle (0001) α-Al_2O_3 substrate,[122] and (iv) the growth on quasi-perfect epitaxially matching orthorhombic substrates: (001) ε-$GaFeO_3$.[129]

Point (i) has been already extensively described in Chapter 4. Regarding (ii), Oshima *et al.*[159] exploited an amorphous SiO_x mask with a well-defined pattern on top of (0001) α-Al_2O_3 to select the in-plane growth orientation of the κ-Ga_2O_3 layers thank to a geometrical natural selection mechanism, *i.e.,* the preferred growth of the κ-Ga_2O_3 domain aligned along the [11$\bar{2}$0] Al_2O_3 in-plane direction, selected through the SiO_x mask. This has been demonstrated to allow regularly patterned 20 μm wide stripes of κ-Ga_2O_3 single domains on (0001) α-Al_2O_3.[159,160] However, (iii) and (iv) are the only two works where the effective suppression of the κ-Ga_2O_3 rotational domains has been reported. In (iii), Zhang *et al.*[122] stated to have successfully obtained the suppression of the rotational domains when the κ-Ga_2O_3 is grown by HVPE on a (0001) α-Al_2O_3 substrate in presence of an unintentional 0.2° miscut angle. The use of the miscut/offcut angle substrates is a widely employed strategy in epitaxy that is taking advantage of a defined step-terrace structure at the surface of the substrate to induce the suppression of rotational domains through the installation of a step-flow growth mode. In particular, this approach was already demonstrated for (-201) β-Ga_2O_3 heteroepitaxial layers grown by HVPE[161,162] and low-pressure CVD[155] on offcut (0001) α-Al_2O_3 substrates. However, with respect to the similar approach applied by Zhang *et al.*[122] for κ-Ga_2O_3 on unintentional 0.2° offcut (0001) α-Al_2O_3 substrates, the reported results are debatable. Indeed, the XRD φ-scan of the (122) κ-Ga_2O_3 reflection reported by Zhang *et al.*[122] [Figure 5.1 (a) in yellow] shows the presence of only four

reflection peaks and discusses this as the evidence of the rotational domains suppression; however, the spacing among the four detected peaks is not consistent with the presence of a single domain, but is rather the proof for the presence of the in plane rotation of the orthorhombic cell as calculated by P. Mazzolini *et al.*[58] [Figure 5.1 (b)]. The absence of the full set of twelve peaks in the φ scan reported by Zhang *et al*. is most likely related to the presence of the substrate offcut that requires the acquisition of a pole figure rather than a single φ-scan; indeed, a single 360° φ rotation around a selected diffraction vector [*e.g.*, (122)], with a fixed in-plane χ angle, would not account for the non-perfect oriented diffraction vector of the selected crystal plane due to the presence of a substrate offcut (for additional details regarding pole figure acquisition see section 3.3.2). Beyond question it is instead the result provided by Nishinaka *et al*.,[129] where the effective suppression of the κ-Ga_2O_3 rotational domains is obtained via mist-CVD growth on top of the ε-$GaFeO_3$ [Figure 5.1 (c)], *i.e.,* substrate that is possessing the same orthorhombic unit cell and very similar lattice parameters (only 1% lattice mismatch) w.r.t. κ-Ga_2O_3.

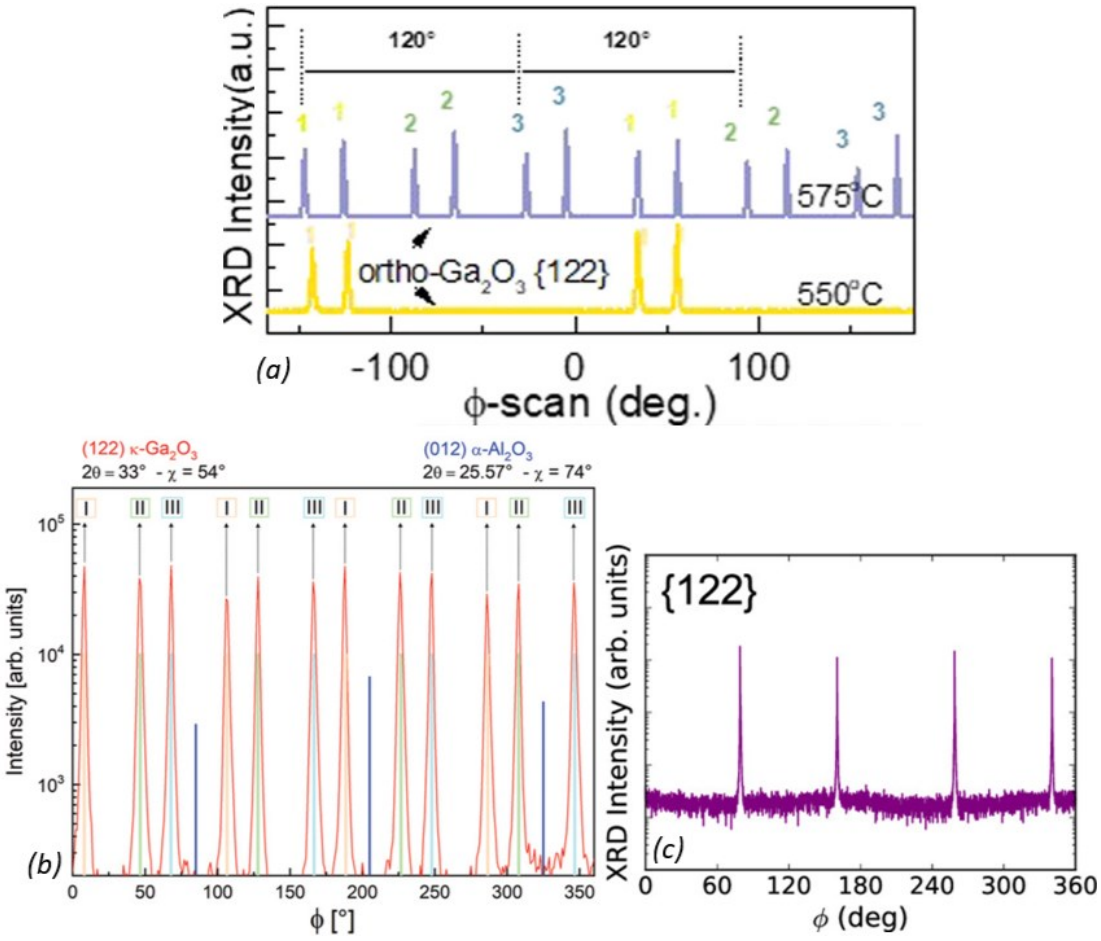

Figure 5.1 φ scans for the (122) reflection of the κ-Ga_2O_3 reported by: (a) Zhang *et al.,*[122] for HVPE growth with (blue) and without (yellow) the rotational domains (adapted with permission from Zhang *et al.*, ACS Applied Electronic Materials, 4, 461-468 (2022).[122] Copyright 2022 American Chemical Society); (b) P. Mazzolini *et al*.[58] The roman numbers (I, II, III) and the vertical lines (orange, green and cyan) highlight the calculated and expected location for the

three rotational domains. Straight blue lines indicate the substrates peak position for (012) reflection (adapted from ref. [58]); (c) H. Nishinaka *et al.*,[129] for the single domain layer grown on top of ε-$GaFeO_3$ (adapted from H. Nishinaka *et al.*, ACS Omega 5, 45, 29585–29592(2020).[129] Copyright 2020 American Chemical Society).

In light of the results reported in the works just described, the candidate attempted the suppression of the κ-Ga_2O_3 rotational domains following two different approaches: deposition on (i) ε-$GaFeO_3$ substrates (substrates purchased by H. Nishinaka - Kyoto Institute of Technology) and (ii) (0001) α-Al_2O_3 substrates with a well-defined intentional offcut, *i.e.,* with 2, 4, 6 and 8° along the [100] in-plane direction.

Two different epitaxial growth techniques were eligible for the candidate: the MOVPE (new reactor installed at IMEM institute in Parma) and the MBE (oxides group at Paul Drude Institute PDI in the framework of a long-time collaboration with UniPr) (see section 3.1 for a detailed description of the two growth systems). The selection of the technique was leaded by several factors, described briefly hereafter. The substrates to be investigated due to economical [cost of offcut 2" (0001) α-Al_2O_3] or technological reasons [irregular and limited size of (001) ε-$GaFeO_3$] required to work either with irregular or with limited sizes ($5 \times 5\, mm^2$). In the case of the MOVPE technique, the fluidodynamics of the precursors on the surface of the substrates is an important aspect to be considered for thin film growth (*i.e.*, in order to maintain laminar flows of the precursors on the surface of the substrates during growth and to keep the substrates steady with the significant rotation speed of the holder – range of 300 rotations per minute); for this reason, the available MOVPE substrate holder was not compatible with the current experimental approach [only 2" substrate pocket – see Figure 5.2 (a)] and the realization of a new properly designed holder was required. On top of that, a new MOVPE reactor had been recently installed at IMEM (Parma) and required significant time for mounting and optimization of the growth parameters. Conversely, the MBE system was already equipped with $5 \times 5\, mm^2$ pockets substrate holder as well as suitable to exploit the In-bonding technique, *i.e.,* physical attachment of the irregular shaped substrate to a 2" Si wafer through melted In[163] [see Figure 5.2 (b)], technique not suitable for MOVPE chamber due to higher substrate rotation speed during growth. In light of this, the PhD candidate spent a total of seven months (three of them funded by Cost OPERA CA20116) at the Paul Drude Institute of Solid State Electronics (PDI, Berlin) where she became fully independent with the MBE growth system.

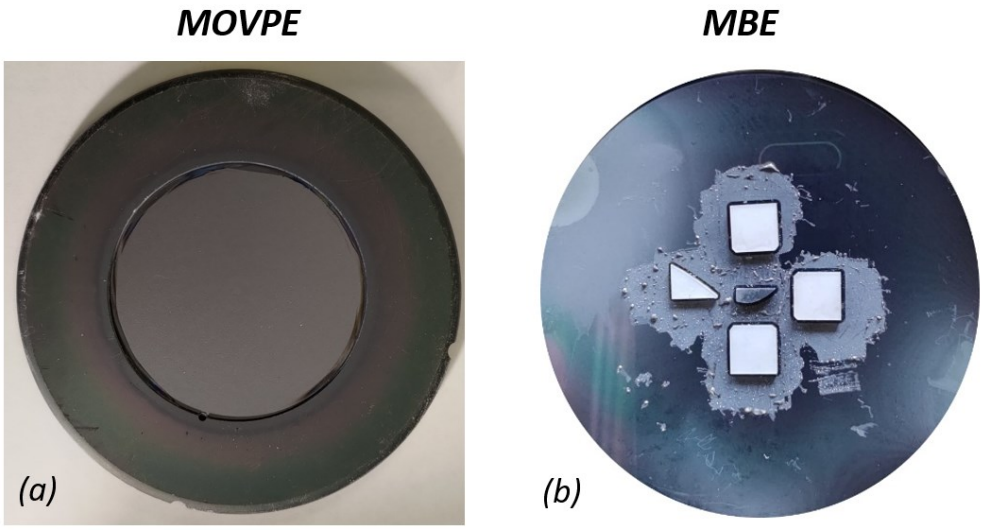

Figure 5.2 (a) The MOVPE substrate holder suitable for 2" wafers. (b) The co-loading of ε-$GaFeO_3$ (center) and α-Al_2O_3 (outer ring) substrates to a 2" Si wafer through In-bonding technique exploited in an exemplary MBE growth experiment.

In the following sections, after a brief introduction on the peculiar growth mechanism (MEXCAT) adopted to stabilize the κ-polymorph via MBE, the results of the growths are reported.

All the substrates pre-treatments and AFM measurements were performed directly by the candidate at PDI with the support of A. Ardenghi (PDI) and under the supervision of P. Mazzolini (UniPr) and O. Bierwagen (PDI). The XRD data, pole figures and reciprocal space maps (RSMs) were acquired by the candidate under the guidance of F. Mezzadri (UniPr). The Raman data and their elaboration were performed by the candidate with the support of H. Tornatzky (PDI), B. Janzen (TU) and M. R. Wagner (TU - PDI). The EBSD measurements were performed by J. Lähnemann (PDI). The TEM investigation were performed by I. Cora and Z. Fogarassy from Hungarian Academy of Science (Budapest). The (001) ε-$GaFeO_3$ substrates were provided by H. Nishinaka from Kyoto Institute of Technology (Japan). The (0001) α-Al_2O_3 substrates were purchased from Cryscore Optoelectronic Limited (Henan, China).

5.1 Stabilization of κ-Ga_2O_3 via PAMBE – MEXCAT technique

In section 3.1.2, the basic principles of the PAMBE growth technique were described. However, an in-depth description of the stabilization method for the metastable κ-polymorph is here provided. As pointed out in section 2.3, the κ-polymorph is one of the metastable phases of Ga_2O_3. Hence, it cannot be grown through bulk methods, but only through epitaxial techniques[39] and it converts to β-polymorphs if brought at $T \geq 700°C$.[119] The first single κ-phase epitaxial thin film was obtained in 2015 by Y. Oshima *et al.*[121] via HVPE growth, on top of different substrates. Since then,

several other CVD techniques were successfully stabilizing pure κ-Ga_2O_3 heteroepitaxial layers.[41,128,164]

In contrast to CVD, the stabilization of the κ-polymorph via PVD epitaxial techniques, *e.g.,* MBE and PLD, needs the introduction of a metal catalyst, *i.e.,* In[113,165] or Sn.[114,124] In 2017, Vogt *et al.*[113] reported the first successful stabilization of the κ-polymorph when an In flux was provided during growth. The involvement of In results in the so called metal-exchange catalysis (MEXCAT). The In-mediated MEXCAT mechanism can be schematically depicted as a consecutive catalytic reaction composed by the formation of In_2O_3 (Equation 5.1) followed by the In-Ga metal-exchange (Equation 5.2) (adsorbate and solid phases are labelled as *a* and *s*, respectively).

$$2In(a) + 3O(a) \rightarrow In_2O_3(s)$$

Equation 5.1

$$2Ga(a) + In_2O_3(s) \rightarrow Ga_2O_3(s) + 2In(a)$$

Equation 5.2

Having In an higher oxidation efficiency $\eta^{(2)}$ w.r.t. Ga, *i.e.,* $\eta_{In} = 2.8\eta_{Ga}$,[113] the formation of In_2O_3 is kinetically favoured; however, In_2O_3 is unstable in presence of Ga, given the stronger nature of the Ga-O bond, resulting in a thermodynamic advantage of Ga_2O_3 over In_2O_3. Hence, the In-Ga exchange takes place with the continuous segregation (followed by a partial desorption) of In on the growth front of the deposited oxide, resulting in a limited In-incorporation in the layer thickness, *i.e.,* 0.02 cat %, under optimized growth conditions.[165] Given the isovalent nature of In with respect to Ga, its incorporation in such concentrations is not significantly affecting the transport properties of the Ga_2O_3 layers. Likewise, Sn-MEXCAT leads to similar result when a Sn-flux is continuously provided during Ga_2O_3 growth[114] or if a thin buffer layer of SnO_x is deposited prior to growth.[127] Noteworthy, Sn is also proven to be a n-type donor for both β-[166] and κ-Ga_2O_3;[131] therefore, for the Sn-MEXCAT technique the donor-catalyst conflicting role of Sn must be considered. Further details regarding the MEXCAT deposition process can be found in ref. [167].

5.1.1 κ-Ga_2O_3 stability window for In-mediated MEXCAT-MBE

A thorough study on the effects of the growth parameters over the phase-control of Ga_2O_3 and related κ/β-$(In_xGa_{1-x})_2O_3$-alloys through In-mediated MEXCAT-MBE was still missing in literature.

[2]The oxidation efficiency η is defined as the fraction of the maximum available O adatoms for metal oxidation at a given partially activated net oxygen flux (the level of activation is *e.g.,* related to the O-plasma *RF* unit efficiency under the specific work conditions employed).

In this framework, the candidate was marginally involved in the work leaded by the PhD student A. Ardenghi (PDI) that resulted in a recently published paper on APL Materials.[125] The core of the work was to study the role of substrate temperature (T_g), oxidizing power (controlled through the plasma power P_{RF} while maintaining the same O-flow), growth rate, and used substrate / nucleation on the Ga_2O_3 phase formation and In incorporation in the layers. Figure 5.3 reports the phase diagram obtained from the In-MEXCAT growths as a function of the T_g and P_{RF}, for fixed metals and oxygen fluxes (BEP values reported in the top-left box in Figure 5.3). The layers were grown on (0001) α-Al_2O_3 with a (-201) β-Ga_2O_3 nucleation layer [*nl*].(3) The stability windows for κ- and β- were identified, as well as the regions of amorphous and mixed κ+β layers. Generally, a decrease of T_g and/or an increase in the P_{RF} resulted in a higher incorporation of In ultimately leading to enough structural disorder to promote the formation of amorphous Ga_2O_3 layers (Figure 5.3). Notably, the T_g -window for phase pure κ-Ga_2O_3 layers is found to be limited to less than 100°C, with the highest temperature being related to the stability temperature of the polymorph as previously reported by Fornari *et al.*[119] Focusing on the overall κ-Ga_2O_3 layer quality, the plasma power is found to play an important role: at a similar $T_g \approx$ 650°C (samples C and E, Figure 5.3), a decrease of P_{RF} (ΔP_{RF} = 30 W) resulted in a rougher layer ($RMS_{\mathrm{SampleC}} = 4.2$ nm; $RMS_{\mathrm{SampleE}} = 13.1$ nm) and worst layer quality ($FWHM_{SampleC} = 0.47°$; $FWHM_{SampleE} = 0.62°$).[125] All the information provided in this work, *i.e.*, the knowledge of the growth window parameters for κ-Ga_2O_3 and their effect on layer quality/In incorporation, were of fundamental importance for the following work of the PhD candidate, constituting the starting point for the MEXCAT-MBE growths on top of different substrates.

[3] The introduction of a 20/30 nm-thick (-201) β-Ga_2O_3 *nl*, deposited by conventional MBE (*i.e.*, without catalyst), at T_g = 550°C, was proven to be beneficial and in most cases necessary for the subsequent growth Ga_2O_3 so to avoid nucleation issues.

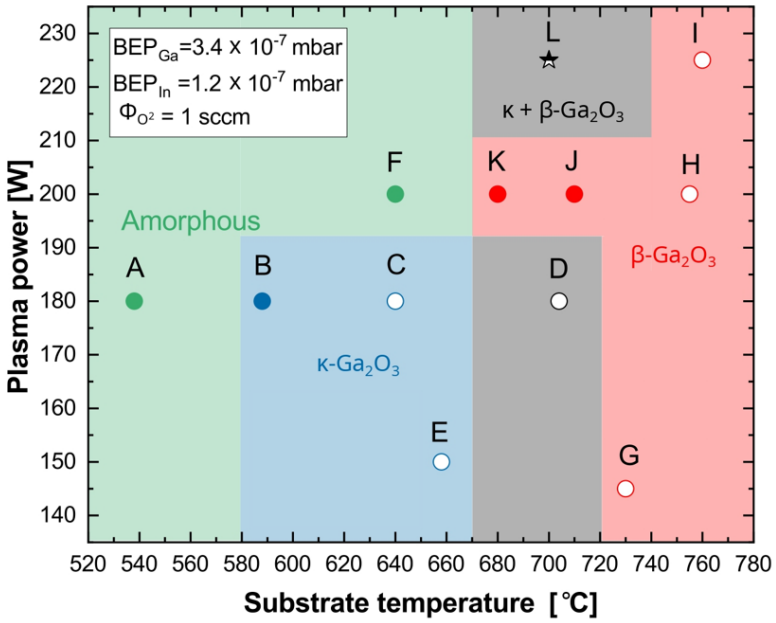

Figure 5.3 Phase diagram built from the MEXCAT-MBE growths as a function of P_{RF} and T_g; filled symbols represent samples with In > 10%, half-filled In = 3%, and open In < 1%. Sample L is reported with a star due to possible nucleation issues. The coloured areas for the different phases are not hard boundaries but more a guide for the eye. Figure adapted from ref. [125].

5.1.2 Role of fluxes/growth rate on the phase-selection

An additional result, reported in the paper here discussed, and relevant in the framework of the PhD candidate work, is the role of the growth rate/metal fluxes on the phase-stabilization in Ga_2O_3. As reported in Table 5.1, three pairs of samples were grown by the PhD candidate herself. Samples M, N, and O ("standard" fluxes) were compared to M', N' and O'("low" fluxes). For both flux regimes, the active-O/Ga flux ratio was approximately maintained, *i.e.,* ≈ 0.2.

Sample ID	T_g [°C]	*nl*	P_{RF} [W]	*G.R.* [nm/min]	BEP_{Ga} [10^{-7} mbar]	BEP_{In} [10^{-7} mbar]	O_{flux} [sccm]
M	640	×	150	6.6	4.95	1.7	1
M'	640	×	180	2.6	2.3	0.6	0.33
N	630	β-Ga_2O_3	160	5.3	4.2	0.8	0.9
N'	630	β-Ga_2O_3	165	2	2.8	0.4	0.6
O	660	SnO_x	175	5.4	5.3	1.6	0.9
O'	660	SnO_x	250	4	1.8	0.5	0.4

Table 5.1 Growth parameters to investigate the effect of the fluxes on the phase stabilization. Table adapted from [125].

The samples were grown on top of three different nucleation layers: (i) direct growth on (0001) α-Al_2O_3 (M and M'), (ii) on a (-201) β-Ga_2O_3 *nl* (N and N') and (iii) on a δ-SnO_x buffer layer (O and O'). The XRD *2θ-ω* scans of each set of samples are reported in Figure 5.4 (a-c). A common trend is highlighted on the intensity ratio of the (-402) and (004) reflections of β- and κ-phase respectively, with low fluxes / growth rates promoting the stabilization of the β- and high fluxes favouring the one

of the κ-phase, regardless of the starting nucleation surface. The negligible shift in the absolute *2θ* position of the peaks w.r.t. the expected positions of both polymorphs (vertical grey dashed lines in Figure 5.4) indicates a negligible In incorporation in the layers. Noteworthy, a similar effect of the fluxes/growth rate over the phase-selection was reported for MOVPE.[120]

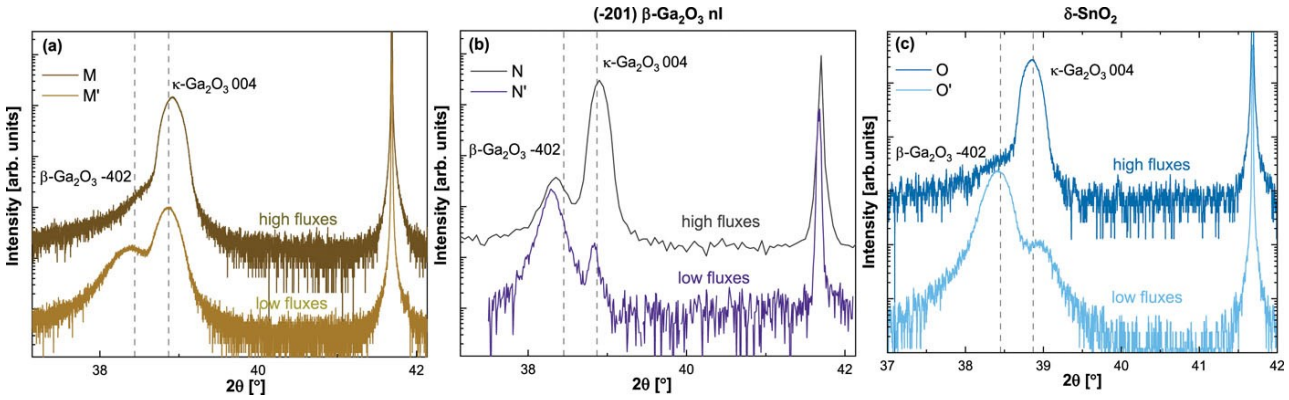

Figure 5.4 XRD *2θ-ω* scans for sample-set grown in different fluxes-regime on top of: (a) (0001) α-Al_2O_3, (b) on (0001) α-Al_2O_3using a (-201) β-Ga_2O_3 nucleation layer and (c) on (0001) α-Al_2O_3 with a δ-SnO_x thin layer. The vertical grey dashed lines indicates the expected position for the (004) κ-Ga_2O_3[20] and (-402) β-Ga_2O_3[110] reflexes without In incorporation. Spectra are vertically offset for sake of clarity. Figure reproduced from [125].

5.2 MEXCAT - MBE growths on ε-$GaFeO_3$ substrates

5.2.1 ε-$GaFeO_3$ substrates: characterization and pre-treatments

The (001) ε-$GaFeO_3$ substrates involved in this work, provided in the framework of a scientific collaboration with H. Nishinaka (Kyoto Institute of Technology, Japan), are the very same substrates involved in the work reporting the first κ-layer single domain obtained by mist-CVD.[129] ε-$GaFeO_3$ is the isomorphic structure of κ-Ga_2O_3, *i.e.,* possessing an orthorhombic unit cell belonging to the same *Pna2₁* symmetry group. Moreover, the lattice parameters are very similar (ε-$GaFeO_3$: $a = 5.077, b = 8.736, c = 9.377$ Å; κ-Ga_2O_3: $a = 5.046, b = 8.702, c = 9.283$ Å), resulting in a lattice mismatch of about 1%.

The ε-$GaFeO_3$ substrates were grown by high-pressure FZ method,[168] and provided by the supplier already sliced in thin wafers and mechanically polished. As for now, these substrates are not commercially available and their preparation steps not yet optimized. Indeed, Figure 5.5 (a) reports the $5 \times 5 \mu m^2$ AFM image of the as received substrate revealing a significant density of particles with ≈ 20 nm of diameter. Their presence was ascribed to residual of the SiO_2 abrasive compound used for the mechanical polishing. Hence, the wafers underwent a wet etching at room temperature in a water-diluted hydrofluoric acid HF solution ($[HF] = 5$ %, $t_{etching} = 60\ s$). The etching parameters were chosen according to the reported HF etching rate of SiO_2.[169] The surface after the etching [Figure 5.5 (b)] is markedly improved with the majority of particles removed, a well-defined step-terrace

morphology highlighted and the smoothness increased (*RMS* = 0.38 nm). The substrates were then annealed in a quartz tubular furnace under continuous flux of O_2 at high temperature ($T_{dwell} = 950\,°C,\ p = 1\,bar,\ t_{dwell} = 1\,h$). The choice was driven by the well-known beneficial effects of an high-temperature O_2 annealing over the substrate surface prior to epitaxial growths,[170,171] and qualitatively confirmed for ε-$GaFeO_3$ substrates by AFM investigation. Figure 5.5 (c) reports the AFM image of the surface after the O_2 annealing, showing an even more defined step-terrace morphology.

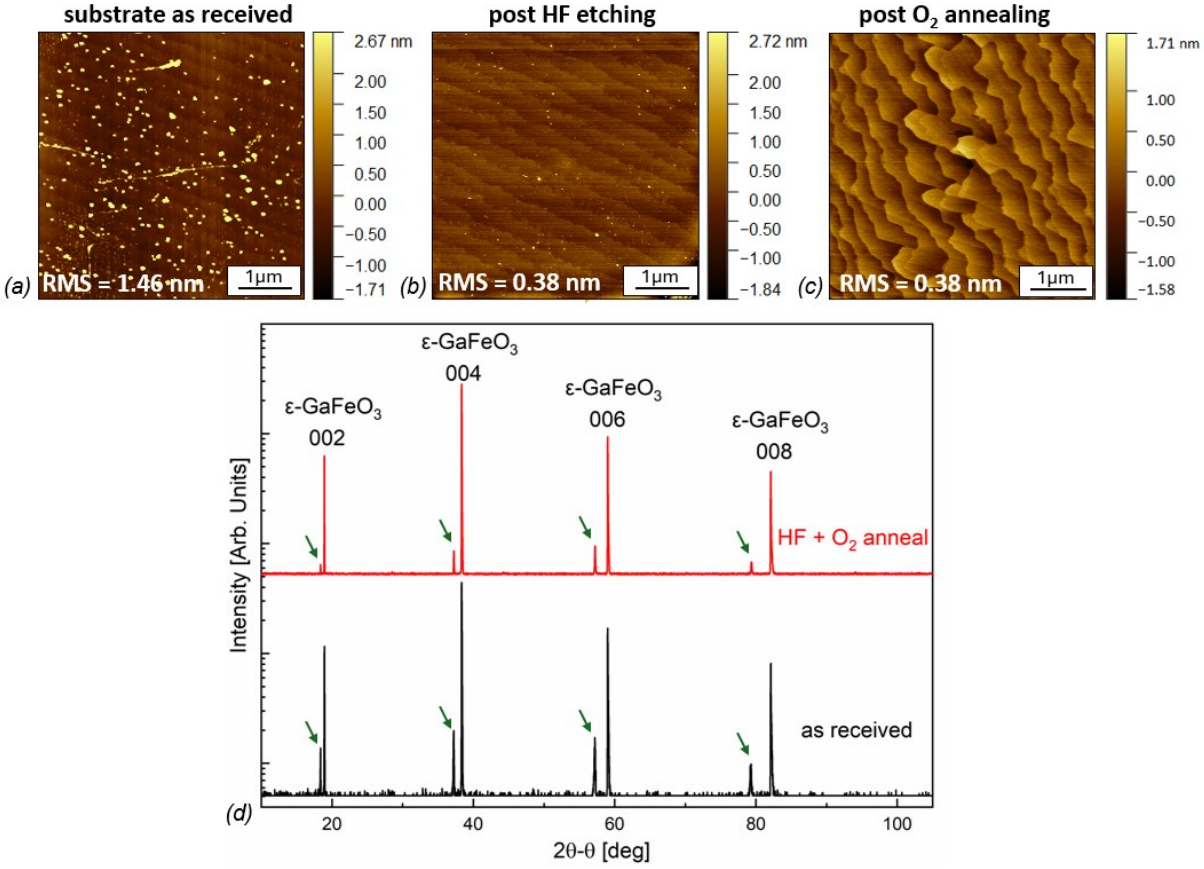

Figure 5.5 (a), (b) and (c) $5 \times 5\ \mu m^2$ AFM images of the same piece of ε-$GaFeO_3$ as received, after HF etching and after O_2 annealing, respectively. (d) The exemplary *2θ-θ* XRD scans of two different pieces of ε-$GaFeO_3$ as received (in black) and after the pre-treatments (in red). The {00l} reflections of the orthorhombic ε-$GaFeO_3$ are labelled. The green arrows highlight the additional peaks assigned to an additional spinel bulk phase of the substrate, γ-$GaFeO_3$.

The ε-$GaFeO_3$ substrates were further characterized through X-ray diffraction prior and after the pre-treatments. Figure 5.5 (d) reports the *2θ-θ* symmetric scans with the expected {00l} peaks family of the orthorhombic $GaFeO_3$. However, a family of additional peaks [see Figure 5.5 (d) - green arrows] is detected for most of the investigated $GaFeO_3$ substrates. From their *2θ* position and spacing, combined with the single-crystal diffractometry analysis, they are assigned to the spinel γ-phase of $GaFeO_3$, space group $Fd\bar{3}m$, cubic unit cell with lattice parameter $a = 8.3527$ Å.

Noteworthy, the presence of these peaks was randomly detected in the substrates analysed, probably depending on non-perfectly homogeneous conditions during the FZ bulk growth of the material.

For each $GaFeO_3$ substrate, the in-plane [010] direction w.r.t. the sample geometry [see an exemplary sample in Figure 5.6 (a)] was identified by the position of the (013) reflection ($2\theta = 30.33°$, $\chi = 20°$) in the φ scan [Figure 5.6 (b)]. Furthermore, the absolute value and direction of the unintentional offcut w.r.t. the in-plane directions was determined acquiring different ω scans of the (004) ε-$GaFeO_3$ at different in-plane orientations, *i.e.*, steps of φ angles [Figure 5.6 (c)]. The shift $\Delta\omega$ w.r.t. the nominal plane reflection, *i.e.*, $\omega = 19.17°$ [vertical dashed line in Figure 5.6 (c)] is calculated and plotted vs. the relative φ angle [Figure 5.6 (d)]. The absolute offcut value and direction are found at the minimum/maximum of the sinusoidal fit [horizontal and vertical dashed lines in Figure 5.6 (d)]. The unintentional offcut for the analysed wafers are in the range of 0.1 – 0.2° while the in-plane offcut direction is randomic.

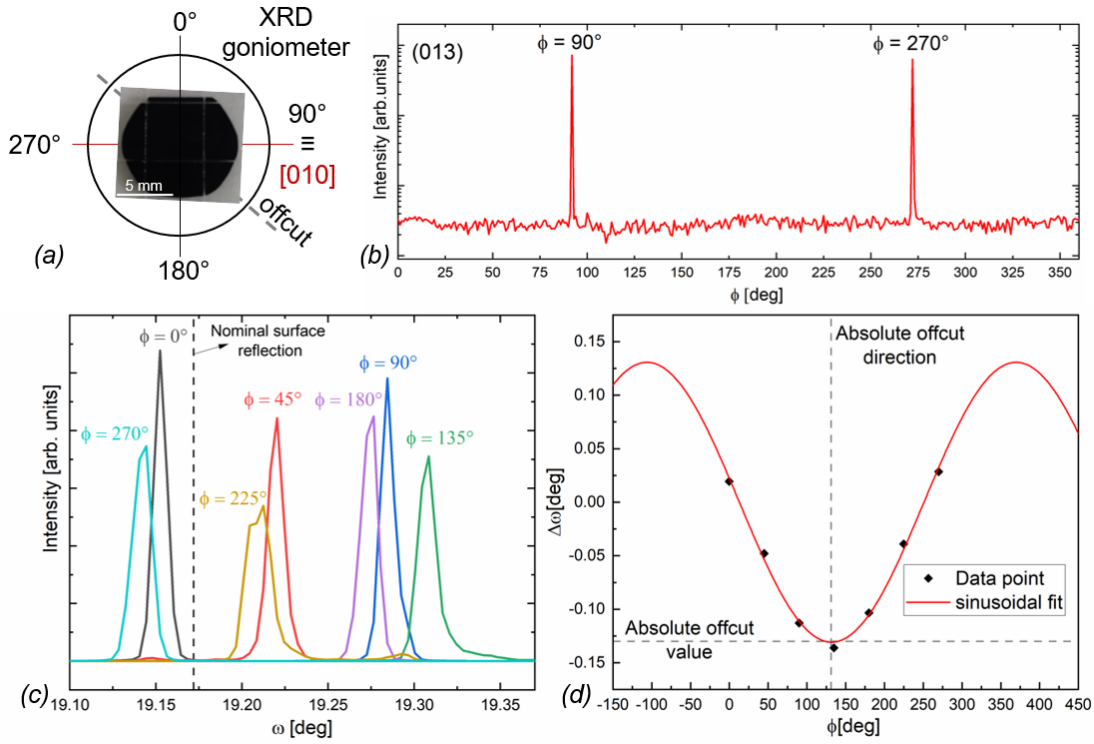

Figure 5.6 (a) Image of an exemplary ε-$GaFeO_3$ crystal after dicing procedure so to obtain a regular 5 × 5 mm^2 substrate as well as other irregular pieces still usable for MBE depositions through In-bonding. The sample in-plane orientation is given according to the diffractometer goniometer and the φ [deg] indication is reported together with the [010] (red line) and offcut direction (dashed gery line). (b) The φ scan of the (013) reflection showing the diffraction peaks at 90° and 270° allowing the identification of the [010] in-plane direction on the sample. (c) The ω scans acquired at the different φ azimuthal positions; the vertical dashed line indicates the position of the nominal ω expected for the (004) reflection (*i.e.*, no offcut condition). (d) The data point of the $\Delta\omega$ [extracted from the curves in (c)] vs. φ are

reported with the corresponding sinusoidal fit. The horizontal and vertical dashed line at the minimum of the curve represent the absolute value (≈ 0.13°) and absolute direction (≈ 131°) of the unintentional offcut.

Next, two pieces of the same ε-$GaFeO_3$ wafers, one as received and one subjected to the pre-treatments, were checked with TEM-EDX combined investigation. The lamellas were prepared with focused-ion beam (FIB) method. Figure 5.7 (a) and (b) report the HRTEM image and corresponding FFT of the ε-$GaFeO_3$ substrates as received and after the pre-treatments, respectively. The investigation confirmed the orthorhombic symmetry of the substrates, not majorly affected by the substrates pre- treatments. In the analysed lamellas, the γ-phase is not detected; this is most likely related to the limited sample area analysed by TEM w.r.t. the larger volume of the sample probed by the XRD analysis. As a result, the combination of TEM and XRD suggests that the minority γ-phase fraction should be present in the volume of the ε-$GaFeO_3$ substrates and is therefore not expected to significantly affect the following heteroepitaxial growth. Figure 5.7 (c) reports the HAADF image and the corresponding Si elemental map for the pre-treated substrate, highlighting a SiO_x contamination on the surface of the ε-$GaFeO_3$. This is probably coming from the quartz tube employed for the high temperature annealing in O_2.

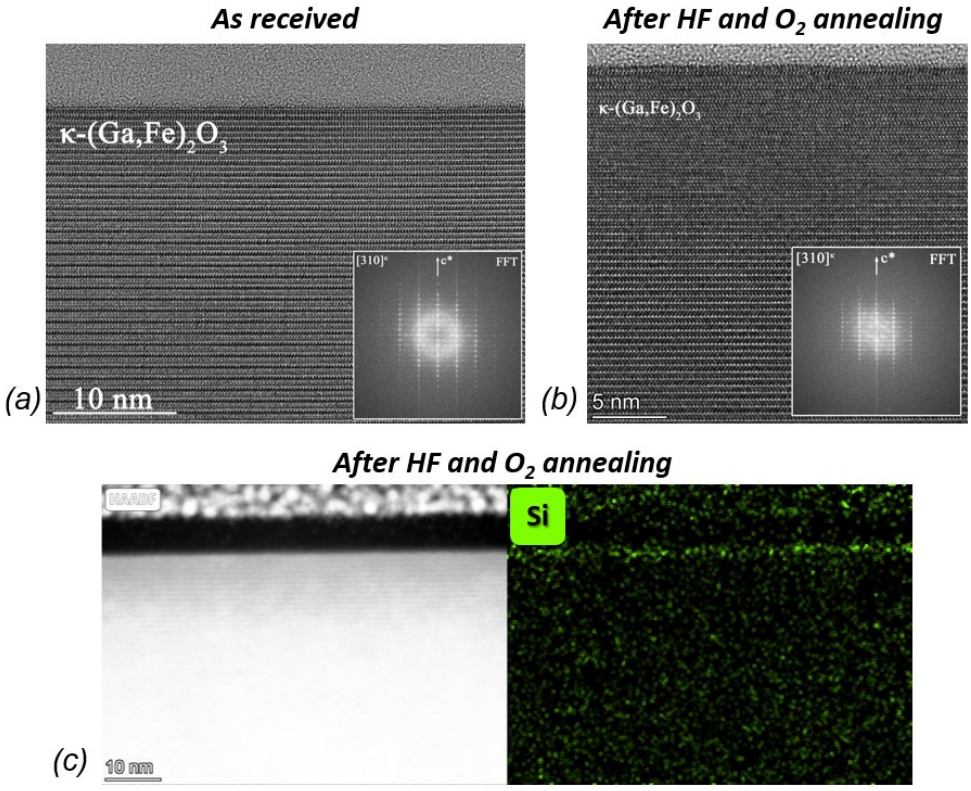

Figure 5.7 (a) and (b) HRTEM images with the corresponding indexed FFT of the ε/κ-$GaFeO_3$[4] substrate as received and after pre-treatments, respectively. (c) HAADF image and corresponding Si elemental map of the κ-$GaFeO_3$ after the pre-treatments.

5.2.2 MBE depositions

The growths were performed following three different approaches: (i) conventional MBE growth (no catalyst involved), (ii) In-mediated MEXCAT and (iii) SnO_x buffer layer followed by In-mediated MEXCAT. The results relative to the three different approaches are shown hereafter separately.

5.2.2.1 (i) Growth without catalyst

Conventional MBE of Ga_2O_3 on ε-$GaFeO_3$ aims at verifying if the presence of an epitaxially matching substrate could itself allow for the stabilization of the metastable κ-polymorph and suppression of its rotational domains. The growth parameters were: $BEP_{Ga} = 2.05 \cdot 10^{-7} mbar, O_{flux} = 0.5\ sccm, P_{RF} = 350W, T_g = 600°C$. The growth conditions resulted in a grow rate *G.R.* ≈ 4 nm/min.

From $5x5\ \mu m^2$ and $1x1\ \mu m^2$AFM images [Figure 5.8 (a) and (b)], the detected surface morphology was resembling the one typically obtained in (-201) β-Ga_2O_3 heteroepitaxy, also characterized by a structural domain structure.[165,172] From XRD *2θ-ω* scans [Figure 5.8 (c)] only the (004) reflection of the ε-$GaFeO_3$ and the contribution from the spinel γ-$GaFeO_3$ are present, with no signal detected for κ-Ga_2O_3. The (-402) β-Ga_2O_3 reflection (expected position indicated with vertical blue dashed line) is not accessible in this measurement geometry, due to the overlapping with the (004) substrate peak. Hence, a dedicated in-plane *φ* scan of the (-401) β-Ga_2O_3 reflection is acquired [Figure 5.8 (d)]. The presence of six broad peaks (labelled with blue triangles) confirmed the presence of the β-phase with rotational domains. In the *φ* scan some contributions from the substrate are detected (labelled with black triangles), even if not assigned here to a specific reflection. In light of these results, the MBE standard growth was abandoned since leading to stabilization of the stable β-polymorph; however it must be pointed out that also the low *G.R.* could play a role in the stabilization of the β-phase.[120,125]

[4] As already mentioned in Section 2.3, the ε-$GaFeO_3$ substrates, even though possessing a orthorhombic unit cell, are commonly labelled with the ε greek letter. However, in this chapter, when discussing TEM investigation of κ-Ga_2O_3 on top of ε-$GaFeO_3$ substrates, the double labelling ε/κ is reported.

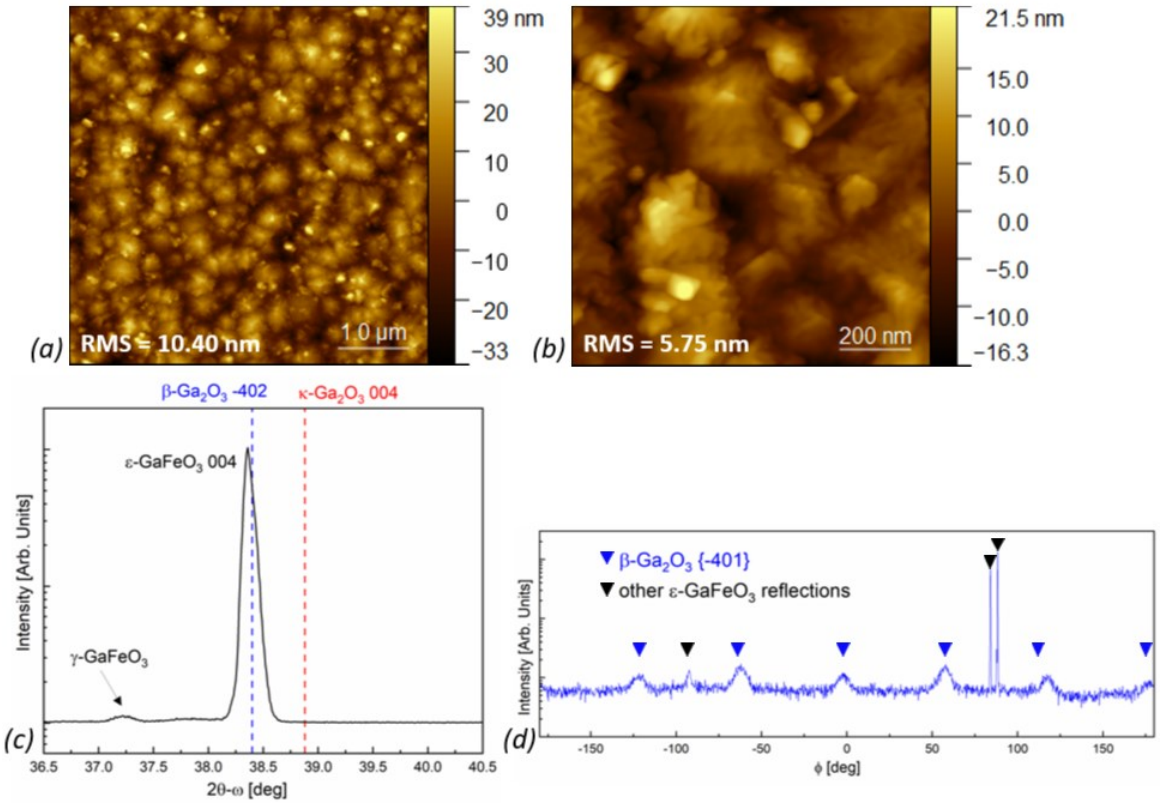

Figure 5.8 (a) and (b) $5 \times 5\ \mu m^2$ and $1 \times 1\ \mu m^2$ AFM images on the sample grown without catalyst, *RMS* values are reported for each image. (c) the XRD symmetric *2θ-ω* scan with the (004) ε- and contribution from γ-$GaFeO_3$ labelled. The vertical blue and red dashed line indicate the positions where the (-402) β- and (004) κ-Ga_2O_3 reflections are expected. (d) the *φ* scan for the (-401) β-Ga_2O_3 reflection. The presence of six broad peaks (labelled with blue triangles) indicates the β-polymorph presence with the rotational domains. The substrate contributions are labelled with black triangle.

5.2.2.2 (ii) Growth with In-MEXCAT

The second approach foresees a continuous flux of the In-catalyst throughout the Ga_2O_3 deposition. The growth parameters were chosen according to the κ-Ga_2O_3 stability window reported in Figure 5.3, and a tuning procedure was followed applying small variations over T_g and P_{RF} (see Table 5.2). All the samples were grown in the "standard" fluxes regime, *i.e.*, $BEP_{Ga} \approx 4.5 \times 10^{-7} mbar, BEP_{In} \approx 1 \times 10^{-7} mbar, O_{flux} = 0.9\ sccm$. The effect of T_g and P_{RF} variation is described hereafter, separately.

Sample ID	T_g *nl* [°C]	T_g [°C]	P_{RF} [W]	*G.R.* [nm/min]	Thickness [nm]	FWHM [°]
S1		615	160	3	240	0.198
S2		615	165	3	250	0.267
S3		615	175	4.5	230	0.629
S4		630	160	5	430	0.326
S5		660	175	3	300	0.33
S6	615	660	165	3.5	500	0.427
S7	615	660	175	5	250	0.488

Table 5.2 Sum-up of the exemplary samples deposited with In-MEXCAT on ε-$GaFeO_3$ substrates. Growth temperature (T_g), plasma power (P_{RF}), growth rate (GR), estimated thicknesses (t) from LR and FWHM values extracted from the ω scans of the (004) κ-Ga_2O_3 reflection are reported.

5.2.2.2.1 Role of P_{RF}

The first experimental evidence detected for the sample series S1-S3, was a worsening of the κ-Ga_2O_3 layer quality when increasing the P_{RF}. This aspect was detected from AFM images [see Figure 5.9 (a - c)] as well as from the FWHM value of the (004) κ-Ga_2O_3 ω scans (reported in Table 5.2). On the AFM side, it is interesting to highlight the presence of a pronounced faceted morphology that, to the best of our knowledge, have never been previously observed in the case of κ-Ga_2O_3 epitaxy. As discussed in section 5.1.1, the general worsening of the crystalline quality while increasing P_{RF} could also be connected to an higher incorporation of In as suggested by the 2θ left-side shift [2θ-ω scans reported in Figure 5.9 (d)]. The effect of worsening of the layer quality/increased In incorporation for higher oxidizing conditions was already reported for MEXCAT-MBE.[29]

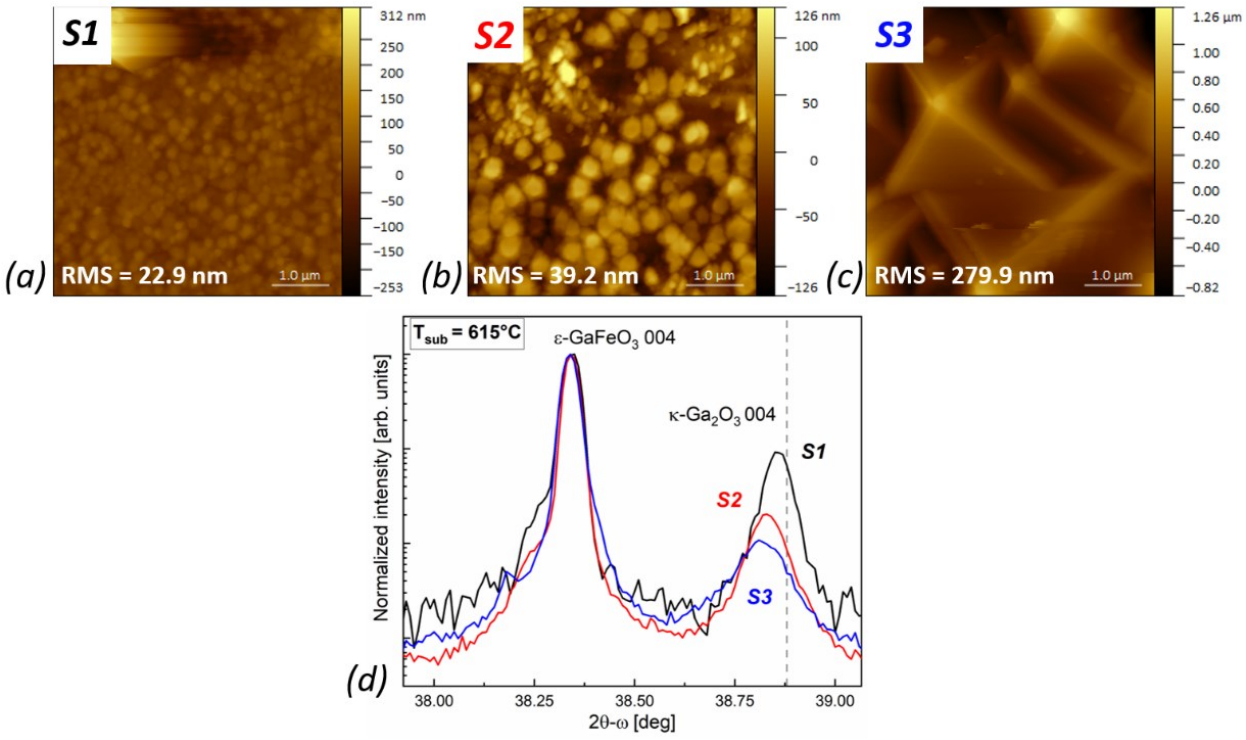

Figure 5.9 (a), (b) and (c) $5 \times 5\ \mu m^2$ images of sample S1, S2 and S3 respectively. The *RMS* values are reported for each sample. (d) 2θ-ω scans of the S1-S3 series. The (004) reflection of the substrate and of the κ-Ga_2O_3 epilayer are labelled while the vertical grey dashed line indicates the expected position of the (004) κ- peak.[20]

Samples S1 and S2 were further analysed with combined SEM-EBSD measurements [see Figure 5.10]. The EBSD maps indexed, for both S1 and S2, the κ-polymorph as hexagonal [ε as reported in Figure 5.10 (e) and (f)] providing an insight on the presence of the rotational domains.

Indeed, the EBSD lateral resolution is limited to several tens of nm; therefore, being the information averaged over such superficial width, the labelling of the hexagonal phase points toward the averaged contribution of the three 120° rotated orthorhombic domains with at best tens of nm-sized distribution. Such a small domain size is typically found in UID κ-Ga_2O_3 heteroepitaxy on sapphire.[20] The presence of κ-Ga_2O_3 120° rotational domains were also confirmed with XRD φ scans of the (122) κ-Ga_2O_3 reflection [not shown here]. Moreover from EBSD, sample S1 appears to be pure κ-phase, while sample S2 also shows β-phase presence [see Figure 5.10 (d) – in purple]. XRD φ scans of the (-202) β-Ga_2O_3 reflection are also acquired to corroborate the EBSD information over the phase purity of the layer (S1); however in both S1 and S2, β-phase is detected [see Figure 5.10 (g)]. In this regard, it is important to highlight that EBSD is a surface-sensitive technique: the eventual presence of the β phase at the substrate/layer interface for S1 could be detected by XRD, but not by EBSD.

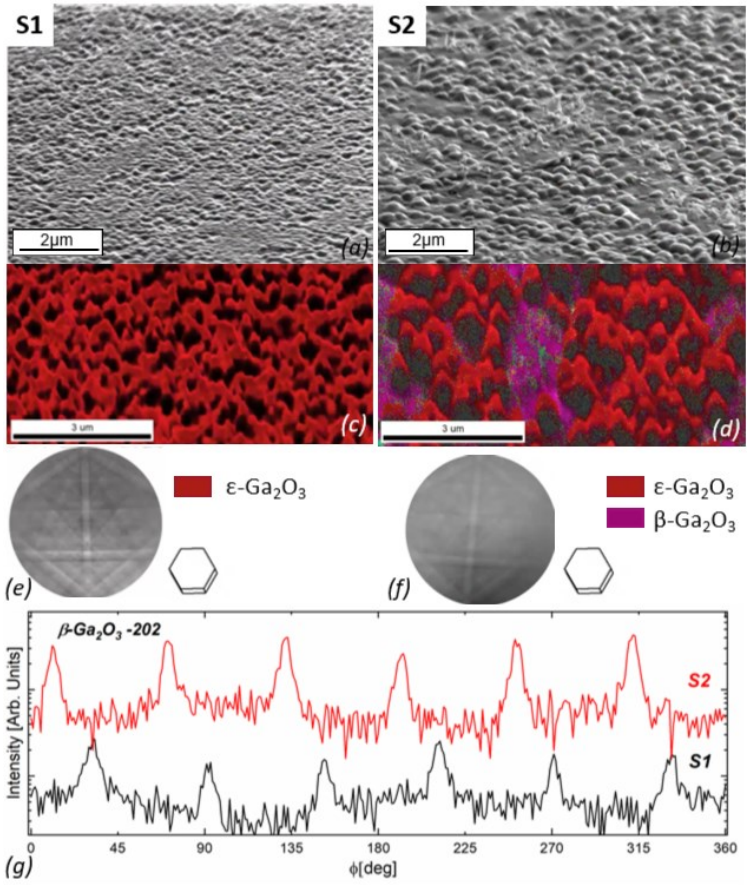

Figure 5.10 (a), (c) and (b), (d) SEM images and EBSD maps of samples S1 and S2, respectively. (e) and (f) the diffraction pattern of the hexagonal ε-phase of Ga_2O_3. (g) φ scans for the (-202) β-Ga_2O_3 phase for S1 (black) and S2 (red). The scans are vertically shifted for sake of clarity.

5.2.2.2.2 Role of T_g

The effect of the growth temperature was investigated as well. In particular, $T_g = 615 - 630 - 660°C$ have been tested (Table 5.2). For the highest deposition temperature, the adoption of

a nucleation layer (*nl*) (adopting In-MEXCAT as well) at lower T_g (615°C) has been also investigated. For all those samples, also the effect of a slight variation of the oxygen plasma power is studied, since T_g and P_{RF} were found to be non-independent variables (see Figure 5.3). Figure 5.11 provides an overview of the $5 \times 5\ \mu m^2$ AFM images of such samples. For both oxidizing conditions, the T_g increase, *i.e,* S1 to S4 and S3 to S5, results in a smoother surface, even though the faceting previously discussed for higher oxidizing conditions is still present. On the other side, the two-step growth, seems to have a beneficial effect only for the higher oxidizing atmosphere, *i.e.,* S7, resulting in a lower *RMS* and FWHM and lower In-Incorporation (see 2θ position in the 2θ-ω scans – Figure 5.11 – bottom right). This would point towards the faceted pyramidal features highlighted in samples S3 and S5 being related to non-homogeneous nucleation conditions over the sample surface. Nevertheless, all the κ-Ga_2O_3 samples described so far were characterized by the presence of the in-plane 120°-rotated domains. Given the very narrow window of T_g and P_{RF} for κ-phase stability (Figure 5.3) and the not successful suppression of the rotational domains when they are varied, a different strategy has been attempted.

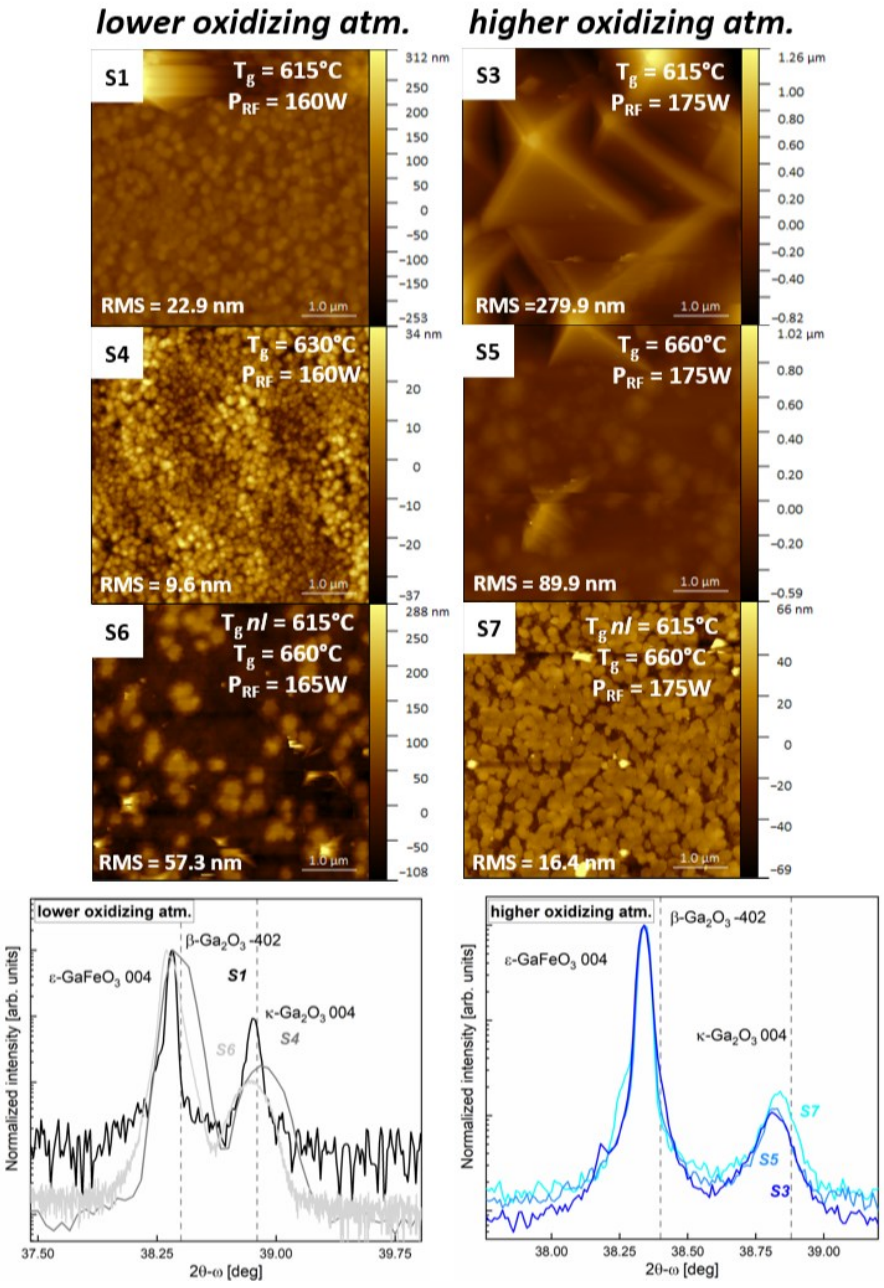

Figure 5.11 $5 \times 5\mu m^2$ AFM images of the samples interested by variation of T_g or introduction of T_g *nl, i.e.,* S1, S3, S4, S5, S6 and S7, divided in two vertical columns for lower (on the left) and higher (on the right) oxidizing atmosphere. The relative growth parameters are reported on each image together with the *RMS* value. The symmetric *2θ-ω* scans are reported as well for the two different oxidizing atmosphere under the relative columns of AFM images. The spectra have been normalized on the (004) substrate peak, for better comparison. The vertical grey dashed line indicates the expected position for (-402) and (004) reflection of β- and κ-Ga_2O_3, respectively.

5.2.2.2.3 *Role of fluxes*

Indeed, the effect of the flux variation over the κ-polymorph stabilization/rotational domains suppression is investigated. In Table 5.3 the growth parameters and metal/oxygen fluxes are reported for three different samples: S7 was grown with "standard" metal fluxes while S8 and S9 decreasing

and increasing them, respectively. The oxidation environment during growth has been varied accordingly by adapting either the O_{flux} or the P_{RF}.

Sample ID	T_g *nl* [°C]	T_g [°C]	P_{RF} [W]	BEP_{Ga} [10^{-7} mbar]	BEP_{In} [10^{-7} mbar]	O_{flux} [sccm]	*G.R.* [nm/min]	FWHM (004) [°]
S7	615	660	165	5.3	1.6	0.9	5	0.488
S8	615	660	250	1.88	0.5	0.4	2.5	--
S9	615	660	240	7.2	2.1	0.9	5	0.47

Table 5.3 Growth parameters, metal and oxygen fluxes, resulting *G.R.* and FWHM of the (004) κ-Ga_2O_3 reflection for samples grown in the framework of understanding the effect of low/high flux regimes for In-MEXCAT growths on ε-$GaFeO_3$ substrates.

Similar to the experimental evidence collected on c-plane sapphire substrates, despite the use of In-mediated MEXCAT and the ε-$GaFeO_3$ substrate, lower fluxes / growth rates were found to promote the stabilization of the β-polymorph instead of κ. Indeed in the *2θ-ω* scan of sample S8 [Figure 5.12 (a)] there is almost no signal of the (004) κ-reflection, while the (004) ε-$GaFeO_3$ peak is showing a shoulder on the right, where the (-402) β-phase is expected. The *φ* scans [Figure 5.12 (b)] confirmed β-phase stabilization for S8. Nonetheless, also the standard and higher fluxes samples (S7, S9) show the presence of β in addition though to a prominent κ-Ga_2O_3 diffraction peak as well. Sample S7 and S8 were also investigated with Raman spectroscopy [Figure 5.12 (c)] where the presence of the β-Ga_2O_3 $A_g^{(3)}$ mode located at 200 cm^{-1} confirmed the almost single β-phase stabilization for the sample S8 grown at lower fluxes. S7 doesn't show the $A_g^{(3)}$ mode, suggesting that the monoclinic phase is just present in a small fraction in the deposited layer. Also, due to the similarity of substrate/epi-layer orthorhombic unit cell, the Raman active modes of sample S7 are overlapping to the substrate ones [Figure 5.12 (c)], not allowing to easily access experimental evidences on the κ-Ga_2O_3 phase with such experimental approach.

Despite the different approaches, *i.e.,* variation of T_g, P_{RF} and fluxes, all the κ-Ga_2O_3 layers deposited with In-MEXCAT on the ε-$GaFeO_3$ were characterized by the presence of the rotational domains and at least small fractions of β-Ga_2O_3. The collected data on S1, *i.e.,* β-Ga_2O_3 detected with XRD (bulk sensitive) but not from EBSD (surface sensitive), suggest that β-phase could be present at the substrate/film interface, hindering the epitaxial match ε-$GaFeO_3$/κ-Ga_2O_3. In order to clarify/confirm the suggested scenario a TEM investigation was conducted on S1 (the sample showing the best Rocking curve).

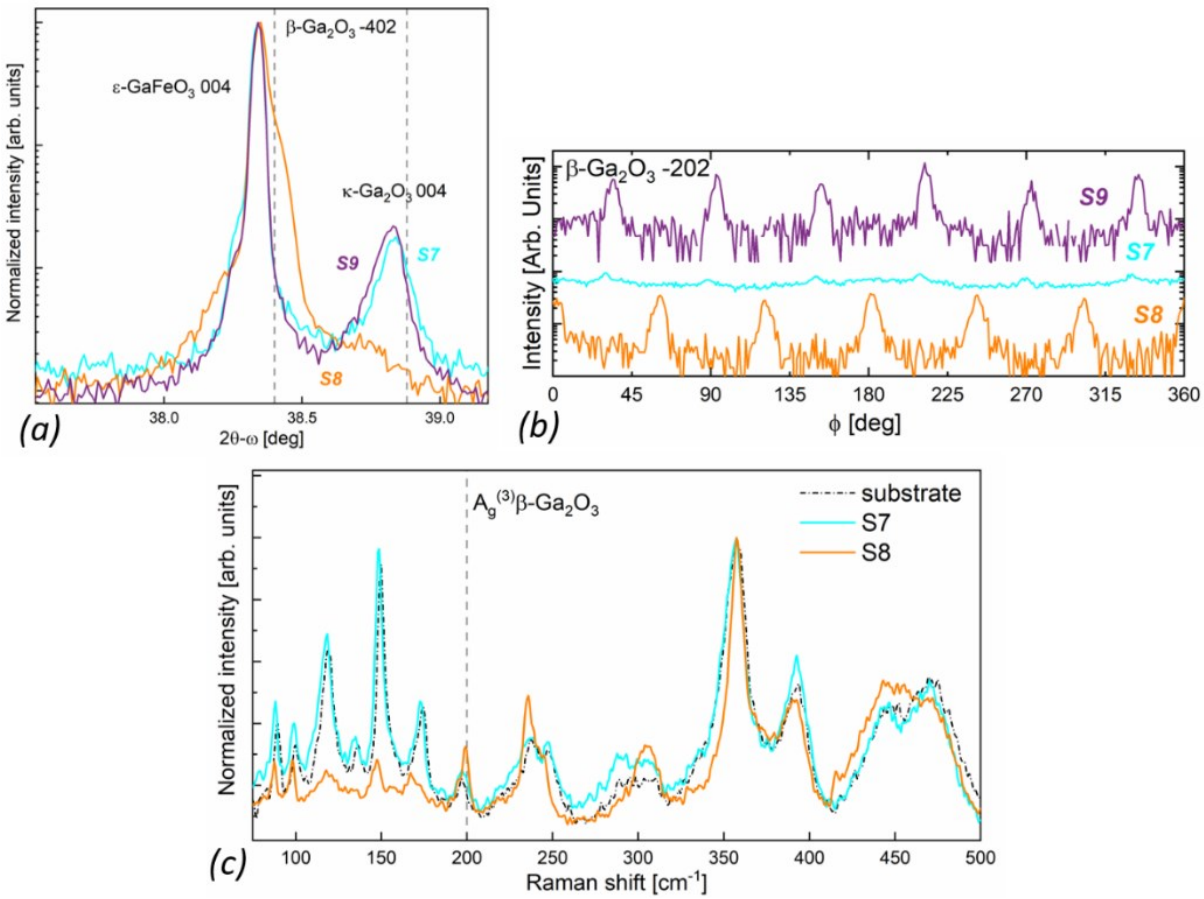

Figure 5.12 (a) The symmetric *2θ-ω* scans for the samples S7-9 deposited with different metal/oxygen fluxes. The spectra are normalized on the (004) substrate peak. The vertical grey dashed line indicates the expected position for (-402) and (004) reflection of β- and κ-Ga_2O_3, respectively. (b) The asymmetric *φ* scans for the (-202) β-Ga_2O_3 reflection, vertically shifted for better comparison. S7 *φ* scan was acquired with a different diffractometer slit configuration resulting in lower intensity of the signal. (c) Raman surface spectra of sample S7 and S8 together with the bare substrate spectrum (black dot-dashed line). The vertical grey dashed line indicates the expected position of the most intense $A_g^{(3)}$ β-Ga_2O_3 mode.[102] The Raman spectra were plotted after background and air spectrum subtraction (see section 4.1.2.5 for better explanation on Raman data elaboration) and they were normalized on the substrate most intense peak (Raman shift = 357 cm^{-1}).

The HRTEM plane-view image [Figure 5.13 (a)] of sample S1 confirmed for the κ-Ga_2O_3 epilayer the presence of rotational domains with an average equivalent diameter ≈ 25 nm, in line with the one reported for UID MOVPE κ-layers on c-plane sapphire.[20,58] From the cross-section HRTEM image [Figure 5.13 (b)], the presence of four different layers on top of the ε/κ-$GaFeO_3$ single-crystal substrate is highlighted. From the top layer surface: (i) the κ-Ga_2O_3 layer with rotational domains; (ii) a ≈ 50 nm thick (-201) β-Ga_2O_3 layer with rotational domains and an irregular interface with (i); (iii) a ≈ 10 nm thick ε/κ-$GaFeO_3$ layer with rotational domains and flat/regular interface with (ii); and (iv) a ≈ 50 nm thick γ-$GaFeO_3$ single-crystal layer with flat/regular interface with (iii) and the single crystalline ε-$GaFeO_3$ substrate beneath it. If layer (i) and (ii) were expected from previous

experimental data on S1, the presence of the additional (iii) and (iv) layer was unforeseen. From the elemental profile #1 [Figure 5.13 (e)], the steady profile of Fe in the layer (iv) of γ-$GaFeO_3$ in contrast to its depletion in the (iii) ε/κ-$GaFeO_3$ layer suggests that the In-mediated MEXCAT Ga_2O_3 growth might have started on top of layer (iv). Unfortunately, the elemental profile of In (used as catalyst in the growth of sample S1) does not reveal accumulation [Figure 5.13 (f)] and is therefore not helpful to corroborate such hypothesis. The FFT of γ-$GaFeO_3$ [Figure 5.13 (c)] reveals a cubic unit cell with parameter $a \approx 8.2 - 8.37$ Å, consistent with the information collected through XRD on the bare ε-$GaFeO_3$ substrates (see section 5.2.1). Given these insights, it is reasonable to assume that such γ-phase is prone to form in the ε-$GaFeO_3$ substrates both in the bulk (during single crystal growth), as well as on their surface. The formation of the γ-$GaFeO_3$ layer on the substrate surface is particularly relevant for the current study, since its presence could hinder the desired epitaxial match between ε-$GaFeO_3$ and κ-Ga_2O_3. Indeed, in such case it would not be surprising to end up with a κ-Ga_2O_3 domain structure, even though the presence of the additional intermediate layers (iii) ε/κ-$GaFeO_3$ and (ii) β-Ga_2O_3 remains puzzling. Regarding layer (iv), *i.e.,* γ-$GaFeO_3$ layer, it was present neither on top of the as received nor treated ε-$GaFeO_3$ substrate surface (see cross-sectional TEM in Figure 5.7); hence, its formation was tentatively related to the exposure to the O-plasma in the MBE chamber immediately before layer nucleation.

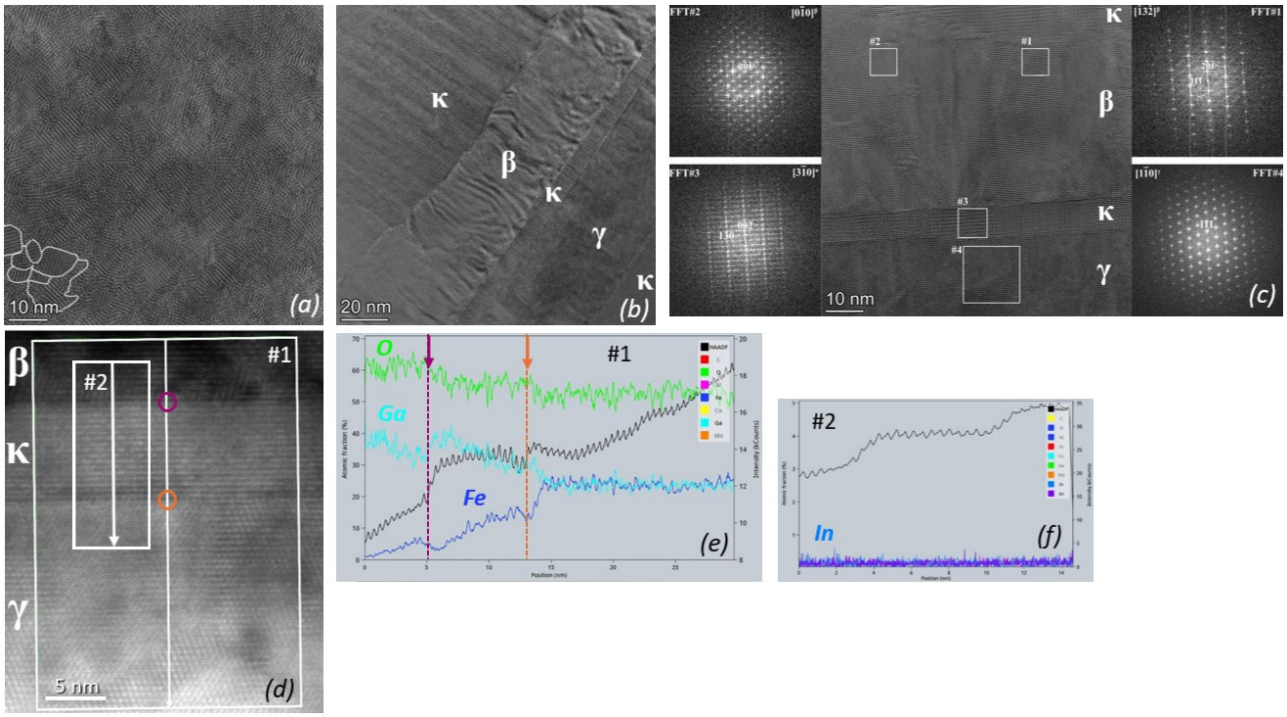

Figure 5.13 TEM investigation of sample S1. (a) HRTEM plan-view image with highlighted the cross section borders of the elongated rotational domains. (b) HRTEM of the cross section with all the epilayers labelled according to their unit cell symmetry, *i.e,* κ-orthorhombic, β-monoclinic, γ-cubic. The sample was tilted by 30° around the axes normal to the surface. (c) HRTEM image of the cross section with the corresponding FFTs showing the epitaxial relationships. β

layer is strongly textured showing two main orientations (FFT #1 and #2). (d) HAADF image from the β-layer down to the γ-$GaFeO_3$ substrate and in (e) and (f) the elemental profiles of O, Ga, Fe and In, relative to scan #1 and #2 respectively.

5.2.2.3 (iii) δ-SnO_x buffer layer followed by In-MEXCAT

The use of a thin δ-SnO_x buffer layer in MBE of Ga_2O_3 was proved to allow the stabilization of the metastable κ-polymorph without the need of continuous Sn-catalyst supply and resulting in sharper interfaces with the underlying substrate with respect to the In-mediated MEXCAT.[127] Moreover, if such approach is followed by a continuous purchase of the In-catalyst during the following growth of κ-Ga_2O_3, this allows to maintain the epilayer smoothness (with In being suggested to be catalyst as well as surfactant).[126] Hence, also this approach was attempted, combining both Sn- and In-mediated MEXCAT following the approach presented in ref.[[127]] as follows: deposition of the δ-SnO_x buffer layer followed by nucleation of Ga_2O_3 with conventional MBE at T_g *nl* = 615°C and then In-mediated MEXCAT growth at higher T_g = 660°C. Table 5.4 reports the growth details, for two samples, S10 and S11, deposited as just described. S10 was grown with "standard" fluxes and the growth parameters used for sample S7 (see Table 5.3); S11 was grown at lower fluxes (as sample S8 – see Table 5.3).

Sample ID	T_g δ-SnOx [°C]	T_g *nl* [°C]	T_g [°C]	P_{RF} [W]	BEP_{Ga} [10^{-7} mbar]	BEP_{In} [10^{-7} mbar]	O_{flux} [sccm]	*G.R.* [nm/min]
S10	615	615	660	175	5.32	1.6	0.9	5
S11	615	615	660	250	1.88	0.5	0.4	4

Table 5.4 Growth parameters, metals and oxygen fluxes for samples grown following approach (iii): deposition of δ-SnO_x buffer layer followed by In-MEXCAT growth.

The deposition of the δ-SnO_x buffer layer was performed thanks to a SnO effusion cell present in the MBE system. The desired SnO flux, *i.e.,* $BEP_{SnO} \approx 2x10^{-8}\ mbar$, was too low to be detected with the BEP ion gauge due to high background pressure in the growth chamber but, the relative cell temperature, *i.e.,* $T_{SnO} = 730°C$, was extracted from standard calibration procedure. The deposition was performed for 180 s, in order to have a couple of monolayer thick δ-SnO_x layer. The RHEED pattern of the substrate was monitored and, as reported in Figure 5.14 (a) and (b), a slight fading was detected, indicating the successful deposition of the buffer layer. The growth was then continued as described just above. The samples were then analysed with AFM [see Figure 5.14 (c) and (d)]: sample S10 reveals a smoother surface w.r.t. sample S7 (Figure 5.11), grown in identical conditions but without the δ-SnO_x buffer layer; while S11, grown at low fluxes, highlighted a non-homogenous surface morphology. Noteworthy, the *G.R.* recorded for S11 (≈ 4 nm/min) is higher than the one

recorded for S8 (≈ 2.5 nm/min – low fluxes regime for In-MEXCAT). This could suggest a faster nucleation induced by Sn.

The *2θ-ω* scans [Figure 5.14 (e) and (f)] reveals once again that the low fluxes regime does not allow the stabilization of κ-polymorph, while in S10 the κ-phase is successfully stabilized, even though with a Rocking curve value of 1.33° and rotational domains [see *φ* scan of the (122) κ-reflection - Figure 5.14 (f-top)]. Interestingly, the XRD φ scans for both samples of the (-401) and (-202) β-reflections [see Figure 5.14 (f)] do not reveal β-phase presence (the only sharp peaks in the (-401) scans are the substrate contribution).

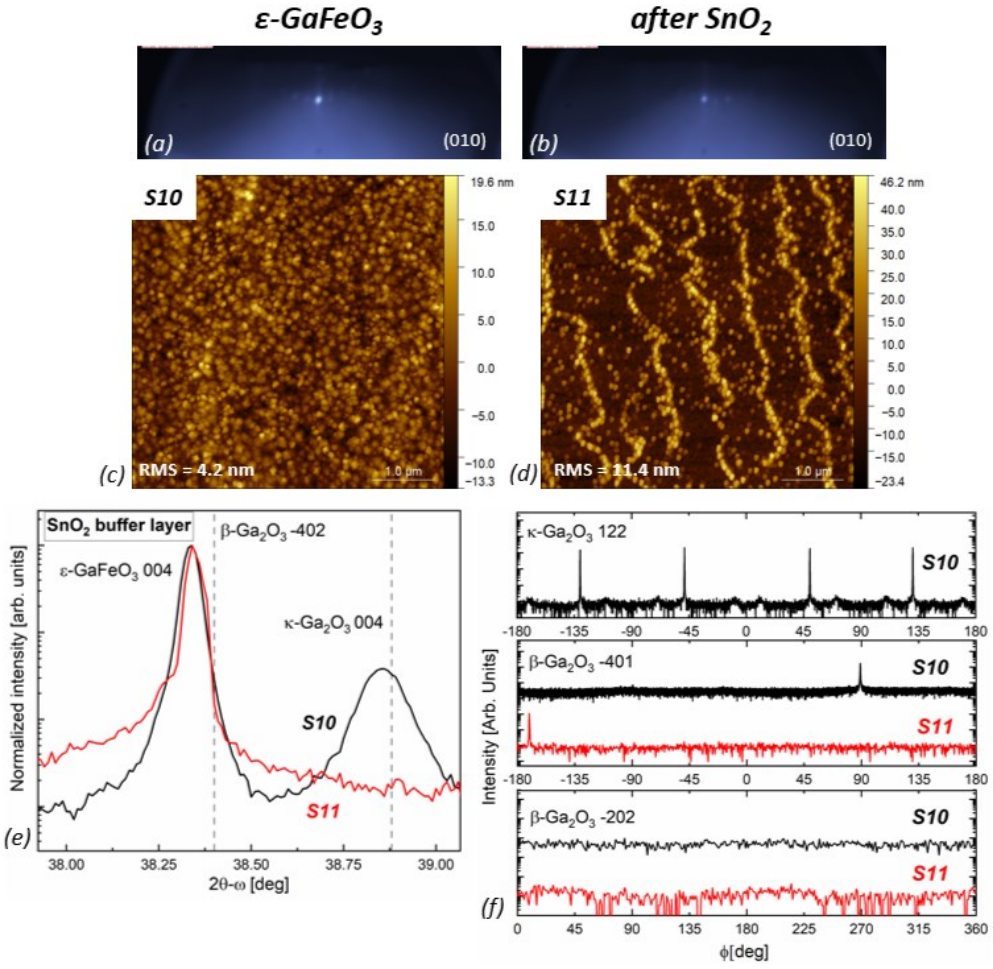

Figure 5.14 (a) and (b) RHEED image of the (010) planes of the ε-$GaFeO_3$ substrate of sample S11 before and after the deposition of the ultrathin δ-SnO_x buffer layer. (c) and (d) $5 \times 5\ \mu m^2$ AFM images of S10 and S11 surface with the relative *RMS* values. In (e) symmetric *2θ-ω* scans of S10 and S11. The (004) ε/κ-$GaFeO_3$ and κ-Ga_2O_3 peaks are labelled. The vertical dotted lines refer to the expected peak position for the (004) κ-Ga_2O_3[20] and (-402) β-Ga_2O_3[110] reflexes for no In incorporation. (f) asymmetric *φ* scans of (-202) and (-402) β- and (122) κ-Ga_2O_3, from the bottom to the top.

The sample S10 was then observed at the TEM (see Figure 5.15). From the plan-view HRTEM image [Figure 5.15 (a)] the rotational domains presence in the κ-Ga_2O_3 deposited layer is confirmed

with a similar average size of about 25 nm as for sample S1 [Figure 5.13 (a)]. The cross-view HRTEM images [Figure 5.15 (b) and (c)], confirms the presence of a γ-$GaFeO_3$ layer on top of the ε-$GaFeO_3$ substrate surface, followed by a thin ε/κ-$GaFeO_3$ layer [see comparison with In-mediated MEXCAT S1 sample in Figure 5.13 (b)]. Also in this case, the steady Fe profile [see Figure 5.15 (e)] suggests the γ layer to be present before the deposition of Ga_2O_3, most likely as a result of the exposure to the O-plasma, as previously discussed; differently, the depleted Fe profile in the ε/κ-$GaFeO_3$ layer [see Figure 5.15 (e-f)] suggests this to be probably the initial deposited structure. The different experimental approach with the δ-SnO_x layer triggering the initial stages of MEXCAT, actually allows to clearly identify two Sn peaks at the ε/κ-$GaFeO_3$ / Ga_2O_3 and at the γ-$GaFeO_3$ / ε/κ-$GaFeO_3$ interfaces [see Figure 5.15 (e) - position #1 and #2, respectively], further corroborating the hypothesis that the deposition starts on top of the γ-$GaFeO_3$ layer. Differently from the S1 sample, the nucleation with the δ-SnO_x layer seems to result in a rather defective nucleation on top of the ε/κ-$GaFeO_3$ layer composed of γ as well as β-Ga_2O_3 grains [Figure 5.15 (b) and (c)]. Such mixed layer is rather thinner with respect to the pure (-201) β-Ga_2O_3 interlayer observed in sample S1; on top of it nucleates the κ-Ga_2O_3 with rotational domains.

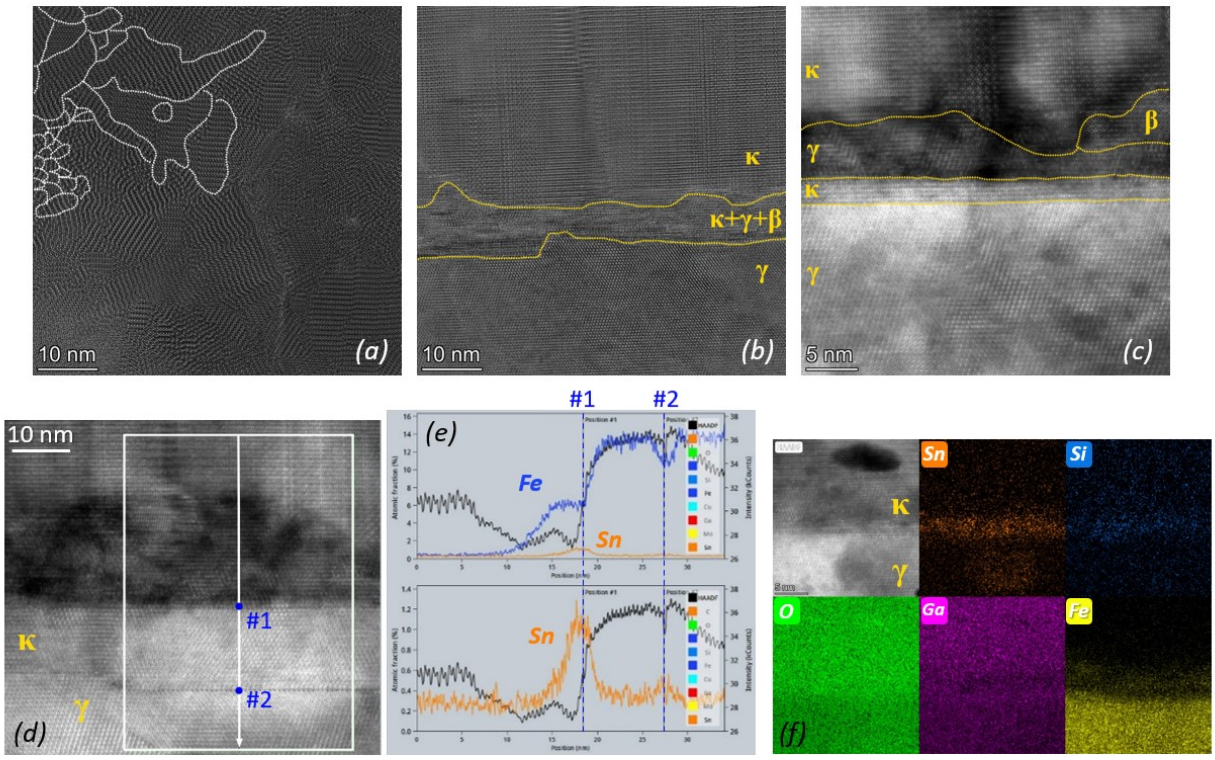

Figure 5.15 TEM investigation of sample S10. (a) HRTEM plane-view image with highlighted the cross section borders of the elongated rotational domains. (b) and (c) HRTEM cross-section images of two different spots, with all the epilayers labelled according to their unit cell symmetry, *i.e,* κ-orthorhombic, β-monoclinic, γ-cubic. (d) HAADF image from the top mixed layer (κ+β+γ)/ε/κ-domained/γ-$GaFeO_3$ IFs (#1 and #2). (e) the elemental profiles of Fe and Sn (zoom on Sn scan at the bottom) with highlighted the IFs #1 and 2#. (f) HAADF image and corresponding elemental maps of Sn, Si, O, Ga and Fe at the κ-domained/γ-$GaFeO_3$ IF.

For samples S1 (pure In-MEXCAT) and S10 (nucleation with δ-SnO_x followed by In-MEXCAT), the XRD reciprocal space maps (RSMs) are acquired to investigate the in-plane strain/relaxation of the deposited κ-Ga_2O_3 epitaxial layers. The RSMs are acquired in the asymmetric geometry configuration (2θ scans for each ω step) and are then translated into the reciprocal lattice coordinates, *i.e.,* Q_z and Q_y or Q_x, as reported in Figure 5.16. According to the described set-up measurements, the two investigated reflections, (057) and (206), provide information about the *b* and *a* in-plane parameters of both the layer and the substrate. From the substrate-epilayer peaks relative positions, the $\Delta Q_{z,y,x}$ [%] were calculated as reported in Table 5.5. The $\Delta Q_{z,x}$ [%] values extracted for the (206) reflection of both samples, are similar to the ones reported by H. Nishinaka *et al.*[129] for the κ-Ga_2O_3 single domain (the $\Delta Q_{z,x}$ [%] values extracted by the PhD candidate and reported in Table 5.5), confirming the in-plane relaxation of both S1 and S10. The RSM of the (057) reflection, as tool to investigate the in-plane *b* direction, is here reported for the first time.

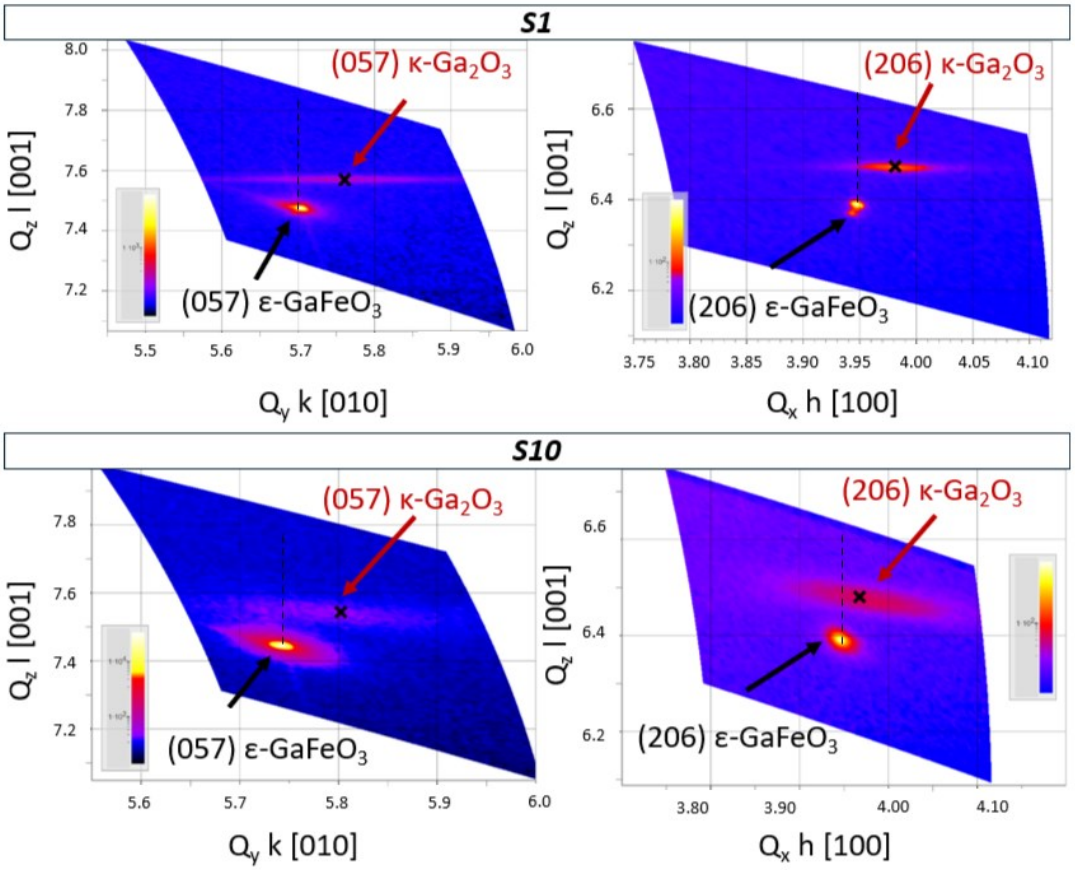

Figure 5.16 RSM of the (057) and (206) reflections of κ-Ga_2O_3/ε-$GaFeO_3$ for samples S1 (on top) and S10 (at the bottom) with the substrate and film peaks highlighted.

Sample ID	Reflection	ΔQ_z [%]	ΔQ_y [%]	ΔQ_x[%]
S1	(057)	9.6	6	
	(206)	7.8		3.7
S10	(057)	8.8	6.3	
	(206)	8.3		2.6
Single domain ref.[129]	(206)	8.1		3

Table 5.5 Values of ΔQ_z, ΔQ_y and ΔQ_x [%] extracted from the substrate-film peaks relative positions in the RSMs of the (057) and (206) reflection, as reported in Figure 5.16. The ΔQ_z, and ΔQ_x [%] extracted by the PhD candidate from the (206) RSM reported by H. Nishinaka *et al.*,[129] are reported as reference.

5.3 MEXCAT-MBE growths on (0001) α-Al_2O_3 substrates with intentional offcuts

The second strategy applied in order to suppress the κ-Ga_2O_3 rotational domains, foresees the involvement of the (0001) α-Al_2O_3 substrates with different degree of the intentional offcut, *i.e.,* 2, 6 and 8°, along the [100] direction. The substrates had the regular size of $5 \times 5\ mm^2$ that allows them to be allocated in the dedicated MBE substrate holder with 5 pockets. The co-loading of the substrates allows to highlight the effect of their offcut on the epi-layers growth while adopting the very same growth parameters; for this purpose, also a nominally oriented (0001) α-Al_2O_3 has been co-loaded. All the (0001) α-Al_2O_3 substrates were solvent cleaned in acetone and isopropanol in an ultrasonic bath prior to growth.

Several different sample set (T*X*) were grown via In-mediated MEXCAT (already described in section 5.2.2.2), varying T_g, P_{RF}, metal/oxygen fluxes and also involving the introduction of a (-201) β-Ga_2O_3 nucleation layer (*nl*) according to the growth space borders of the orthorhombic phase already highlighted in Figure 5.3. The growth details of each set of co-loaded substrates (*i.e*, 0, 2, 6 and 8°) are reported in Table 5.6. Only the T1 deposition was performed directly on top of (0001) α-Al_2O_3, while all the other set foreseen the introduction of a (-201) β-Ga_2O_3 *nl* (explanation will be provided right after).

Sample ID	*nl*	T_g [°C]	P_{RF} [W]	Fluxes regime	*G.R.* [nm/min]	Thickness [nm]
T1	×	640	150	standard	6.6	400
T2	β-Ga_2O_3	650	150	standard	7	2000
T3	β-Ga_2O_3	640	150	low	2.7	240
T4	β-Ga_2O_3	660	150	low	2	700
T5	β-Ga_2O_3	650	140	low	1.5	900

Table 5.6 Sum-up of the growth parameters applied for the sample series (T*X*) grown of (0001) α-Al_2O_3 tilted substrates. Flux regime indicated as "standard" correspond to: $BEP_{Ga} \approx 5 \times 10^{-7} mbar, BEP_{In} \approx 1.6 \times 10^{-7} mbar, O_{flux} = 1\ sccm$, flux regime indicated as "low" correspond to: $BEP_{Ga} \approx 1.6 \times 10^{-7} mbar, BEP_{In} \approx 5.7 \times 10^{-8} mbar, O_{flux} = 0.33\ sccm$.

For the direct growth with In-MEXCAT on top of the bare sapphire (sample set T1) the κ-Ga_2O_3 was obtained and a strong effect of the absolute offcut of the substrates over the layer morphology [AFM in Figure 5.17 (a - d)] and crystalline quality [FWHM of the ω-scans of the (004) κ-Ga_2O_3 reflection vs. offcut angle in Figure 5.17 (e)] was detected. In order to investigate the rotational domains presence of κ-Ga_2O_3, the pole figure of the (122) reflection must be acquired, *i.e.,* consecutive φ scans at fixed 2θ =33°, varying χ angle from the nominal value of the (122) reflection, *i.e.,* χ = 54°, in a range of $\Delta\chi$ = 54° ± (substrate offcut angle)(see section 3.3.2 for additional details on pole figures acquisition). This measurement set-up allows for the investigation of the epi-layer grown even in presence of a miscut angles of the substrate, as reported in Figure 5.17 (f) and (e), for the 0° (centrosymmetric pole figure) and 8° (asymmetric pole figure) offcut. Nevertheless, the three 120° rotated domains [*i.e.,* 12 diffraction peaks for the (122) reflection] are still present for all the T1 layers.

The study at this point was addressed at improving the results by further tuning the growth parameters. Unluckily, the results obtained for the T1 set were not reproducible due to nucleation problems on the bare sapphire surface. The only experimental approach that allowed to overcome this issue was the initial deposition of a (-201) β-Ga_2O_3 nucleation layer (sample set T2 to T5). Figure 5.18 reports the AFM and XRD analysis of set T2, highlighting a similar trend of the miscut angles on morphology and layer quality reported for T1. More in detail, the different nucleation surface for κ-Ga_2O_3 results in the case of the 0° offcut in a well-defined hexagonal morphology [AFM of sample T2 in Figure 5.18 (a)]; such sample morphology is well known for κ-Ga_2O_3 epilayers characterized by rotational domains,[128,154] as confirmed by the XRD analysis [not shown]. The presence of the offcut though shows an overall better crystallinity with respect to the nominally oriented substrate, again with surface features suggesting the probable effect on nucleation of the miscut-related step-terrace structure [AFM of sample set T2 in Figure 5.18 (b - d)]. Also samples in set T2 were characterized by the presence of the rotational domains [Figure 5.18 (f,g)]. Interestingly, both the T1 and T2 growths, suggest that the lowest tested offcut of 2° results in the best crystalline quality despite the initial surface of nucleation, with the layer deposited on the β nucleation showing the relative best Rocking curve of around 0.3° [Figure 5.17 (e) and Figure 5.18 (e)].

Also on the miscut substrates, the growth in the low fluxes regimes was attempted (set T3-T5). As already reported for the growths on nominally oriented sapphire[125] and ε-$GaFeO_3$ substrates (section 5.2.2.2.3) the low fluxes regime favours the β-Ga_2O_3 stabilization over κ also for miscut substrates. The AFM images of samples set T5 [see Figure 5.19 (a) – (c)] reveal a morphology resembling the one reported in section 5.2.2.1, Figure 5.8 (a), for conventional MBE growth on ε-$GaFeO_3$. For the highest 8° offcut though [Figure 5.19 (d)], the morphology seems to recall the step-

terrace one of the miscut substrate. The relative intensity of the (-402) and (004) reflection of β- and κ-phase in the *2θ-ω* scans [Figure 5.19 (e)], confirmed preferential stabilization of β but also highlighted the offcut effect on the phase selection. In particular, 6° and 8° offcut promotes only β-phase while 0° and 2° promotes a mixed layer stabilization. Nevertheless, also in the case of pure β-Ga_2O_3 layers, the suppression of its twin domains is not achieved, differently from the experimental findings of Rafique *et al.*[155] by low pressure chemical vapor deposition. In this regard though it is important to highlight that in this work the focus was not addressed to an optimization of the deposition parameters for pure β-Ga_2O_3 heteroepitaxy.

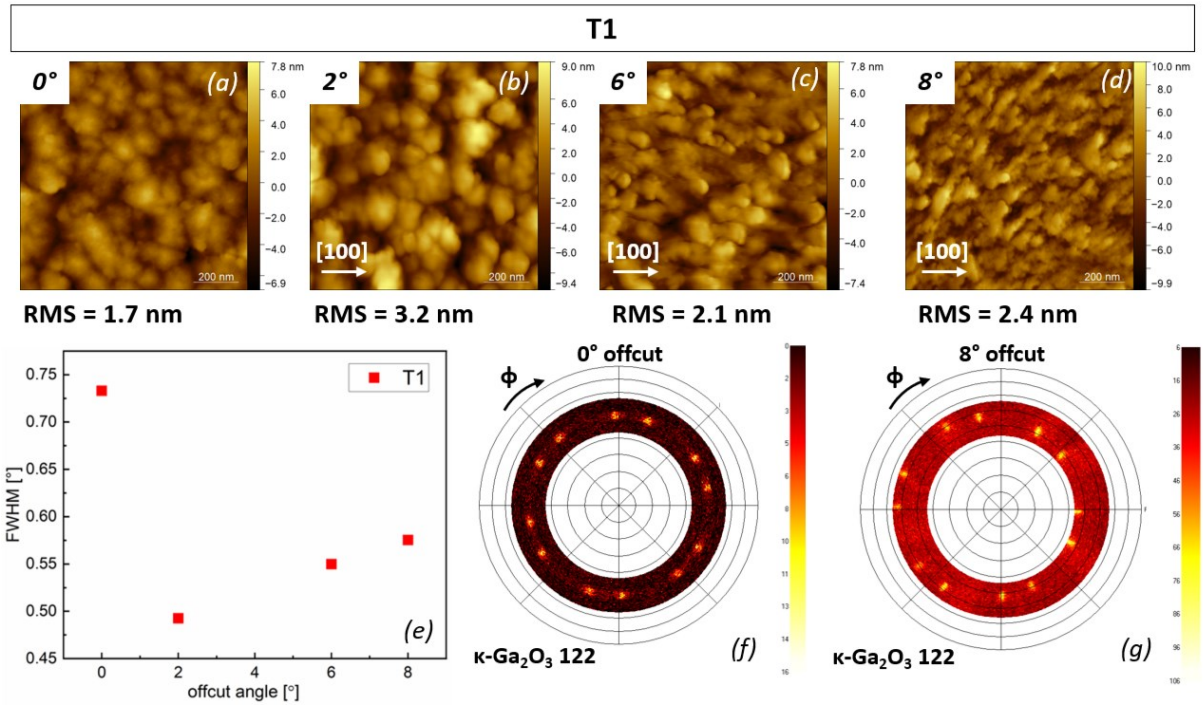

Figure 5.17 (a) – (d) $1 \times 1\ \mu m^2$ AFM images of set T1, grown on (0001) α-Al_2O_3 substrates with 0, 2, 6, and 8° offcut along [100] direction. The *RSM* values and offcut direction are reported on each image. (e) FWHM [°] vs. offcut angle [°] trend. (f) and (g), XRD pole figure of the (122) κ-Ga_2O_3 reflection for sample grown on 0° and 8° substrate offcut, respectively.

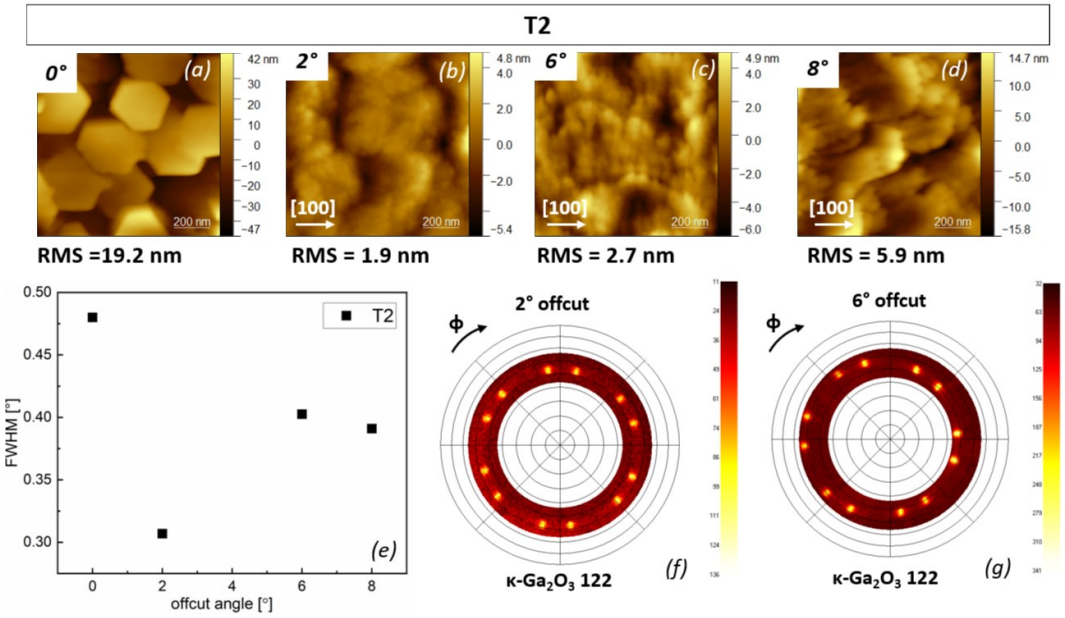

Figure 5.18 (a) – (d) $1 \times 1\mu m^2$ AFM images of set T2, grown on (-201) β-Ga_2O_3 nucleation layer on top of (0001) α-Al_2O_3 substrates with 0, 2, 6, and 8° offcut along [100] direction. The *RSM* values and offcut direction are reported on each image. (e) FWHM [°] vs. offcut angle [°] trend. (f) and (g), XRD pole figure of the (122) κ-Ga_2O_3 reflection for sample grown on 2° and 6° substrate offcut, respectively.

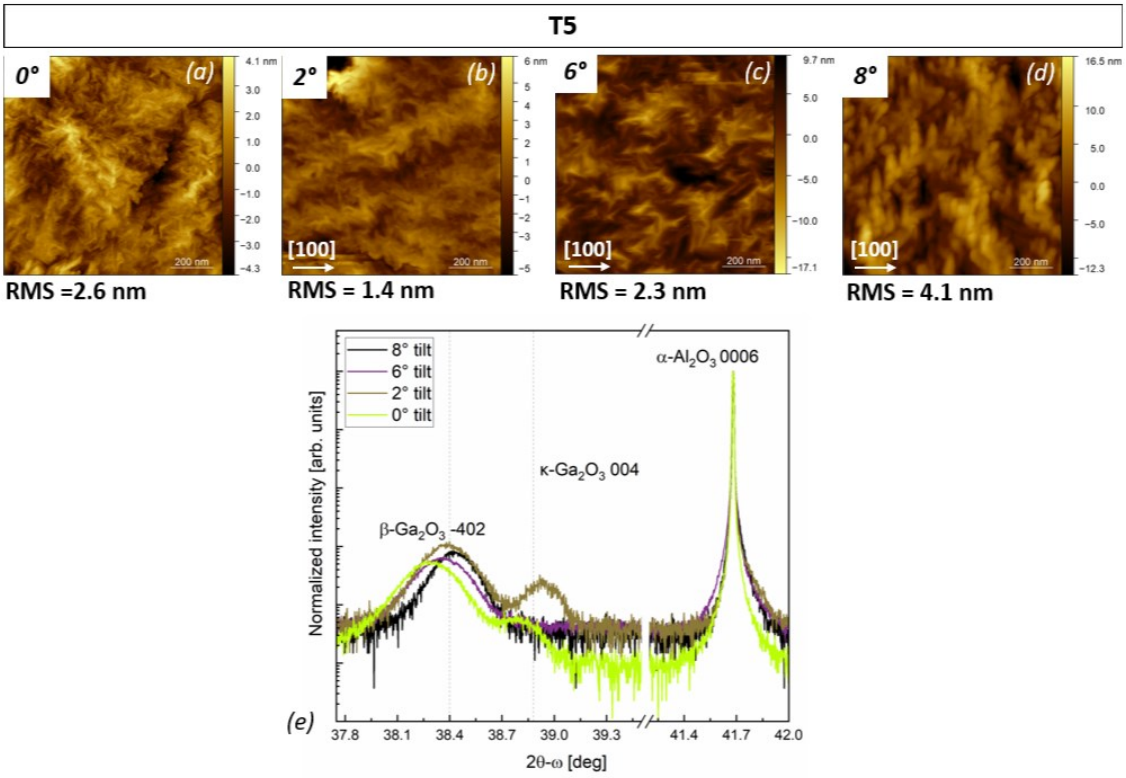

Figure 5.19 (a) – (d) $1 \times 1\mu m^2$ AFM images of set T5, grown in the low fluxes regime on (-201) β-Ga_2O_3 nucleation layer on top of (0001) α-Al_2O_3 substrates with 0, 2, 6, and 8° offcut along [100] direction. The *RSM* values and offcut direction are reported on each image. (e) *2θ-ω* scans of the four different offcut degree with labelling of the (-402) β-, (004) κ-Ga_2O_3 and (0006) α-Al_2O_3 peaks.

5.4 Conclusions and outlooks

The work described above, constitutes a comprehensive investigation on two different strategies to tackle the suppression of rotational domains in κ-Ga_2O_3 heteroepitaxy through MBE: the use of an epitaxially matched ε-$GaFeO_3$ substrate (section 5.2) and of a well-defined offcut on c-plane sapphire substrates (section 5.3). The data collected from the MBE growths performed by the PhD candidate in the framework of the periods spent at PDI (Berlin), confirmed that to stabilize the metastable κ-phase through MBE, the catalyst presence is mandatory even when using an epitaxially-matched substrate and that lower metal fluxes / growth rates are detrimental since they tend to stabilize the thermodynamically stable β-Ga_2O_3 polymorph. Nevertheless, the two different MEXCAT approaches, *i.e.,* In-mediated MEXCAT and δ-SnO_x assisted In-MEXCAT, as well as the two different substrates typology involved, *i.e.,* ε-$GaFeO_3$ and intentionally offcut (0001) α-Al_2O_3 did not succeed in the suppression of rotational domains in κ-Ga_2O_3 heteroepitaxy.

As for the MBE growths on the ε-$GaFeO_3$, the thorough experimental investigation (involving AFM, XRD, EBSD, Raman, TEM) allowed to clarify that the probable cause lays on the formation of an intermediate γ-$GaFeO_3$ interlayer on the substrate surface when exposed to the O-plasma environment in the MBE chamber. Therefore, a future step for this work foresees the involvement of a different epitaxial technique: the MOVPE, more similar to the mist-CVD that has been already proven successful for the obtainment of a single domain κ-Ga_2O_3 layer on ε-$GaFeO_3$. As already mentioned in section 3.1.1, this is not a ultra-high vacuum deposition technique, and does not require the oxygen activation via plasma nor the catalyst presence to promote the κ-Ga_2O_3 polymorph stabilization; these aspects could overcome the issues encountered in the MBE growths.

In the approach with intentionally offcut (0001) α-Al_2O_3 substrates, the effect of a well-defined step-terrace structure has been found to affect both the morphology as well as the crystalline quality of the κ-Ga_2O_3 layers. It has still to be ruled out the possible effect of the metal catalyst necessary in the case of MBE growth for the orthorhombic polymorph. Different growth techniques could allow for longer diffusion lengths of the adsorbed species during growth, potentially allowing to unlock a step-flow growth method necessary for domain suppression.

The new MOVPE reactor installed in March 2023 at CNR-IMEM in Parma is currently reaching the full optimization of the growth parameters for κ-Ga_2O_3. Thanks to the recent realization of a substrate holder with 5×5 and $10 \times 10\ mm^2$ dedicated pockets, the ε-$GaFeO_3$ and offcut sapphire substrates can be accommodated. The PhD candidate plan to sum-up in a manuscript the comparison between the here-reported results for MBE and future results from MOVPE.

6 Point defects in κ-Ga_2O_3

This chapter focuses on the investigation of shallow and deep level defects in κ-Ga_2O_3 thin films grown by two different epitaxial techniques: MOVPE and MBE. The chapter content is mostly based on a recent publication in which the candidate was actively involved.[174] After a brief overview of the state-of-the-art understanding of point defects in κ-Ga_2O_3, section 6.1 outlines the study of MOVPE and MBE κ-Ga_2O_3 UVC photodetectors (PDs) performances subjected to annealing treatments in different atmospheres (O_2 and H_2). The findings were integrated with additional experimental - *i.e.,* XPS, SIMS, PL and PLE (section 6.2) - and theoretical (section 6.3) investigations. Such thorough work aims to provide a better understanding of different point defects in κ-Ga_2O_3 and their direct effect on its functional properties (*e.g.*, PD performances).

As described in section 2.3, κ-Ga_2O_3, is possessing a wide band gap $E_g \approx 4.9 - 5.0\ eV$, that makes it a valid candidate for, among other application, solar blind UVC photodetectors. Indeed, in 2018 M. Pavesi *et al.*,[130] reported the first metal-semiconductor-metal (MSM) UVC-PD and, in few years the κ-Ga_2O_3 based PDs reported competitive performances w.r.t. the most investigated β-Ga_2O_3 based ones.[123,175,176] The one of the PD, is just an example of the different possible application fields of κ-Ga_2O_3; in fact, its large intrinsic polarization and suggested ferroelectricity drives most of the hype behind this polymorph, even though the presence of large amounts of structural defects are probably not compatible with high power device structures, However, a detailed understanding of the nature and role of point defects in the κ-polymorph is still lacking, which remains a significant barrier to its possible broader device application. In this regard, the analysis of the photoresponse (see section 3.3.3.2) at different wavelengths of κ-Ga_2O_3 PDs, combined with different experimental techniques, could be used to gain insights into the shallow and deep level defects. For instance, M. Pavesi *et al.*,[130] coupled the PDs device characterization with a cathodoluminescence (CL) and absorption study. The CL spectrum of κ-Ga_2O_3 appears as a broad blue emission, peaked at ≈ 2.6 eV (477 nm), tentatively fitted with three convoluted bands, *i.e.,* 2.3 eV (530 nm), 2.6 eV (464 nm) and 2.75 eV (450 nm), and assigned to native deep levels. No signal for the band-to-band emission is detected, features already reported for β and ascribed to self-trapped holes (STHs).[177] Moreover, a deep donor level located at about 0.7 eV from the CB was detected from absorption measurements (onset of the photocurrent and absorption just below the band-gap). Angular resolved photoelectron spectroscopy (ARPES)[178] study confirmed this level (similar feature was reported also for β-Ga_2O_3).[179] In 2021 Montedoro *et al.*,[180] investigated the luminescence of MOVPE κ-Ga_2O_3 layers grown in different atmospheres, *i.e.,* different gas carriers (H_2, He and N_2). All the recorded spectra displayed similar characteristics, consistent with the one reported by M. Pavesi *et al.*,[130] regardless of the carrier gas type, suggesting

the emissions to be related to native defects, typical of the MOVPE deposition techniques. In analogy with the β-polymorph, the source of these emissions was ascribed to Ga vacancies (V_{Ga})/related complexes. However, a remarkable difference in the luminescence intensity was recorded, with the H_2-grown sample reporting the highest. This suggested an effect of the growth-atmosphere over the defects density. Furthermore, the H_2 grown κ-Ga_2O_3 layers were characterized by a lower resistivity w.r.t. to the ones grown with He carrier gas ($\rho_{H_2} \approx 10^7 \Omega cm$; $\rho_{He} \approx 10^{13} \Omega cm$). It sounded reasonable to assume that an H-rich growth environment was promoting a higher density of shallow levels. The same year, Li *et al.*,[181] observed the beneficial effect of an O_2 annealing on the MOVPE κ-Ga_2O_3 PD performances, *i.e.,* dark current (I_{dark}) reduction, rejection ration (R_R) and charge/discharge speed increase. The observed results were ascribed to the filling of oxygen vacancies (V_O), *i.e,* deep-level defects acting as recombination centers for electron-hole pairs. In 2022, A. Parisini *et al.*,[182] combining several experimental techniques, shed lights on the deep and shallow electronic state in MOVPE grown κ-Ga_2O_3 layers, suggesting V_{Ga} and their complexes as deep acceptors, V_O as deep donors, and H_i as shallow donors. Nevertheless, a clear assignment of the observed levels of defects to specific point defects/complexes was still missing.

In the work here discussed, an important contribution to understand point defects in the κ-Ga_2O_3 material system is provided combining two different epitaxial growth techniques (MOVPE, MBE), annealing treatments in different background atmospheres (H_2, O_2), different characterization techniques (*e.g.*, photodetector characterization, XRD, PL/PLE, XPS, SIMS), as well as ab-initio theoretical calculations.

The PDs characterization and data elaboration reported in section 6.1 were performed by the candidate with the guidance of M. Pavesi, A. Parisini, S. Vantaggio, and P. Mazzolini (UniPr). The MOVPE κ-Ga_2O_3 samples were grown by L. Seravalli, M. Bosi and P. Mazzolini (IMEM). The MBE κ-Ga_2O_3 samples were grown by A. Ardenghi (PDI) that also performed XRD (XRD characterization was also performed at UniPr by F. Mezzadri and P. Mazzolini) and XPS measurements, providing data analysis/interpretation. ToF-SIMS investigation was done by A. Falkenstein and J. Kler (RWTH). The PL and PLE analysis were conducted by B. M. Janzen and M. R. Wagner (TU-PDI). The theoretical contribution was provided by J. B. Varley (Lawrence Livermore National Laboratory).

6.1 MOVPE and MBE κ-Ga_2O_3 photodetectors (PDs)

6.1.1 Samples details and experimental design

Two categories of unintentionally doped (UID) κ-Ga_2O_3 epitaxial layers are studied: MOVPE and MBE grown on (0001) α-Al_2O_3. The MOVPE layers were grown in standard conditions (see section 3.1.1) with He as carrier gas (T_g = 650°C). The MBE layers were deposited with O-plasma

assisted In-mediated MEXCAT on top of a (-201) β-Ga_2O_3 nucleation layer (*nl*) (see section 5.1.1). The thickness of all κ-Ga_2O_3 layers was in the 500 – 700 nm range. The layers possess comparable crystal quality, no matter the epitaxial deposition techniques involved, as XRD investigation highlights [see Figure 6.1 (a)]. Focusing on the XRD *2θ-ω* scan of the MBE layer, it is possible to highlight (i) a shift of the (004) κ-Ga_2O_3 peak and (ii) an additional lower intensity reflection at its left side; as of (i) this is due to partial In incorporation from MEXCAT technique, while (ii) is related to the (-402) reflection of the (-201)-oriented β-*nl* (see for both previous discussion in section 5.1.1). The (i) presence of In, assessed to be below 1 cat. % by calibrated SIMS (not shown here, see ref.[[174]]), does not significantly impact the layer properties (*i.e.*, isovalent to substituting Ga and negligible bandgap variation) and will therefore not affect the data interpretation within this framework. As expected, both the MOVPE and MBE κ-layers are characterized by three in-plane rotational domains [*φ*-scans of the (122) reflection reported in Figure 6.1 (d) and (e)]. According to P. Mazzolini *et al.*,[58] (see section 4.1.2), the similar rocking curve recorded for the two layers [≈ 0.48°, Figure 6.1 (b)] qualitatively suggests a similar mean rotational domain size distribution. Furthermore, all the MBE and MOVPE layers where studied with ToF-SIMS detecting a Si concentration on the edge of the detection limit ($\approx 2 \times 10^{17} cm^{-3}$). On the other side, impurities quantification, e.g., H/C, was not allowed due to residual gas absorption onto the sample in the UHV chamber during analysis.

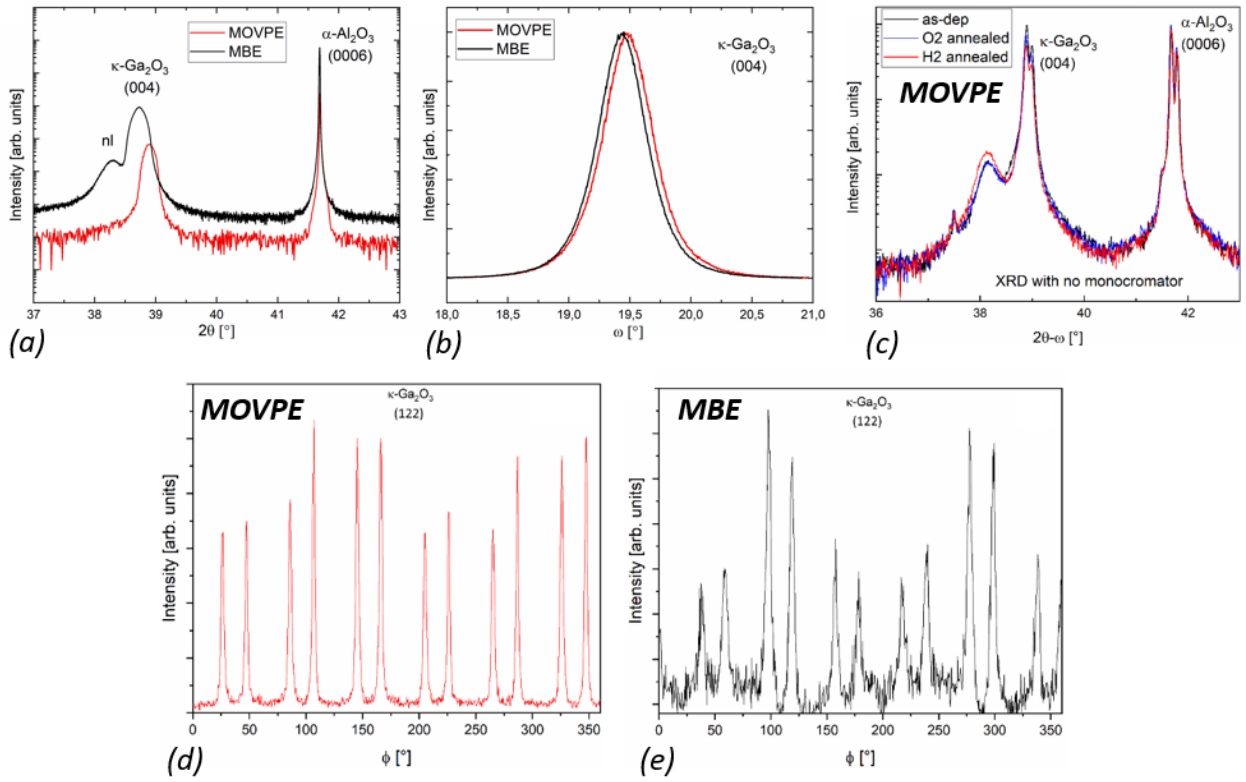

Figure 6.1 (a) and (b) symmetric out-of-plane *2θ-ω* and (b) *ω* XRD scans of the κ-Ga_2O_3 as deposited by MOVPE and MBE (red and black curves, respectively) on c-plane sapphire. For the MBE layer, "*nl*" stands for a 20 nm thick (-201)-

oriented epitaxial β-Ga_2O_3 nucleation layer [(-402) reflection]. Measurements were performed with monochromatic Cu Kα1 radiation. (c) XRD *2θ-ω* scan of the MOVPE layers before and after ex-situ thermal treatments collected with non-monochromatic Cu $K\alpha_{1,2}$ incident beam. (d, e) report the *φ*-scans referred to the (122) reflection of the κ-Ga_2O_3 layers deposited by MBE and MOVPE, respectively; both layers show the presence of twelve peaks in the *φ*-scans generated by the presence of 120° in-plane rotated domains. Images readapted from ref. [174].

The MOVPE and MBE layers were sectioned into pieces of approximately 5 × 5 mm². Some of these samples underwent thermal treatment (T_{dwell} = 500°C, t_{dwell} = 2h), in atmospheres of either O_2 (using naturally abundant ^{16}O) or H_2. The annealing process was conducted in a tubular oven or in the MOVPE reactor chamber (at 1 bar or 800 mbar, respectively). XRD characterization was performed on the samples after annealing and compared to the as-deposited layer, revealing no detectable differences [Figure 6.1 (c)]. The MSM PDs were then fabricated by RT sputter-deposition of ohmic SnO_{2-x}/ITO/Au contacts through a shadow mask, according to ref. [143]. Figure 6.2 (a) shows a sketch of the contact geometry, resulting in PDs with an area (highlighted in red in the picture) of approximately $\approx 0.8\ mm^2$, whose characterization is detailed in the following section.

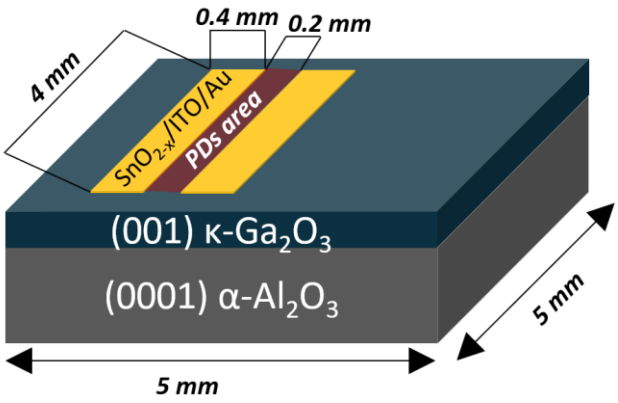

Figure 6.2 Schematic representation of the PDs fabricated for the MOVPE and MBE κ-Ga_2O_3 layers on top of (0001) α-Al_2O_3 substrates. The PDs geometry details and area are reported.

6.1.2 PDs response in dark and in illuminated conditions

The electro-optical response of the PDs was investigated with the set-up described in section 3.3.3.2. The samples were connected using copper wire bonds anchored with silver paste placed in a specially designed box to allow the metal contact connection to the Keithley source-meter (model 2400 – sensitivity 0.1 nA). The samples were first checked in dark conditions. *I-V* characteristic in dark (samples exposed neither to monochromatic nor to ambient light) are acquired in the voltage range V= [-200; +200] V. For each step of bias applied, the *I* value is recorded as the average over 30 measures, to obtain its stabilization. The linear *I-V* characteristic (see Figure 6.3) confirmed the ohmic nature of the contacts and the dark current (I_{dark}) at 200 V bias are reported in Table 6.1 for all the samples investigated.

Sample ID	Annealing	Growth	I_{dark} @ 200 V [nA]	R_R
As dep	--	MOVPE	≈ 3	1.3×10^4
O_2 ann	O_2	MOVPE	≈ 1	1.4×10^5
H_2 ann	H_2	MOVPE	≈ 100	1.7×10^3
As dep	--	MBE	≈ 0.3	2.6×10^4
O_2 ann	O_2	MBE	≈ 0.3	2.4×10^4
H_2 ann	H_2	MBE	≈ 0.9	4.1×10^4

Table 6.1 Details for the MOVPE and MBE sample set and relative indicative value of I_{dark} at 200 V bias and rejection ratio R_R values extracted from responsivity measurements.

The data collected under dark conditions reveal a significant impact of the thermal treatments on the MOVPE κ-Ga_2O_3 layers: the O_2 annealing reduces the I_{dark} by a factor of three compared to the as-deposited sample, whereas the H_2 one has the opposite effect, increasing I_{dark} by nearly one-and-a-half orders of magnitude. A qualitative similar effect in increasing the I_{dark} upon H_2 annealing is reported also in the case of the MBE layers, even though its magnitude (increase of about a factor three with respect to as deposited I_{dark}) is significantly lower with respect to the one recorded for the MOVPE samples; on the other hand, no detectable variation of the I_{dark} is recorded upon O_2 annealing for the MBE layers. Furthermore, it is noteworthy the overall lower I_{dark} values reported for the MBE samples w.r.t. the MOVPE ones.

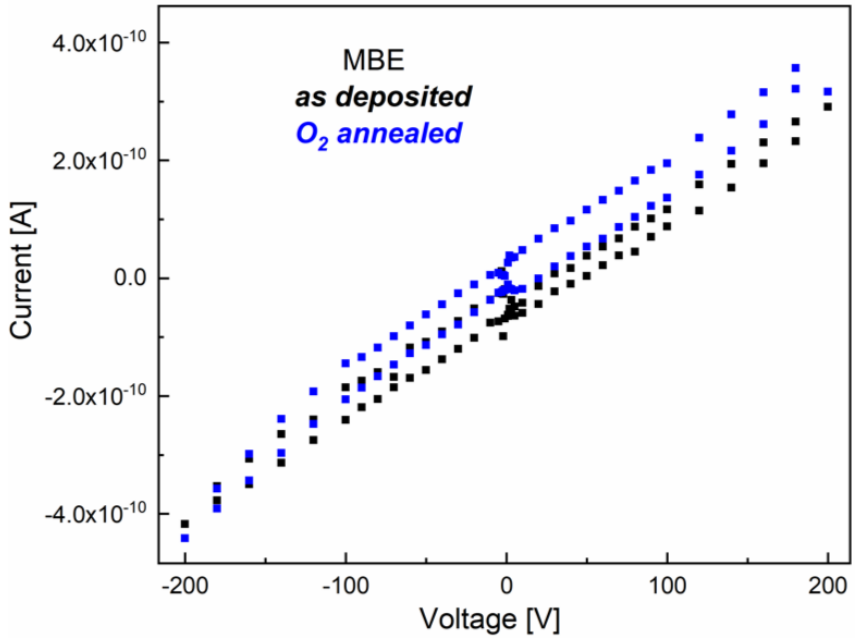

Figure 6.3 *I-V* characteristics acquired in dark for the MBE κ-Ga_2O_3 as deposited (in black) and O_2 annealed (in blue)

The PDs, with a constant 200 V bias applied between the contacts, were then illuminated with a quartz tungsten halogen (QTH) lamp; the incident wavelength was selected through a monochromator (1 nm resolution) in the range λ = [250-650] nm. The spectral photoresponse is then

normalized by the incident power of the lamp (acquired through a calibrated Newport 818 UV photodiode sensor) with respect to the PDs area. This procedure allows to obtain the responsivity curves reported in Figure 6.4 (a) and (b) for MOVPE and MBE samples respectively. The PD of the MOVPE O_2 annealed sample is showing a significant improvement of its solar-blind characteristic [see yellow area highlighted in Figure 6.4 (a)] as well as a small reduction of the response at the bandgap light, *i.e.*, $R_{\lambda_{250nm_{O2-ann}}} = 34\ A/W$ *vs.* $R_{\lambda_{250nm_{as-dep}}} = 55\ A/W$. On the other hand, the H_2 annealing on the MOVPE layer causes a shift of the overall responsivity curve to higher values, significantly worsening the PD behaviour w.r.t. the as deposited one. In order to quantitatively evaluate the performance of the PDs, the rejection ratio (R_R) value can be extracted for each responsivity curve as a conventional figure of merit to assess the effective solar-blindness of UVC PDs. R_R is not uniquely defined in literature and should be therefore considered just for an comparison among the investigated PDs; in this work the R_R is defined as: $R_R = \frac{responsivity_{\lambda=250\ nm}}{responsivity_{\lambda=500\ nm}}$. The R_R values of the MOVPE samples (see Table 6.1) confirmed the opposite effect of the O_2 and H_2 annealing on the PDs performances. For the MBE samples, the O_2 annealing is not affecting the responsivity and relative R_R, while H_2 is showing the same effect detected for MOVPE, *i.e.*, the overall responsivity up-shift and lower R_R (R_R values for MBE samples reported in Table 6.1 as well). Among all the PDs investigated, the one fabricated with the κ-Ga_2O_3 deposited by MOVPE annealed in O_2 showed the best performance.

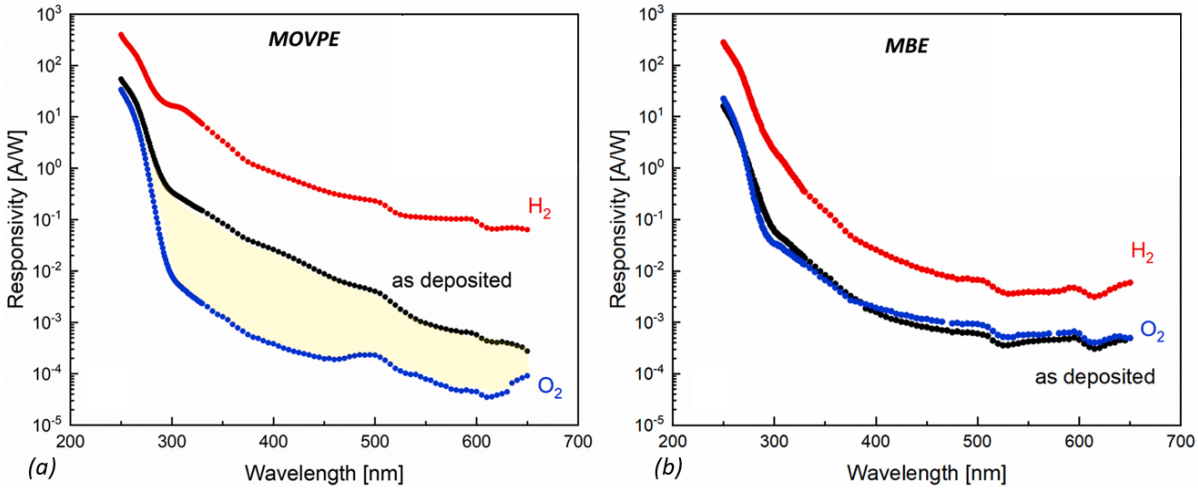

Figure 6.4 PDs responsivity of (a) MOVPE and (b) MBE κ-Ga_2O_3 layers as-deposited, O_2- and H_2-annealed (black, blue, and red curves, respectively). The yellow region in (a) highlights the drop of responsivity in the 300–600 nm range for the O_2-annealed material w.r.t. the PD fabricated with the MOVPE as-deposited material. Images readapted from ref. [174].

6.1.3 PDs response in time

The time response of the PDs was analysed by means of on-off cycles in the same measurement setup used for photoresponse acquisition. The on-off cycle involved illuminating the samples for 110 seconds at $\lambda_{on} = 250\ nm$, followed by 110 seconds in darkness, with this cycle repeated several times. During the entire process, the samples were maintained at 200 V bias and the photocurrent was recorded throughout the cycles. The resulting on-off curves are presented as photocurrent vs. time, in Figure 6.5 (a) and (b). It is here evident that, for all the samples the selected delay time does not allow the photocurrent to reach a plateaux during either the charging or discharging phases; this leads to a buildup of current, which is particularly noticeable in the dark current at the end of the cycle iterations. This process is not irreversible, as the current gradually decays back to its original I_{dark} values after a prolonged period without light exposure. This buildup effect was also highlighted in section 4.1.1 concerning the *I-V* characteristics of κ-Ga_2O_3/C:GaN/α-Al_2O_3 structures. This effect though is present at different magnitudes according to both the different deposition mean (MBE or MOVPE) as well as the thermal treatment. In particular, the buildup effect is less prominent in the O_2 annealed MOVPE, as well as in the as-deposited and O_2 annealed MBE PDs; on the contrary, the build-up effect is magnified upon H_2 annealing for both deposition means, even though its magnitude is more severe in the case of MOVPE layer.

Figure 6.5 (c) and (d) reports the 3rd cycle, normalized, for both the sets of MOVPE and MBE samples. The characteristics times, τ_{on} and τ_{off}, were extrapolated as the time required to go from 10% to 90% of the photocurrent and vice versa (refer to Table 6.2). The data indicate that the O_2-annealed samples exhibit the fastest response times for both the tested growth techniques. In contrast, the H_2-annealed samples demonstrate the slowest response, particularly during the discharging phase, *i.e.,* longest τ_{off}.

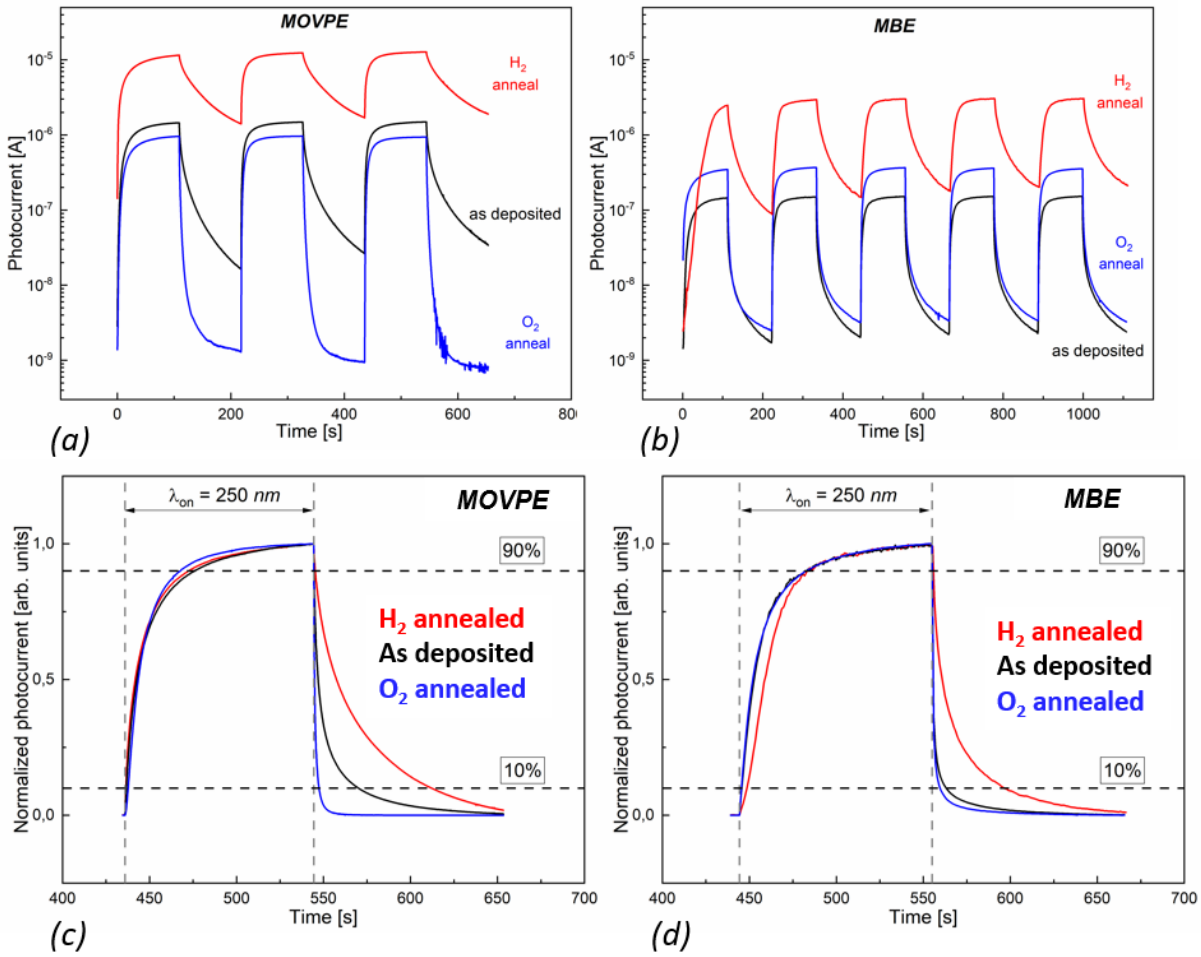

Figure 6.5 (a) and (b) non normalized full series of on-off cycles (λon = 250 nm, $t_{on\text{-}off}$ = 110s) for PDs based on MOVPE and MBE material. (c) and (d) 3rd normalized cycle for PDs fabricated with MOVPE and MBE layers respectively. Images readapted from ref. [174].

Growth	Sample ID	τ_{on} [s]	τ_{off} [s]
MOVPE	As dep	39.6	26.4
	O_2 ann	29.6	3.1
	H_2 ann	37.0	66.4
MBE	As dep	35.9	9.5
	O_2 ann	37.6	5.0
	H_2 ann	39.5	40.9

Table 6.2 Characteristic τ_{on} and τ_{off} times extracted from the 3rd on-off cycle reported in Figure 6.5 (c) and (d) for the MOVPE and MBE set of samples.

The overall results indicate that (i) the as-deposited κ-Ga_2O_3 MBE material outperforms the MOVPE as-deposited one, (ii) the O_2 annealing treatment significantly enhances the performance of the PDs, with the most pronounced improvement observed in the MOVPE-deposited samples and (iii) the H_2 treatment negatively impacts the performances by increasing I_{dark}, reducing the R_R, and slowing down the PDs discharging speed for both MOVPE and MBE material.

The insights gained from the characterization of these PDs serves as an indirect method to initiate the thorough investigation on point defects in the κ-Ga_2O_3 material system presented in the following sections.

6.2 Characterization of the κ-Ga_2O_3 layers

6.2.1 XPS

XPS investigation was performed on all the MBE and MOVPE layers. The focus was set at the O1s core level peak. The peak, reported in Figure 6.6 (a - c) for the MOVPE set of samples, can be fitted considering two different contributions: (i) the O_I at ≈ 530 eV is the footprint of the lattice oxygen and (ii) the O_{II} at higher binding energies (≈ 531-532 eV) could be assigned to either adventitious hydroxyls (-OH) groups or carbonates, both being surface adsorbates commonly found in various oxide material systems by XPS investigation.[183–185] Regarding (ii), it is noteworthy to mention that such O_{II} component has been several times attributed to oxygen vacancies V_O;[186,187] nevertheless, it is recently reported to be a misconception, since the XPS signal arising from core oxygen levels should be attributed to different coordination of oxygen atoms rather than the lack of it, as thoroughly discussed by H. Idriss.[188]

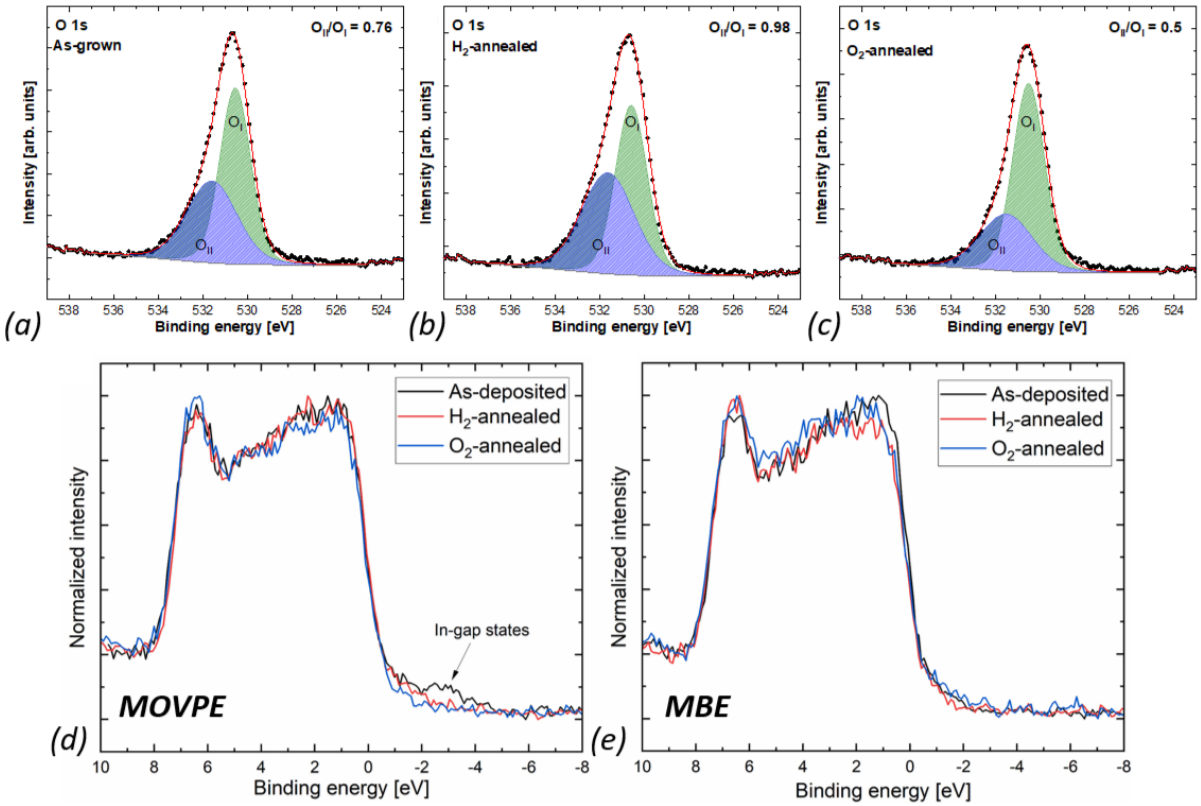

Figure 6.6 (a), (b) and (c) XPS O1s core level spectra for as-deposited, H_2- and O_2-annealed MOVPE layers, respectively. (d) and (e) XPS valence band spectra of the MOVPE and MBE samples, respectively. The 50 % intensity of the VBMs were aligned at 0 eV for direct comparison. The image is readapted from ref. [174].

Hence, considering the MOVPE κ-layers here investigated, the reported decrease of the O_{II}/O_I ratio upon O_2 annealing w.r.t. the as-deposited sample [see Figure 6.6 (a) and (c)], erroneously interpreted by Li *et al.*[181] as indication of V_O filling, is here ascribed to the reduction of (-OH) groups concentration on the sample's surface. On the other side, the O_{II}/O_I ratio increases for the sample treated in H_2 atmosphere [see Figure 6.6 (b)],it is reasonable linked to a higher concentration of (-OH) groups on the Ga_2O_3 surface. Regarding the MBE κ-layers, due to the In-MEXCAT growth mechanism, a certain segregation of the In-catalyst on the surface of the layer is expected.[126,127] Indeed, this has been confirmed and quantified by the XPS analysis of the MBE layers here investigated ($In_{as-dep} \approx 18.5\ cat.\%; In_{O_2-ann} \approx 17.1\ cat.\%; In_{H_2-ann} \approx 11.6\ cat.\%$). Due to the additional presence of In/In_2O_3 at the surface, the overall O1s shape significantly differs from the one collected for the MOVPE samples. Therefore, the interpretation of the XPS spectra collected for the MBE layers is challenging and will not be further discussed in this framework. It must be stressed out that this rather high In content highlighted by XPS is just related to the surface of the layers (*i.e.*, the very-first nanometres of the layers, related to the XPS probing depth), while the bulk In content was assessed with SIMS and XRD to be < 1cat. %.

Notably, the comparison of the valence band maximum (VBM) for the MOVPE and MBE samples [Figure 6.6 (d) and (e)] reveals the presence of in-gap states exclusively in the MOVPE as-deposited sample, suggesting that it may be related to a difference in the initial distribution of deep defects associated with the epitaxial growth technique. This observation is likely linked to the deep-levels previously identified in MOVPE κ-layers.[178,182] Based on the linear extrapolation method for VBM determination, this in-gap state location can be roughly estimated to be ≈ 2.7 eV above the VBM.

6.2.2 PLE and PL spectroscopy

The investigation of MOVPE and MBE samples using Photoluminescence Excitation (PLE) is reported in Figure 6.7 [RT (a-b) and T-dependent (c-d) PLE], where the PLE spectra are obtained integrating the entire energetic range of luminescence bands, *i.e.*, from 1.8 to 4.0 eV (see PL for all the investigated MBE and MOVPE layers in Figure 6.8). In this way it is possible to compare the absorption onset for the set of MBE and MOVPE layers. The absorption onset of the MBE layers is almost superimposed among the as deposited, O_2 and H_2 layers; differently, for the MOVPE samples a shift below the band edge (4.5 – 4.9 eV) is reported towards lower and higher energies for the H_2 and the O_2 annealed samples, respectively [Figure 6.7 (a)]. The direct comparison MOVPE/MBE [see Figure 6.7 (b)] showed the highest differences reported by the H_2 annealed samples, while very similar excitation are shown for the O_2 annealed layers. Furthermore, from PLE the suggested energy gap of κ-Ga_2O_3 is about 5 eV, which aligns well with theoretical predictions[189] and is slightly higher

than the one of the β polymorph. The *T*-dependent (*T* range 300 K-5 K) PLE spectra [Figure 6.7 (c-d)] showed invariant behaviour of the MBE as well as of the as-deposited and O_2 annealed MOVPE layer over the full temperature range. Differently, the MOVPE H_2 annealed sample reveals a pronounced excitation of PL via sub-band gap states, for excitation energies around 4.4 and 4.9 eV when $T < 100$K [see Figure 6.7 (c)].

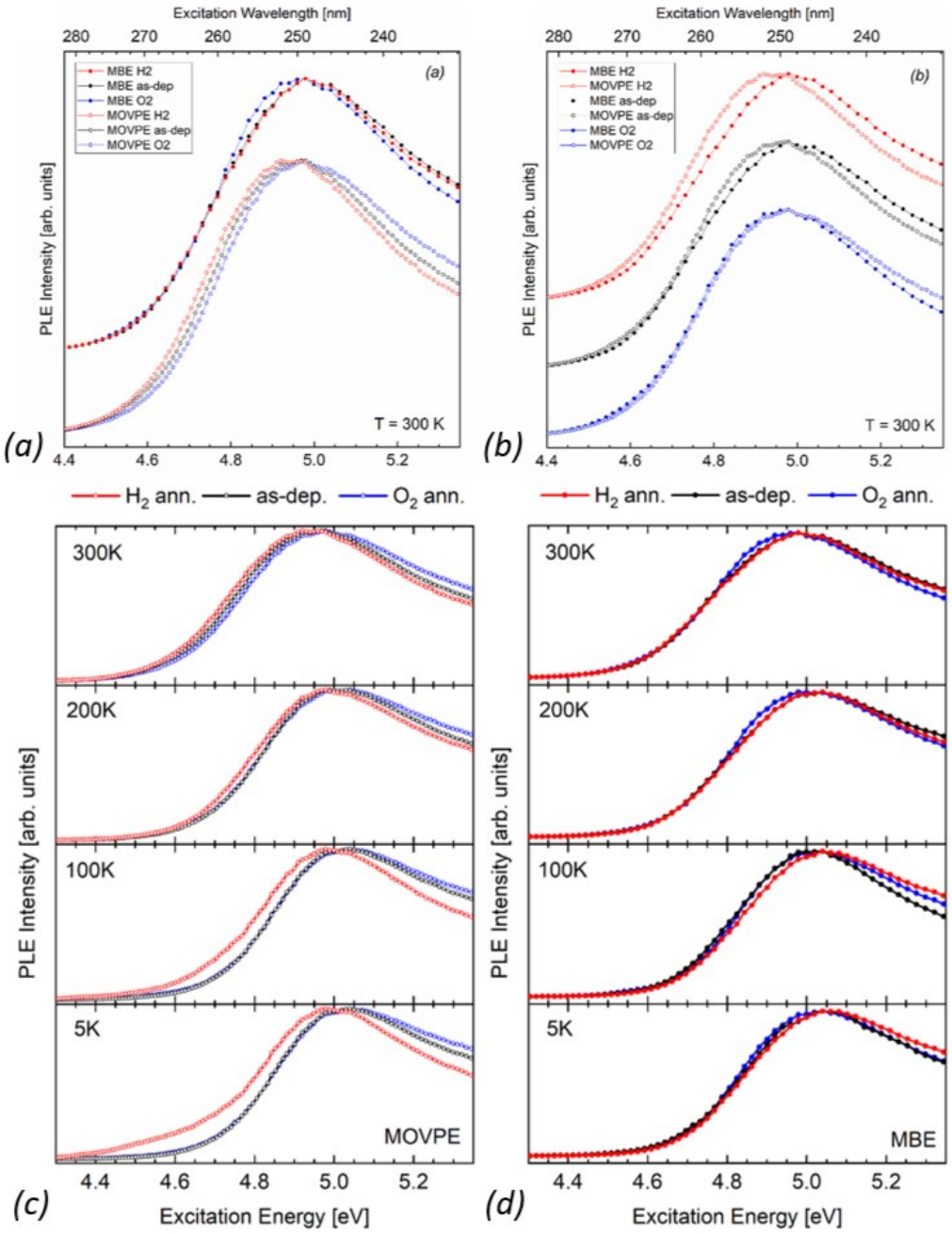

Figure 6.7 (a) and (b) RT PLE spectra (normalized) for the as grown, O_2, and H_2 annealed (black, blue, red respectively) MOVPE and MBE (empty and filled circles) κ-Ga_2O_3 thin films. The two graphs report the same data, displayed in such a way to better compare (a) the layers deposited with the same technique (MOVPE or MBE) but treated in different environment (as deposited, O_2, H_2) and (b) the same thermal treatment but different growth method. PLE spectra displayed for integrated detection energies over the entire luminescence bands (1.8 eV and 4.0 eV). (c) and

(d) temperature dependent PLE of MBE and MOVPE grown κ-Ga_2O_3 samples for detection energies between 1.8 eV to 4.0 eV, respectively. The images are readapted from ref. [174].

Figure 6.8 (a) shows the PL emission spectra recorded at different temperatures for a sub-bandgap excitation of 4.7 eV. The MOVPE H_2 annealed sample is indeed showing, for $T \leq 100K$, a remarkable shift of its broad emission band towards higher energies (behaviour reported neither for the as-dep or O_2 annealed MOVPE nor for the MBE samples), as well as the appearance of a weak luminescence band located around 3.6 and 3.8 eV. To further investigate this additional luminescence band, the PLE *T*-dependent spectra were recorded, for selected detection energies from 3.6 to 3.8 eV [see Figure 6.8 (b)]. This allows to highlight the presence of a new excitation channel just in the H_2 annealed MOVPE sample, peaked at 4.7 eV for $T = 5K$, *i.e.*, a defect state located at ≈ 300 meV below the CB. This excitation channel is then accounted responsible for the emission recorded in the PL spectrum around 3.7 eV [see Figure 6.8 (a)]. Therefore, considering the 5 eV bandgap of the κ-Ga_2O_3 polymorph, these experimental data suggest the presence of a deep level defect at around 1 eV from the VB that is just detected upon H_2 annealing for the MOVPE layer.

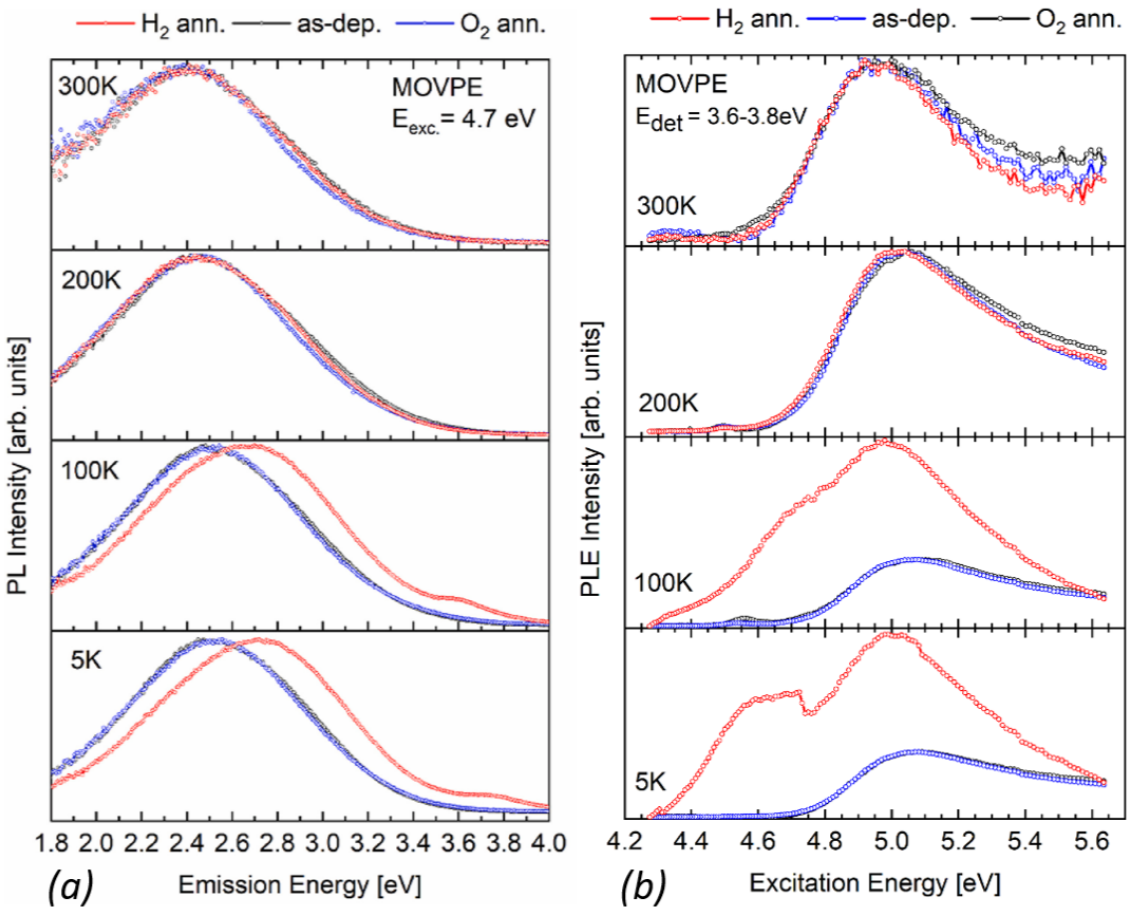

Figure 6.8 (a) PL spectra of the MOVPE κ-Ga_2O_3 as-deposited, O_2, and H_2 annealed, measured at $T = 5 - 100 - 200 - 300\ K$ acquired with sub band edge excitation (4.7 eV). (b) Temperature dependent PLE spectra of MOVPE grown κ-Ga_2O_3 samples for a detection energy range from 3.6 eV to 3.8 eV. The image is readapted from ref. [174].

Therefore, the experimental evidences collected so far suggest that the mild annealing treatments (550°C) are capable to affect (depending on the background atmosphere) both shallow and deep level defects in κ-Ga_2O_3. Moreover, such changes are most likely affecting the overall layer thickness, since they end up in a significant variation of the performances of the corresponding PDs. Generally though, the significant or shallow differences among as deposited and annealed MOVPE and MBE layers should depend on a different initial concentration of point defects related to the distinct growth processes. In the next section, these results are tentatively connected to *ab-intio* theoretical calculations in κ-Ga_2O_3.

6.3 Theroetical calculations

The study of the role of point defects in κ-Ga_2O_3 was performed with the Heyd-Scuseria-Ernzhof screened hybrid functional and projector-augmented wave approach (for further details see ref.[[174]]), considering the six distinct O sites (O_1 – O_6) and four Ga sites (Ga_1 – Ga_4) (see section 2.3.1 for the κ-Ga_2O_3 unit cell and atoms sites identification where the roman numbers $O_{I\text{-}VI}$ and $Ga_{I\text{-}IV}$ corresponds here to arabic numerals) and their interaction with hydrogen. As already reported for β-polymorph, V_O behave as deep donor and V_{Ga} as deep acceptor, for fermi level close to 3 eV [see Figure 6.9 (a) and (b)], *i.e.,* typical for n-type material.[90] V_O and V_{Ga} are more prone to form, as expected, in O-poor and O-rich conditions, respectively. Again in similarity to the β-polymorph, split Ga vacancies (V_{Ga}^i)[190–194] are stable and prone to form especially in a site between Ga_1 and Ga_4.[195] Moreover, considering the similarities with the β phase, it is reasonable to assume the V_{Ga}^i being mobile at the mild *T* involved in the annealing treatments here investigated.[196]

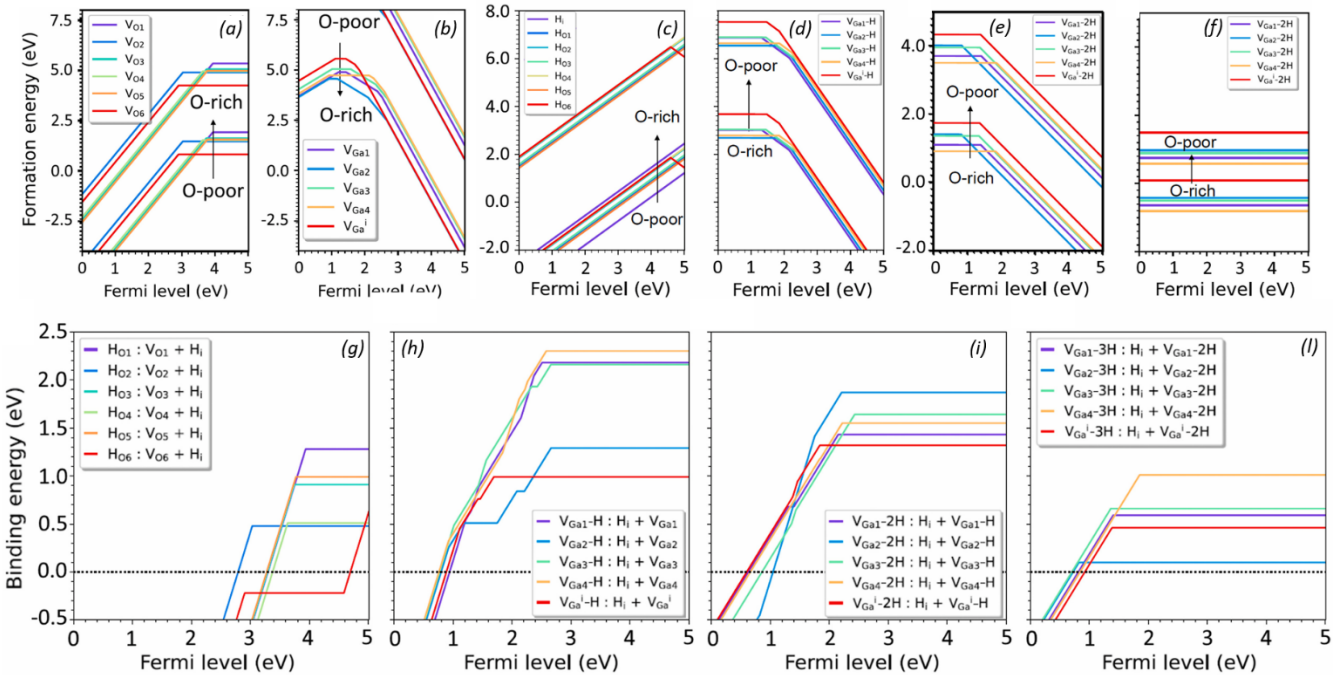

Figure 6.9 Formation energy diagram for (a) V_O, (b) V_{Ga}, (c) H interstitials (H_i) and their complexes with oxygen vacancies, and (d – f) their complexes with gallium vacancies with 1H, 2H and 3H, respectively, shown as a function of the Fermi level for the limiting extremes of O-rich and O-poor (Ga-rich) conditions in κ-Ga_2O_3. (g – l) Plot of the calculated binding energies for hydrogen-related complexes with respect to oxygen sites H_O, singly-hydrogenated V_{Ga}-H, doubly-hydrogenated V_{Ga}-2H and triply-hydrogenated V_{Ga}-3H. The binding energies are calculated as a function of the Fermi level according to the formation energies labelled in the legends, where a positive binding energy indicates a favourable complex with respect to the isolated constituents. The image is readapted from ref. [174].

An extrinsic defect that has been experimentally and theoretically found to play an important role in the point defects of β-Ga_2O_3 is hydrogen.[90,195,197] To evaluate the possible role of H in the κ-Ga_2O_3 material system, the formation energies for H_i, H_O as well as several V_{Ga}-nH ($1 \leq n \leq 3$) complexes were calculated [Figure 6.9 (c-f)]. H_i appears to be the most favourable shallow donor level followed by H_{On} with $1 \leq n \leq 5$, while H_{O6} can act as a deep acceptor above the (+/0) transition (4.58 eV above the VBM), similarly to β-Ga_2O_3.[198] Interesting enough, the hydrogenation of an O-deficient material could either result in an increase of shallow donor states, *i.e.,* H_i and $H_{O1\text{-}5}$, or in a compensation acceptors for H_{O6}, considering that V_{O6} is the most favourable site in n-type material [see Figure 6.9 (a)].

To evaluate the stability of these different H-related defect complexes, their relative binding energies were calculated, defined as the formation energies from the individual defects, *e.g.,* H_{O1}: V_{O1} + H_i (same stands for V_{Ga}-nH complexes) [see Figure 6.9 (g-l)]. It appears that the H_O defects are rather easy to be dissociated and, considering the low migration energies reported for H_i in other Ga_2O_3 polymorphs,[195,199] H_i could migrate and interact with other defects at temperatures even lower than the annealing ones. On the other side, the deep-acceptor V_{Ga}-nH complexes are very prone to

form (low formation energies) especially when the E_F is approaching the CB minimum; additionally, they are also showing relatively low binding energies w.r.t. the β-polymorph.[190,195,198,200] In particular, the V_{Ga}-*n*H complexes in β-Ga_2O_3 were suggested to be affected just at $T \geq 800$°C, while for the κ polymorph temperatures in the range of 500°C are found to be sufficient to dissociate them.

6.4 Discussion

The combination of the experimental data and calculations allows to have a clearer picture over the native point-defects concentration according to the epitaxial technique involved, *i.e.,* MOVPE and MBE, and their redistribution upon annealing in different background atmospheres. It is also plausible that hydrogen could play an important role in this framework. In this regard, it is reasonable to assume that the as deposited MOVPE layers (TMG and H_2O precursors) should be characterized by an initial larger concentration of H with respect to the MBE deposited ones (ultra-high vacuum technique, high purity metal Ga and In + O-plasma involved in the process). Similarly, also the initial concentration of native defects (e.g., V_{Ga}^{i} and V_O) could be related to different growth conditions (O-/Me- rich).

Starting from the PDs characterization, the higher I_{dark} reported for the as-deposited MOVPE sample w.r.t the MBE one (section 6.1.2) is pointing toward a higher concentration of H-related shallow-defects (*e.g.*, H_i and/or H_O) in the first one. Moreover, a larger concentration of deep level defects in the MOVPE layer is suggested from the in-gap state band detected from XPS.

The mild annealing treatments in the different atmospheres applied to the investigated κ-Ga_2O_3 layers, are theoretically found to allow for a significant redistribution of the population of different H-related point defect complexes. In order to sum-up the information provided, a schematic picture of the band diagram is reported in Figure 6.10.

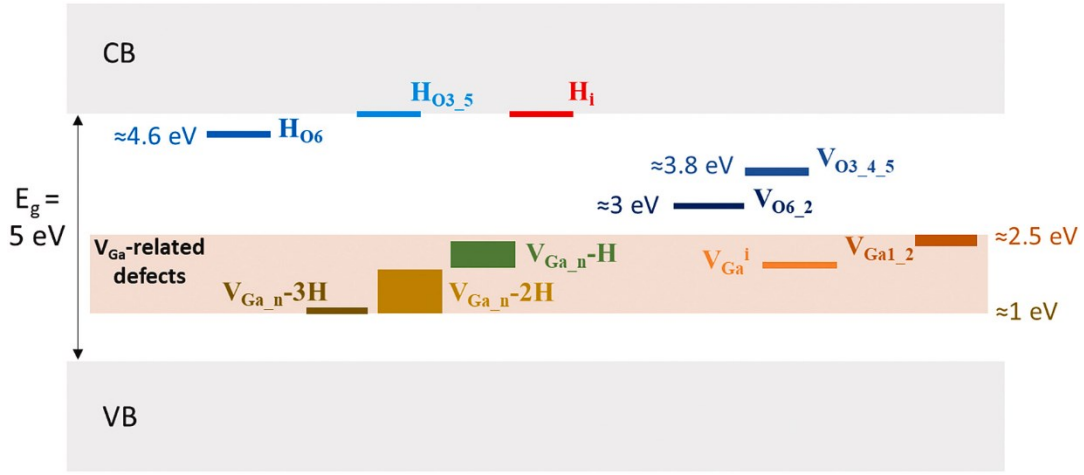

Figure 6.10 Simplified band-diagram sketch reporting some of the most energetically favourable defect levels in κ-Ga_2O_3 from theoretical calculations. Energies are given relative to the valence band maximum. The image is reproduced from ref. [174].

The annealing treatments are found to have an higher impact on the MOVPE layers as observed in PDs responsivities and luminescence spectroscopy [Figure 6.4 and Figure 6.7 (a)]. Indeed, the MOVPE O_2 annealed sample reports an improvement in solar blindness directly related to the increase of I_{dark} and a faster transient at the gap light. These effects can be explained in the framework of dissociation of H_O and hydrogenated complexes followed by H desorption. On the other side, the MBE O_2 annealed sample does not show any significant difference w.r.t to the as-deposited MBE layer, indicating a lower initial concentration of defects. Regarding the H_2 annealing, both MOVPE and MBE samples are affected, even though on a different scale, with the MOVPE showing the highest differences. H_2 annealing results in a double effect: (i) the increase in I_{dark} and responsivity values and (ii) loss in solar blindness (lower R_R – see Table 6.1) and longer discharging times (see Table 6.2). (i) and (ii) can be both explained considering a higher concentration of H, behaving as shallow donor so increasing the I_{dark}, and hydrogenating the complexes so increasing the carrier traps and slowing down the response in time. Also, the trapping times longer than the photocarrier transient time can result in an excess of the collected charge at the electrode contributing as well to a slower response in time and enhanced photo gain.

Regarding the PLE spectra, the same trend of the annealing effect is reported, having higher impact on the MOVPE layers. The different onset in the absorption reported for the H_2 and O_2 annealed samples supports the interpretation of higher and lower shallow defects concentration mediated by the annealing treatment itself. More insights on the deep levels are provided from the PL spectra [see Figure 6.8 (a)]. The broad convoluted band, reported for all MOVPE and MBE layers, is showing only for the H_2 annealed MOVPE sample remarkable differences as (i) significant shift to higher energies for low T and (ii) the appearance of an additional luminescence band at 3.8 eV

(already assigned to an excitation channel located at 4.7 eV). The punctual assignment of these features to a particular defect went through the simulation of absorption and emission profiles for several different defects showing that H_{O6} defects is the most favourable candidate to explain both (i) and (ii). This investigation enables the construction of the schematic band diagram shown in Figure 6.10, where defect levels are now attributed to their corresponding defects, providing a new level of insight into point defects in κ-Ga_2O_3.

6.5 Conclusions

The combined investigation here presented provided a comprehensive understanding of the point-defects in κ-Ga_2O_3. It was highlighted how the native defects as well as H-related-levels are strictly linked to the epitaxial technique involved. The as deposited MOVPE material showed indeed a higher concentration of H either potentially capable of acting as a shallow donor as well as a deep acceptor level. This could be related to the different growth environment/precursors involved w.r.t the MBE growth. It was also detected that, even mild annealing, are strongly affecting the defects distribution, especially of the hydrogenated complexes. The study is also relevant in the framework of κ-Ga_2O_3-based PDs optimization since it was shown that a tuning of the defects and consequently of the performances of the related devices can be obtained without affecting the phase stability and quality of the κ-layers.

To conclude, it must be pointed out that two relevant features were not taken in account in this study: (i) the effect of the vertically oriented structural defects of κ-Ga_2O_3 and (ii) the possible presence of other extrinsic impurities in the layers (*e.g.*, C). Regarding (i) the rotational domains may play a significant role in terms of defects distribution/concentration and in/out diffusion (as will be further discussed in Chapter 7). Even though both the sets of samples here investigated (MOVPE and MBE) were affected by a similar structural defective structure, the provided data interpretation is significantly supported by the experimental and theoretical data. As per (ii) C is known to play a significant role in β-phase acting either as a shallow donor (C_i) as well as a deep acceptor level (as O substitutional).[199] Nevertheless, it was not possible to detect C from SIMS measurements, even though it is reasonable to assume its higher concentration in the MOVPE layers (e.g., metalorganic TMG precursor).

7 Li diffusion in Ga_2O_3 thin films

The focus of this chapter lies on the study of the effect of *ex-situ* Li-diffusion in four different Ga_2O_3 material systems: amorphous, orthorhombic, monoclinic hetero- and homoepitaxial layers. Section 7.1 reports the designed *ex-situ* experimental approach together with the details of the four Ga_2O_3 thin films investigated; section 7.2 reports the experimental results collected through different techniques. In section 7.3 the theoretical input and possible interpretation of the observed phenomena are reported.

This chapter is an investigation on point defects, in which though the structural defectivity must be carefully considered as well; this study encompasses not only the orthorhombic κ-polymorph but also the amorphous and the monoclinic β-phase. The thermal diffusion (T_{max} = 550°C) of Li within the Ga_2O_3 layers is investigated, together with the evaluation of its impact on its functional properties. The driving force behind this study is settled by the recent widespread of all-oxide *pn*-heterojunctions based on Ga_2O_3. As discussed in Chapter 2, the *n*-type conductivity in Ga_2O_3 has been demonstrated for β- and κ-polymorph as well as for the amorphous structure when extrinsically doped with Si[31,131] or Sn.[131,201–204] On the other side, the *p*-type conductivity is not achievable in the Ga_2O_3 material system, due to the interplay between high hole effective mass and self-trapping of holes (STHs) mechanism.[93,205] This does not allow to design *pn*-homojunctions, therefore limiting the available architectures for power electronic devices. Hence, the development of Ga_2O_3-based *pn*-heterojunctions requires the coupling with a different p-type material, *e.g.,* SiC,[206] GaN,[207] SnO[153,157] and NiO.[208–215] Among the explored p-type materials, the metal oxides, *i.e.,* SnO and NiO, are preferred for a twofold reason: the precluded undefined oxidation at the interface and the higher compatibility of processing steps. Among the suggested p-type oxides, NiO is showing the highest band-gap, *i.e.,* $E_g \approx 3.6$ eV, and the possibility to tune its *p*-type conductivity through Li extrinsic doping.[216,217] In 2016, Kokobun *et al.*,[208] developed the first Li:NiO/β-Ga_2O_3 device. Since then, several studies have been reported on the optimization of the synthesis processes, architecture of devices and effect of Li-doping over the NiO functional properties.[218–220] Furthermore, a relatively new Li-Ga-based oxide compound, *i.e.,* $LiGa_5O_8$,[221] has been recently suggested to show good *p*-type conductivity and, even though the real p-type nature of the compound is currently under debate,[222] the implementation of a *p*-$LiGa_5O_8$/*n*-β-Ga_2O_3 has been already reported.[223] Thus, the development of Ga_2O_3 based *pn*-junctions involving Li, drives the interest of this work towards their stability.

The role of Li in different metal oxides (besides the already mentioned NiO) has been reported, *e.g.,* in TiO_2, SnO_2, ZnO and CeO_2 nanoparticles,[224] as well as ZnO,[225,226] and SnO_2[227] thin films. The

highly reducing nature of Li drives its effect over defects densities (*e.g.*, O-stoichiometry), potentially modifying the transport properties in the investigated oxide material systems. However, concerning Ga_2O_3, Li effect has been only marginally investigated in (i) the Czochralski bulk growth of β-Ga_2O_3[228] and (ii) the synthesis of Ga_2O_3 nanostructures.[229,230] While (i) did not report Li incorporation in β-Ga_2O_3 due to thermodynamic conditions, (ii) reached the effective incorporation of Li, resulting in the activation of a Li-related Raman mode and a red-near-IR emission (detected with CL and PL investigation). The latter feature was also predicted by density functional theory for a Li-absorbed Ga_2O_3 monolayer.[231] Furthermore, M. Kyrstos *et al.*,[205] calculated the ionization energies of different substitutional cations in Ga_2O_3, predicting for Li a deep-acceptor behaviour as Ga substitutional (Li_{Ga}). This is suggested to be feasible despite the difference in the Shannon ionic radii[5] between Li^{1+} and Ga^{3+}, *i.e.*, $\Delta r \approx 23\%$.[228] However, similarly to the ZnO material system, it is reasonable to assume that Li could potentially be incorporated also in interstitial sites (Li_i), possibly acting as a shallow donor.

In the following sections, the effective ex-situ diffusion of Li in Ga_2O_3 thin films is reported for the first time. The overall coordination of the works together with the XRD, AFM and PDs characterization was performed by the candidate. The κ-Ga_2O_3 layers were grown by M. Bosi, L. Seravalli and P. Mazzolini (IMEM - Parma). The amorphous layers were grown by G. Foti (UniPr). The design of the diffusion treatments was the idea of M. Sidoli and P. Mazzolini (UniPr). The MBE β-heteroepitaxial and homoepitaxial growths and the XPS investigation and data elaboration were performed by A. Ardenghi (PDI). The ToF-SIMS measurements were performed by A. Falkenstein and J. Kler (RWTH) and the diffusion data interpretation provided by M. Martin and R. De Souza (RWTH). The Li-implantation standards were provided by K. Mizohata and F. Tuomisto (University of Helsinki). The DRCL measurements and their interpretation were performed by D. Spallek and J. Lähnemann (PDI). The Raman analysis was performed by H. Tornatzky and M. R. Wagner (PDI). The metal-contacts deposition was performed by S. Pasini and A. Bosio (UniPr). The CV measurements were performed by A. Ardenghi and O. Bierwagen (PDI). The VdP/Hall measurements were performed by S. Vantaggio and A. Parisini (UniPr). The theoretical calculations were performed by J.B. Varley (Lawrence Livermore National Laboratory).

[5] The difference in Shannon ionic radii [Δr %] is calculated as: $\Delta r = \left[\frac{r[dopant]}{r[Ga^{3+}]} - 1\right] \times 100\%$. For Li_{Ga} in tetrahedral/octahedral site, r[Li^{1+}] = 0.59 Å/0.76 Å, substituting r[Ga^{3+}]= 0.47 Å/0.62 Å.[228,232]

7.1 *Ex-situ* Li-diffusion

7.1.1 Ga_2O_3 thin films

Three different types of Ga_2O_3 thin films have been involved in this study: (i) orthorhombic κ-, (ii) amorphous a-, (iii) heteroepitaxial (-201) β- and (iv) homoepitaxial (010) β-Ga_2O_3. (i) The orthorhombic κ-layers were grown by MOVPE at a partial pressure of 100 mbar, T_g = 650°C; trimethylgallium (TMG) and H_2O were used as metal precursor and oxidizing agent (standard conditions); He was used as gas carrier (He_{flux} = 400 sccm). (ii) The a-Ga_2O_3 was grown by room temperature RF magnetron sputtering on soda-lime glass substrates (growth parameters: P = 100 W: T_g = 25 °C; t = 500 nm); (iii) The heteroepitaxial (-201) β-layers were grown by MBE on top of (0001) α-Al_2O_3 substrates (BEP_{Ga} = 5.74 ·10^{-7} mbar; T_g = 500 °C, O_{flux} = 1 sccm, P_{RF} = 250 W, t = 400 nm). (iv) The homoepitaxial (010) β-Ga_2O_3 layers were grown by MBE on top of (010) bulk substrates (BEP_{Ga} = 3.4 ·10^{-7} mbar; T_g = 660 °C, O_{flux} = 1 sccm, P_{RF} = 250 W, t = 900 nm). Table 7.1 sums up the details of the four different categories of Ga_2O_3 thin films and reports also the Si concentration background, when available. Indeed, even though the layers are nominally undoped and insulating, in both the MOVPE and MBE chambers Si contamination can originate either from previous Si-doped samples growths in the chambers or, in the case of MBE, from the quartz cavity of the RF plasma source.

Category	Ga_2O_3 layer	Substrate	thickness [nm]	Si background range [cm^{-3}]
(i)	orthorhombic κ-	(0001) α-Al_2O_3	400-800	$10^{17[*]}$
(ii)	amorphous a-	soda-lime glass	500	no data
(iii)	monoclinic (-201) β-	(0001) α-Al_2O_3	400	no data
(iv)	monoclinic (010) β-	(010) β-Ga_2O_3	900	10^{18}

Table 7.1 Sum-up of the four different categories of the Ga_2O_3 layers interested by the study here reported. The substrate, thickness and unintentional doping level of Si are reported. [*] The value is not extracted directly for the layers here investigated but is given considering the ToF-SIMS Si levels detected in UID κ-Ga_2O_3 samples grown in the reactor and in identical growth conditions.

The involvement of (i) the orthorhombic polymorph, (ii) the amorphous layers, , characterized by vertically oriented structural defects,[20] (iii) the (-201) β-heteroepitaxial layer, characterized by poly-oriented structural defects[172] and (iv) the (010) β-homoepitaxial film nominally free of structural defects,[166] would allow the study of the Li-diffusion mechanism and to evaluate in this framework the impact of different structurally-defective structures.

7.1.2 Experimental Li-diffusion

To achieve the diffusion of Li in the Ga_2O_3 thin films, an *ex-situ* procedure has been designed: a lithium salt, *i.e.,* lithium azide (LiN_3), was dissolved in defined concentrations in an ethanol (EtOH) solution and then drop-casted on the surface of the layers (i)-(iv). The procedure was performed in a glow-box with an argon-controlled atmosphere to face the hygroscopic nature of LiN_3. After the EtOH evaporation, the samples were transferred in an Ar-filled glass vial out of the glow box; the vial was then connected to a turbo-pump in order to perform thermal treatments using a tubular furnace (pressure ≈ 10^{-6} mbar). The vacuum thermal treatment foresees slow multi-steps heating ramps [see Figure 7.1], especially in the *T* interval close to the LiN_3 melting point, *i.e.,* 115 °C, up to the reported temperature range of decomposition, *i.e.,* 185°C < $T_{decomposition}$ < 220°.[233] Such low ramps were employed to avoid the damage of the sample surface during the thermal decomposition process of the LiN_3 (see Equation 7.1)

$$2LiN_3 \rightarrow 2Li + 3N_2$$

Equation 7.1 Reaction of thermal decomposition of LiN_3 as reported by ref. [233].

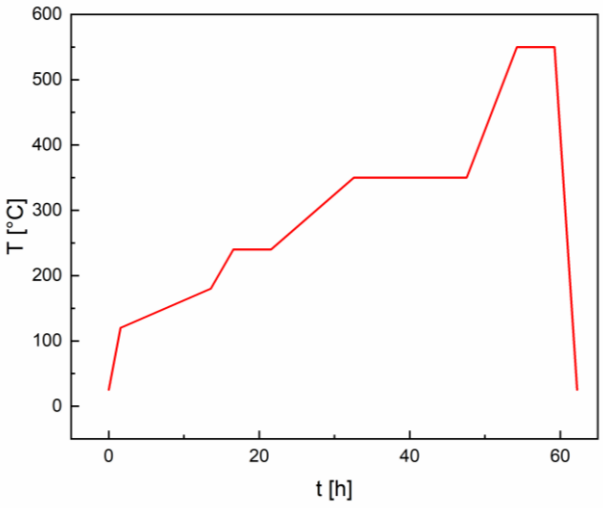

Figure 7.1 Thermal ramps and steps involved in the annealing treatments. The reported one is referring to the harshest applied conditions, *i.e.,* T_{dwell} = 550°C and t_{dwell} = 5h. See Table 7.2 for further details.

An extensive study was performed on category (i) and (ii), varying T_{dwell}, t_{dwell} and LiN_3 concentrations [LiN_3/EtOH] [g/ml], because of larger availability of material. The harshest tested thermal conditions and optimal [LiN_3/EtOH] concentration were then also tested for categories (iii) and (iv). The details of the different attempted treatment parameters are reported in Table 7.2. The temperature range investigated in this work, *i.e.,* 350°C ≤ T_{dwell} ≤ 550°C, was chosen considering the thermal window stabilities for the a- and κ-Ga_2O_3 layers and above all the temperature usually

involved either in deposition as well as in post-growth annealing steps for development of Li-containing metal-oxide/β-Ga_2O_3 *pn* heterojunctions.[209–213,223,234]

Category	Sample	T_{dwell} [°C]	t_{dwell} [h]	[LiN_3/EtOH] [mg/ml]
(i)	(001) κ-Ga_2O_3/(0001) α-Al_2O_3	350	2	40; 20; 8; 4; 1.6; 0.8; 0.54; 0.4
		450	2	0.8
		550	2	1.6; 0.8
		550	5	0.8
(ii)	a-Ga_2O_3/glass	350	2	40; 20; 4
(iii)	(-201) β-Ga_2O_3/(0001) α-Al_2O_3	550	5	0.8
(iv)	(010) β-Ga_2O_3/ β-Ga_2O_3	550	5	0.8

Table 7.2 Sum-up of the different thermal parameters (T_{dwell} and t_{dwell}) and [LiN_3/etOH] concentrations attempted on the four different categories of Ga_2O_3 layers investigated.

According to the different [LiN_3/EtOH] concentrations (as reported in Table 7.2), the expected maximum Li concentrations (N_{Li}) in the layers are calculated, considering: the initial [LiN_3/etOH] in solution, the volume of the solution drop-casted on the Ga_2O_3 surface (≈ 8 µl), the geometrical parameters of the treated samples (area ≈ 10 mm^2 and layer thicknesses) and considering homogeneous Li penetration over the full layer thicknesses. The expected N_{Li} are reported in Table 7.3, for the most relevant [LiN_3/EtOH] concentrations.

Category	Average thickness [nm]	[LiN_3/EtOH] [mg/ml]	N_{Li} [cm^{-3}]
(i)	650[§]	1.6; 0.8	$3.8 \times 10^{20}; 1.9 \times 10^{20}$
(ii)	500	40; 20; 4	$1.2 \times 10^{22}; 6.2 \times 10^{21}; 1.2 \times 10^{21}$
(iii)	400	1.6; 0.8	$6.2 \times 10^{20}; 3.1 \times 10^{20}$
(iv)	900	0.8	2.7×10^{20}

Table 7.3 Maximum expected Li concentrations (N_{Li}) calculated considering different initial [LiN_3/EtOH] in solution, the volume of solution drop casted on the Ga_2O_3 surface (≈ 8 µl) and the geometrical parameters of the treated samples (area ≈ 10 mm^2 and thickness), considering Li penetration interesting the full layer thicknesses. [§] For category (i), given the range of thicknesses of the layers investigated, an average indicative value of 650 nm is considered for the calculation of N_{Li}.

After the thermal treatment, each sample underwent a 5 min bath in EtOH under sonication, to remove possible unreacted LiN_3, and a wet etching at room temperature in a water-diluted hydrochloric acid HCl solution ([HCl] = 37 %vol, $t_{etching}$ = 5 min). The wet etching in HCl was performed in order to remove a possible passivation layer that could be formed over the Ga_2O_3 surface. Indeed, as reported by Ou *et al.*,[224] the highly reducing nature of Li tends to stabilize the oxide compound Li_2O, soluble in HCl. Considering the possible presence of residual oxygen in the vacuum annealing atmosphere, as well as the possible out-take of oxygen from the Ga_2O_3 thin film surface (as already reported in the case of other oxide material systems),[224] the formation of a lithium oxide based compound is likely. Its eventual presence/removal was thoroughly investigated through

XPS as shown hereafter together with the whole experimental investigation carried out on the various Li-diffused Ga_2O_3 layers, detailing the results for each category of samples individually.

7.2 Post-diffusion characterization

7.2.1 (001) κ-Ga_2O_3

7.2.1.1 Surface investigation - XPS and AFM

The κ-Ga_2O_3 epi-layers underwent an extensive experimental investigation. The first step was to address the abovementioned passivation layer nature/presence. Hence, an XPS investigation was performed on the layers after the annealing treatments followed by standard solvent cleaning, *i.e.*, sonication for 5'' in acetone and 5'' in isopropanol, and then after the HCl etching. Figure 7.2 reports the XPS investigation. The signals of Ga2p, O1s and C1s core levels are reported in Figure 7.2 (a), (b) and (c), respectively, for the treated samples just after the solvent cleaning (in black) and the HCl etching (in red). The increase of Ga2p and O1s signals together with the decrease of C1s and disappearance of its component ≈ 288 eV, points toward the effective removal of a superficial layer. The actual composition of such layer was not further investigated but it is reasonable to assume to be related to a Li-O-C compound. C presence on the κ-Ga_2O_3 layer can be ascribed to residual from the TMG metalorganic precursor and/or contamination from the graphite susceptor or from the Ar glow box (where the LiN_3 drop casting has been performed) that is routinely employed for C-based compounds. Figure 7.2 (d) reports the survey over the entire range of binding energies for the sample after the HCl etching; it was possible to detect the peak of Li 1s core level ≈ 55.8 eV [zoom in Figure 7.2 (d) inset]. The slight shift of the peak w.r.t. the expected position for the metallic Li, *i.e.,* 55 eV, can be related to a Li-O bond.

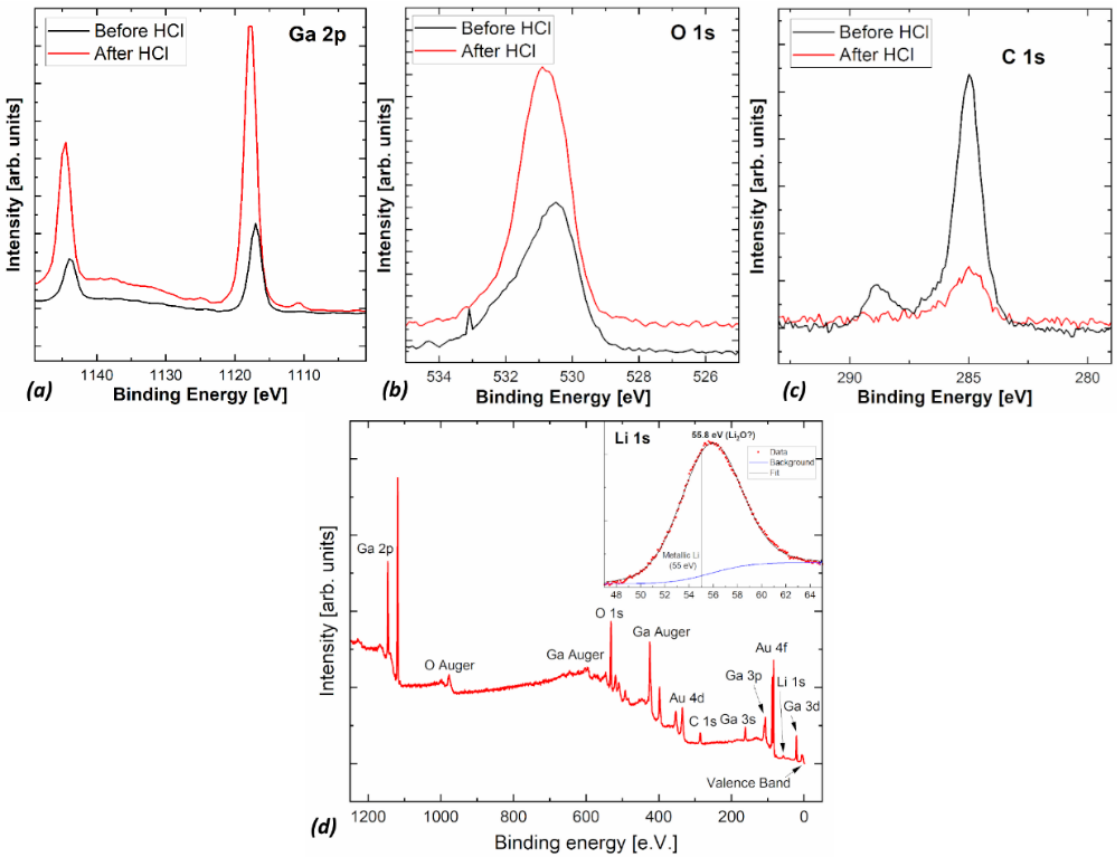

Figure 7.2 (a), (b) and (c) Ga 2p, O 1s and C 1s core level signals for the κ-Ga_2O_3 sample treated at T_{dwell} = 350°C and t_{dwell} = 2h, after the Li-diffusion thermal treatment that underwent only an organic solvent cleaning (in black) and after the HCl etching (in red). In (d) the survey of the same sample after the HCl etching is reported. In the inset, zoom over the Li 1s core level with corresponding fit and background.

The surface of the layers was investigated with AFM (see Figure 7.3). The 10×10 μm^2 and 5×5 μm^2 AFM images of a κ-Ga_2O_3 layer as deposited (a), Li-diffused (T_{dwell} = 350°C; t_{dwell} = 2h) pre [(b) and (d)] and post HCl [(c) and (e)], reveals a inhomogeneity of the surface of the layer upon the diffusion treatment with a relative high *RMS* value. The homogeneity of the surface seems to be restored after the HCl etching, recording also a decrease in the *RMS* value that might also suggest a mild etching of the κ-Ga_2O_3 surface.

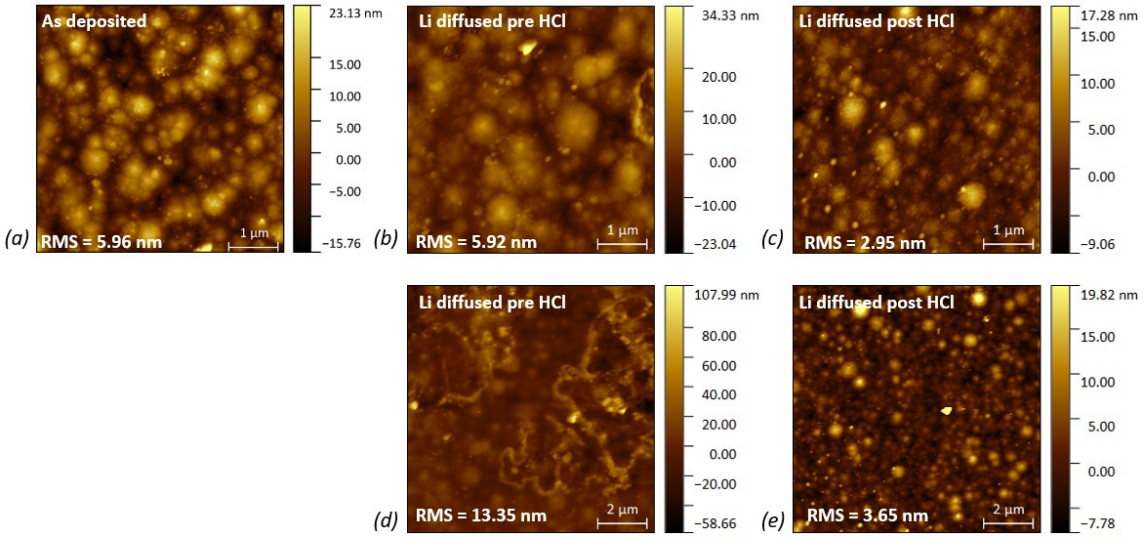

Figure 7.3 In (a), (b) and (c) $5 \times 5\ \mu m^2$ AFM images of the κ-Ga_2O_3 layers as deposited, Li-diffused (T_{dwell} = 350°C; t_{dwell} = 2h) before and after HCl etching, respectively. In (d) and (e), $10 \times 10\ \mu m^2$ of the Li-diffused sample before and after HCl etching respectively.

7.2.1.2 Structural characterization - XRD and Raman

XRD and Raman analysis were conducted to assess the stability of the κ-polymorph upon the thermal treatment and to exclude the stabilization of Li-related phases. Figure 7.4 (a) reports the symmetric *2θ-ω* XRD scans of two κ-Ga_2O_3 samples treated at T_{dwell} = 350 °C (in yellow) and 450 °C (in red), with t_{dwell} = 2h, after HCl etching. The characteristic diffraction peaks of {001} κ-Ga_2O_3 (epi-layer) and {0001} α-Al_2O_3 (substrate) are labelled: no additional phases are detected. In the inset, the close-up on the (004) κ-phase reflection and (0006) α-Al_2O_3 is reported, highlighting no presence of β-phase (vertical dashed-grey line located at (-402) β-phase *2θ* expected position). This confirmed the stability of the κ-polymorph upon the applied T_{dwell}, well under the reported transition temperature to β, *i.e.*, $T_{dwell} < T_{\kappa \to \beta} \geq 700°C$. The effect of the [$LiN_3$/EtOH] solution concentration, investigated with XRD [Figure 7.4 (b)] and Raman [Figure 7.4 (c)], reported no significant changes of the layers crystal structure for different concentration solutions investigated.

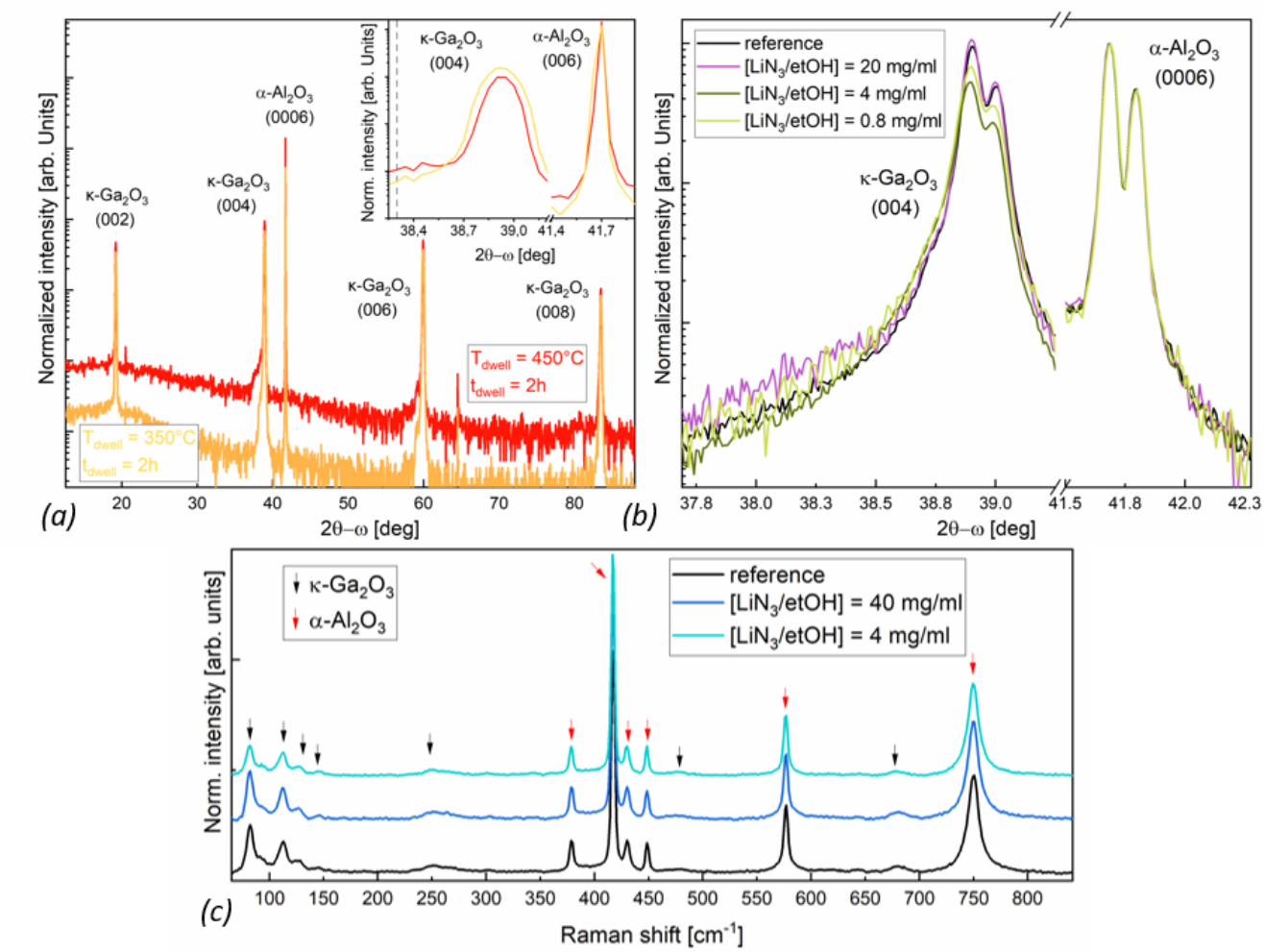

Figure 7.4 (a) symmetric 2θ-ω XRD scans in semi-logarithmic scale of two κ-Ga_2O_3 samples treated at different T_{dwell}, [350°C (in yellow) and 450°C (in red)], for the same t_{dwell} = 2h and [LiN_3/EtOH] = 0.8 mg/ml. The scans were acquired with a monochromatic Cu $K_{\alpha1}$ incident beam and vertically shifted for better comparison; the inset reports the close up on the (004) κ-Ga_2O_3 and (0006) α-Al_2O_3 reflection, after normalization of the spectra on the substrate peak, highlighting the absence of the (-402) β-Ga_2O_3 peak expected at $2\theta \approx 38.25°$, where the grey dashed line is drawn. (b) symmetric 2θ-ω XRD scans in semi-logarithmic scale closed-up on the (004) κ-Ga_2O_3 and (0006) α-Al_2O_3 peak reflection for samples treated under the same annealing parameter, *i.e.*, T_{dwell} = 350°C and t_{dwell} = 2h, but with different LiN_3 concentration in the drop casted solution; the scans were acquired with a non-monochromatic Cu $K_{\alpha1,2}$ incident beam and were normalized on the (0006) substrate peak located at $2\theta = 41.7°$. (c) Raman spectra for κ-Ga_2O_3 reference sample (in black) and two samples Li-diffused at T_{dwell} = 350°C and t_{dwell} = 2h at different [LiN_3/EtOH] concentration. The spectra were acquired with a red laser [λ = 633 nm] and were normalized on the substrate peak located at Raman shift = 416 cm^{-1} after background and air signal subtraction [see section 4.1.2.5 for further details]; all Raman spectra underwent a rigid vertical shift for a better comparison. κ-Ga_2O_3 and α-Al_2O_3 Raman modes are labelled with black and red arrows, respectively.

7.2.1.3 ToF – SIMS

ToF-SIMS measurements confirmed the successful diffusion of Li into the κ-Ga_2O_3 epilayers. The reproducibility of the diffusion process is demonstrated by the overlapping profiles shown in

Figure 7.5 (a) for three different samples, all treated under identical conditions - [LiN_3/etOH] = 0.8 mg/ml, T_{dwell} = 350°C, and t_{dwell} = 2h - across different experiments. Figure 7.5 (b) reveals a clear trend of Li penetration as a function of dwell temperature and time: as T_{dwell} and t_{dwell} increase, both the Li concentration and penetration depth rise. The quantification of Li was achieved by measuring the relative sensitivity factor (*RSF*) for Li in the κ-Ga_2O_3 matrix through a Li implantation standard; this was obtained with a fluence of $1.43 \times 10^{14} at/cm^2$ and an implantation energy of 28 keV (further details regarding the implantation standard, the RSF and Li concentration extrapolation can be found in Appendix A).

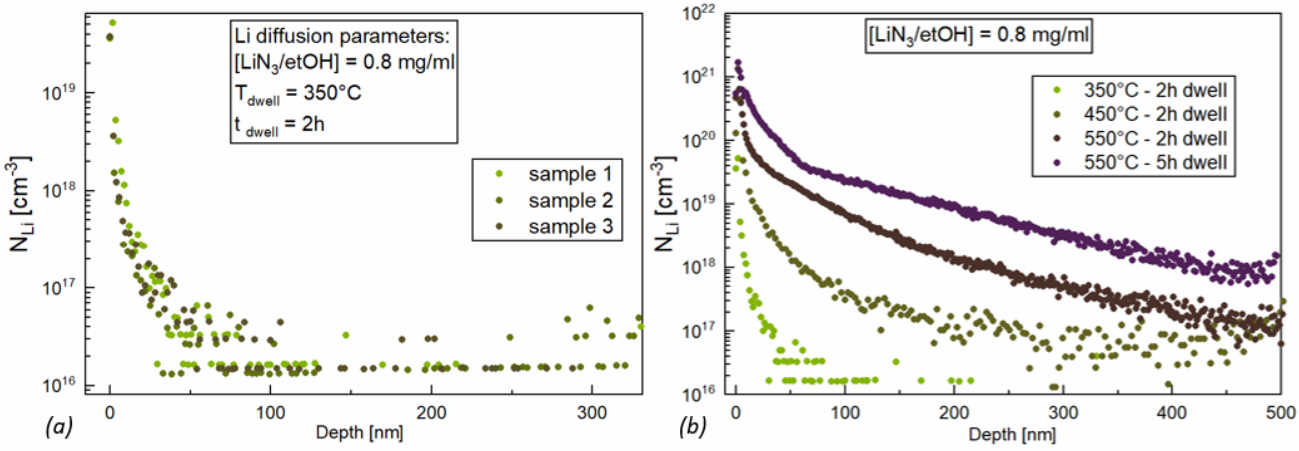

Figure 7.5 SIMS Li profiles for (a) three different samples that underwent the same Li diffusion treatment (T_{dwell} = 350°C , t_{dwell} = 2h, [LiN_3/EtOH] = 0.8 mg/ml) and in (b) increasing T_{dwell} and t_{dwell}.

Analysing the Li profiles obtained with the highest diffusion temperature, *i.e.*, T_{dwell} = 550 °C and t_{dwell} = 2 and 5 h [Figure 7.5 (b)], two distinct regions can be identified in both profiles. The first region (up to ≈ 50 nm from the layer surface) can be described using the thin-film solution of the diffusion equation which provides a tentative bulk Li-diffusion coefficient ($D_{Li,bulk}$) as reported in Table 7.4, extracted for the two different t_{dwell}.

Profile	$D_{Li,bulk}$ [cm^2s^{-1}]	$D_{Li,2D}$ [cm^2s^{-1}]
T_{dwell} = 550°C, t_{dwell} = 2h	$2.8 \cdot 10^{-16}$	$1.4 \cdot 10^{-13}$
T_{dwell} = 550°C, t_{dwell} = 5h	$9.1 \cdot 10^{-17}$	$6.9 \cdot 10^{-14}$
Average values	$1.9 \cdot 10^{-16}$	$1.0 \cdot 10^{-13}$

Table 7.4 Diffusion coefficients of Li in the bulk ($D_{Li,bulk}$) and along the 2d-defects ($D_{Li,2D}$) in κ-Ga_2O_3 layers diffused at T_{dwell} = 550 °C and two different dwell times.

The second region fits a solution of the diffusion equation according to the Harrison type B classification.[235,236] In this case, the diffusion profile arises from faster diffusion along 2D-defects, *e.g.*, grain/domain boundaries, combined with slower diffusion perpendicular to these boundaries into the bulk material. In the Harrison type B analysis, only the product of the 2D defect thickness (d_{2D})

and the diffusion coefficient along the 2D defects, ($D_{Li,2D}$), can be determined. Assuming then the d_{2D} =1 nm, the $D_{Li,2D}$ values are obtained, as reported in Table 7.4. (Additional details for both the thin film and Harrison type B solution are reported in Appendix A).

The differences reported for $D_{Li,bulk}$ and $D_{Li,2D}$ for the two different profiles, *i.e.*, different t_{dwell}, can be ascribed to the rather short profiles. Moreover, for a more detailed analysis also the heating and cooling periods should be taken in account. However, the values can be considered consistent with the provided interpretation of the two diffusion mechanisms. Furthermore, comparing the average values calculated (reported in Table 7.4), the bulk diffusion is showing about three orders of magnitude lower diffusion coefficient w.r.t. the defect-mediated one, hence, being the latter the fastest and favourable one. For the Li-profiles obtained at lower T_{dwell}, the distinction of the two region is not present thus the separation in bulk and defects mediated diffusion is not possible.

7.2.1.4 Depth resolved cathodoluminescence (DRCL)

DRCL investigation was performed on the HCl-etched layer Li-diffused in the harshest thermal conditions (T_{dwell} = 550°C and t_{dwell} = 5h) and compared to an as-deposited κ-Ga_2O_3 layer. The luminescence spectra for both samples, reported in semi-logarithmic scale in Figure 7.6 (a) and (b), show a broad band peaked in the spectral range 400 – 700 nm (≈ 3.1 – 1.77 eV), as already widely reported in literature[130,180,182] and discussed in Chapter 6.

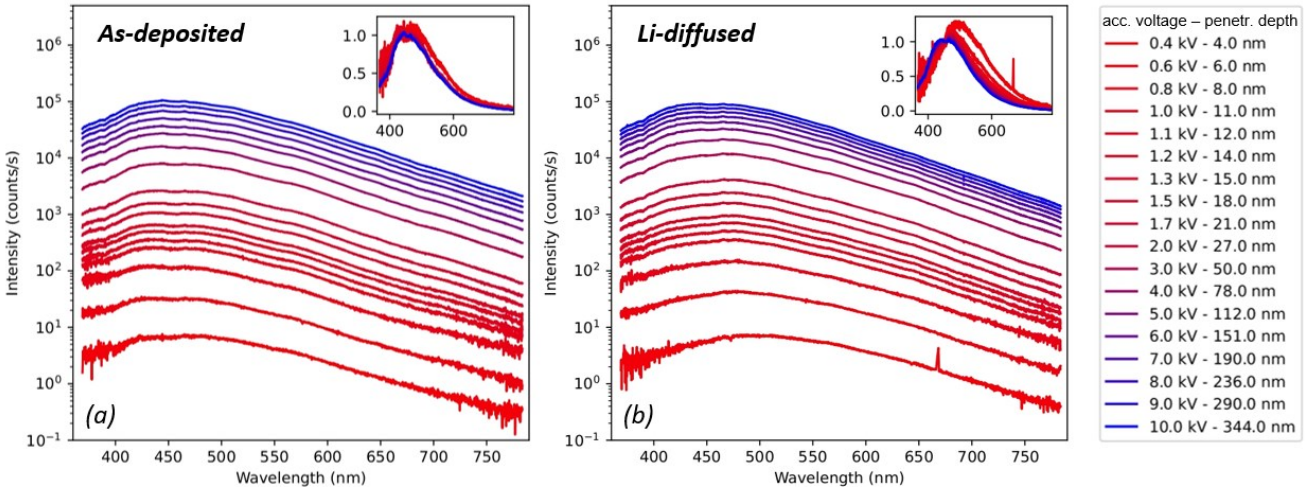

Figure 7.6 DRCL spectra evolution with increasing acceleration voltages for (a) as deposited and (b) Li-diffused κ-Ga_2O_3. Spectra are plotted in semilogarithmic scale. Colour scale going from red to blue for increasing acceleration voltage/probing depth. On the right, the colour scale correspondence to acceleration voltages and relative probing depth estimated with Monte Carlo method is reported and valid for both (a) and (b). In the insets, the same spectra are reported in linear scale and normalized on the intensity at 425 nm, for better comparison.

For the as-deposited layer the spectrum is consistent over the full range of acceleration voltages/penetration depths; on the other hand, the Li-diffused sample is showing a change in the

peak relative intensity for increasing acceleration voltages, *i.e.*, penetration depths.[6] This feature is particularly emphasized in the insets of Figure 7.6 (a) and (b), where the spectra were normalized on the intensity of the peak at 425 nm, and could suggest an effect of Li over the defects levels concentration over the first ≈ 20 nm of the Li-diffused sample. However, considering the experimental procedure employed, *i.e.*, drop casting followed by wet etching, the top nanometeres of the layer could have been altered, leading to a slightly different luminescence signal. Therefore, attributing the observed effect to the Li in-diffusion based solely on this evidence could be misleading.

7.2.1.5 Electro-optical PDs characterization

In order to investigate the possible effect of Li over the transport properties, the electro-optical characterization of the PDs fabricated with the κ-Ga_2O_3 layers that underwent the Li-diffusion process in the harshest thermal conditions was performed and compared to an as deposited as well as a thermal treated reference (same thermal cycle and atmosphere employed for the Li diffusion experiments). The PDs design and characterization procedures are exactly the same as the ones described in section 6.1.

Table 7.5 reports some experimental data obtained for the three photodetectors. Despite of showing some slight variations, no significant trend can be highlighted. Moreover, the responsivity vs. wavelength curves [see Figure 7.7 (a)] of the three different PDs are similar. The slight shift towards higher and lower responsivity values for the thermal treated and Li-diffused sample, respectively, can be ascribed to the unknown nature of the residual partial pressure of the annealing environment, in light also of what have been discussed in Chapter 6. The R_R values, *i.e.*, $\text{responsivity}_{\lambda = 250\ \text{nm}}$/ $\text{responsivity}_{\lambda = 500\ \text{nm}}$, are all around middle 10^3/low 10^4 [see Table 7.5].

Photodetector ID	I_{dark} @ 200 V [nA]	R_R	τ_{ON} [s]	τ_{OFF} [s]
as-deposited	4.5	7.8×10^3	100.3	43.8
Li-diffused	3.65	4.3×10^3	108.7	83.4
thermal ref.	13.1	1.3×10^4	83.8	40.9

Table 7.5 I_{dark}, R_R, τ_{ON} and τ_{OFF} values for PDs based on the as-deposited, Li-diffused and thermal reference κ-Ga_2O_3 layers.

The time-dependent behaviour of the PDs is studied with on-off cycles of 300 s (150 s with λ_{ON} = 250 nm) [see Figure 7.7 (b)], and the characteristic τ_{ON} and τ_{OFF} (*i.e.*, the time required for the photocurrent to go from 10% to 90% and vice versa) are reported in Table 7.5. A similar τ_{ON} for the

[6] The acceleration voltage / penetration depth relation was calculated with Monte Carlo simulation. However, even though in Figure 7.6 the exact number is provided for the penetration depth, it must be considered as indicative, considering that the luminescence signal is collected from a volume.

as-deposited and Li-diffused sample is reported, while the thermal reference exhibited a faster one. When in dark, the Li-diffused sample displayed the slowest photocurrent decay, with a τ_{OFF} nearly twice as long compared to the as-deposited and thermal reference. This could suggest a higher concentration of defects for the Li-diffused κ-Ga_2O_3 PD, just in this framework similar to what had been highlighted for the H_2 annealing treatments (see Chapter 6); the differences with respect to the H_2 annealing lays in the unchanged I_{dark} w.r.t. the as-deposited layer, as well as similar shape of their respective responsivity curves.

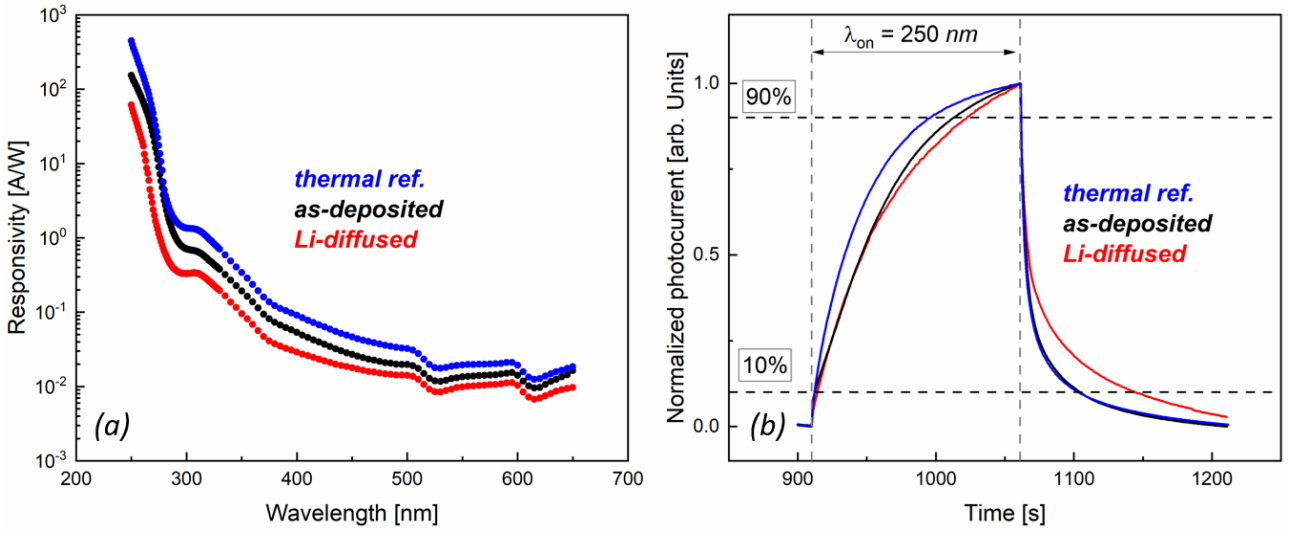

Figure 7.7 (a) Responsivity vs. wavelength for the as deposited (black), Li-diffused (red) and thermal reference (blue) κ-Ga_2O_3 based PDs. (b) the normalized photocurrent vs. time of the PDs for the 4th cycle acquired; for the first 150 s the samples were illuminated at λ_{ON} = 250 nm.

Noteworthy is the overlapping of the discharge section of the PDs based on the as-deposited and thermal treated κ-Ga_2O_3 epi-layer. Indeed, as discussed in Chapter 6 for H-related shallow and deep defects, the T_{dwell} here involved, *i.e.,* 550°C, should be enough to possibly induce the desorption of hydrogen from interstitial as well as related complexes (e.g., V_{Ga}-nH$_i$).[174] However, the atmosphere here involved is not well defined and this could explain the different behaviour reported w.r.t to κ-Ga_2O_3 based PD annealed in a well-defined atmosphere of O_2.

7.2.2 a-Ga_2O_3

The a-Ga_2O_3, as reported in Table 7.2, were involved only in the treatments at the lowest T_{dwell} = 350 °C. The mild temperature was chosen in order to avoid their crystallization, reported to happen for $T \geq 450$ °C.[237] Indeed, Raman spectra acquired post annealing treatment confirmed the amorphous structure of the layers, with only detection of the broad bands related to the soda-lime glass substrate [see Figure 7.8 (a)]. Nevertheless, the a-Ga_2O_3 layers were not further investigated since the wet etching in HCl, etched completely the a-Ga_2O_3 layers. The evidence was recorded by optical

microscope images, as reported in Figure 7.8 (b) and (c) for the layers after the annealing treatment and after the wet etching in HCl, respectively. The disappearance of the interference fringes indicates the complete etching of the amorphous film, hindering the continuation of the study on this category of samples.

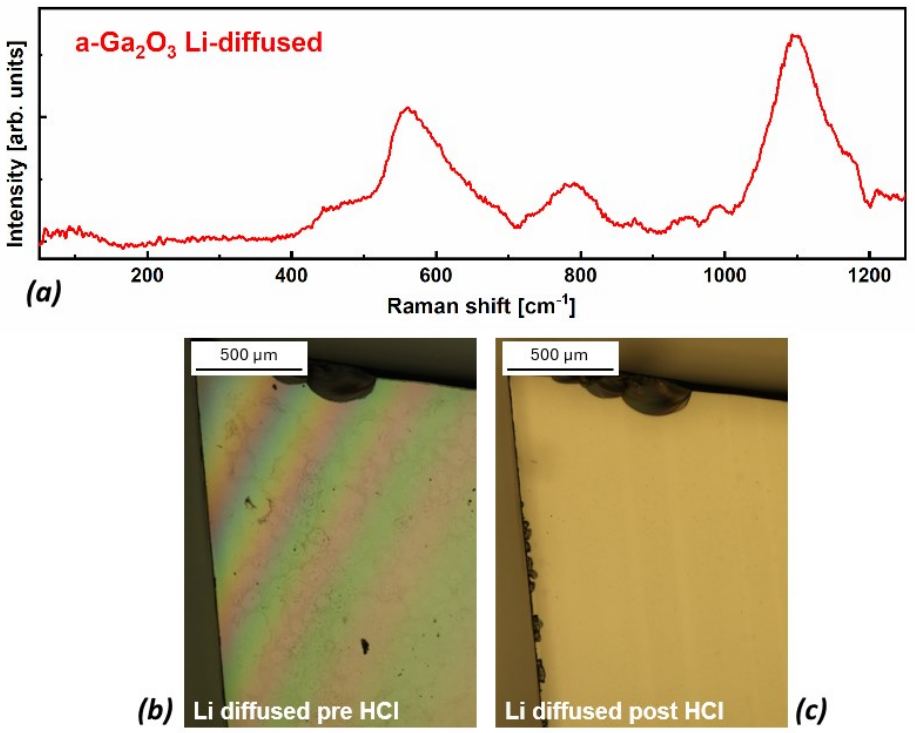

Figure 7.8 In (a) Raman spectrum of a-Ga_2O_3 after thermal Li-diffusion. The only visible broad bands are related to the soda-lime glass (substrate). The spectrum have been plotted after background and air spectrum subtraction. In (b) and (c) optical microscope images acquired with 50x objective magnification of the a-Ga_2O_3 layer on soda lime glass after Li-diffusion, pre (b) and post (c) HCl etching. From the disappearance of the interference fringes upon HCl etching the etching of the a-Ga_2O_3 by the HCl is evident.

7.2.3 (-201) β-Ga_2O_3 heteroepitaxial

For the Li-diffused (-201) β-Ga_2O_3 layers, the experimental investigation was conducted directly by means of ToF-SIMS, DRCL and electro-optical PDs characterization. Indeed, the insights collected on the κ-polymorph already stated that the Li-diffusion followed by an HCl etching did not majorly alter the surface morphology and the crystal structure of the layers. Nonetheless, there could be an effect of these cycles potentially independent from the Li diffusion itself.

The Li-profile recorded with ToF-SIMS for the β-heteroepitaxial layer after HCl etching [see Figure 7.9 (a)] confirmed the effective diffusion of Li in this epi-layer as well. However, the physical interpretation of the profile in terms of diffusion mechanism and the relative extraction of the diffusion coefficient was not possible for this sample. This could be related to the necessary condition

for the diffusion equation solution that here is not enforceable, *i.e.*, homogenous distribution of defects.[172] In this framework, it might be useful to remind that, differently from the case of the (001) κ-layers (*i.e.*, vertically oriented structural defects), in the case of (-201) β epitaxy the structural defects (*e.g.*, rotational domains) are not vertically oriented; in fact, they are distributed in a rather complicated symmetry due to the combined effect of the growth orientation and the monoclinic angle of its unit cell. Such more complicated system could complicate the interpretation of the experimentally obtained diffusion profile.

The Li-diffused sample was investigated with DRCL and compared to an as-deposited one. The evolution of the luminescence over the investigated acceleration voltages are reported in semilogarithmic scale in Figure 7.9 (b) and (c). In the insets, the spectra are reported in linear scale and normalized over the intensity at 450 nm. The spectra for both samples are consistent all over the range of acceleration voltages/penetration depths investigated. For the lowest acceleration voltages and small-wavelengths, the remarkable higher noise level of the acquired spectra is ascribed to a lower signal intensity of the samples w.r.t. the κ-layers [see Figure 7.6], and lower sensitivity of the detector for small wavelengths that resulted in a higher level of noise. However, the information is not compromised and no significant difference is detected for this Ga_2O_3 epilayer upon Li-diffusion.

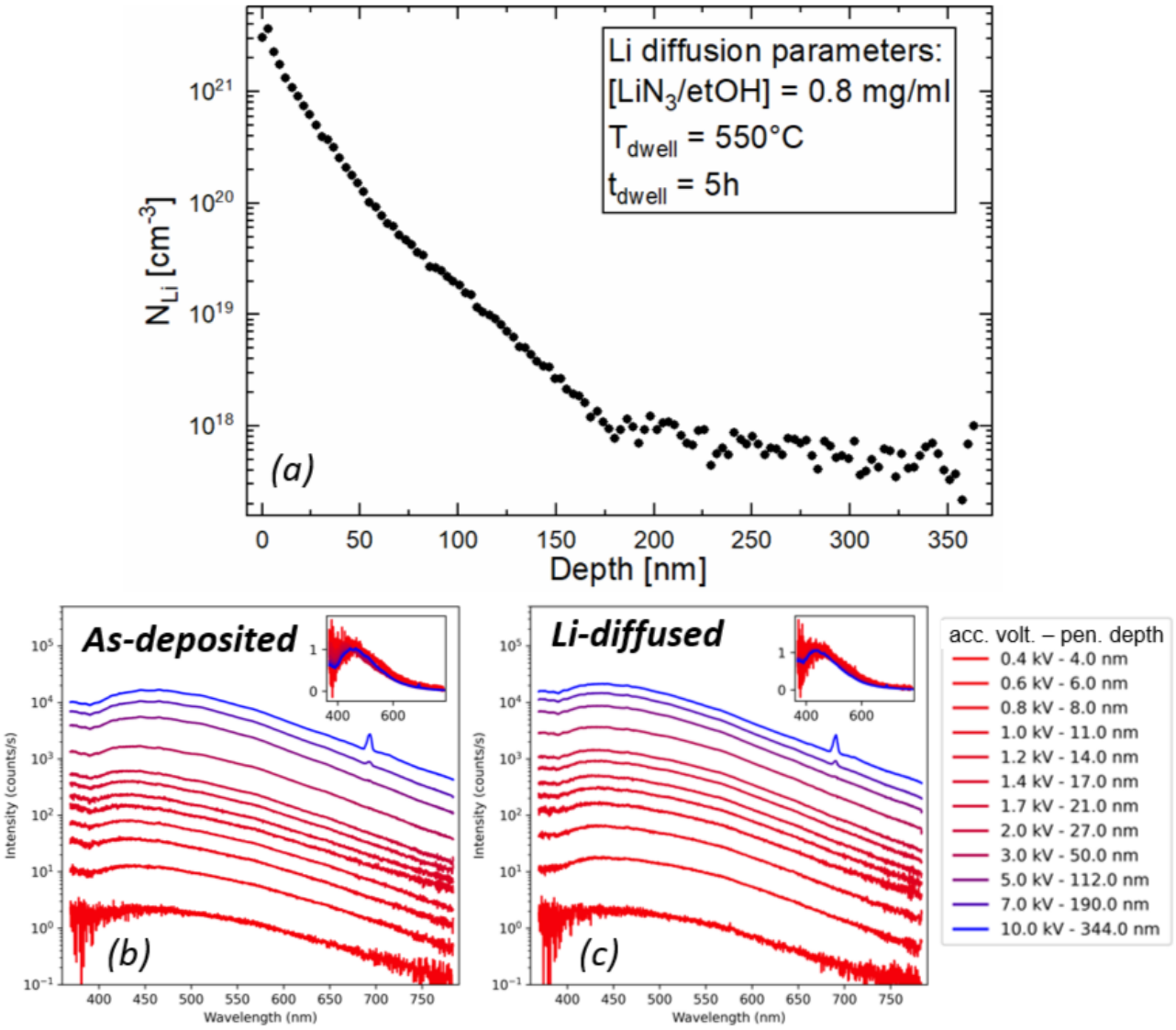

Figure 7.9 (a) Semilogarithmic scale of Li concentration vs. penetration depth in the (-201) β-Ga_2O_3 heteroepitaxial sample treated at T_{dwell} = 550°C for t_{dwell} = 5h. The thermal parameters and [LiN_3/EtOH] in solution are reported in the inset box. (b) and (c) DRCL spectra evolution with increasing acceleration voltages for the as deposited and Li-diffused (-201) β-Ga_2O_3, respectively. The spectra are plotted in semilogarithmic scale with colour scale going from red to blue for increasing acceleration voltage/probing depth. On the right, the colour scale correspondence to acceleration voltages and relative probing depth estimated with Monte Carlo method is reported and valid for both (b) and (c). In the insets, the same spectra are reported in linear scale and normalized on the intensity at 450 nm, for better comparison. The sharp peak located at $\lambda \approx 690$ nm for the highest acceleration voltages is the substrate contribution. This is reasonable considering the thickness of the (-201) β-layers (400 nm). According to [6], the Monte Carlo estimate of the penetration depth is consistent.

The PDs based on the Li-diffused, as-deposited and thermal treated (-201) β-layers were investigated as well [same approach described for the κ-Ga_2O_3 epi-layers]. In Table 7.6 some significant parameters are reported, *i.e.*, I_{dark}, R_R and the characteristic times τ_{ON} and τ_{OFF}. The responsivity vs. wavelength [see Figure 7.10 (a)] and the behaviour of the PDs in time [see Figure 7.10 (b)] reveals a way worst solar-blind performances with respect to the κ-Ga_2O_3 layers (as

highlighted by an about one order of magnitude lower R_R, compare Table 7.6 with Table 7.5). These experimental data generally suggest a higher density of defects in the β (-201) heteroepitaxial layers w.r.t. the κ ones. The Li-diffused sample is showing the same trend reported for the κ-Ga_2O_3 layer, with a shift towards lower responsivity values accompanied by a slightly lower I_{dark} and reporting the slowest discharge behaviour, *i.e.,* slowest τ_{OFF}.

Sample ID	I_{dark} @ 200 V [μA]	R_R	τ_{ON} [s]	τ_{OFF} [s]
as-deposited	0.1	1.8×10^2	75.7	98.5
Li-diffused	0.09	4.6×10^2	81.1	113.6
thermal ref.	0.02	2.5×10^2	54.2	88.1

Table 7.6 I_{dark}, R_R, τ_{ON} and τ_{OFF} values for PDs based on the as-deposited, Li-diffused and thermal treated. of the (-201) β-layers.

It is worth to mention that, differently from the κ polymorph,[195] in the case of β-Ga_2O_3 grown by MBE the presence of a large concentration of H-related complexes is not expected; such H-complexes should anyhow not be effected at such investigated annealing temperature (T_{dwell} = 550°C).[195] The limited variations in PD performance recorded upon vacuum annealing treatment are likely related to different defects / defect complexes, and possibly tightly bonded to the structural defectivity of the investigated layer. Similarly, also in the case of the Li diffused sample it is rather complicated to draw any significant conclusion solely based on these experimental data, apart from the fact that Li is indeed capable to thermally diffused in the β (-201) heteroepitaxial layers at the investigated experimental conditions.

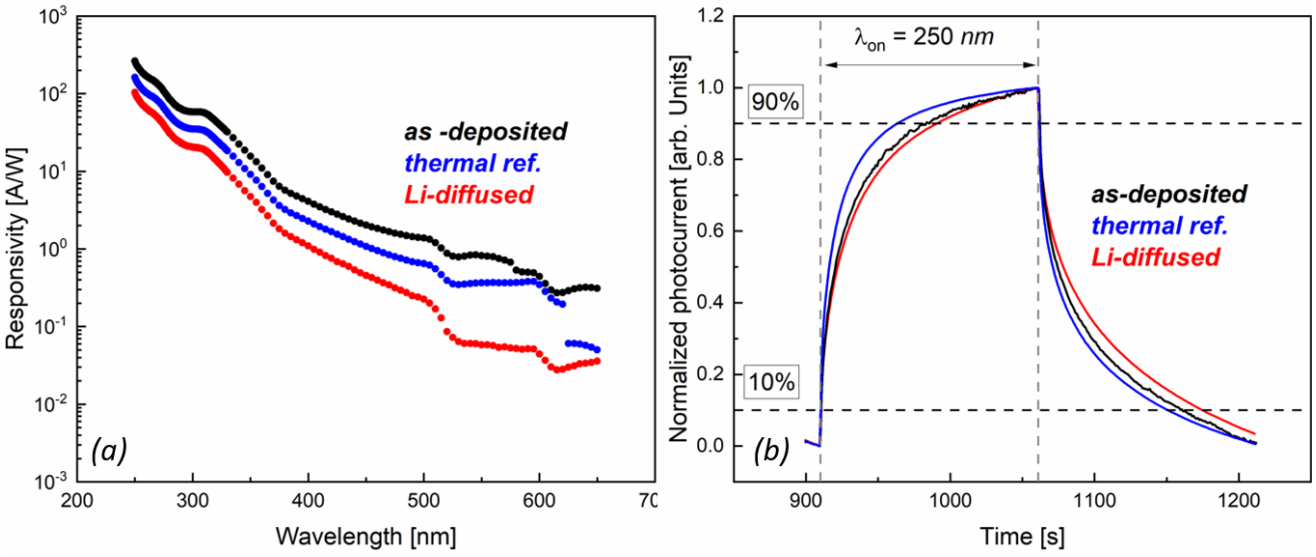

Figure 7.10 (a) PD responsivity vs. wavelength for the as deposited, Li-diffused and thermal reference (-201) β-Ga_2O_3. (b) the normalized photocurrent vs. time of the PDs is reported for the 4th cycle acquired; for the first 150 s the samples were illuminated at λ_{ON} = 250 nm.

7.2.4 (010) β-Ga_2O_3 homoepitaxial

For the (010) β-Ga_2O_3 homolayer, the ToF-SIMS upon thermal treatment in presence of the LiN_3 (T_{dwell} = 550°C, t_{dwell} = 5 h) clearly demonstrates that Li can indeed diffuse also in such material system [see Figure 7.11 (a) – black profile]. This immediately proofs that the Li diffusion is not strictly connected to the presence of structural defects in this material system, given the high crystal quality of (010) homoepitaxy. Indeed, the Li-profile extracted with ToF-SIMS well fits a bulk diffusion mechanism [inset of Figure 7.11 (a)], allowing for the extraction of a bulk diffusion coefficient for Li in the β-Ga_2O_3 matrix along [010], *i.e.,* $D_{Li,bulk} = 5.9 \times 10^{-16}\ cm^2 s^{-1}$. If compared with the one calculated for the bulk diffusion in the κ-Ga_2O_3 layer [Table 7.4], they are reasonably similar.

Differently from all the other Li-diffused material systems here investigated, the (010) homolayer transport properties (in dark) are significantly affected. Indeed, the sample, initially electrically insulating, becomes conductive upon the Li-diffusion process. A carrier system is detected with Hg-probed Current-Voltage (CV) measurements [see Figure 7.11 (a) – purple profile] up to 200 nm (*i.e.,* instrumental probing limit), suggesting an almost steady carrier system in the range of $n_{3D} \approx 4 \times 10^{17}\ cm^{-3}$. The n-type conductivity of the (010) homoepitaxial layer upon Li-diffusion is independently confirmed by Hall measurements in VdP configuration; the temperature-dependent behaviour of the carrier sheet density [n_{2D}] and mobility [μ] is reported in Figure 7.11 (b,c). The carrier system is characterized by a RT $n_{2D} = 1.7 \times 10^{13}\ cm^{-2}$ and mobility $\mu = 30\ cm^2 V^{-1} s^{-1}$. By combining data obtained from CV and Hall measurements (the 3D and 2D carrier densities, respectively) and considering a constant carrier profile (as suggested by the CV measurement), the thickness of the region affected by the carrier system can be estimated to be in the range of about 400 nm.

These results suggest that the Li-diffusion could have indeed affected the transport properties of the (010) layer. Nonetheless, it is fundamental to highlight the differences between the carrier system detected through CV, showing a steady carrier profile throughout the probed depth, and the Li diffusion profile [see Figure 7.11 (a) – purple and black curve, respectively]. Indeed, it is unlikely to directly relate the flat free-carrier profile of CV ($n_{3D} \approx 4 \times 10^{17}\ cm^{-3}$) and the SIMS diffusion one for Li. However, a valid hypothesis foresees Li playing an active role in the passivation of deep level acceptors (*e.g.*, V_{Ga}-related defects) present in the as deposited (010) β homo-layer. In such scenario,

the (at least partial) activation of the Si background [in the range of $2 \times 10^{18}\ cm^{-3}$, see Figure 7.11 (a) – blue curve] could justify the presence of the almost flat carrier profile.

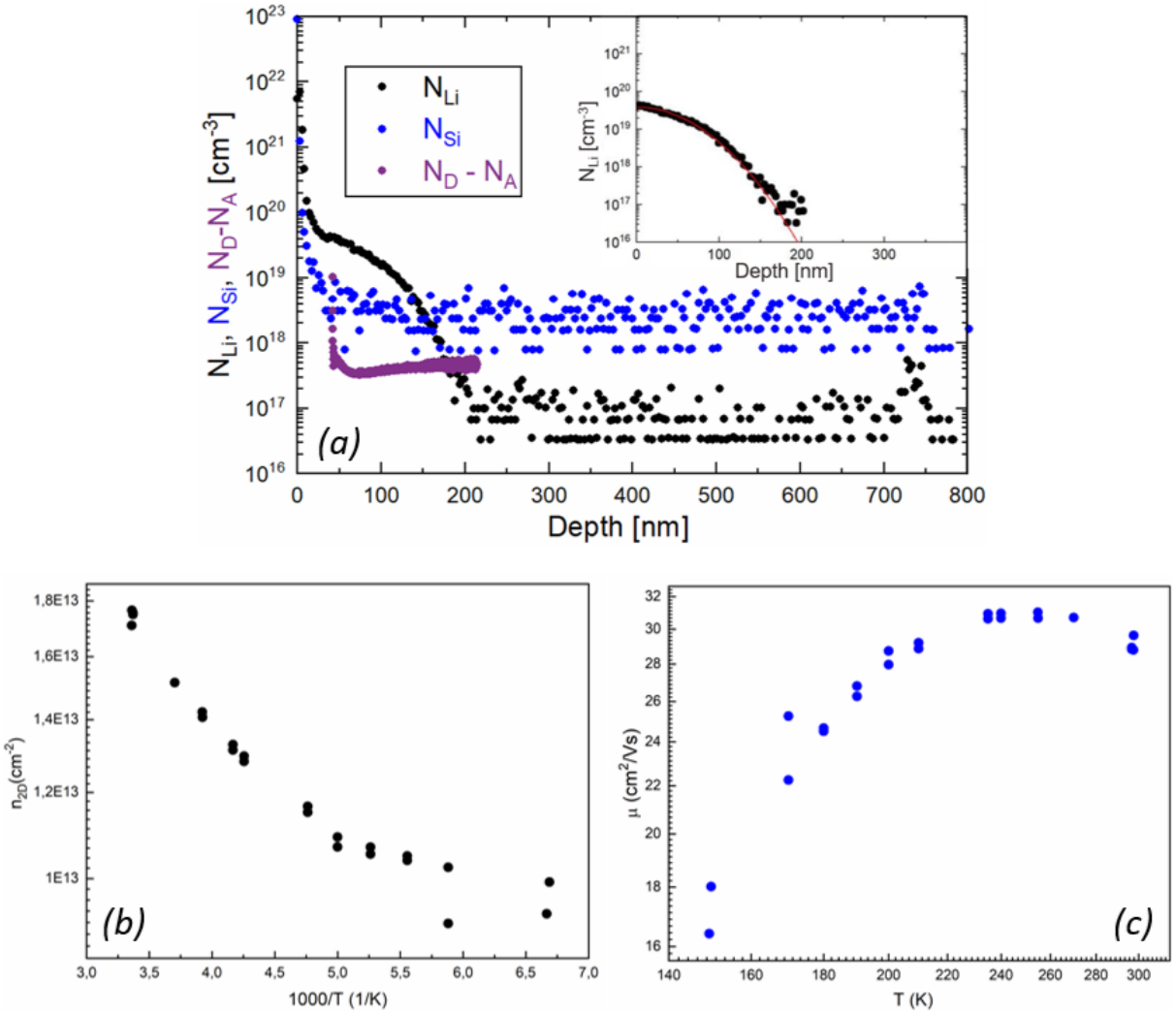

Figure 7.11 In (a) the ToF-SIMS concentration of Li (in black) and Si (in blue) together with the net donor density (N_D-N_A) detected with Hg-probed CV measurements (in purple) of the Li-diffused (010) β-Ga_2O_3 homoepitaxial layer. In the inset the fit of the Li-profile concentration. In (b) and (c) temperature dependence of sheet carrier density n_{2D} and mobility μ extracted from Hall measurements.

To further investigate the Li-diffused (010) β-layer, DRCL investigation was performed. Figure 7.12 (a-d) report the spectra acquired on (a) the Li-diffused, (b) an as-deposited conductive reference, as well as an insulating reference before (c) and after (d) the very same thermal treatment in vacuum but in a Li-free environment. The references samples, both conductive and insulating, have also a comparable Si background concentration to the one of the Li-diffused sample ($n \approx 10^{18}$ cm^{-3}). The origin of the different conductivity on those three as-deposited homo-layers can be justified by slight variations in the growth conditions (*e.g.,* ΔT_g), that are though the topic of another investigation and will be therefore not further commented in the framework of this thesis.

According to the DRCL spectra, all samples exhibit the intrinsic UV emission ($\lambda \approx 350$ nm), typically associated with self-trapped exciton recombination, which is known to be independent of the type of layer (*e.g.*, nominally undoped or extrinsically *n*-type doped).[238] Since the Li-diffused sample had not been investigated by DRCL before the Li-diffusion process (when it was electrically insulating), the as-deposited insulating layer [Figure 7.12 (c)] could be considered as its reference before the treatment. The insulating sample consistently displays the blue emission ($\lambda \approx 450$ nm), regardless of thermal treatment, usually attributed to donor-acceptor recombination and sometimes linked in literature to a higher concentration of oxygen vacancies (V_O).[238,239] Interestingly, while the emission from both conductive and as deposited insulating sample remains unchanged with increasing acceleration voltage, the Li-diffused sample shows a different behaviour. Specifically, at lower acceleration voltages, the blue emission is present and diminishes as the probing depth increases, suggesting an effect of Li over the local distribution of defects especially in the first 50 nm of the layer; nonetheless, slight variations of the collected CL spectra can be appreciated down to at least 200 nm penetration depths. In the case of the insulating sample that underwent a reference thermal cycle without Li in the annealing environment, just a relatively small variation is detected for the lowest acceleration voltage (penetration depth 4 nm), pointing towards a clear difference with respect to the Li-based treatment.

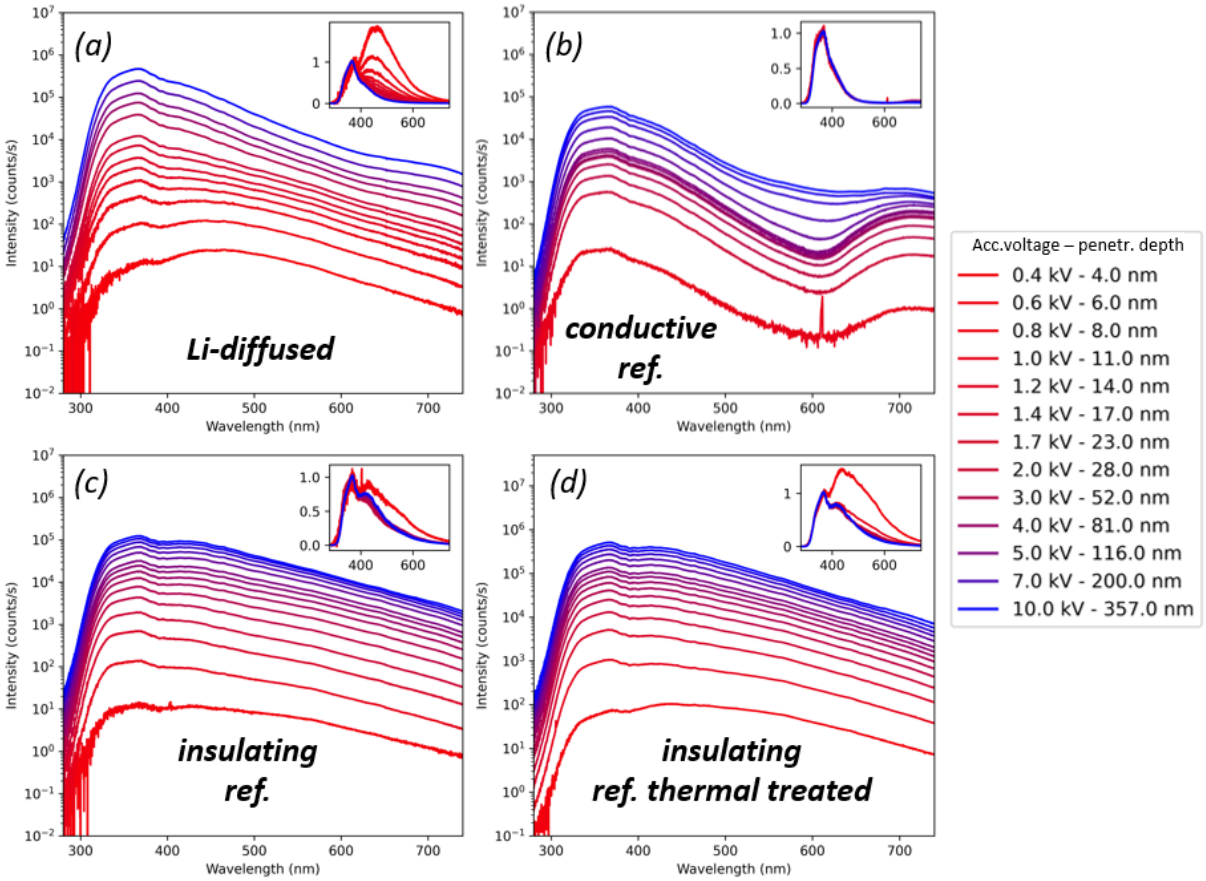

Figure 7.12 DRCL spectra of (a) Li-diffused, (b) an as-deposited conductive reference, (c) and (d) an insulating reference as deposited and after a thermal treatment in a Li free environment, respectively. In the inset of each figure, the DRCL spectra normalized on the intensity at 370 nm. In the box in the right the acceleration voltage-penetration depth relationship from Monte Carlo simulations.

The last experimental investigation performed on the Li-diffused (010) β-Ga_2O_3 homoepitaxial layer is Raman spectroscopy [see Figure 7.13]. The Raman spectrum of the Li-diffused sample was acquired using a UV laser (λ = 244 nm) to limit the most the probed thickness (*i.e.*, trying to be mostly sensitive to the Li-diffused part of the homoepitaxial layer). Indeed, the Li-diffused sample displays an additional vibrational mode at a Raman shift of 435 cm^{-1}, not shown by the two different references, *i.e.,* insulating and conductive (pink and green curves, respectively). Vibrational modes near this position have been attributed to Li-O vibrations in the LiO_4 tetrahedra in various Li- and O-containing compounds.[240,241]

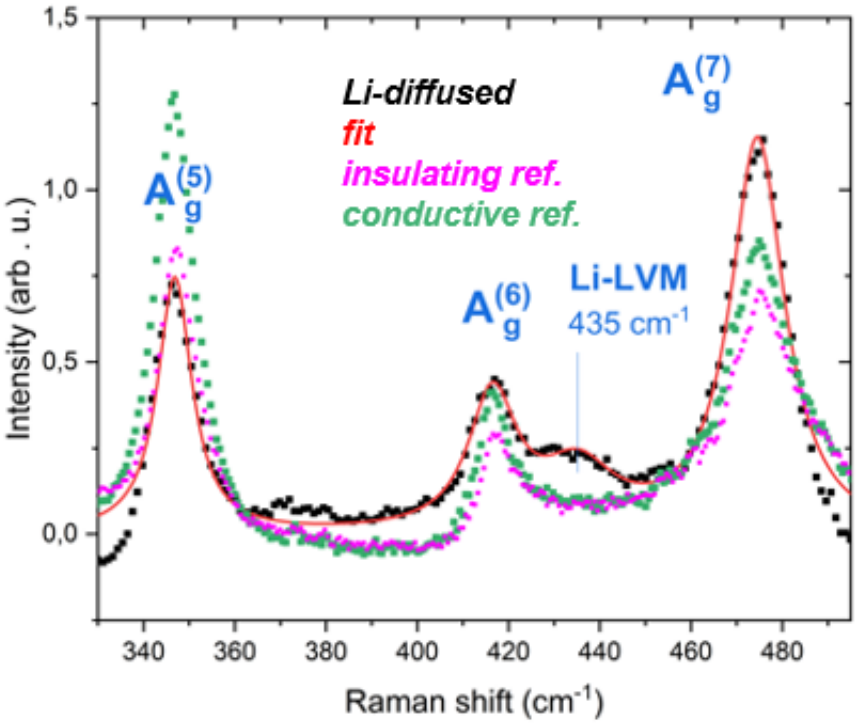

Figure 7.13 Raman spectra of the Li-diffused sample and relative fit (black and red curves) and the references samples, conductive (in green) and insulating (in pink).

All the information collected so far seems to point towards the fact that (i) Li could indeed diffuse in (010) β-Ga_2O_3, and that (ii) the absence of large amounts of structural defects in this homo-layer system allows to highlight its active role in affecting the transport properties of β-Ga_2O_3. In order to further investigate point (ii), some theoretical calculations have been added to this investigation as reported in the section below.

7.3 Theoretical inputs

Ab-initio DFT theoretical calculations were performed considering the monoclinic β-phase. As already pointed out in Section 6.3, strong analogies are present w.r.t. the κ-polymorph that allows to reasonably assume also in that material system a qualitatively similar behaviour of Li (even if in presence of potentially different energy barriers for diffusion / complexes dissociations). The formation energy diagrams for Li interstitials (Li_i) and substitutional in the two inequivalent Ga sites (Li_{GaI} and Li_{GaII}) are reported in Figure 7.14 (a) and (b) for Ga-rich and O-rich conditions, respectively. Li_i is expected to be a shallow donor, more prone to be formed under Ga-rich conditions. Moreover, a migration barrier of ≈ 0.4 eV was calculated for Li_i along the [010] of β-Ga_2O_3. Li_{Ga} are expected to behave as deep acceptor levels for n-type samples; their formation is more energetically favourable with respect to Li_i especially in O-rich conditions (for $E_F > 3$ eV).

According to the collected theoretical inputs and considering the relatively low concentration of carriers w.r.t. the actual Li concentration detected by SIMS in the Li-diffused (010) β-layer [see Figure 7.11 (a)], the possible interpretation of the Li diffusion mechanism foresees the Li to mostly passivate V_{Ga}. In fact, due to the charge states of Li^{+1} and V_{Ga}^{+3}, each V_{Ga} defects could accommodate up to three Li^{+1}, with a similar mechanism wr.t. the one reported for Zn diffusion in β-Ga_2O_3 layers.[242] In this framework, the background Si-concentration (considering Si_{Ga} as a shallow donor in the monoclinic structure)[243] could become the main source of the carrier system detected upon the Li-diffusion. Additional theoretical calculations should also address whether a similar situation could be expected in presence of split gallium vacancies, which should be the most favourable acceptor like defects expected in the β-Ga_2O_3 material system up to concentrations exceeding the mid 10^{18} cm^{-3}.[194,244]

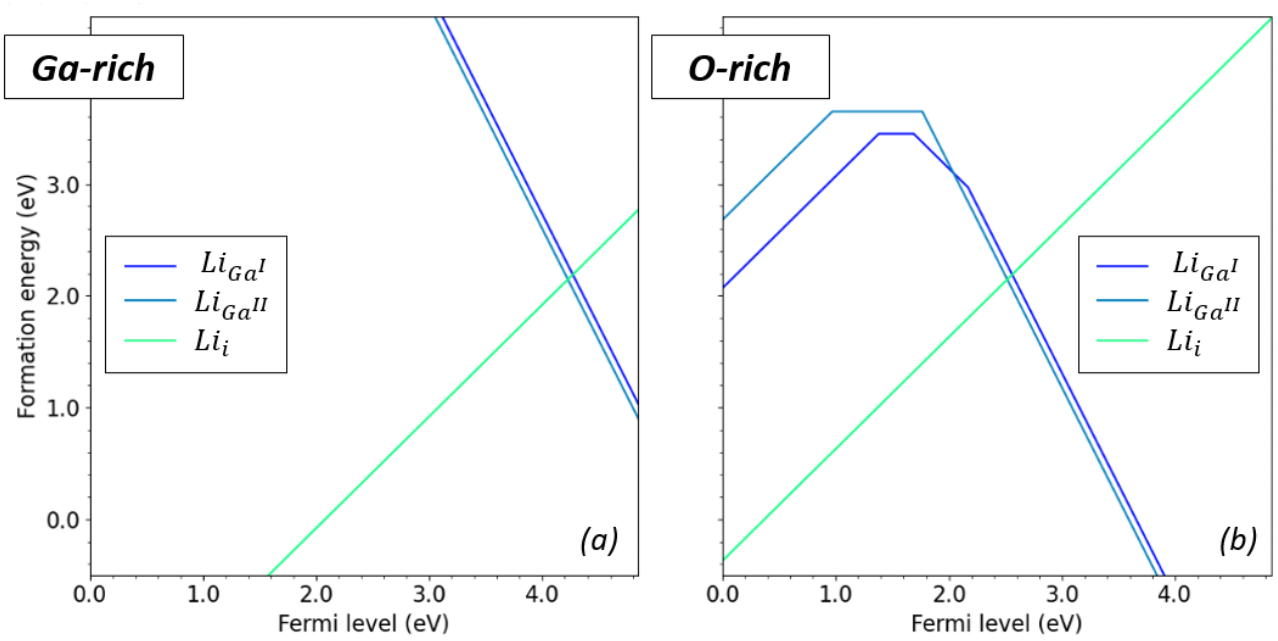

Figure 7.14 (a) and (b) formation energy diagrams for Li substitutional in Ga^I and Ga^{II} site as well as Li interstitial for Ga-rich and O-rich conditions, respectively.

7.4 Conclusions

Given the collected results on the different Ga_2O_3 thin films, it clearly appears that Li-diffusion should be taken into account even at mild temperatures, *i.e.*, $T \geq 350$ °C; the diffusion temperatures considered for this study are in line with the ones commonly used in (i) post-growth annealing treatment of Ga_2O_3 (for the realization of Ti/Au Ohmic contacts)[143] as well as (ii) for the deposition of Li:NiO or $LiGa_5O_8$ *p*-type layers.[209,234,245] Therefore the Li diffusion should be carefully considered for the realization of *pn*-heterojunctions involving Li.[213,234]

Thanks to this investigation, the bulk diffusion coefficient of Li in the Ga_2O_3 matrix has been extracted for the first time, *i.e.,* $D_{Li,bulk} = 2 - 6 \cdot 10^{-16} cm^2 s^{-1}$. However, even though Li-diffusion was effective in the three different epi-layers (amorphous layers are not included in the discussion), a different effect was detected according to the defective nature of the layers. In κ-Ga_2O, characterized by vertically oriented structural defects, a combined bulk/2D defects-mediated diffusion was recorded. A slight effect on the functional properties was recorded over the superficial layer through DRCL and even in the PDs performances, especially concerning the photocurrent time decay. These evidences suggest an effect of Li over the local distribution of defects especially in the first nanometers of the layers, interested by bulk diffusion. However, it is reasonable to assume that the fastest Li diffusion through defects, higher $D_{Li,2D}$ diffusion coefficient, would account for Li-segregation at the grain/domains borders. In this regard, the different nature of structural defects (*e.g.*, possibly leading to non-saturated dandling bonds) and possible interaction with the diffused Li must still be well understood. A similar interpretation can be provided for Li-diffusion in the (-201) β-heteroepitaxial layers, where even though Li was effectively diffusing, the intrinsic randomly oriented defective structure does not allowed for an interpretation of the diffusion mechanism of Li; nevertheless, in the defective (-201) β-heteroepitaxial layers the Li diffusion was not found to significantly affect the functional properties of the epi-layers.

A different scenario is reported for (010) β-homoepitaxy. Indeed, this is the only case where a clear effect over the transport properties have been reported upon Li-diffusion for the layer. In this regard, the detected conductivity should be most likely related to the passivation of deep level defects by Li, with the consequent activation of an unintentional Si-background present in the homo-layers deposited by MBE. Additional experiments (*e.g.*, Li diffusion on homoepitaxial β-Ga_2O_3 with lower background concentration of Si) could be performed to clarify the possible role as shallow donor of Li_i.

8 Conclusions and outlooks

The work here discussed was focused on the relation between epitaxial growth and functional properties of Ga_2O_3 thin films, with particular focus on the metastable orthorhombic polymorph (κ). After a general overview over the Ga_2O_3 material system (Chapter 2), the attention has been mostly drawn on κ-Ga_2O_3. The possibility to fully exploit / demonstrate its theoretically predicted great potential in new generation electronic devices (considering its large predicted spontaneous polarization and suggested ferroelectric behaviour) is not trivial. In fact, this is currently hindered by the inherent defective structure related to the κ-Ga_2O_3 heteroepitaxy, mostly dominated by a large concentration of vertically oriented structural defect (*e.g.*, anti-phase boundaries and rotational domains). Indeed, in Chapter 4, the first proof of the defect-mediated transport anisotropy in κ-Ga_2O_3 epitaxy is provided thanks to a direct comparison of the in-plane and out-of-plane conductivity. Moreover, a throughout study was conducted over the effect of a Φ_{SiH4} (Si-source for extrinsic doping) on MOVPE grown κ-Ga_2O_3 layers; particularly, the experimental data highlight (i) a direct relation between the Φ_{SiH4} and the significant enlargement of the rotational domains average size resulting in (ii) an indicative improvement of the in-plane electrical properties of the layers. This work furnished then a possible approach to mitigate the defective nature of this material and a definitive proof of the role of structural defects over the transport properties of the material. In this framework, a methodology to qualitatively investigate the rotational domains average size in this material system by means of non-destructive techniques was also provided, *i.e.,* through Raman and XRD. Moreover, the characterization of a SnO/κ-Ga_2O_3 *pn* planar diode, further supports the insights gathered so far, emphasizing how the performances of the device are closely linked to the structural defective nature of the κ-Ga_2O_3 heteroepitaxy, at least when in-plane transport is involved. These findings could be significant for the development of novel device architectures, where different engineering strategies should be considered to overcome the in-plane conduction limitations in κ-Ga_2O_3 epitaxial layers.

Hence, after an overview over the state-of-the-art approaches to mitigate / suppress the presence of rotational domains in κ-Ga_2O_3 heteroepitaxy, Chapter 5 reported the epitaxial growths performed by the candidate via MBE on top of different substrates, *i.e.,* epitaxially matched ε-$GaFeO_3$ and (0001) α-Al_2O_3 with defined in-plane offcut. The extensive work conducted for substrates characterization and pre-treatments as well as to explore different MBE synthesis conditions that could allow to stabilize the metastable κ-phase (*e.g.,* conventional MBE, In-MEXCAT, δ-SnO_x MEXCAT) is reported. In particular, a thorough characterization of the deposited layers allowed to highlight how the growth parameters (*i.e.,* T_g, P_{RF}, metal / O fluxes) play a significant role over the κ-phase stability and layer quality. Even though the work here reported did not obtain the suppression

of the κ-Ga_2O_3 rotational domains, the collected results shade light on the possible issues strictly related to the catalyst-mediated MBE technique adopted. In this framework, the MOVPE technique (new reactor installed and growth parameters now optimized in IMEM-UniPr) will be soon exploited in this framework. Indeed, the different MOVPE growth conditions (*e.g.*, no need of O-plasma nor additional metal catalyst) could help mitigating the issues encountered with the MBE growths.

In Chapter 6, an in-depth study focusing on the point defects in κ-Ga_2O_3 is presented. By comparing the performance of κ-Ga_2O_3-based photodetectors fabricated via MOVPE and MBE, and subjected to thermal treatments in different environments (O_2 and H_2), alongside experimental (structural – optical) and theoretical investigations, the role of native defects and common impurities (such as hydrogen) in the κ-Ga_2O_3 material system is better understood. Additionally, this study provides an effective method for engineering the concentration of different H-related defects, demonstrating the related potential for κ-Ga_2O_3-based devices.

Finally, Chapter 7 reports the first *ex-situ* lithium diffusion in different Ga_2O_3 structures. It is demonstrated that Li can diffuse in Ga_2O_3 even at mild temperatures ($T \geq 350$°C). Furthermore, the study allowed for an estimation of the Li bulk diffusion coefficient in both the β and the κ-Ga_2O_3 polymorphs and provides an experimental demonstration of its active role in a Si-doped (010) β-Ga_2O_3 homoepitaxial layer. Generally, the determination of the role of Li as a shallow / deep level defect upon diffusion is suggested to be strictly connected to the intimate defective structure of the analysed epilayers. Theoretical inputs also suggested a possible role of Li in passivating/mitigating the deep native defects. These results should be considered when designing metal oxide/Ga_2O_3 based *pn* heterojunctions where Li is involved (*e.g.,* Li:NiO, $LiGa_5O_8$).

Appendix A

Implantation standard

In order to quantify the Li-amount detected with ToF-SIMS measurements in the Li-diffused layers, a Li-implantation standard sample in UID κ- and β-Ga_2O_3 matrices were provided by K. Mizohata and F. Tuomisto from University of Helsinki. The implantations were performed with an implantation energy of 28 keV and 7° tilt angle at two different fluences, *i.e.,* $1.43 \cdot 10^{13}\ at/cm^2$ and $1.43 \cdot 10^{14}\ at/cm^2$. The ToF-SIMS measurement performed on the implantation standard samples allows for the extraction of the relative sensitivity factor (*RSF*). Table A.1 reports the *RSF* values for the κ- and β-Ga_2O_3 matrices implanted at the two different fluences. In the κ-layer implanted at lower fluence [I1], Li-signal was not detected and it was not possible to extract the RSF.

Sample	Matrix	Fluence [at/cm^{-2}]	*RSF* [at/cm^{-3}]
I1	κ-Ga_2O_3	$1.43 \cdot 10^{13}$	/
I2	κ-Ga_2O_3	$1.43 \cdot 10^{14}$	$2.51 \cdot 10^{22}$ $2.49 \cdot 10^{22}$
I3	β-Ga_2O_3	$1.43 \cdot 10^{13}$	$1.94 \cdot 10^{22}$ $2.90 \cdot 10^{22}$
I4	β-Ga_2O_3	$1.43 \cdot 10^{14}$	$2.08 \cdot 10^{22}$

Table A.1 Sum-up of the Li implantation standard parameters performed in the κ- and β-Ga_2O_3 matrices at two different implantation fluences and relative *RSF* extracted.

The *RSF* values allows for the quantification of Li according to Equation A.1.

$$N_{Li}[cm^{-3}] = \frac{I(Li^+)}{I(Ga^+)} \cdot RSF$$

Equation A.1

ToF-SIMS diffusion mechanism interpretation

The Li-profiles detected in the κ-Ga_2O_3 layers treated under more severe thermal conditions [see Figure 7.5 (b)] are showing two distinct regions with two different slopes associated to two different diffusion mechanism. The first part of the profiles is ascribed to a bulk diffusion. It can be fitted with the thin-film solution of the diffusion equation allowing extraction of the Li-bulk diffusion coefficient ($D_{Li,bulk}$) according to Equation A.2. The $D_{Li,bulk}$ values are reported in Table 7.4.

$$\ln[N_{Li}(x)] \sim \frac{x^2}{4D_{Li,bulk}t}$$

Equation A.2 Thin film solution fitting for $D_{Li,bulk}$ extraction, with $N_{Li}(x)$ the Li concentration at the penetration depth x and t is diffusion time, here considered equal to the dwell time.

Profile	$D_{Li,bulk}$ [cm^2s^{-1}]	$d_{2D} \cdot D_{Li,2D}$ [cm^3s^{-1}]	$D_{Li,2D}$ *for* d_{2D} = 1 nm [cm^2s^{-1}]
T_{dwell} = 550°C, t_{dwell} = 2h	$2.8 \cdot 10^{-16}$	$1.4 \cdot 10^{-20}$	$1.4 \cdot 10^{-13}$
T_{dwell} = 550°C, t_{dwell} = 5h	$9.1 \cdot 10^{-17}$	$6.9 \cdot 10^{-21}$	$6.9 \cdot 10^{-14}$
Average values	$1.9 \cdot 10^{-16}$	$1.0 \cdot 10^{-20}$	$1.0 \cdot 10^{-13}$

Table A.2 Values of the bulk diffusion coefficients of Li ($D_{Li,bulk}$), the product of the thickness of the 2D defects (d_{2D}) and the diffusion coefficient along the 2D defects ($D_{Li,2D}$) and the $D_{Li,2D}$ calculated assuming d_{2D} = 1 nm, for κ-Ga_2O_3 layers treated at T_{dwell} = 550°C and different dwell times. The average values are reported as well.

The second part of the profiles is associated to a combination of fast diffusion along 2D extended defects and slower diffusion into the bulk, perpendicularly to the defects borders. It was fitted according to the Harrison type B classification using the solution of the diffusion equation suggested by Chung *et al.*[236] Here, first the parameter η as function of the penetration depth x is calculated according to Equation A.3.

$$\eta = \frac{x}{\left(D_{Li,bulk}t\right)^{1/2}}$$

Equation A.3 Definition of η parameter as function of the penetration depth x, the bulk-diffusion coefficient $D_{Li,bulk}$, obtained from the first part of the profile fitted with the thin-film solution equation, and the diffusion time t.

From the behaviour of the $\ln[N_{Li}(x)]$ vs. $\eta^{6/5}$ (see Figure A.1), the slope m of the linear fit (red curve) can be extracted.

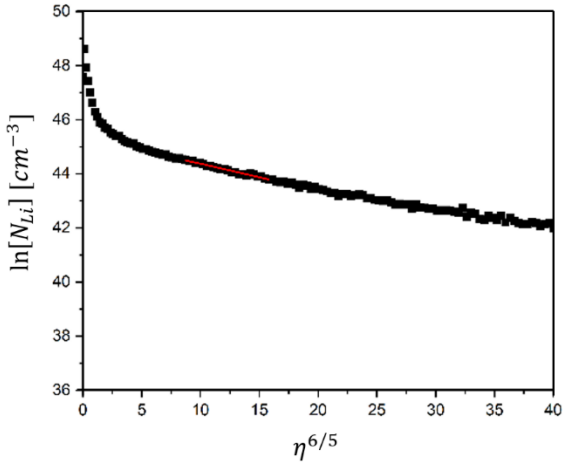

Figure A.1 The $ln[N_{Li}]$ vs. $\eta^{6/5}$ and the corresponding linear fit (red curve) for the extraction of m value.

The value of m yields then to Equation A.4, that allows for the calculation of the product of the thickness of the 2D defects (d_{2D}) and the diffusion coefficient along the 2D defects ($D_{Li,2D}$). The values of the product so calculated are reported in Table 7.4, for the Li-profiles investigated. Assuming then, the thickness of the defects d_{2D} = 1nm, the $D_{Li,2D}$ can be calculated, as reported as well in Table 7.4.

$$d_{2D}D_{Li,2D} = \left(D_{Li,bulk}\right)^{1.5} t^{0.5} 10^{A} (-m)^{B}$$

Equation A.4 Definition of the product of the thickness of the 2D defects (d_{2D}) and the diffusion coefficient along such defects ($D_{Li,2D}$) as function of $D_{Li,bulk}$, diffusion time t, the slope extracted from the linear fit m (see in Figure A.1) and A and B, parameters according to Chung *et al.*[236]

Bibliography

[1] M. Riordan, L. Hoddeson, and C. Herring, “The invention of the transistor,” Rev. Mod. Phys. **71**(2), S336–S345 (1999).

[2] H. Morkoc, and P.M. Solomon, “The hemt: A superfast transistor: An experimental GaAs-AlGoAs device switches in picoseconds and generates little heat. This is just what supercomputers need,” IEEE Spectr. **21**(2), 28–35 (1984).

[3] R. Dupuis, “An introduction to the development of the semiconductor laser,” IEEE J. Quantum Electron. **23**(6), 651–657 (1987).

[4] S. Nakamura, and M.R. Krames, “History of Gallium–Nitride-Based Light-Emitting Diodes for Illumination,” Proc. IEEE **101**(10), 2211–2220 (2013).

[5] H. Riechert, “Lighting the 21st century,” Phys. Status Solidi A **212**(5), 893–896 (2015).

[6] J.Y. Tsao, J. Han, R.H. Haitz, and P.M. Pattison, “The Blue LED Nobel Prize: Historical context, current scientific understanding, human benefit,” Ann. Phys. Leipz. **527**(5–6), (2015).

[7] G. Cassabois, P. Valvin, and B. Gil, “Hexagonal boron nitride is an indirect bandgap semiconductor,” Nat. Photonics **10**(4), 262–266 (2016).

[8] J.Y. Tsao, S. Chowdhury, M.A. Hollis, D. Jena, N.M. Johnson, K.A. Jones, R.J. Kaplar, S. Rajan, C.G. Van de Walle, E. Bellotti, C.L. Chua, R. Collazo, M.E. Coltrin, J.A. Cooper, K.R. Evans, S. Graham, T.A. Grotjohn, E.R. Heller, M. Higashiwaki, M.S. Islam, P.W. Juodawlkis, M.A. Khan, A.D. Koehler, J.H. Leach, U.K. Mishra, R.J. Nemanich, R.C.N. Pilawa-Podgurski, J.B. Shealy, Z. Sitar, M.J. Tadjer, A.F. Witulski, M. Wraback, and J.A. Simmons, “Ultrawide-Bandgap Semiconductors: Research Opportunities and Challenges,” Adv. Electron. Mater. **4**(1), 1600501 (2018).

[9] J. Shi, J. Zhang, L. Yang, M. Qu, D.-C. Qi, K. H. L. Zhang, “Wide Bandgap Oxide Semiconductors: from Materials Physics to Optoelectronic Devices,” Advanced Materials - Wiley Online Library,” **33**, 2006230 (2021).

[10] M.H. Wong, O. Bierwagen, R.J. Kaplar, and H. Umezawa, “Ultrawide-bandgap semiconductors: An overview,” J. Mater. Res. **36**(23), 4601–4615 (2021).

[11] M. Zhang, Z. Liu, L. Yang, J. Yao, J. Chen, J. Zhang, W. Wei, Y. Guo, and W. Tang, “β-Ga2O3-Based Power Devices: A Concise Review,” Crystals **12**(3), 406 (2022).

[12] M. Higashiwaki, “β-Ga2O3 material properties, growth technologies, and devices: a review,” AAPPS Bull. **32**(1), 3 (2022).

[13] M. Higashiwaki, and S. Fujita, editors , *Gallium Oxide: Materials Properties, Crystal Growth, and Devices* (Springer International Publishing, Cham, 2020).

[14] R. Roy, V.G. Hill, and E.F. Osborn, “Polymorphism of Ga2O3 and the System Ga2O3-H2O,” J. Am. Chem. Soc. **74**(3), 719–722 (1952).

[15] M. Feneberg, J. Bläsing, T. Sekiyama, K. Ota, K. Akaiwa, K. Ichino, and R. Goldhahn, “Anisotropic phonon properties and effective electron mass in α-Ga2O3,” Appl. Phys. Lett. **114**(14), 142102 (2019).

[16] S. Yoshioka, H. Hayashi, A. Kuwabara, F. Oba, K. Matsunaga, and I. Tanaka, “Structures and energetics of Ga2O3 polymorphs,” J. Phys. Condens. Matter **19**(34), 346211 (2007).

[17] J. Furthmüller, F. Bechstedt, “ Quasiparticle bands and spectra of Ga2O3 polymorphs,” Phys. Rev. B **93**, 115204 (2016).

[18] T. Oshima, T. Nakazono, A. Mukai, and A. Ohtomo, "Epitaxial growth of γ-Ga2O3 films by mist chemical vapor deposition," J. Cryst. Growth **359**, 60–63 (2012).

[19] T. Kato, H. Nishinaka, K. Shimazoe, K. Kanegae, and M. Yoshimoto, "Demonstration of Bixbyite-Structured δ-Ga2O3 Thin Films Using β-Fe2O3 Buffer Layers by Mist Chemical Vapor Deposition," ACS Appl. Electron. Mater. **5**(3), 1715–1720 (2023).

[20] I. Cora, F. Mezzadri, F. Boschi, M. Bosi, M. Čaplovičová, G. Calestani, I. Dódony, B. Pécz, and R. Fornari, "The real structure of ε-Ga $_2$ O $_3$ and its relation to κ-phase," CrystEngComm **19**(11), 1509–1516 (2017).

[21] Z. Galazka, "Growth of bulk β-Ga2O3 single crystals by the Czochralski method," J. Appl. Phys. **131**(3), 031103 (2022).

[22] Y. Tomm, P. Reiche, D. Klimm, and T. Fukuda, "Czochralski grown Ga2O3 crystals," J. Cryst. Growth **220**(4), 510–514 (2000).

[23] M. Higashiwaki, K. Sasaki, H. Murakami, Y. Kumagai, A. Koukitu, A. Kuramata, T. Masui, and S. Yamakoshi, "Recent progress in Ga2O3 power devices," Semicond. Sci. Technol. **31**(3), 034001 (2016).

[24] H. Aida, K. Nishiguchi, H. Takeda, N. Aota, K. Sunakawa, and Y. Yaguchi, "Growth of β-Ga2O3 Single Crystals by the Edge-Defined, Film Fed Growth Method," Jpn. J. Appl. Phys. **47**(11R), 8506 (2008).

[25] A. Kuramata, K. Koshi, S. Watanabe, Y. Yamaoka, T. Masui, and S. Yamakoshi, "High-quality β-Ga2O3 single crystals grown by edge-defined film-fed growth," Jpn. J. Appl. Phys. **55**(12), 1202A2 (2016).

[26] N. Ueda, H. Hosono, R. Waseda, and H. Kawazoe, "Synthesis and control of conductivity of ultraviolet transmitting β-Ga2O3 single crystals," Appl. Phys. Lett. **70**(26), 3561–3563 (1997).

[27] E.G. Víllora, K. Shimamura, Y. Yoshikawa, K. Aoki, and N. Ichinose, "Large-size β-Ga2O3 single crystals and wafers," J. Cryst. Growth **270**(3), 420–426 (2004).

[28] K. Hoshikawa, E. Ohba, T. Kobayashi, J. Yanagisawa, C. Miyagawa, and Y. Nakamura, "Growth of β-Ga2O3 single crystals using vertical Bridgman method in ambient air," J. Cryst. Growth **447**, 36–41 (2016).

[29] X. Gao, K. Ma, Z. Jin, D. Wu, J. Wang, R. Yang, N. Xia, H. Zhang, and D. Yang, "Characteristics of 4-inch (100) oriented Mg-doped β-Ga2O3 bulk single crystals grown by a casting method," J. Alloys Compd. **987**, 174162 (2024).

[30] E.G. Víllora, K. Shimamura, Y. Yoshikawa, T. Ujiie, and K. Aoki, "Electrical conductivity and carrier concentration control in β-Ga2O3 by Si doping," Appl. Phys. Lett. **92**(20), 202120 (2008).

[31] A. Ardenghi, O. Bierwagen, A. Falkenstein, G. Hoffmann, J. Lähnemann, M. Martin, and P. Mazzolini, "Toward controllable Si-doping in oxide molecular beam epitaxy using a solid SiO source: Application to β-Ga2O3," Appl. Phys. Lett. **121**(4), 042109 (2022).

[32] J. Yang, F. Ren, S.J. Pearton, and A. Kuramata, "Vertical Geometry, 2-A Forward Current Ga $_2$ O $_3$ Schottky Rectifiers on Bulk Ga $_2$ O $_3$ Substrates," IEEE Trans. Electron Devices **65**(7), 2790–2796 (2018).

[33] J. Yang, S. Ahn, F. Ren, S.J. Pearton, S. Jang, J. Kim, and A. Kuramata, "High reverse breakdown voltage Schottky rectifiers without edge termination on Ga2O3," Appl. Phys. Lett. **110**(19), 192101 (2017).

[34] S.J. Pearton, F. Ren, M. Tadjer, and J. Kim, "Perspective: Ga2O3 for ultra-high power rectifiers and MOSFETS," J. Appl. Phys. **124**(22), 220901 (2018).

[35] T. Oshima, T. Okuno, N. Arai, N. Suzuki, S. Ohira, and S. Fujita, "Vertical Solar-Blind Deep-Ultraviolet Schottky Photodetectors Based on β-Ga2O3 Substrates," Appl. Phys. Express **1**(1), 011202 (2008).

[36] Y. Kokubun, K. Miura, F. Endo, and S. Nakagomi, "Sol-gel prepared β-Ga2O3 thin films for ultraviolet photodetectors," Appl. Phys. Lett. **90**(3), 031912 (2007).

[37] Y.-C. Chen, Y.-J. Lu, Q. Liu, C.-N. Lin, J. Guo, J.-H. Zang, Y.-Z. Tian, and C.-X. Shan, "Ga2O3 photodetector arrays for solar-blind imaging," J. Mater. Chem. C **7**(9), 2557–2562 (2019).

[38] X. Yu, T.J. Marks, and A. Facchetti, "Metal oxides for optoelectronic applications," Nat. Mater. **15**, 383 (2016).

[39] M. Bosi, P. Mazzolini, L. Seravalli, and R. Fornari, "Ga $_2$ O $_3$ polymorphs: tailoring the epitaxial growth conditions," J. Mater. Chem. C **8**(32), 10975–10992 (2020).

[40] R. Schewski, G. Wagner, M. Baldini, D. Gogova, Z. Galazka, T. Schulz, T. Remmele, T. Markurt, H. von Wenckstern, M. Grundmann, O. Bierwagen, P. Vogt, and M. Albrecht, "Epitaxial stabilization of pseudomorphic α-Ga2O3on sapphire (0001)," Appl. Phys. Express **8**(1), 011101 (2014).

[41] H. Nishinaka, D. Tahara, and M. Yoshimoto, "Heteroepitaxial growth of ε-Ga2O3 thin films on cubic (111) MgO and (111) yttria-stablized zirconia substrates by mist chemical vapor deposition," Jpn. J. Appl. Phys. **55**(12), 1202BC (2016).

[42] H. Nishinaka, H. Komai, D. Tahara, Y. Arata, and M. Yoshimoto, "Microstructures and rotational domains in orthorhombic ε-Ga2O3 thin films," Jpn. J. Appl. Phys. **57**(11), 115601 (2018).

[43] M.B. Maccioni, and V. Fiorentini, "Phase diagram and polarization of stable phases of (Ga1−xInx)2O3," Appl. Phys. Express **9**(4), 041102 (2016).

[44] J. Kim, D. Tahara, Y. Miura, and B.G. Kim, "First-principle calculations of electronic structures and polar properties of (κ,ε)-Ga2O3," Appl. Phys. Express **11**(6), 061101 (2018).

[45] K. Shimada, "First-principles study of crystal structure, elastic stiffness constants, piezoelectric constants, and spontaneous polarization of orthorhombic Pna21-M2O3 (M = Al, Ga, In, Sc, Y)," Mater. Res. Express **5**(3), 036502 (2018).

[46] F. Mezzadri, G. Calestani, F. Boschi, D. Delmonte, M. Bosi, and R. Fornari, "Crystal Structure and Ferroelectric Properties of ε-Ga2O3 Films Grown on (0001)-Sapphire," Inorg. Chem. **55**(22), 12079–12084 (2016).

[47] M. Kneiß, A. Hassa, D. Splith, C. Sturm, H. von Wenckstern, M. Lorenz, and M. Grundmann, "Epitaxial stabilization of single phase κ-(InxGa1−x)2O3 thin films up to x = 0.28 on c-sapphire and κ-Ga2O3(001) templates by tin-assisted VCCS-PLD," APL Mater. **7**(10), 101102 (2019).

[48] M. Kneiß,, P. Storm, A. Hassa, D. Splith, H. von Wenckstern, M. Lorenz, M. Grundmann, "Epitaxial Growth of κ-$(Al_xGa_{1-x})_2O_3$ Layers and Superlattice Heterostructures up to $x = 0.48$ on Highly Conductive Al-Doped ZnO Thin-Film Templates by Pulsed Laser Deposition", Phys. Status Solidi B, **258**, 2000359 (2021)

[49] P. Storm, M. Kneiß, A. Hassa, T. Schultz, D. Splith, H. von Wenckstern, N. Koch, M. Lorenz, and M. Grundmann, "Epitaxial κ-(AlxGa1−x)2O3 thin films and heterostructures grown by tin-assisted VCCS-PLD," APL Mater. **7**(11), 111110 (2019).

[50] T. Schultz, M. Kneiß, P. Storm, D. Splith, H. von Wenckstern, M. Grundmann, and N. Koch, "Band Offsets at κ-([Al,In]xGa1–x)2O3/MgO Interfaces," ACS Appl. Mater. Interfaces **12**(7), 8879–8885 (2020).

[51] R. Kumaran, T. Tiedje, S.E. Webster, S. Penson, and W. Li, "Epitaxial Nd-doped α-(Al1−xGax)2O3 films on sapphire for solid-state waveguide lasers," Opt. Lett. **35**(22), 3793 (2010).

[52] M.S. Williams, M. Alonso-Orts, M. Schowalter, A. Karg, S. Raghuvansy, J.P. McCandless, D. Jena, A. Rosenauer, M. Eickhoff, and P. Vogt, "Growth, catalysis, and faceting of α-Ga2O3 and α-(InxGa1−x)2O3 on m-plane α-Al2O3 by molecular beam epitaxy," APL Mater. **12**(1), 011120 (2024).

[53] M. Baldini, D. Gogova, K. Irmscher, M. Schmidbauer, G. Wagner, and R. Fornari, "Heteroepitaxy of Ga2(1-x)In2xO3 layers by MOVPE with two different oxygen sources," Cryst. Res. Technol. **49**(8), 552–557 (2014).

[54] P. Mazzolini, C. Wouters, M. Albrecht, A. Falkenstein, M. Martin, P. Vogt, and O. Bierwagen, "Molecular Beam Epitaxy of β-(InxGa1–x)2O3 on β-Ga2O3 (010): Compositional Control, Layer Quality, Anisotropic Strain Relaxation, and Prospects for Two-Dimensional Electron Gas Confinement," ACS Appl. Mater. Interfaces **16**(10), 12793–12804 (2024).

[55] P. Ranga, S.B. Cho, R. Mishra, and S. Krishnamoorthy, "Highly tunable, polarization-engineered two-dimensional electron gas in ε-AlGaO3/ε-Ga2O3 heterostructures," Appl. Phys. Express **13**(6), 061009 (2020).

[56] S.B. Cho, and R. Mishra, "Epitaxial engineering of polar ε-Ga2O3 for tunable two-dimensional electron gas at the heterointerface," Appl. Phys. Lett. **112**(16), 162101 (2018).

[57] H.Y. Kang, M.J. Yeom, J.Y. Yang, Y. Choi, J. Lee, C. Park, G. Yoo, and R.B. Kyu Chung, "Epitaxial κ-Ga2O3/GaN heterostructure for high electron-mobility transistors," Mater. Today Phys. **31**, 101002 (2023).

[58] P. Mazzolini, Z. Fogarassy, A. Parisini, F. Mezzadri, D. Diercks, M. Bosi, L. Seravalli, A. Sacchi, G. Spaggiari, D. Bersani, O. Bierwagen, B.M. Janzen, M.N. Marggraf, M.R. Wagner, I. Cora, B. Pécz, A. Tahraoui, A. Bosio, C. Borelli, S. Leone, and R. Fornari, "Silane-Mediated Expansion of Domains in Si-Doped κ-Ga2O3 Epitaxy and its Impact on the In-Plane Electronic Conduction," Adv. Funct. Mater. **33**(2), 2207821 (2023).

[59] M. Kneiß, D. Splith, P. Schlupp, A. Hassa, H. von Wenckstern, M. Lorenz, and M. Grundmann, "Realization of highly rectifying Schottky barrier diodes and *pn* heterojunctions on κ -Ga 2 O 3 by overcoming the conductivity anisotropy," J. Appl. Phys. **130**(8), 084502 (2021).

[60] B.M. Janzen, "Vibrational and optical properties of gallium oxide polymorphs," (2024).

[61] T. Oshima, Y. Kato, M. Imura, Y. Nakayama, and M. Takeguchi, "α-Al2O3 / Ga2O3 superlattices coherently grown on r -plane sapphire," Appl. Phys. Express **11**(6), 065501 (2018).

[62] M. Kracht, A. Karg, M. Feneberg, J. Bläsing, J. Schörmann, R. Goldhahn, and M. Eickhoff, "Anisotropic Optical Properties of Metastable $(01 \bar{1} 2)$ $\alpha - Ga_2O_3$ Grown by Plasma-Assisted Molecular Beam Epitaxy," Phys. Rev. Appl. **10**(2), (2018).

[63] A. Segura, L. Artús, R. Cuscó, R. Goldhahn, and M. Feneberg, "Band gap of corundumlike α-Ga2O3 determined by absorption and ellipsometry," Phys. Rev. Mater. **1**(2), 024604 (2017).

[64] T. Kawaharamura, G.T. Dang, and M. Furuta, "Successful Growth of Conductive Highly Crystalline Sn-Doped α-Ga2O3 Thin Films by Fine-Channel Mist Chemical Vapor Deposition," Jpn. J. Appl. Phys. **51**(4R), 040207 (2012).

[65] T. Uchida, K. Kaneko, and S. Fujita, "Electrical characterization of Si-doped n-type α-Ga2O3 on sapphire substrates," MRS Adv. **3**(3), 171–177 (2018).

[66] K. Akaiwa, K. Kaneko, K. Ichino, and S. Fujita, "Conductivity control of Sn-doped α-Ga2O3 thin films grown on sapphire substrates," Jpn. J. Appl. Phys. **55**(12), 1202BA (2016).

[67] D. Shinohara, and S. Fujita, "Heteroepitaxy of Corundum-Structured α-Ga2O3 Thin Films on α-Al2O3 Substrates by Ultrasonic Mist Chemical Vapor Deposition," Jpn. J. Appl. Phys. **47**(9R), 7311 (2008).

[68] T. Oshima, T. Okuno, and S. Fujita, “Ga2O3 Thin Film Growth on c-Plane Sapphire Substrates by Molecular Beam Epitaxy for Deep-Ultraviolet Photodetectors,” Jpn. J. Appl. Phys. **46**(11R), 7217 (2007).

[69] K. Kaneko, H. Kawanowa, H. Ito, and S. Fujita, “Evaluation of Misfit Relaxation in α-Ga2O3 Epitaxial Growth on α-Al2O3 Substrate,” Jpn. J. Appl. Phys. **51**(2R), 020201 (2012).

[70] S.-D. Lee, Y. Ito, K. Kaneko, and S. Fujita, “Enhanced thermal stability of alpha gallium oxide films supported by aluminum doping,” Jpn. J. Appl. Phys. **54**(3), 030301 (2015).

[71] K. Kaneko, S. Fujita, T. Shinohe, and K. Tanaka, “Progress in α-Ga2O3 for practical device applications,” Jpn. J. Appl. Phys. **62**(SF), SF0803 (2023).

[72] L.E. Ratcliff, T. Oshima, F. Nippert, B.M. Janzen, E. Kluth, R. Goldhahn, M. Feneberg, P. Mazzolini, O. Bierwagen, C. Wouters, M. Nofal, M. Albrecht, J.E.N. Swallow, L.A.H. Jones, P.K. Thakur, T.-L. Lee, C. Kalha, C. Schlueter, T.D. Veal, J.B. Varley, M.R. Wagner, and A. Regoutz, “Tackling Disorder in γ-Ga2O3,” Adv. Mater., (2022).

[73] H.Y. Playford, A.C. Hannon, E.R. Barney, and R.I. Walton, “Structures of Uncharacterised Polymorphs of Gallium Oxide from Total Neutron Diffraction,” Chem. – Eur. J. **19**(8), 2803–2813 (2013).

[74] T. Oshima, Y. Kato, M. Oda, T. Hitora, and M. Kasu, “Epitaxial growth of γ-(AlxGa1−x)O3 alloy films for band-gap engineering,” Appl. Phys. Express **10**(5), 051104 (2017).

[75] K. Jiang, J. Tang, M.J. Cabral, A. Park, L. Gu, R.F. Davis, and L.M. Porter, “Layered phase composition and microstructure of κ-Ga2O3-dominant heteroepitaxial films grown via MOCVD,” J. Appl. Phys. **131**(5), 055305 (2022).

[76] Th. Dittrich, A. Parisini, M. Pavesi, A. Baraldi, A. Sacchi, F. Mezzadri, P. Mazzolini, M. Bosi, L. Seravalli, A. Bosio, and R. Fornari, “Electronic states near surfaces and interfaces of β-Ga2O3 and κ-Ga2O3 epilayers investigated by surface photovoltage spectroscopy, photoconductivity and optical absorption,” Surf. Interfaces **51**, 104642 (2024).

[77] Y. Xu, J.-H. Park, Z. Yao, C. Wolverton, M. Razeghi, J. Wu, and V.P. Dravid, “Strain-Induced Metastable Phase Stabilization in Ga2O3 Thin Films,” ACS Appl. Mater. Interfaces **11**(5), 5536–5543 (2019).

[78] J. Furthmüller, and F. Bechstedt, “Quasiparticle bands and spectra of Ga2O3 polymorphs,” Phys. Rev. B **93**(11), 115204 (2016).

[79] J. Ahman, G. Svensson, and J. Albertsson, “A Reinvestigation of β-Gallium Oxide,” Acta Crystallogr. Sect. C **52**(6), 1336–1338 (1996).

[80] H.H. Tippins, “Optical Absorption and Photoconductivity in the Band Edge of β-Ga2O3,” Phys Rev **140**(1A), A316–A319 (1965).

[81] F. Ricci, F. Boschi, A. Baraldi, A. Filippetti, M. Higashiwaki, A. Kuramata, V. Fiorentini, and R. Fornari, “Theoretical and experimental investigation of optical absorption anisotropy in β-Ga2O3,” J. Phys. Condens. Matter **28**(22), 224005 (2016).

[82] T. Matsumoto, M. Aoki, A. Kinoshita, and T. Aono, “Absorption and Reflection of Vapor Grown Single Crystal Platelets of β-Ga2O3,” Jpn. J. Appl. Phys. **13**(10), 1578 (1974).

[83] T. Onuma, S. Saito, K. Sasaki, T. Masui, T. Yamaguchi, T. Honda, and M. Higashiwaki, “Valence band ordering in β-Ga2O3 studied by polarized transmittance and reflectance spectroscopy,” Jpn. J. Appl. Phys. **54**(11), 112601 (2015).

[84] A. Navarro-Quezada, S. Alamé, N. Esser, J. Furthmüller, F. Bechstedt, Z. Galazka, D. Skuridina, and P. Vogt, "Near valence-band electronic properties of semiconducting β-Ga2O3 (100) single crystals," Phys. Rev. B **92**(19), 195306 (2015).

[85] A. Mock, R. Korlacki, C. Briley, V. Darakchieva, B. Monemar, Y. Kumagai, K. Goto, M. Higashiwaki, and M. Schubert, "Band-to-band transitions, selection rules, effective mass, and excitonic contributions in monoclinic β-Ga2O3" Phys. Rev. B **96**(24), 245205 (2017).

[86] J.A. Spencer, A.L. Mock, A.G. Jacobs, M. Schubert, Y. Zhang, and M.J. Tadjer, "A review of band structure and material properties of transparent conducting and semiconducting oxides: Ga2O3, Al2O3, In2O3, ZnO, SnO2, CdO, NiO, CuO, and Sc2O3," Appl. Phys. Rev. **9**(1), 011315 (2022).

[87] H. Peelaers, and C.G. Van de Walle, "Brillouin zone and band structure of β-Ga2O3," Phys. Status Solidi B **252**(4), 828–832 (2015).

[88] K. Yamaguchi, "First principles study on electronic structure of β-Ga2O3," Solid State Commun. **131**(12), 739–744 (2004).

[89] H. He, M.A. Blanco, and R. Pandey, "Electronic and thermodynamic properties of β-Ga2O3," Appl. Phys. Lett. **88**(26), 261904 (2006).

[90] J.B. Varley, J.R. Weber, A. Janotti, and C.G. Van de Walle, "Oxygen vacancies and donor impurities in β-Ga2O3," Appl. Phys. Lett. **97**(14), 142106 (2010).

[91] L. Dong, R. Jia, B. Xin, B. Peng, and Y. Zhang, "Effects of oxygen vacancies on the structural and optical properties of β-Ga2O3," Sci. Rep. **7**, 40160 (2017).

[92] T. Gake, Y. Kumagai, and F. Oba, "First-principles study of self-trapped holes and acceptor impurities in Ga2O3 polymorphs," Phys. Rev. Mater. **3**(4), 044603 (2019).

[93] J.B. Varley, A. Janotti, C. Franchini, and C.G. Van de Walle, "Role of self-trapping in luminescence and p-type conductivity of wide-band-gap oxides," Phys. Rev. B **85**(8), 081109 (2012).

[94] B.E. Kananen, L.E. Halliburton, K.T. Stevens, G.K. Foundos, and N.C. Giles, "Gallium vacancies in β-Ga2O3 crystals," Appl. Phys. Lett. **110**(20), 202104 (2017).

[95] T. Zacherle, P.C. Schmidt, and M. Martin, "Ab initio calculations on the defect structure of β-Ga2O3," Phys. Rev. B **87**(23), 235206 (2013).

[96] J. Lee, S. Ganguli, A.K. Roy, and S.C. Badescu, "Density functional tight binding study of β-Ga2O3: Electronic structure, surface energy, and native point defects," J. Chem. Phys. **150**(17), 174706 (2019).

[97] S. Lany, "Defect phase diagram for doping of Ga2O3," APL Mater. **6**(4), 046103 (2018).

[98] J. L. Lyons, "A survey of acceptor dopants for β-Ga2O3," Semicond. Sci. Technol. **33**(5), 05LT02 (2018).

[99] A. Kyrtsos, M. Matsubara, and E. Bellotti, "Migration mechanisms and diffusion barriers of vacancies in Ga2O3," Phys. Rev. B **95**(24), 245202 (2017).

[100] H. Peelaers, J.L. Lyons, J.B. Varley, and C.G. Van de Walle, "Deep acceptors and their diffusion in Ga2O3," APL Mater. **7**(2), 022519 (2019).

[101] X. Wang, T. Liu, Y. Lu, Q. Li, R. Guo, X. Jiao, and X. Xu, "Thermodynamic of intrinsic defects in β-Ga2O3," J. Phys. Chem. Solids **132**, 104–109 (2019).

[102] B.M. Janzen, P. Mazzolini, R. Gillen, A. Falkenstein, M. Martin, H. Tornatzky, J. Maultzsch, O. Bierwagen, and M.R. Wagner, "Isotopic study of Raman active phonon modes in β-Ga2O3," J. Mater. Chem. C **9**(7), 2311–2320 (2021).

[103] A. Mauze, Y. Zhang, T. Itoh, E. Ahmadi, and J.S. Speck, "Sn doping of (010) β-Ga2O3 films grown by plasma-assisted molecular beam epitaxy," Appl. Phys. Lett. **117**(22), 222102 (2020).

[104] S.C. Siah, R.E. Brandt, K. Lim, L.T. Schelhas, R. Jaramillo, M.D. Heinemann, D. Chua, J. Wright, J.D. Perkins, C.U. Segre, R.G. Gordon, M.F. Toney, and T. Buonassisi, "Dopant activation in Sn-doped Ga2O3 investigated by X-ray absorption spectroscopy," Appl. Phys. Lett. **107**(25), 252103 (2015).

[105] M. Baldini, M. Albrecht, A. Fiedler, K. Irmscher, R. Schewski, and G. Wagner, "Si- and Sn-Doped Homoepitaxial β-Ga2O3 Layers Grown by MOVPE on (010)-Oriented Substrates," ECS J. Solid State Sci. Technol. **6**(2), Q3040–Q3044 (2017).

[106] E. Ahmadi, O.S. Koksaldi, S.W. Kaun, Y. Oshima, D.B. Short, U.K. Mishra, and J.S. Speck, "Ge doping of β-Ga2O3 films grown by plasma-assisted molecular beam epitaxy," Appl. Phys. Express **10**(4), 041102 (2017).

[107] W. Zhou, C. Xia, Q. Sai, and H. Zhang, "Controlling n-type conductivity of β-Ga2O3 by Nb doping," Appl. Phys. Lett. **111**(24), 242103 (2017).

[108] A.J. Green, J. Speck, and G. Xing, "β-Gallium oxide power electronics," APL Mater., 41 (2022).

[109] P. Vogt, and O. Bierwagen, "The competing oxide and sub-oxide formation in metal-oxide molecular beam epitaxy," Appl. Phys. Lett. **106**(8), 081910 (2015).

[110] P. Mazzolini, A. Falkenstein, C. Wouters, R. Schewski, T. Markurt, Z. Galazka, M. Martin, M. Albrecht, and O. Bierwagen, "Substrate-orientation dependence of β-Ga2O3 (100), (010), (001), and (-201) homoepitaxy by indium-mediated metal-exchange catalyzed molecular beam epitaxy (MEXCAT-MBE)," APL Mater. **8**(1), 011107 (2020).

[111] P. Mazzolini, A. Falkenstein, Z. Galazka, M. Martin, and O. Bierwagen, "Offcut-related step-flow and growth rate enhancement during (100) β-Ga2O3 homoepitaxy by metal-exchange catalyzed molecular beam epitaxy (MEXCAT-MBE)," Appl. Phys. Lett. **117**(22), 222105 (2020).

[112] R. Schewski, K. Lion, A. Fiedler, C. Wouters, A. Popp, S.V. Levchenko, T. Schulz, M. Schmidbauer, S. Bin Anooz, R. Grüneberg, Z. Galazka, G. Wagner, K. Irmscher, M. Scheffler, C. Draxl, and M. Albrecht, "Step-flow growth in homoepitaxy of β-Ga2O3 (100)—The influence of the miscut direction and faceting," APL Mater. **7**(2), 022515 (2018).

[113] P. Vogt, O. Brandt, H. Riechert, J. Lähnemann, and O. Bierwagen, "Metal-Exchange Catalysis in the Growth of Sesquioxides: Towards Heterostructures of Transparent Oxide Semiconductors," Phys. Rev. Lett. **119**(19), 196001 (2017).

[114] M. Kracht, A. Karg, J. Schörmann, M. Weinhold, D. Zink, F. Michel, M. Rohnke, M. Schowalter, B. Gerken, A. Rosenauer, P.J. Klar, J. Janek, and M. Eickhoff, "Tin-Assisted Synthesis of ε−Ga2O3 by Molecular Beam Epitaxy," Phys Rev Appl. **8**(5), 054002 (2017).

[115] P. Vogt, F.V.E. Hensling, K. Azizie, J.P. McCandless, J. Park, K. DeLello, D.A. Muller, H.G. Xing, D. Jena, and D.G. Schlom, "Extending the Kinetic and Thermodynamic Limits of Molecular-Beam Epitaxy Utilizing Suboxide Sources or Metal-Oxide-Catalyzed Epitaxy," Phys. Rev. Appl. **17**(3), 034021 (2022).

[116] T.-S. Chou, P. Seyidov, S. Bin Anooz, R. Grüneberg, T.T.V. Tran, K. Irmscher, M. Albrecht, Z. Galazka, J. Schwarzkopf, and A. Popp, "Fast homoepitaxial growth of (100) β-Ga2O3 thin films via MOVPE," AIP Adv. **11**(11), 115323 (2021).

[117] T.S. Ngo, D.D. Le, J. Lee, S.-K. Hong, J.-S. Ha, W.-S. Lee, and Y.-B. Moon, "Investigation of defect structure in homoepitaxial ($2\bar{0}1$) β-Ga2O3 layers prepared by plasma-assisted molecular beam epitaxy," J. Alloys Compd. **834**, 155027 (2020).

[118] A. Fiedler, R. Schewski, M. Baldini, Z. Galazka, G. Wagner, M. Albrecht, and K. Irmscher, "Influence of incoherent twin boundaries on the electrical properties of β-Ga2O3 layers homoepitaxially grown by metal-organic vapor phase epitaxy," J. Appl. Phys. **122**(16), 165701 (2017).

[119] R. Fornari, M. Pavesi, V. Montedoro, D. Klimm, F. Mezzadri, I. Cora, B. Pécz, F. Boschi, A. Parisini, A. Baraldi, C. Ferrari, E. Gombia, and M. Bosi, "Thermal stability of ε-Ga2O3 polymorph," Acta Mater. **140**(Supplement C), 411–416 (2017).

[120] M. Bosi, L. Seravalli, P. Mazzolini, F. Mezzadri, and R. Fornari, "Thermodynamic and Kinetic Effects on the Nucleation and Growth of ε/κ- or β-Ga2O3 by Metal–Organic Vapor Phase Epitaxy," Cryst. Growth Des. **21**(11), 6393–6401 (2021).

[121] Y. Oshima, E.G. Víllora, Y. Matsushita, S. Yamamoto, and K. Shimamura, "Epitaxial growth of phase-pure ε-Ga2O3 by halide vapor phase epitaxy," J. Appl. Phys. **118**(8), 085301 (2015).

[122] Y. Zhang, Y. Gong, X. Chen, Y. Kuang, J. Hao, F.-Fang. Ren, S. Gu, R. Zhang, and J. Ye, "Unlocking the Single-Domain Heteroepitaxy of Orthorhombic κ-Ga2O3 via Phase Engineering," ACS Appl. Electron. Mater., (2021).

[123] Y. Cai, K. Zhang, Q. Feng, Y. Zuo, Z. Hu, Z. Feng, H. Zhou, X. Lu, C. Zhang, W. Tang, J. Zhang, and Y. Hao, "Tin-assisted growth of ε-Ga2O3 film and the fabrication of photodetectors on sapphire substrate by PLD," Opt. Mater. Express **8**(11), 3506 (2018).

[124] M. Kneiß, A. Hassa, D. Splith, C. Sturm, H. von Wenckstern, T. Schultz, N. Koch, M. Lorenz, and M. Grundmann, "Tin-assisted heteroepitaxial PLD-growth of κ-Ga2O3 thin films with high crystalline quality," APL Mater. **7**(2), 022516 (2018).

[125] A. Ardenghi, O. Bierwagen, J. Lähnemann, E. Luna, J. Kler, A. Falkenstein, M. Martin, A. Sacchi, and P. Mazzolini, "Phase-selective growth of κ- vs β-Ga2O3 and (InxGa1−x)2O3 by In-mediated metal exchange catalysis in plasma-assisted molecular beam epitaxy," APL Mater. **12**(10), 101103 (2024).

[126] A. Karg, A. Hinz, S. Figge, M. Schowalter, P. Vogt, A. Rosenauer, and M. Eickhoff, "Indium: A surfactant for the growth of ε/κ-Ga2O3 by molecular beam epitaxy," APL Mater. **11**(9), 091114 (2023).

[127] A. Karg, M. Kracht, P. Vogt, A. Messow, N. Braud, J. Schörmann, M. Rohnke, J. Janek, J. Falta, and M. Eickhoff, "Enhanced epitaxial growth of Ga2O3 using an ultrathin SnO2 layer," J. Appl. Phys. **132**(19), 195304 (2022).

[128] F. Boschi, M. Bosi, T. Berzina, E. Buffagni, C. Ferrari, and R. Fornari, "Hetero-epitaxy of ε-Ga2O3 layers by MOCVD and ALD," J. Cryst. Growth **443**, 25–30 (2016).

[129] H. Nishinaka, O. Ueda, D. Tahara, Y. Ito, N. Ikenaga, N. Hasuike, and M. Yoshimoto, "Single-Domain and Atomically Flat Surface of κ-Ga2O3 Thin Films on FZ-Grown ε-GaFeO3 Substrates via Step-Flow Growth Mode," ACS Omega, (2020).

[130] M. Pavesi, F. Fabbri, F. Boschi, G. Piacentini, A. Baraldi, M. Bosi, E. Gombia, A. Parisini, and R. Fornari, "ε-Ga2O3 epilayers as a material for solar-blind UV photodetectors," Mater. Chem. Phys. **205**, 502–507 (2018).

[131] A. Parisini, A. Bosio, V. Montedoro, A. Gorreri, A. Lamperti, M. Bosi, G. Garulli, S. Vantaggio, and R. Fornari, "Si and Sn doping of ε-Ga 2 O 3 layers," APL Mater. **7**(3), 031114 (2019).

[132] H.J. von Bardeleben, J.L. Cantin, A. Parisini, A. Bosio, and R. Fornari, "Conduction mechanism and shallow donor properties in silicon-doped ε-Ga2O3 thin films: An electron paramagnetic resonance study," Phys. Rev. Mater. **3**(8), 084601 (2019).

[133] Y. Tsai, Y. Hashimoto, Z. Sun, T. Moriki, T. Tadamura, T. Nagata, P. Mazzolini, A. Parisini, M. Bosi, L. Seravalli, T. Matsushita, and Y. Yamashita, "Photoelectron Holographic Study for Atomic Site Occupancy for Si Dopants in Si-Doped κ-Ga2O3(001)," Nano Lett. **24**(13), 3978–3985 (2024).

[134] S. Leone, R. Fornari, M. Bosi, V. Montedoro, L. Kirste, P. Doering, F. Benkhelifa, M. Prescher, C. Manz, V. Polyakov, and O. Ambacher, "Epitaxial growth of GaN/Ga2O3 and Ga2O3/GaN heterostructures for novel high electron mobility transistors," J. Cryst. Growth **534**, 125511 (2020).

[135] T. Schultz, M. Kneiß, P. Storm, D. Splith, H. von Wenckstern, C.T. Koch, A. Hammud, M. Grundmann, and N. Koch, "Growth of κ-([Al,In]xGa1-x)2O3 Quantum Wells and Their Potential for Quantum-Well Infrared Photodetectors," ACS Appl. Mater. Interfaces **15**(24), 29535–29541 (2023).

[136] Y. Yao, R.F. Davis, and L.M. Porter, "Metal Organic Chemical Vapor Deposition 2," in *Gallium Oxide Mater. Prop. Cryst. Growth Devices*, edited by M. Higashiwaki and S. Fujita, (Springer International Publishing, Cham, 2020), pp. 171–184.

[137] M. Budde, Heteroepitaxy, Surface- and Bulk Hole Transport, and Application of the p-Type Semiconducting Oxides NiO and SnO", Doctoral Dissertation, Humboldt-Universität zu Berlin, Mathematisch-Naturwissenschaftliche Fakultät (2020)

[138] T.J. Asel, E. Steinbrunner, J. Hendricks, A.T. Neal, and S. Mou, "Reduction of unintentional Si doping in β-Ga2O3 grown via plasma-assisted molecular beam epitaxy," J. Vac. Sci. Technol. A **38**(4), 043403 (2020).

[139] T. Kamimura, Y. Nakata, M.H. Wong, and M. Higashiwaki, "Normally-Off Ga 2 O 3 MOSFETs With Unintentionally Nitrogen-Doped Channel Layer Grown by Plasma-Assisted Molecular Beam Epitaxy," IEEE Electron Device Lett. **40**(7), 1064–1067 (2019).

[140] F. Baiutti, "Heterogeneous Doping and Superconductivity in La2CuO4-Based Heterostructures", Doctoral Dissertation, Max-Planck-Institut für Festkörperforschung-Stuttgart (2015)

[141] U. Korte, and G. Meyer-Ehmsen, "Transmission features in RHEED from flat surfaces," Surf. Sci. **232**(3), 367–378 (1990).

[142] M.A. Hafez, M.K. Zayed, and H.E. Elsayed-Ali, "Review: Geometric interpretation of reflection and transmission RHEED patterns," Micron **159**, 103286 (2022).

[143] A. Bosio, C. Borelli, A. Parisini, M. Pavesi, S. Vantaggio, and R. Fornari, "A Metal-Oxide Contact to ε-Ga2O3 Epitaxial Films and Relevant Conduction Mechanism," ECS J. Solid State Sci. Technol. **9**(5), 055002 (2020).

[144] S. Grover, S. Sahu, P. Zhang, K.O. Davis, and S.K. Kurinec, "Standardization of Specific Contact Resistivity Measurements using Transmission Line Model (TLM)," in *2020 IEEE 33rd Int. Conf. Microelectron. Test Struct. ICMTS*, (2020), pp. 1–6.

[145] L. J. van der Pauw, "A method of measuring specific resistivity and Hall effect of dises of arbitrary shape," Philips. Res. Repts, **13**, 1-9 (1958).

[146] "Charge-Based and Probe Characterization," in *Semicond. Mater. Device Charact.*, (John Wiley & Sons, Ltd, 2005), pp. 523–562.

[147] G.A. Perley, "Measurements with the Dropping Mercury Electrode," Trans. Electrochem. Soc. **76**(1), 91 (1939).

[148] B.M. Janzen, P. Mazzolini, R. Gillen, V.F.S. Peltason, L.P. Grote, J. Maultzsch, R. Fornari, O. Bierwagen, and M.R. Wagner, "Comprehensive Raman study of orthorhombic κ/ε-Ga 2 O 3 and the impact of rotational domains," J. Mater. Chem. C **9**(40), 14175–14189 (2021).

[149] "Chemical and Physical Characterization," in *Semicond. Mater. Device Charact.*, (John Wiley & Sons, Ltd, 2005), pp. 627–688.

[150] N.P. Lockyer, S. Aoyagi, J.S. Fletcher, I.S. Gilmore, P.A.W. van der Heide, K.L. Moore, B.J. Tyler, and L.-T. Weng, "Secondary ion mass spectrometry," Nat. Rev. Methods Primer **4**(1), 1–21 (2024).

[151] S. Courtas, M. Grégoire, X. Federspiel, N. Bicaïs-Lepinay, and C. Wyon, "Electron BackScattered Diffraction (EBSD) use and applications in newest technologies development," Microelectron. Reliab. **46**(9), 1530–1535 (2006).

[152] L.J. Brillson, "Applications of depth-resolved cathodoluminescence spectroscopy," J. Phys. Appl. Phys. **45**(18), 183001 (2012).

[153] A. Parisini, P. Mazzolini, O. Bierwagen, C. Borelli, K. Egbo, A. Sacchi, M. Bosi, L. Seravalli, A. Tahraoui, and R. Fornari, "Study of SnO/ε-Ga2O3 p–n diodes in planar geometry," J. Vac. Sci. Technol. A **40**(4), 042701 (2022).

[154] O.F. Vyvenko, S.V. Shapenkov, E.V. Ubyivovk, A.S. Bondarenko, A.I. Pechnikov, V.I. Nikolaev, and S.I. Stepanov, "Twin domain and antiphase boundaries in microcrystals of K-phase Ga2O3," Materialia **32**, 101942 (2023).

[155] S. Rafique, L. Han, A.T. Neal, S. Mou, J. Boeckl, and H. Zhao, "Towards High-Mobility Heteroepitaxial β-Ga 2 O 3 on Sapphire − Dependence on The Substrate Off-Axis Angle," Phys. Status Solidi A **215**(2), 1700467 (2018).

[156] I. Cora, Zs. Fogarassy, R. Fornari, M. Bosi, A. Rečnik, and B. Pécz, "*In situ* TEM study of κ→β and κ→γ phase transformations in Ga2O3," Acta Mater. **183**, 216–227 (2020).

[157] M. Budde, D. Splith, P. Mazzolini, A. Tahraoui, J. Feldl, M. Ramsteiner, H. von Wenckstern, M. Grundmann, and O. Bierwagen, "SnO/β-Ga2O3 vertical pn heterojunction diodes," Appl. Phys. Lett. **117**(25), 252106 (2020).

[158] M. Kneiß, P. Storm, A. Hassa, D. Splith, H. von Wenckstern, M. Lorenz, and M. Grundmann, "Growth, structural and optical properties of coherent κ-(AlxGa1−x)2O3/κ-Ga2O3 quantum well superlattice heterostructures," APL Mater. **8**(5), 051112 (2020).

[159] Y. Oshima, K. Kawara, T. Oshima, and T. Shinohe, "In-plane orientation control of (001) κ-Ga2O3 by epitaxial lateral overgrowth through a geometrical natural selection mechanism," Jpn. J. Appl. Phys. **59**(11), 115501 (2020).

[160] V.I. Nikolaev, A.Y. Polyakov, A.V. Myasoedov, I.S. Pavlov, A.V. Morozov, A.I. Pechnikov, I.-H. Lee, E.B. Yakimov, A.A. Vasilev, M.P. Scheglov, A.I. Kochkova, and S.J. Pearton, "Editors' Choice—Structural, Electrical, and Luminescent Properties of Orthorhombic κ-Ga2O3 Grown by Epitaxial Lateral Overgrowth," ECS J. Solid State Sci. Technol. **12**(11), 115001 (2023).

[161] Y. Oshima, E.G. Víllora, and K. Shimamura, "Quasi-heteroepitaxial growth of β-Ga2O3 on off-angled sapphire (0001) substrates by halide vapor phase epitaxy," J. Cryst. Growth **410**, 53–58 (2015).

[162] W. Xu, J. Shi, Y. Li, X. Xiu, S. Ding, Z. Xie, T. Tao, P. Chen, B. Liu, R. Zhang, and Y. Zheng, "Study of β-Ga2O3 films hetero-epitaxially grown on off-angled sapphire substrates by halide vapor phase epitaxy," Mater. Lett. **289**, 129411 (2021).

[163] P. Vogt, "Growth Kinetics, Thermodynamics, and Phase Formation of Group-III and IV Oxides during Molecular Beam Epitaxy", Doctoral Dissertation, Humboldt-Universität zu Berlin, Mathematisch-Naturwissenschaftliche Fakultät (2017).

[164] X. Xia, Y. Chen, Q. Feng, H. Liang, P. Tao, M. Xu, and G. Du, "Hexagonal phase-pure wide band gap ε-Ga2O3 films grown on 6H-SiC substrates by metal organic chemical vapor deposition," Appl. Phys. Lett. **108**(20), 202103 (2016).

[165] A. Ardenghi, O. Bierwagen, J. Lähnemann, J. Kler, A. Falkenstein, M. Martin, and P. Mazzolini, "Phase-selective growth of κ- vs β-Ga2O3 and (InxGa1-x)2O3 by In-mediated metal exchange catalysis in plasma-assisted molecular beam epitaxy," arXiv.Org, (2023).

[166] K. Sasaki, A. Kuramata, T. Masui, E.G. Víllora, K. Shimamura, and S. Yamakoshi, "Device-Quality β-Ga2O3 Epitaxial Films Fabricated by Ozone Molecular Beam Epitaxy," Appl. Phys. Express **5**(3), 035502 (2012).

[167] O. Bierwagen, P. Vogt, and P. Mazzolini, "Plasma-Assisted Molecular Beam Epitaxy 2," in *Gallium Oxide Mater. Prop. Cryst. Growth Devices*, edited by M. Higashiwaki and S. Fujita, (Springer International Publishing, Cham, 2020), pp. 95–121.

[168] T. Arima, D. Higashiyama, Y. Kaneko, J.P. He, T. Goto, S. Miyasaka, T. Kimura, K. Oikawa, T. Kamiyama, R. Kumai, and Y. Tokura, "Structural and magnetoelectric properties of Ga 2 − x Fe x O 3 single crystals grown by a floating-zone method," Phys. Rev. B **70**(6), 064426 (2004).

[169] C.C. Mai, "Thermal growth and chemical etching of silicon dioxide film," Doctoral Dissertation, Oregon State University (1965).

[170] F. Cuccureddu, S. Murphy, I.V. Shvets, M. Porcu, H.W. Zandbergen, N.S. Sidorov, and S.I. Bozhko, "Surface morphology of c-plane sapphire (α-alumina) produced by high temperature anneal," Surf. Sci. **604**(15), 1294–1299 (2010).

[171] R. Verre, R.G.S. Sofin, V. Usov, K. Fleischer, D. Fox, G. Behan, H. Zhang, and I.V. Shvets, "Equilibrium faceting formation in vicinal Al2O3 (0001) surface caused by annealing," Surf. Sci. **606**(23), 1815–1820 (2012).

[172] Y. Li, X. Xiu, W. Xu, L. Zhang, Z. Xie, T. Tao, P. Chen, B. Liu, R. Zhang, and Y. Zheng, "Microstructural analysis of heteroepitaxial β-Ga2O3 films grown on (0001) sapphire by halide vapor phase epitaxy," J. Phys. Appl. Phys. **54**(1), 014003 (2020).

[173] P. Mazzolini, C. Wouters, M. Albrecht, A. Falkenstein, M. Martin, P. Vogt, and O. Bierwagen "Molecular Beam Epitaxy of β-(InxGa1–x)2O3 on β-Ga2O3 (010): Compositional Control, Layer Quality, Anisotropic Strain Relaxation, and Prospects for Two-Dimensional Electron Gas Confinement," ACS Applied Materials & Interfaces, **16**(19), 12793-12804 (2024).

[174] P. Mazzolini, J.B. Varley, A. Parisini, A. Sacchi, M. Pavesi, A. Bosio, M. Bosi, L. Seravalli, B.M. Janzen, M.N. Marggraf, N. Bernhardt, M.R. Wagner, A. Ardenghi, O. Bierwagen, A. Falkenstein, J. Kler, R.A. De Souza, M. Martin, F. Mezzadri, C. Borelli, and R. Fornari, "Engineering shallow and deep level defects in κ-Ga2O3 thin films: comparing metal-organic vapour phase epitaxy to molecular beam epitaxy and the effect of annealing treatments," Mater. Today Phys. **45**, 101463 (2024).

[175] D. Kaur, and M. Kumar, "A Strategic Review on Gallium Oxide Based Deep-Ultraviolet Photodetectors: Recent Progress and Future Prospects," Adv. Opt. Mater. **9**(9), (2021).

[176] C. Borelli, A. Bosio, A. Parisini, M. Pavesi, S. Vantaggio, and R. Fornari, "Electronic properties and photo-gain of UV-C photodetectors based on high-resistivity orthorhombic κ-Ga2O3 epilayers," Mater. Sci. Eng. B **286**, 116056 (2022).

[177] Y.K. Frodason, K.M. Johansen, L. Vines, and J.B. Varley, "Self-trapped hole and impurity-related broad luminescence in β-Ga2O3," J. Appl. Phys. **127**(7), 075701 (2020).

[178] M. Mulazzi, F. Reichmann, A. Becker, W.M. Klesse, P. Alippi, V. Fiorentini, A. Parisini, M. Bosi, and R. Fornari, "The electronic structure of ε-Ga2O3," APL Mater. **7**(2), 022522 (2019).

[179] K. Irmscher, Z. Galazka, M. Pietsch, R. Uecker, and R. Fornari, "Electrical properties of β-Ga2O3 single crystals grown by the Czochralski method," J. Appl. Phys. **110**(6), 063720 (2011).

[180] V. Montedoro, A. Torres, S. Dadgostar, J. Jimenez, M. Bosi, A. Parisini, and R. Fornari, "Cathodoluminescence of undoped and Si-doped ε-Ga2O3 films," Mater. Sci. Eng. B **264**, 114918 (2021).

[181] S. Li, J. Yue, X. Ji, C. Lu, Z. Yan, P. Li, D. Guo, Z. Wu, and W. Tang, "Oxygen vacancies modulating the photodetector performances in ε-Ga2O3 thin films," J. Mater. Chem. C **9**(16), 5437–5444 (2021).

[182] A. Parisini, A. Bosio, H.J. von Bardeleben, J. Jimenez, S. Dadgostar, M. Pavesi, A. Baraldi, S. Vantaggio, and R. Fornari, "Deep and shallow electronic states associated to doping, contamination and intrinsic defects in *ε*-Ga2O3 epilayers," Mater. Sci. Semicond. Process. **138**, 106307 (2022).

[183] J. Stoch, and J. Gablankowska-Kukucz, "The effect of carbonate contaminations on the XPS O 1s band structure in metal oxides," Surf. Interface Anal. **17**(3), 165–167 (1991).

[184] A. Shchukarev, and D. Korolkov, "XPS Study of group IA carbonates," Open Chem. **2**(2), 347–362 (2004).

[185] J.E.N. Swallow, J.B. Varley, L.A.H. Jones, J.T. Gibbon, L.F.J. Piper, V.R. Dhanak, and T.D. Veal, "Transition from electron accumulation to depletion at β-Ga2O3 surfaces: The role of hydrogen and the charge neutrality level," APL Mater. **7**(2), 022528 (2019).

[186] Y. An, S. Wang, L. Duan, J. Liu, and Z. Wu, "Local Mn structure and room temperature ferromagnetism in Mn-doped In2O3 films," Appl. Phys. Lett. **102**(21), 212411 (2013).

[187] D.Y. Guo, Z.P. Wu, Y.H. An, X.C. Guo, X.L. Chu, C.L. Sun, L.H. Li, P.G. Li, and W.H. Tang, "Oxygen vacancy tuned Ohmic-Schottky conversion for enhanced performance in β-Ga2O3 solar-blind ultraviolet photodetectors," Appl. Phys. Lett. **105**(2), 023507 (2014).

[188] H. Idriss, "On the wrong assignment of the XPS O1s signal at 531–532 eV attributed to oxygen vacancies in photo- and electro-catalysts for water splitting and other materials applications," Surf. Sci. **712**, (2021).

[189] T. Gake, Y. Kumagai, and F. Oba, "First-principles study of self-trapped holes and acceptor impurities in Ga2O3 polymorphs," Phys. Rev. Materials **3**, 044603 (2019).

[190] A. Karjalainen, P.M. Weiser, I. Makkonen, V.M. Reinertsen, L. Vines, and F. Tuomisto, "Interplay of vacancies, hydrogen, and electrical compensation in irradiated and annealed n-type β-Ga2O3," J. Appl. Phys. **129**(16), 165702 (2021).

[191] A. Karjalainen, V. Prozheeva, K. Simula, I. Makkonen, V. Callewaert, J.B. Varley, and F. Tuomisto, "Split Ga vacancies and the unusually strong anisotropy of positron annihilation spectra in β-Ga2O3" Phys. Rev. B **102**(19), 195207 (2020).

[192] A. Karjalainen, I. Makkonen, J. Etula, K. Goto, H. Murakami, Y. Kumagai, and F. Tuomisto, "Split Ga vacancies in n-type and semi-insulating β-Ga2O3 single crystals," Appl. Phys. Lett. **118**(7), 072104 (2021).

[193] F. Tuomisto, A. Karjalainen, and I. Makkonen, "Split Ga vacancies: abundant defects in beta-Ga2O3," in *Oxide-Based Mater. Devices XII*, (SPIE, 2021), pp. 8–14.

[194] F. Tuomisto, "Ga vacancies in β-Ga2O3: split or not?," Jpn. J. Appl. Phys. **62**(SF), SF0802 (2023).

[195] J.B. Varley, H. Peelaers, A. Janotti, and C.G.V. de Walle, "Hydrogenated cation vacancies in semiconducting oxides," J. Phys. Condens. Matter **23**(33), 334212 (2011).

[196] Y.K. Frodason, J.B. Varley, K.M.H. Johansen, L. Vines, and C.G. Van De Walle, "Migration of Ga vacancies and interstitials in β-Ga2 O3," Phys. Rev. B **107**(2), (2023).

[197] W.B. Fowler, M. Stavola, Y. Qin, and P. Weiser, "Trapping of multiple H atoms at the Ga(1) vacancy in β-Ga2O3," Appl. Phys. Lett. **117**(14), 142101 (2020).

[198] Y. K. Frodason, C. Zimmermann, E.F. Verhoeven, P.M. Weiser, L. Vines, and J.B. Varley, "Multistability of isolated and hydrogenated Ga--O divacancies in β-Ga2O3" Phys. Rev. Mater. **5**(2), 025402 (2021).

[199] S. Mu, M. Wang, J.B. Varley, J.L. Lyons, D. Wickramaratne, and C.G. Van de Walle, "Role of carbon and hydrogen in limiting n-type doping of monoclinic AlxGax-2O3" Phys. Rev. B **105**(15), 155201 (2022).

[200] J.M. Johnson, Z. Chen, J.B. Varley, C.M. Jackson, E. Farzana, Z. Zhang, A.R. Arehart, H.-L. Huang, A. Genc, S.A. Ringel, C.G. Van de Walle, D.A. Muller, and J. Hwang, "Unusual Formation of Point-Defect Complexes in the Ultrawide-Band-Gap Semiconductor β − Ga 2 O 3," Phys. Rev. X **9**(4), 041027 (2019).

[201] S. J. Pearton, J. Yang, P. H. Patrick, F. Ren, J. Kim, M. J. Tadjer, Michael A. Mastro, "A review of Ga2O3 materials, processing, and devices," Applied Physics Reviews, AIP Publishing, **5**(1), 011301 (2018).

[202] A. Bosio, A. Parisini, A. Lamperti, C. Borelli, L. Fornasini, M. Bosi, I. Cora, Z. Fogarassy, B. Pécz, Z. Zolnai, A. Németh, S. Vantaggio, and R. Fornari, "n-Type doping of ε-Ga2O3 epilayers by high-temperature tin diffusion," Acta Mater. **210**, 116848 (2021).

[203] D. Seo, J. Baek, S. Kim, B.J. Cho, and W.S. Hwang, "Sn-doped n-type amorphous gallium oxide semiconductor with energy bandgap of 4.9 eV," Mater. Sci. Semicond. Process. **169**, 107922 (2024).

[204] M.D. Heinemann, J. Berry, G. Teeter, T. Unold, and D. Ginley, "Oxygen deficiency and Sn doping of amorphous Ga2O3," Appl. Phys. Lett. **108**(2), 022107 (2016).

[205] A. Kyrtsos, M. Matsubara, and E. Bellotti, "On the feasibility of p-type Ga2O3," Appl. Phys. Lett. **112**(3), 032108 (2018).

[206] Y. Qu, Z. Wu, M. Ai, D. Guo, Y. An, H. Yang, L. Li, and W. Tang, "Enhanced Ga2O3/SiC ultraviolet photodetector with graphene top electrodes," J. Alloys Compd. **680**, 247–251 (2016).

[207] W.Y. Weng, T.J. Hsueh, S.J. Chang, G.J. Huang, and H.T. Hsueh, "A β -Ga2O3/GaN Hetero-Structured Solar-Blind and Visible-Blind Dual-Band Photodetector," IEEE Sens. J. **11**(6), 1491–1492 (2011).

[208] Yoshihiro Kokubun and Shohei Kubo and Shinji Nakagomi, "All-oxide p–n heterojunction diodes comprising p-type NiO and n-type β-Ga 2 O 3," Appl. Phys. Express **9**(9), 091101 (2016).

[209] Y. Wang, H. Gong, Y. Lv, X. Fu, S. Dun, T. Han, H. Liu, X. Zhou, S. Liang, J. Ye, R. Zhang, A. Bu, S. Cai, and Z. Feng, "2.41 kV Vertical P-Nio/n-Ga2O3 Heterojunction Diodes With a Record Baliga's Figure-of-Merit of 5.18 GW/cm2," IEEE Trans. Power Electron. **37**(4), 3743–3746 (2022).

[210] X. Lu, X. Zhou, H. Jiang, K.W. Ng, Z. Chen, Y. Pei, K.M. Lau, and G. Wang, "1-kV Sputtered p-NiO/n-Ga2O3 Heterojunction Diodes With an Ultra-Low Leakage Current Below 1 \mu A/cm2," IEEE Electron Device Lett. **41**(3), 449–452 (2020).

[211] P. Schlupp, D. Splith, H. von Wenckstern, and M. Grundmann, "Electrical Properties of Vertical p-NiO/n-Ga2O3 and p-ZnCo2O4/n-Ga2O3 pn-Heterodiodes," Phys. Status Solidi A **216**(7), 1800729 (2019).

[212] J. Zhang, S. Han, M. Cui, X. Xu, W. Li, H. Xu, C. Jin, M. Gu, L. Chen, and K.H.L. Zhang, "Fabrication and Interfacial Electronic Structure of Wide Bandgap NiO and Ga2O3 p–n Heterojunction," ACS Appl. Electron. Mater. **2**(2), 456–463 (2020).

[213] K.-H. Li, N. Alfaraj, C.H. Kang, L. Braic, M.N. Hedhili, Z. Guo, T.K. Ng, and B.S. Ooi, "Deep-Ultraviolet Photodetection Using Single-Crystalline β-Ga2O3/NiO Heterojunctions," ACS Appl. Mater. Interfaces **11**(38), 35095–35104 (2019).

[214] Y. Deng, Z. Yang, T. Xu, H. Jiang, K.W. Ng, C. Liao, D. Su, Y. Pei, Z. Chen, G. Wang, and X. Lu, "Band alignment and electrical properties of NiO/β-Ga2O3 heterojunctions with different β-Ga2O3 orientations," Appl. Surf. Sci. **622**, 156917 (2023).

[215] M.J. Tadjer, L.E. Luna, E. Cleveland, K.D. Hobart, and F.J. Kub, "(Invited) Fabrication and Characterization of β-Ga2O3 Heterojunction Rectifiers," ECS Trans. **85**(7), 21 (2018).

[216] J. van Elp, H. Eskes, P. Kuiper, and G.A. Sawatzky, "Electronic structure of Li-doped NiO," Phys. Rev. B **45**(4), 1612–1622 (1992).

[217] W.-L. Jang, Y.-M. Lu, W.-S. Hwang, and W.-C. Chen, "Electrical properties of Li-doped NiO films," J. Eur. Ceram. Soc. **30**(2), 503–508 (2010).

[218] S. Sikdar, B.P. Sahu, and S. Dhar, "Investigation of lithium (Li) doping on the resistive switching property of p-Li:NiO/n-β-Ga2O3 thin-film based heterojunction devices," Appl. Phys. Lett. **122**(2), 023501 (2023).

[219] K. Danno, M. Kado, T. Hara, T. Takasugi, H. Yamano, Y. Umetani, and T. Shoji, "Large critical field of Li-doped NiO investigated by p+-NiO/n+-Ga2O3 heterojunction diodes," Jpn. J. Appl. Phys. **62**(SF), SF1007 (2023).

[220] X. Lu, Y. Deng, Y. Pei, Z. Chen, and G. Wang, "Recent advances in NiO/Ga2O3 heterojunctions for power electronics," J. Semicond. **44**(6), 061802–15 (2023).

[221] K. Zhang, V.G.T. Vangipuram, H.-L. Huang, J. Hwang, and H. Zhao, "Discovery of a Robust P-Type Ultrawide Bandgap Oxide Semiconductor: LiGa5O8," Adv. Electron. Mater. **11**, 2300550, (2025).

[222] J.L. Lyons, "Deep polaronic acceptors in LiGa5O8," J. Appl. Phys. **135**(16), 165705 (2024).

[223] K. Zhang, V.G. Thirupakuzi Vangipuram, C. Chae, J. Hwang, and H. Zhao, "Experimental determination of the band offsets at the UWBG p-LiGa5O8/Ga2O3 interface," Appl. Phys. Lett. **124**(12), 122106 (2024).

[224] G. Ou, Y. Xu, B. Wen, R. Lin, B. Ge, Y. Tang, Y. Liang, C. Yang, K. Huang, D. Zu, R. Yu, W. Chen, J. Li, H. Wu, L.-M. Liu, and Y. Li, "Tuning defects in oxides at room temperature by lithium reduction," Nat. Commun. **9**(1), 1302 (2018).

[225] P. Ščajev, R. Durena, P. Onufrijevs, S. Miasojedovas, T. Malinauskas, S. Stanionyte, A. Zarkov, A. Zukuls, I. Bite, and K. Smits, "Morphological and optical property study of Li doped ZnO produced by microwave-assisted solvothermal synthesis," Mater. Sci. Semicond. Process. **135**, 106069 (2021).

[226] J.G. Lu, Y.Z. Zhang, Z.Z. Ye, Y.J. Zeng, H.P. He, L.P. Zhu, J.Y. Huang, L. Wang, J. Yuan, B.H. Zhao, and X.H. Li, "Control of p- and n-type conductivities in Li-doped ZnO thin films," Appl. Phys. Lett. **89**(11), 112113 (2006).

[227] D. O. Scanlon, and G. W. Watson, "On the possibility of p-type SnO 2," J. Mater. Chem. **22**(48), 25236–25245 (2012).

[228] Z. Galazka, K. Irmscher, R. Schewski, I.M. Hanke, M. Pietsch, S. Ganschow, D. Klimm, A. Dittmar, A. Fiedler, T. Schroeder, and M. Bickermann, "Czochralski-grown bulk β-Ga2O3 single crystals doped with mono-, di-, tri-, and tetravalent ions," J. Cryst. Growth **529**, 125297 (2020).

[229] I. López, M. Alonso-Orts, E. Nogales, B. Méndez, and J. Piqueras, "Influence of Li doping on the morphology and luminescence of Ga2O3microrods grown by a vapor-solid method," Semicond. Sci. Technol. **31**(11), 115003 (2016).

[230] J. Jiang, J. Zhang, J. Li, and D. Xu, "Red-light emission of Li-doped Ga2O3 one-dimensional nanostructures and the luminescence mechanism," Chem. Phys. Lett. **719**, 8–11 (2019).

[231] Z. Cui, and H. Wu, "Metal atoms adsorbed Ga2O3 monolayer: As a potential application in optoelectronic devices," Micro Nanostructures **180**, 207613 (2023).

[232] "Database of Ionic Radii: http://abulafia.mt.ic.ac.uk/shannon/ptable.php."

[233] E.G. Prout, and V.C. Liddiard, "The thermal decomposition of lithium azide," J. Inorg. Nucl. Chem. **35**(7), 2183–2193 (1973).

[234] Y. Kokubun, S. Kubo, and S. Nakagomi, "All-oxide p–n heterojunction diodes comprising p-type NiO and n-type β-Ga2O3," Appl. Phys. Express **9**(9), 091101 (2016).

[235] R.A. De Souza, and M. Martin, "Probing Diffusion Kinetics with Secondary Ion Mass Spectrometry," MRS Bull. **34**(12), 907–914 (2009).

[236] Y. Chung, and B.J. Wuensch, "An improved method, based on Whipple's exact solution, for obtaining accurate grain-boundary diffusion coefficients from shallow solute concentration gradients," J. Appl. Phys. **79**(11), 8323–8329 (1996).

[237] J. Wu, C. Li, X. Rong, P. Cao, S. Han, Y. Zeng, W. Liu, D. Zhu, and Y. Lu, "Temperature-Dependent Crystallization of Ga2O3 for Ultraviolet Photodetectors," J. Electron. Mater. **49**(8), 4581–4588 (2020).

[238] L. Binet, and D. Gourier, "Origin of the blue luminescence of β-Ga2O3," J. Phys. Chem. Solids **59**(8), 1241–1249 (1998).

[239] Q.D. Ho, T. Frauenheim, and P. Deák, "Origin of photoluminescence in β-Ga2O3," Phys. Rev. B **97**(11), 115163 (2018).

[240] K. Hara, and Y. Ishibashi, "Raman Scattering Study of Lithium Gallate LiGa5O8," J. Phys. Soc. Jpn. **55**(12), 4500–4503 (1986).

[241] C. Julien, M. Massot, R. Baddour-Hadjean, S. Franger, S. Bach, and J.P. Pereira-Ramos, "Raman spectra of birnessite manganese dioxides," Solid State Ion. **159**(3), 345–356 (2003).

[242] Y. K. Hommedal, Y. K. Frodason, L. Vines, and K. M. H. Johansen, "Trap-limited diffusion of Zn in β-Ga2O3," Phys. Rev. Materials **7**, 035401 (2023).

[243] E.G. Víllora, K. Shimamura, Y. Yoshikawa, T. Ujiie, and K. Aoki, "Electrical conductivity and carrier concentration control in β-Ga2O3 by Si doping," Appl. Phys. Lett. **92**(20), 202120 (2008).

[244] E. Korhonen, F. Tuomisto, D. Gogova, G. Wagner, M. Baldini, Z. Galazka, R. Schewski, and M. Albrecht, "Electrical compensation by Ga vacancies in Ga2O3 thin films," Appl. Phys. Lett. **106**(24), 242103 (2015).

[245] Y. Wang, C. Wu, D. Guo, P. Li, S. Wang, A. Liu, C. Li, F. Wu, and W. Tang, "All-Oxide NiO/Ga2O3 p–n Junction for Self-Powered UV Photodetector," ACS Appl. Electron. Mater. **2**(7), 2032–2038 (2020).